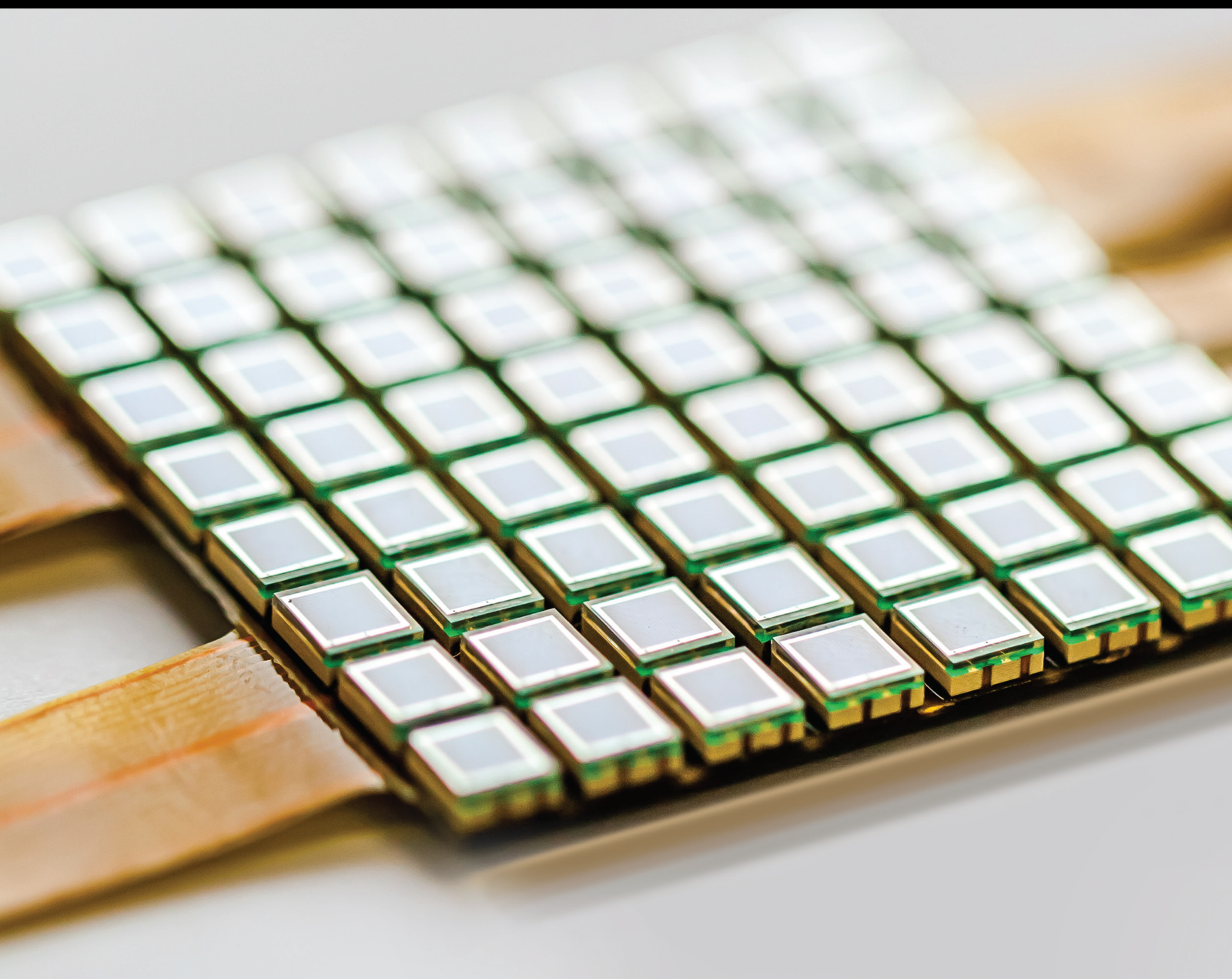


Sensor Physical Interpretation, Signal and Artificial Intelligence Processing

Lead Guest Editor: Bin Gao

Guest Editors: Yuyu Zhu, Wai Lok Woo, and Guiyun Tian





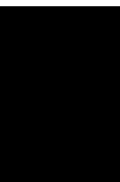
Sensor Physical Interpretation, Signal and Artificial Intelligence Processing

Journal of Sensors

**Sensor Physical Interpretation, Signal
and Artificial Intelligence Processing**

Lead Guest Editor: Bin Gao

Guest Editors: Yuyu Zhu, Wai Lok Woo, and
Guiyun Tian






Copyright © 2020 Hindawi Limited. All rights reserved.

This is a special issue published in "Journal of Sensors." All articles are open access articles distributed under the Creative Commons Attribution License, which permits unrestricted use, distribution, and reproduction in any medium, provided the original work is properly cited.

Chief Editor

Harith Ahmad , Malaysia

Associate Editors

Duo Lin , China
Fanli Meng , China
Pietro Siciliano , Italy
Guiyun Tian, United Kingdom

Academic Editors

Ghufran Ahmed , Pakistan
Constantin Apetrei, Romania
Shonak Bansal , India
Fernando Benito-Lopez , Spain
Romeo Bernini , Italy
Shekhar Bhansali, USA
Matthew Brodie, Australia
Ravikumar CV, India
Belén Calvo, Spain
Stefania Campopiano , Italy
Binghua Cao , China
Domenico Caputo, Italy
Sara Casciati, Italy
Gabriele Cazzulani , Italy
Chi Chiu Chan, Singapore
Sushank Chaudhary , Thailand
Edmon Chehura , United Kingdom
Marvin H Cheng , USA
Lei Chu , USA
Mario Collotta , Italy
Marco Consales , Italy
Jesus Corres , Spain
Andrea Cusano, Italy
Egidio De Benedetto , Italy
Luca De Stefano , Italy
Manel Del Valle , Spain
Franz L. Dickert, Austria
Giovanni Diraco, Italy
Maria de Fátima Domingues , Portugal
Nicola Donato , Italy
Sheng Du , China
Amir Elzawwy, Egypt
Mauro Epifani , Italy
Congbin Fan , China
Lihang Feng, China
Vittorio Ferrari , Italy
Luca Francioso, Italy



Libo Gao , China
Carmine Granata , Italy
Pramod Kumar Gupta , USA
Mohammad Haider , USA
Agustin Herrera-May , Mexico
María del Carmen Horrillo, Spain
Evangelos Hristoforou , Greece
Grazia Iadarola , Italy
Syed K. Islam , USA
Stephen James , United Kingdom
Sana Ullah Jan, United Kingdom
Bruno C. Janegitz , Brazil
Hai-Feng Ji , USA
Shouyong Jiang, United Kingdom
Roshan Prakash Joseph, USA
Niravkumar Joshi, USA
Rajesh Kaluri , India
Sang Sub Kim , Republic of Korea
Dr. Rajkishor Kumar, India
Rahul Kumar , India
Nageswara Lalam , USA
Antonio Lazaro , Spain
Chengkuo Lee , Singapore
Chenzong Li , USA
Zhi Lian , Australia
Rosalba Liguori , Italy
Sangsoon Lim , Republic of Korea
Huan Liu , China
Jin Liu , China
Eduard Llobet , Spain
Jaime Lloret , Spain
Mohamed Louzazni, Morocco
Jesús Lozano , Spain
Oleg Lupan , Moldova
Leandro Maio , Italy
Pawel Malinowski , Poland
Carlos Marques , Portugal
Eugenio Martinelli , Italy
Antonio Martinez-Olmos , Spain
Giuseppe Maruccio , Italy
Yasuko Y. Maruo, Japan
Zahid Mehmood , Pakistan
Carlos Michel , Mexico
Stephen. J. Mihailov , Canada
Bikash Nakarmi, China

Ehsan Namaziandost , Iran
Heinz C. Neitzert , Italy
Sing Kiong Nguang , New Zealand
Calogero M. Oddo , Italy
Tinghui Ouyang, Japan
SANDEEP KUMAR PALANISWAMY ,
India
Alberto J. Palma , Spain
Davide Palumbo , Italy
Abinash Panda , India
Roberto Paolesse , Italy
Akhilesh Pathak , Thailand
Giovanni Pau , Italy
Giorgio Pennazza , Italy
Michele Penza , Italy
Sivakumar Poruran, India
Stelios Potirakis , Greece
Biswajeet Pradhan , Malaysia
Giuseppe Quero , Italy
Linesh Raja , India
Maheswar Rajagopal , India
Valerie Renaudin , France
Armando Ricciardi , Italy
Christos Riziotis , Greece
Ruthber Rodriguez Serrezuela , Colombia
Maria Luz Rodriguez-Mendez , Spain
Jerome Rossignol , France
Maheswaran S, India
Ylias Sabri , Australia
Sourabh Sahu , India
José P. Santos , Spain
Sina Sareh, United Kingdom
Isabel Sayago , Spain
Andreas Schütze , Germany
Praveen K. Sekhar , USA
Sandra Sendra, Spain
Sandeep Sharma, India
Sunil Kumar Singh Singh , India
Yadvendra Singh , USA
Afaque Manzoor Soomro , Pakistan
Vincenzo Spagnolo, Italy
Kathiravan Srinivasan , India
Sachin K. Srivastava , India
Stefano Stassi , Italy

Danfeng Sun, China
Ashok Sundramoorthy, India
Salvatore Surdo , Italy
Roshan Thotagamuge , Sri Lanka
Guiyun Tian , United Kingdom
Sri Ramulu Torati , USA
Abdellah Touhafi , Belgium
Hoang Vinh Tran , Vietnam
Aitor Urrutia , Spain
Hana Vaisocherova - Lislalova , Czech
Republic
Everardo Vargas-Rodriguez , Mexico
Xavier Vilanova , Spain
Stanislav Vitek , Czech Republic
Luca Vollero , Italy
Tomasz Wandowski , Poland
Bohui Wang, China
Qihao Weng, USA
Penghai Wu , China
Qiang Wu, United Kingdom
Yuedong Xie , China
Chen Yang , China
Jiachen Yang , China
Nitesh Yelve , India
Aijun Yin, China
Chouki Zerrouki , France


Contents

A Computer Simulator Model for Generating Sulphuric Acid and Improve the Operational Results, Using Operational Data from a Chemical Plant

Claudio Leiva , Víctor Flores , and Carolina Aguilar


Research Article (10 pages), Article ID 8873039, Volume 2020 (2020)

Energy-Efficient Time-Domain Equilibrium Scheduling and Optimization Scheme for Energy Harvesting-Powered D2D Communication

Ying Luo , Min Zeng, Hong Jiang, and Bin Han


Research Article (16 pages), Article ID 8839681, Volume 2020 (2020)

Parameter Recognition of Mode-Converted Wave in Single-Source Ultrasound Using Gabor Transform for Bolt Axial Stress Evaluation

Ping Chen , Xingliang He, and Wei Song

Research Article (11 pages), Article ID 8883845, Volume 2020 (2020)

Active Vibration Control of PID Based on Receptance Method

Lijuan Peng, Jian Wang , Guicheng Yu, Zuoxue Wang, Aijun Yin, and Hongji Ren


Research Article (8 pages), Article ID 8811448, Volume 2020 (2020)

A Multifrequency Heterodyne Phase Error Compensation Method for 3D Reconstruction

Zihao Yu , Jin Liu , Haima Yang , Bo Huang, and Yumei Jian



Research Article (10 pages), Article ID 8833305, Volume 2020 (2020)

Feedback-Dubins-RRT Recovery Path Planning of UUV in an Underwater Obstacle Environment

Bing Hao , Zheping Yan, Xuefeng Dai, and Qi Yuan



Research Article (9 pages), Article ID 8824202, Volume 2020 (2020)

Research on an Improved Metal Surface Defect Detection Sensor Based on a 3D RFID Tag Antenna

Qiang Li , Jianbin Chen , and Liang Zhao


Research Article (13 pages), Article ID 8824091, Volume 2020 (2020)

Estimation of Particulate Levels Using Deep Dehazing Network and Temporal Prior

SeHee Jung , SungMin Yang, Eunseok Lee, YongHak Lee, Jisun Ko, Sungjae Lee, JunSang Cho, Jaehwa Lee, and SungHwan Kim 

Research Article (9 pages), Article ID 8841811, Volume 2020 (2020)

Fast Traffic Sign Detection Approach Based on Lightweight Network and Multilayer Proposal Network

Hoanh Nguyen 

Research Article (13 pages), Article ID 8844348, Volume 2020 (2020)

Research Article

A Computer Simulator Model for Generating Sulphuric Acid and Improve the Operational Results, Using Operational Data from a Chemical Plant

Claudio Leiva ¹, Víctor Flores ², and Carolina Aguilar¹

¹Department of Chemical Engineering, Universidad Católica del Norte, 1270709 Antofagasta, Chile

²Department of Systems and Computer Engineering, Universidad Católica del Norte, 1270709 Antofagasta, Chile

Correspondence should be addressed to Víctor Flores; vflores@ucn.cl

Received 12 March 2020; Revised 6 August 2020; Accepted 28 August 2020; Published 8 September 2020

Academic Editor: Bin Gao

Copyright © 2020 Claudio Leiva et al. This is an open access article distributed under the Creative Commons Attribution License, which permits unrestricted use, distribution, and reproduction in any medium, provided the original work is properly cited.

The integration of both sensors and simulation in some industrial processes has received a large increase in the recent years, thanks to results such as increase in production indices or improvement in economic indicators. This document describes the development and validation of a simulation-based computer process for generating sulphuric acid. For this process, the data generated by simulation between the fixed beds of a catalytic reactor versus the results obtained using real data from a sulphuric acid production plant in the Antofagasta Region, Chile, have been used. This sulphuric acid production plant is designed for producing 720,000 tons of sulphuric acid annually, with a production capacity of 26 MW, which is used for both its own consumption and the Big North Interconnected System (SING, for its acronym in Spanish) and a sulphur consumption of 240,000 tons/year. For the simulation process, converter input variables such as temperature and gas flow to later observe the oxidation behavior under different operational scenarios were considered. To do it, a working method has been proposed and the software Aspen HYSYS[®] was used for the simulation. The simulation result was validated using design operational data provided by the company. The real results show a 99.9% of adjustment concerning the values obtained using the simulation. Based on the findings, a new operational scenario was created, and the economic indicators of the simulator implementation were determined: NPV = CLP 161,695,000 and IRR = 53% with a 6% monthly production increase.

1. Introduction

In copper mining production by leaching, one of the most important inputs is sulphuric acid. Recently, the production of sulphuric acid has increased, particularly in the last few decades, owing to the creation of leaching piles, as an attempt to make copper mining more sustainable and a respectful activity for the environment. In a typically industrial process, the sulphuric acid production usually consumes great amounts of energy. As an alternative for this energy consumption and as a kind of circular economy, in some specific production plants, electric energy production is currently being implemented in conjunction with the same sulphuric acid production cycle.

One way of producing sulphuric acid is using solid sulphur as input. In northern Chile, particularly in Antofagasta Region, an elemental sulphur combustion process is being

used to produce sulphuric acid and electric energy, which is utilized for its own consumption (about 30% of the electric energy produced annually), the rest being incorporated into the electric network in the called Big North Interconnected System (SING, for its acronym is Spanish). The company is obtaining good profits with this process; nevertheless, it is far from achieving optimal performance, according to its installed capacity. The plant is designed for producing 720,000 tons of sulphuric acid annually and, due to the heat generated by sulphur combustion, it can also produce 26 MW of electric energy. Previous experiences as those described in [1–4] indicate that the plant design allows producing input for a profitable activity such as copper mining.

According to the plant design, production amounts approximately to 2,060 metric tons of sulphuric acid per day, representing 24,720 metric tons per year (about 5% of

its capacity). To do this, about 680 tons of sulphur must be used daily. On the other hand, by means of an efficient cogeneration process, the company injects SING with about 145 GWh per year, efficiently using the heat produced during the sulphuric acid production process. The company reports 240,000 tons/year of sulphur consumption for both products. This kind of work enables the company to generate both products, partially meeting the needs of the market requiring sulphuric acid and obtaining additional profits by selling electric energy. In this context, the company set the following objective: improving the plant performance through the optimization of the production processes involved.

To achieve this objective and follow the authors as [5–11], a simulation process for study the sulphuric acid and electric energy production was proposed. This paper focuses on the relevance of the simulation conducted with a software specialized for simulating chemical process plant operations and the conclusions obtained after comparing simulation results with the real results obtained from the plant operation. Using this way of working, an operational scenario that allows increasing production and improving the company profitability was identified. According to the above, a proposal was made to conduct the catalytic converter simulation by using the software Aspen HYSYS® Educational license provided by Aspen Technology, Inc., which has been widely used for an in-depth analysis and optimization of various productive processes [12–18]. This tool allows analyzing performance by means of operational changes and simulating the process using design data provided by the company.

The purpose of the simulator is to evaluate the operational parameters previously in order to optimize the oxidation in each bed and, in this way, produce a greater amount of sulphuric acid. In brief, the aim is to implement a simulator for the catalytic converter using the software Aspen HYSYS® (version 9.0–educational software license), validate and establish the simulator ranges for the catalytic converter, and finally, economically evaluate the impact of applying the simulator to new operational scenarios.

In previous works like [11, 19], the use and validation of results of the Aspen HYSYS® software has been presented, and other previous studies use some similar simulation process to learn and improve the results on chemical plants. For example, in [20], a model based on the simulation and analysis results of real operational cases in a Chilean plant is described. For this case, the process and operational conditions were analyzed to improve the conversion of the system. Some works such as those described above incorporate sensor signals and data processing techniques in order to improve the precision capacity of simulation and the results. Examples of this kind of work are described in [21, 22] where the distributed control system (DSC) is used in conjunction with simulation for the aforementioned purposes.

2. Materials and Method

This study used simulation data obtained from the plant production process. The processes involved are liquid sulphur filtration and storage, sulphur combustion and SO₂ generation, catalytic oxidation from SO₂ to SO₃, sulphur acid pro-

duction, high- and low-pressure steam production, and electric energy generation.

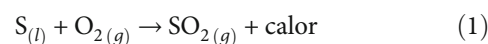
The main input for this production process is liquid sulphur. Liquid sulphur production consists of the following operations: solid sulphur reception, smelting, filtration, and storage. Figure 1 shows the sulphur acid and electric energy production process described below.

Solid sulphur is received by an ATS tower (Figure 1) and then sent by conveyor belts to the stockpile area close to the melting and filtration sections. The melting tank consists of two sections. The first one receives the solid sulphur and melts it by means of steam coils, sending it later as liquid sulphur to the second section. There are two alternatives for controlling liquid sulphur temperature. In the first one, steam coils submerged in the tank provide it with sulphur condensation heat. The second alternative is to use a sulphur recirculation pump that makes part of the liquid sulphur pass through a heat exchanger (IC, for its acronym in Spanish). This increases the sulphur temperature and returns it to the tank to facilitate smelting.

The second section of the melting tank containing liquid sulphur operates as a precapped zone. Here, a submerged impure sulphur pump feeds sulphur from the tank to the primary sulphur filter, which is a kind of sheet filter.

The following systems are involved in SO₂ generation: sulphur combustion, boiler, air drying, and diesel supply.

In this stage of the process, the following reaction occurs:



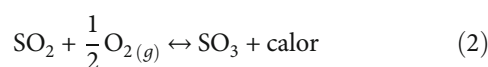
The liquid sulphur from the storage tank acts as a primary fuel. The main function of the boiler is to transfer the heat from the sulphur combustion gases to the water that will be used in the steam cycle. As a result, the gas flow cools down to 420°C and then goes into the converter. The drying air is obtained from the atmosphere and sent by a blower to the drying tower, to later enter as dried air into the combustion stage. If humidity is present, unwanted secondary reactions damaging the burner or the furnace take place. Drying occurs in the drying tower when wet air gets in contact with sulphur acid.

The drying tower (DT) is a piece of equipment coated inside with acid-resistant ceramic bricks. It has a dome of the same material where the filling, also made of ceramics, is supported. The filling is 3.5 m high and is used for increasing the gas-liquid exchange surface. On top, the tower has irrigation systems that allow a uniform distribution of the acid and mesh filters catching acid fog drops dragged by the upward gas flow.

In changing SO₂ to SO₃, the following systems are involved:

- (i) Catalytic converter
- (ii) Economizer 1, overheater 1, and overheater 2
- (iii) Gas-gas IC

In this stage of the process, the following reaction occurs:



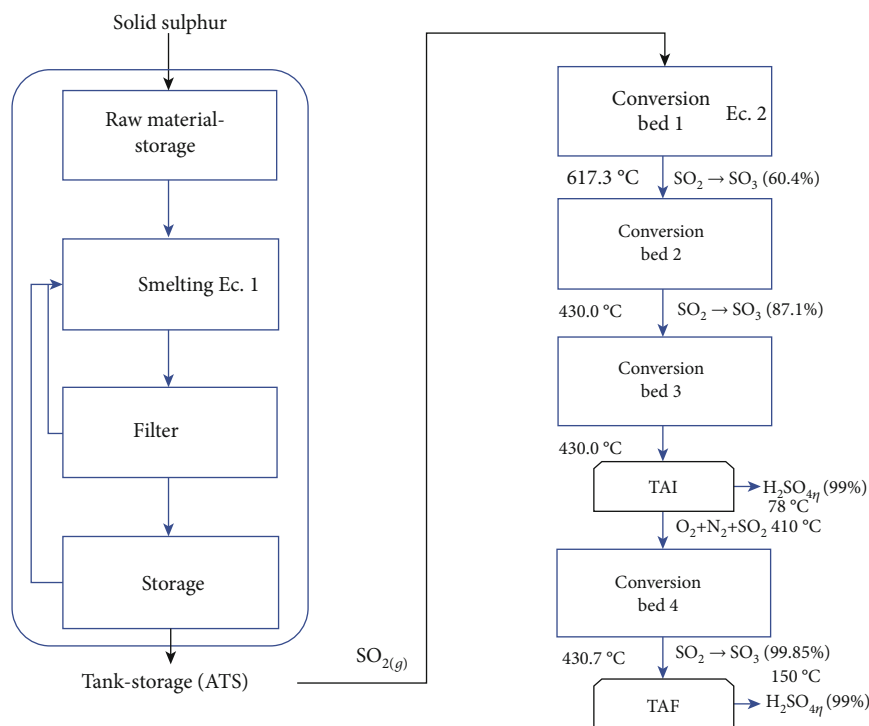


FIGURE 1: Flowchart of the process to convert $\text{SO}_{2(g)}$ into $\text{SO}_{3(g)}$ and $\text{H}_2\text{SO}_{4(l)}$ production.

SO_2 from the combustion furnace enters the 4-step catalytic converter at a flow close to $167,000 \text{ Nm}^3/\text{h}$ and 420°C . The converter is made of 304H stainless steel to support the high operational temperatures. Three ranges for temperature used in the process have been defined; labels of high, medium, and low have been assigned to ranges as detailed in Table 1.

The separation plates between individual racks are soldered. The catalyst, vanadium pentoxide (V_2O_5) in the form of pellets, is supported in stainless steel racks with spaced holes and covered with a layer of intalox ceramic saddles.

The thermal insulation of the converter meets the following requirements: optimizing high-level energy recovery, minimizing losses due to high-level energy radiation, protecting equipment at temperatures lower than the dew point and its subsequent corrosion, and keeping the heat within the system.

After entering the catalytic converter, sulphur dioxide (SO_2) reacts into the first bed, reaching a 60.4% conversion. This gas containing sulphur trioxide (SO_3) goes out at medium temperature label, due to the heat liberated during the reaction and must be cooled down before going into bed 2. Overheater 2 fulfills this task, like the other IC since the heat liberated during oxidation is transferred to the steam cycle. Once the gas is cooled down to low temperature label, it goes into the converter again through bed 2, where oxidation continues and SO_2 reaches an 87.1% cumulative conversion. Again, the gas goes out and exchanges heat with overheater 1, cooling down from medium to low, the temperature at which it goes into bed 3. Here, SO_2 reaches a 95.2%

conversion and the gas goes out at medium to the gas-gas exchanger.

This IC cools down the gas to low label, the temperature at which it feeds the intermediate absorption tower (TAI, for its acronym in Spanish). SO_3 reacts in this tower by changing into sulphuric acid, while the gas in it goes out at low temperature label. This gas contains only oxygen, nitrogen, and SO_2 that did not react. For this reason, the gas goes to bed 4, previously passing through the gas-gas exchanger where it heats up to medium label. In bed 4, SO_2 reaches a 99.85% conversion. The gas goes out at medium temperature label, to the economizer, which cools it down to low label, the necessary temperature for feeding the final absorption tower (TAF, for its acronym in Spanish).

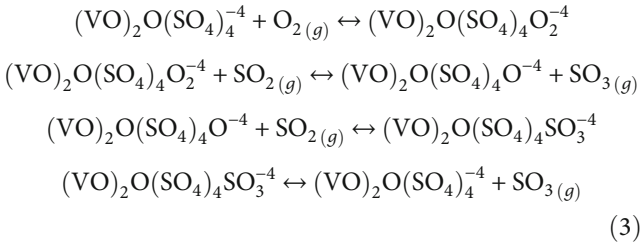
The gas-gas IC consists of a vertical and a horizontal section, which are considered separate pieces of equipment. Its function is to cool down the gas going out of bed 3 toward TAI (Figure 1), putting it in countercurrent contact with the gas from the same tower that needs to be heated to return to the converter.

Industrial SO_2 oxidation must be conducted in catalyst beds because oxidation in the gaseous phase of sulphur dioxide is kinematically inhibited, making it virtually impossible without a catalyst at a certain temperature. At normal temperature the reaction is so slow that, in practice, it does not occur. Currently, catalysts available in the market are daisy-shaped ring, simple ring, and ball-shaped catalysts. Of all the types in the market, the company uses the daisy-shaped ring since it has a bigger contact surface and less resistance to the gas flow.

TABLE 1: Temperature ranges and labels defined for the simulation process.

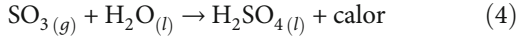
Temperature label	Ranges (°C)
Low	(100-450)
Medium	(451-520)
High	(521-750)

The reaction occurring at ionic level in the catalyst is as follows: SO₂ oxidation consists of smelting one layer on the catalyst surface. SO₂ oxidation occurs with dissolved complexes of vanadium, sulphur, and oxygen, as shown in



The reactions described above must be conducted efficiently. To do this, the bed temperature must remain over low temperature label because, below this temperature, the catalyst is deactivated, and oxidation does not occur. The following systems are involved in sulphur acid production: absorption tower, common acid tank and pumps, common acid coolers, product acid tank, and funnel.

In this stage of the process, the following reaction occurs:



The process is conducted in packed bed towers with a concave bottom and coated inside with at least two acid-resistant brick layers. The biggest amount of sulphur acid is produced in TAI. The gas from bed 3 enters through the lower side of the tower at a flow close to 157,600 Nm³/h at 205°C and 11.49% of SO₃ volumetric concentration. This gas gets in contact with the sulphur acid sprayed from the upper part and reacts to form more sulphur acid, which reaches the bottom of the tower at a greater concentration. To make the acid go out at 98.5% again, it is necessary to regulate its concentration with water and acid from the ATS. This is done automatically by means of control links. The output flow then goes into the common sulphur acid tank.

TAF receives gas with SO₂-SO₃ at a low concentration from the last bed of the catalytic converter. Its packing is different so that it can absorb all the SO₃. Due to the acid concentration at the output not increasing too much, thus, it is discharged directly into the storage tank. The final gas in this tower is discharged into the atmosphere through a funnel. An SO₂ automatic analyzer is installed at the outlet to monitor the gas emitted. Additionally, the oxygen content is measured, being used as an indicator for calculating the SO₂ content at the converter inlet.

To avoid damaging other pieces of equipment and unwanted atmospheric effluents, there is a gas filter on top

of the three towers. In TAI and TAF, acid fog is created by condensation. Therefore, the particles are smaller than in the first tower. It is possible to filtrate these particles with candle filters whose efficiency is higher than 95% and are located on the acid distribution systems. All the sulphuric acid circuits are connected to a common pump tank coated with two acid-resistant brick layers. This is recirculated to the towers by means of acid pumps. The tank is kept at high temperature since exothermic reactions occurring during the process heat the acid going into the tank. However, in order to use it, its temperature must be decreased by means of coolers.

In steam production, the following systems are involved: water treatment, heat exchangers, and waste heat absorption. The heat produced by sulphur combustion and SO₂ oxidation is recovered to produce high-pressure overheated steam necessary for generating electric energy. The pieces of equipment in charge of recovering this heat are the boiler, overheater 1, overheater 2, and economizer.

The plant uses seawater that first passes through a reverse osmosis plant and then a demineralization plant. After each treatment, the water is stored in tanks and then treated to be used for different purposes in the plant. The demineralized water is fed to a deaerator tank, which removes gases that do not condensate to avoid corrosion of the overheaters, IC, or the boiler. In addition, this tank receives condensates and low-pressure steam from other stages. Table 2 contains a brief description of the equipment used in the process and their function: heaters 1 and 2, economizer, and boiler.

Economizer 1 is used for cooling down the gas going out of bed 4 to TAF. This is done because it receives demineralized and water. The water goes to the steam dome, where it loses some of its pressure and is heated, going out as saturated steam to overheater 1. The steam going out of this device is enough to make the turbine work. In passing through the turbine, part of the steam goes to an overheater which, owing to water injection, changes it into low-pressure steam. Part of this steam is used for heating the melting tank, while the rest returns to the deaerator. Most of the steam used by the turbine goes to a series of condensers and then returns as a condensate to the deaerator, where the cycle starts again.

The equipment in charge of recovering the heat generated in the combustion furnace is the boiler and the steam dome. Most of the high-pressure steam from the plant is sent to the turbine to generate electric energy. A small part of the steam is extracted from the turbine and returned to the plant to be used at the melting and heating area. The turbine, designed for generating 26 MW, is the main equipment in this stage and is used for changing the rotating mechanical energy obtained from high-pressure steam into electric energy. The steam going out of the turbine is condensed in a condenser cooled by water. The condensate is recycled in the water-feeding tank of the plant.

3. Methodology

The methodology consists of four stages. The following variables are considered in the process: the temperature and

TABLE 2: Equipment used to transport and use gas flows between the different beds and other equipment for electric energy production.

Name	Description
Overheater 1	Overheater 1 is an IC (heat exchanger). It is a piece of equipment consisting of a shell and tubes, whose function is to transfer gas from bed 2 to bed 3, by overheating the gas
Overheater 2	Overheater 2 is also an IC. It is used for transferring overheated steam going out of bed 1 to the turbine
Economizer 1	Economizer 1 is a vertical IC, used to cool down the gas going out of bed 4 to TAF
Boiler	1,700 m ² surface, 167,000 m ³ /hr. output flow
Turbine	Vapor pressure 60 bar and medium temperature label, connected to a 26 MW generator

outlet and inlet flow of each bed (4 beds are considered in both the simulation and real operation); SO₂, SO₃, O₂, and N₂ volumetric percentage; and cumulative conversion.

- (i) Process Study. In this stage, a study to know how the plant works to obtain sulphuric acid and electric energy is conducted. The goal is to learn about it and prepare experimentation properly
- (ii) Simulation. In this stage, data are generated and prepared in accordance with the simulation characteristics
- (iii) Model Visualization and Validation. In this stage, simulation results are observed and the values of the parameters of interest and the process output (sulphuric acid and electric energy) are compared with the values of the real operation to check their validity. To define a parameter for determining the validation of results, the r^2 linear regression coefficient was obtained among the values provided by the simulator, by comparing them with data provided by the company. To validate results, the values were adjusted for each variable greater or equal to 0.95, as agreed with the company
- (iv) Result Analysis. In this stage, the analysis is aimed at establishing if results are interesting for the company. This was done by analyzing whether the results of the simulations in the different beds do or do not result in a production increase or whether the use of resources is or is not optimized in these processes

The methodological steps are further described below. Stage 1 begins with the study of the company production process, particularly the study of the catalytic converter to later develop a simulator. For systems where only gases interact, several models such as SRK, APL, and Peng-Robinson equations were examined, as shown in Equation (5).

The simulation model is based on equations that are highlighted below. First on our work, the general process is based on the thermodynamic model described in Equation (5). This model of Equation (5) is the most suitable because it is the less erratic for obtaining pressure and temperature results, according to the specific chemical process. A simulation strategy was used for the catalytic converter and the dif-

ferent heat exchangers taking part in the process. Each bed was addressed independently, that is, each bed was simulated as a continuous stirred tank reactor (CSTR) and the different heat exchangers as shell and tube IC.

$$P = \frac{RT}{(v_m - b_m)} - \frac{a_m a_i}{(v_m^2 + 2v_m b_m - b_m^2)}. \quad (5)$$

Additionally, for the simulation of the mathematical model, the balances of matter, energy, and pressure drop were made. For this purpose, Equations (6)–(8) were used.

$$F_{AO} \frac{dX}{dW} = -r_A, \quad (6)$$

$$\frac{dT}{dW} = \frac{r_A \Delta H_{rx}(T)}{F_{AO} (\sum \theta_i C_{pi} + \Delta C_p X)}, \quad (7)$$

$$\frac{dP}{dZ} = .$$

To simulate the reactor beds, first, the following velocity constants, activation energy (E_a) and the preexponential factor (A), must be solved to introduce them in the program and then select the most suitable reactor, according to the characteristics of the simulation. The reaction conducted in these reactors must be programmed in HYSYS®, based on the velocity constant, as shown in

$$r = \frac{K_1 P_{O_2} P_{SO_2} \left(1 - P_{SO_3} / \left(P_{SO_2} \sqrt{P_{O_2} K_p}\right)\right)}{22,414 \left(1 + K_2 P_{SO_2} + K_3 P_{SO_3}\right)^2}, \quad (8)$$

$$K_1 = e^{(12,160 - (5473/T))}, \quad (9)$$

$$K_2 = e^{(-9,953 + (8619/T))}, \quad (10)$$

$$K_3 = e^{(-71,745 + (52596/T))} \quad (11)$$

$$K_p = e^{(-10,68 + (11300/T))}. \quad (12)$$

To enter these data into Aspen HYSYS®, the reaction parameters must be thermodynamically consistent, the velocity constants being given by Equation (13). Following as is summarized in Equation , the activation energy (E_a) and the preexponential factor (A) are processing and

incorporated to the simulation.

$$K = AT^n * \exp\left(\frac{-E_a}{RT}\right), \quad (13)$$

$$K_1 = \exp\left(12,160 - \frac{5473}{T}\right), \quad (14)$$

$$K_1 = \exp(12,16) * \exp\left(\frac{-5473}{T}\right), \quad (15)$$

$$K_1 = 190995 * \exp\left(\frac{-5473}{T}\right), \quad (16)$$

$$A_1 = 190995, \quad (17)$$

with $n = 0$ and $T = 698$ K

$$K_1 = 19448$$

$$\ln(K_1) = \ln(A_1) * \left(\frac{-E_a}{RT}\right) \quad (18)$$

Follow with the ideal gas constant $R = 8,314$ (J/mol K) and $T = 698$ K, data known is replaced as shown in

$$\ln(19448) = \ln(190995) * \left(\frac{-E_a}{5803,17}\right), \quad (19)$$

$$E_{a1} = -4712,93 \text{ (J/mol)}.$$

This process is conducted for all speed constants, resulting in

$$A_2 = 0,000048 \rightarrow E_{a2} = 6455,01 \left(\frac{\text{J}}{\text{mol}}\right)$$

$$A_3 = 6,942 * 10^{-32} \rightarrow E_{a3} = 992,763 \left(\frac{\text{J}}{\text{mol}}\right), \quad (20)$$

$$A_p = 0,000023 \rightarrow E_{ap} = 1715,44 \left(\frac{\text{J}}{\text{mol}}\right).$$

There are two reaction models in Aspen HYSYS®. In this study, the reaction model utilizing kinetic parameters was used. They involve the flow pattern and geometric characteristics of the reactor in the simulation. In addition, the expression of the reaction velocity must be selected. In this case, it was catalytic heterogeneous. The configuration of the reaction process simulation is shown in Figure 2; the process flow is from left to right.

For the reactor simulation, the most suitable is the continuous stirred-tank reactor (CSTR), since it calculates the conditions of the reactor output currents, considering that it is perfectly mixed and the concentration in each point of the reactor is the same. This type of reactor can be used for reactions in the liquid or gaseous phase, though it must be determined. In this case, it was used in the gaseous phase. To determine CSTR, it is necessary to associate one or several reactions and define the following: reactor volume, product output temperature or heat transferred, product output pres-

sure or pressure decrease inside, reaction stoichiometry, and reaction velocity parameters for each reaction. As to dimensions, one of the following measures must be determined: volume, diameter, and height (specified in a horizontal tank).

If the cylindrical tank volume is defined, then the relationship Length/Diameter of the reactor is 3:2, by default. To simulate the whole converter, each bed was divided and simulated separately, that is, each bed was dealt with as an independent reactor (CSTR). For the fourth bed, the simulation had to be adjusted and work was done with constants different from the first three since this bed only oxidizes 4% of the total and, more than used for getting a bigger final production, this bed is utilized for complying with law no. 19,300, which sets the rules for establishing the environmental quality norms and those concerning SO₂ emission into the atmosphere.

To study the simulator behavior, the following variables were manipulated at the reactor input current: temperature, gas flow. The input current must be manipulated because it is the only one that has to be specified. The output currents of each reactor are calculated by the simulator. In the last bed, where the input current must also be specified, a 100% efficiency is assumed in the absorption tower. In other words, SO₃ going into the tower is changed into acid. For this step, the control variable is the reactor efficiency in SO₂ oxidation, that is, the SO₂ percentage going out at the end of the oxidation process.

Finally, an economic analysis was made by comparing the plant production with the new production that could be obtained based on the new operational scenario using the simulator and, in this way, to analyze the extent to which production can be increased. To accomplish the validation (the last part of stage 3) and the last stage of the methodology, the design data provided by the company were compared with the results provided by the simulator. By using the validated simulator, tests were made to estimate the best operational configurations and/or parameters to optimize the process.

4. Results and Discussion

A total of 603 sets of simulation data were obtained from 21 simulation cycles. As stated above, the variables and parameters used in the simulator for each bed were compared with the ones described in the plant design report, which shows the temperature and input and output flow of each bed; SO₂, SO₃, O₂, and N₂ volumetric percentage; pressure; and accumulated conversion. Table 3 shows an example of the input process (on the left) and the output values of the variables; molar flow; and SO₂, SO₃, O₂, and N₂ (on the right) for each simulation cycle moment.

Table 4 summarizes the r^2 values and error percentage in the simulation of each of the variables of interest in the simulation process. One of the most important variables in SO₂ oxidation is temperature since this one depends on the catalyst activation or deactivation. A big decrease results in less oxidation and, as a result, a smaller amount of the product. With the equations programmed in the simulator, a 0.99 r^2 regression coefficient was obtained for this variable, as shown

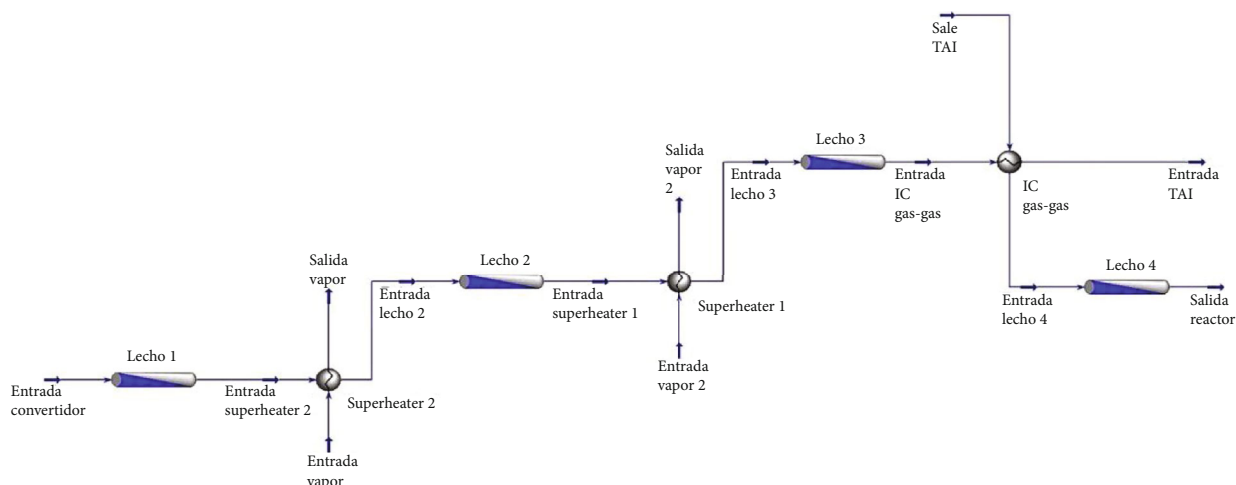


FIGURE 2: Configuration of Aspen Hysys® modelling.

TABLE 3: An example of the input and output values of a simulation cycle.

Operational ID	Flow [Nm ³ /Hr]	Bed-1 feeding				Presión [bar]	Flujo molar [Nm ³ /Hr]	Bed-1 output			
		fluid mixture			Temperatura °C			fluid mixture			N ₂
		SO ₂	O ₂	N ₂			SO ₂	SO ₃	O ₂	N ₂	
1	140000	11.5	9.24	79.26	420	1.25	134880.072	4.33	7.6	5.79	82.28
1	140500	11.5	9.24	79.26	420	1.25	135373.235	4.34	7.6	5.79	82.27
1	141000	11.5	9.24	79.26	420	1.25	135866.398	4.35	7.59	5.8	82.26
1	141500	11.5	9.24	79.26	420	1.25	136337.144	4.36	7.58	5.8	82.26
1	142000	11.5	9.24	79.26	420	1.25	136830.307	4.36	7.57	5.8	82.27
1	145000	11.5	9.24	79.26	420	1.25	139766.868	4.41	7.53	5.82	82.24
1	145500	11.5	9.24	79.26	420	1.25	140237.615	4.41	7.52	5.83	82.24
1	146500	11.5	9.24	79.26	420	1.25	141223.941	4.43	7.5	5.84	82.23
1	146500	11.5	9.24	79.26	420	1.25	141223.941	4.43	7.5	5.84	82.23
1	147000	11.5	9.24	79.26	420	1.25	141717.104	4.44	7.49	5.84	82.23
1	147500	11.5	9.24	79.26	420	1.25	142187.85	4.44	7.49	5.84	82.23
1	148000	11.5	9.24	79.26	420	1.25	142681.013	4.45	7.48	5.85	82.22
1	148500	11.5	9.24	79.26	420	1.25	143174.176	4.46	7.47	5.85	82.22
1	149000	11.5	9.24	79.26	420	1.25	143644.923	4.46	7.46	5.85	82.23
1	149500	11.5	9.24	79.26	420	1.25	144138.086	4.47	7.46	5.86	82.21
1	150000	11.5	9.24	79.26	420	1.25	144631.249	4.48	7.45	5.86	82.21

TABLE 4: Description of variables used in simulation and related r^2 and Error values.

Variable	r^2	Error (%)
Temperature	0.99	0.60
Molar flow	0.99	0.04
SO ₂	0.99	0.50
SO ₃	0.99	0.50
O ₂	0.99	0.40

in Figure 3. The error in the input and output temperatures of the different converter beds was 0.6%.

Another important variable to be validated is molar flow since it represents the amount of final product, thus providing the amount of flow circulating through the converter, consider-

ing losses between beds. Figure 4 shows that the adjustment value is 0.99, with a 0.04% error for all the input and output flows of the different beds, So, the variable can be accepted as validated. Once the molar flow was validated, its components were validated separately to make sure that the data obtained were reliable. The validation began with sulphuric dioxide because when it oxidizes it becomes the raw material of SO₃ sulphuric acid; its monitoring making it possible to control proper oxidation. It also allows detecting the amount of SO₂ liberated into the environment since, when it goes out of the fourth bed, it cannot be eliminated. In this case, the value of the r^2 linear regression coefficient is 0.99 with a 0.5% error.

As stated above, SO₃ is the raw material for producing sulphuric acid. Therefore, it is essential that the simulator provides accurate values of the percentage of this component

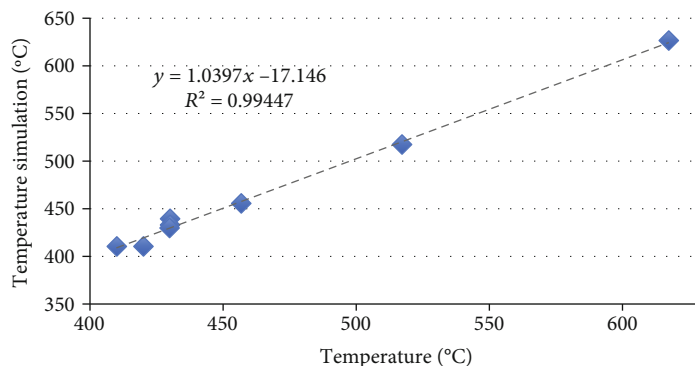


FIGURE 3: Converter temperature validation.

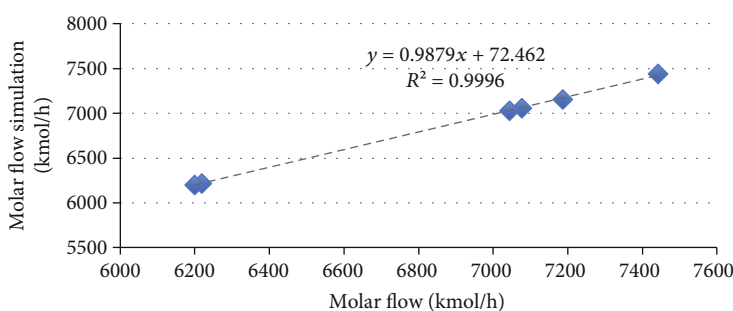


FIGURE 4: Molar flow validation.

in the gas. To check the validity of the values provided by the simulator, a linear regression was performed, resulting in a 0.99 r^2 coefficient and a 0.5% error.

The O_2 component plays a fundamental role in changing SO_2 to SO_3 , thus, knowing the amount of it in the converter facilitates oxidation control. The validation of this variable in the simulator and the resulting accurate values of the amount of oxygen in the flow provide valuable data to the operator. Checking the values provided and knowing if the equations proposed and entered to the simulator are correct, the linear regression is performed, resulting in a 0.99 r^2 regression coefficient and a 0.4% error, thus validating the variable. From the values described above and shown in Table 4, it is possible to conclude that the simulation model is valid since the results obtained show a 0.99 r^2 mean regression coefficient. In this way, this component is validated, and the gas composition is also thoroughly validated.

Figure 5 shows that, at constant temperature, the greater the oxidation, the lower the gas flow and, on the contrary, the greater the gas flow, the less the oxidation. This may happen because there is a lower amount of gas flow, and therefore, it has a greater surface in contact with vanadium pentoxide, thus producing greater oxidation. Figure 5 shows the oxidation behavior when different gas flows are kept constant and the reactor input temperature is manipulated, showing that the lower the temperature, the greater the oxidation. Thus, the temperature used must produce enough SO_3 so that the process can be viable, the catalyst is at activation temperature, and the reaction velocity is high enough.

5. Conclusions and Future Work

In the copper industry, one of the most used inputs to recover copper is sulphuric acid, which can be produced using solid sulphur as input. But frequently, the sulphuric acid production process is usually expensive, due to both energy consumption and solid sulphur and other resources such as water consumption.

In this work, a technique to simulate and evaluate the catalytic conversion process for the production of sulphuric acid has been proposed and developed, and its practical utility has been validated. Additionally, as a result of this process, the production of electrical energy has also been monitored and suggestions to improve the energy generation have been provided, based on simulations and visualization of the results.

In order to achieve the above described, operational data obtained from the operation of a plant in Antofagasta have been used. Real data generated during approximately 3 months has been used to generate appropriate data that was used as input to the simulation, visualization, and validation process.

A concrete conclusion is that the simulation process generates results very close to the real process, since the error is less than 1%, with a converter input temperature in low value (in the range between 300°C and 460°C) and a gas flow between 140.00 and 180.00 Nm^3/h . Other highlight conclusions are as follows:

- (i) The simulation process has allowed the identification of process characteristics that could affect

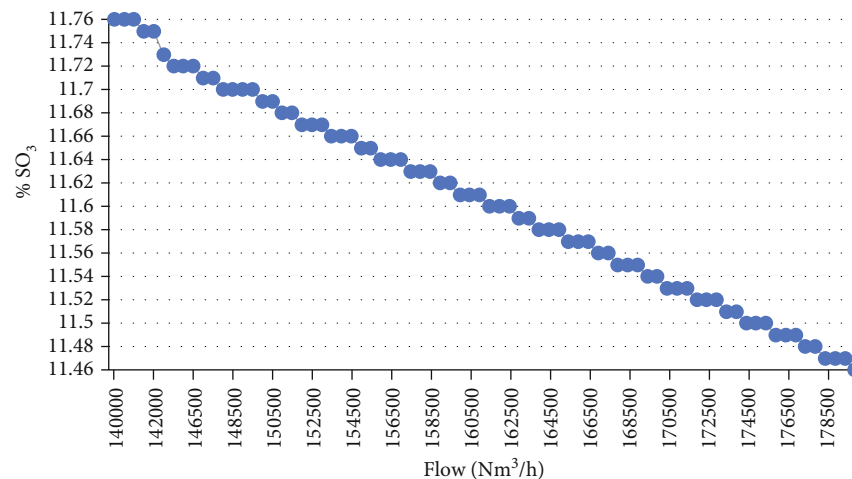


FIGURE 5: Oxidation behavior at different input flows.

greater production and better use of inputs. For example, tests made in the simulator show that the optimal input temperature is low, and the recommended gas flow is $150.50 \text{ Nm}^3/\text{h}$, using these new operational parameters configuration, sulphuric acid production should increase in 4 metric tons/day

- (ii) A quantitative analysis of the average daily production of the plant was carried out using the simulation software. The results obtained with the simulator contrasted with the operational results over a period of 6 months. In this analysis, a new operational scenario was defined, and the temperature, pressure, and flow parameters were the most relevant to improve the results. The company has proposed to monitor these parameters according to the simulation results, to obtain a daily increase of 0.2% in the production of sulphuric acid. According to this scenario at CLP 161,695,000 NPV and 53% IRR could be obtained. These results represent an increase of 6% on the monthly production of sulphuric acid, with respect to the previous real operational results
- (iii) The simulation using Aspen HYSYS® considered the contact stage of the process. This was conducted with 4 CSTR reactors and 3 shell and tube heat exchangers to evaluate and validate the system. After validating the simulator and using the plant design data, it was observed that the error between the design variables and the values obtained from the simulator is lower than 1%. During the simulation process, it was proved that the greatest conversion occurs when the temperature and the flow are at low and 150,500, respectively.

Data Availability

All raw data remains the property of the company that allowed this study. The input data (anonymized data) used

to support the findings of this study could be available from the corresponding author upon request.

Conflicts of Interest

The authors declare no conflict of interest.

Authors' Contributions

All the authors collaborated in the design, experiments, result analyses, and paper writing.

Acknowledgments

The authors wish to acknowledge Carolina Aguilar for contributing materials from her undergraduate thesis and Universidad Católica del Norte for the use of the educational license of Aspen HYSYS® software.

References

- [1] A. Lovato, C. Legorreta, and V. Andersson, "Heat recovery from sulphuric acid plants for seawater desalination," *Desalination*, vol. 136, no. 1-3, pp. 159–168, 2001.
- [2] A. O. Oni, D. A. Fadare, S. Sharma, and G. P. Rangaiah, "Multi-objective optimisation of a double contact double absorption sulphuric acid plant for cleaner operation," *Journal of Cleaner Production*, vol. 181, pp. 652–662, 2018.
- [3] J. Albrecht, "Revamp and upgrade possibilities in sulphuric acid plants," *Procedia Engineering*, vol. 138, pp. 184–198, 2016.
- [4] M. Kemmerich and H. Storch, "Process heat recovery and digitalisation in sulphuric acid plants," *Procedia Engineering*, vol. 138, pp. 220–230, 2016.
- [5] C. F. Porisini, "Selection and evaluation of materials for the construction of a pre-pilot plant for thermal decomposition of sulphuric acid," *International Journal of Hydrogen Energy*, vol. 14, no. 4, pp. 267–274, 1989.
- [6] C. Hurt, M. Brandt, S. S. Priya et al., "Combining additive manufacturing and catalysis: a review," *Catalysis Science & Technology*, vol. 7, no. 16, pp. 3421–3439, 2017.

- [7] B. G. Reis, A. L. Araújo, C. Vieira, M. C. Santos Amaral, and H. Ferraz, "Assessing potential of nanofiltration for sulfuric acid plant effluent reclamation: operational and economic aspects," *Separation and Purification Technology*, vol. 222, pp. 369–380, 2019.
- [8] A. Kiss, C. Bildea, and J. Grievink, "Dynamic modeling and process optimization of an industrial sulfuric acid plant," *Chemical Engineering Journal*, vol. 158, no. 2, pp. 241–249, 2010.
- [9] P. Sørensen, M. Møllerhøj, and K. Christensen, "New dynamic models for simulation of industrial SO₂ oxidation reactors and wet gas sulfuric acid plants," *Chemical Engineering Journal*, vol. 278, pp. 421–429, 2015.
- [10] D. Taieb and A. Ben Brahim, "Electrochemical method for sulphur dioxide removal from flue gases: application on sulphuric acid plant in Tunisia," *Comptes Rendus Chimie*, vol. 16, no. 1, pp. 39–50, 2013.
- [11] Q. Smejkal and M. Šoóš, "Comparison of computer simulation of reactive distillation using ASPEN PLUS and HYSYS software," *Chemical Engineering and Processing: Process Intensification*, vol. 41, no. 5, pp. 413–418, 2002.
- [12] V. Flores, B. Keith, and C. Leiva, "Using artificial intelligence techniques to improve the prediction of copper recovery by leaching," *Journal of Sensors*, vol. 2020, pp. 1–12, 2020.
- [13] Z. Liu and I. Karimi, "Simulating combined cycle gas turbine power plants in Aspen HYSYS," *Energy Conversion and Management*, vol. 171, pp. 1213–1225, 2018.
- [14] F. Abdollahi-Demneh, M. L. Moosavian, M. R. Omidkhan, and H. Bahmanyar, "Calculating exergy in flowsheeting simulators: a HYSYS implementation," *Energy*, vol. 36, no. 8, pp. 5320–5327, 2011.
- [15] A. Sunny, P. A. Solomon, and K. Aparna, "Syngas production from regasified liquefied natural gas and its simulation using Aspen HYSYS," *Journal of Natural Gas Science and Engineering*, vol. 30, pp. 176–181, 2016.
- [16] L. E. Øi, T. Bråthen, C. Berg et al., "Optimization of configurations for amine based CO₂ absorption using Aspen HYSYS," *Energy Procedia*, vol. 51, pp. 224–233, 2014.
- [17] T. Saadi, M. Jeday, and J. Jaubert, "Exergetic analysis of an LPG production plant using HYSYS software," *Energy Procedia*, vol. 157, pp. 1385–1390, 2019.
- [18] T. Biyanto, H. E. G. Prasetya, R. Bayuaji, G. Nugroho, and T. Soehartanto, "Design plant-wide control to waste heat recovery generation on cement industry based HYSYS," *Procedia Computer Science*, vol. 72, pp. 170–177, 2015.
- [19] C. A. Leiva, D. A. Poblete, T. L. Aguilera, C. A. Acuña, and F. J. Quintero, "Air separation units (ASUs) simulation using Aspen Hysys® at Oxinor I of air Liquid Chile S.A plant," *Polish Journal Chemical Technology*, vol. 22, no. 1, pp. 10–17, 2020.
- [20] A. M. Borreguero, J. L. Valverde, J. M. García-Vargas, and L. Sánchez-Silva, "Simulator-based learning in the teaching of chemical engineering," *Computer Applications in Engineering Education*, vol. 27, no. 5, pp. 1267–1276, 2019.
- [21] W. L. Woo and B. Gao, "Sensor signal and information processing II," *Sensors*, vol. 20, no. 13, p. 3751, 2020.
- [22] G. Yang, S. Q. Cao, and Y. Wu, "Recent advancements in signal processing and machine learning," *Journal of Sensors*, vol. 2014, 4 pages, 2014.

Research Article

Energy-Efficient Time-Domain Equilibrium Scheduling and Optimization Scheme for Energy Harvesting-Powered D2D Communication

Ying Luo , Min Zeng, Hong Jiang, and Bin Han

Network and Communication Research Institute, College of Information Engineering, Southwest University of Science and Technology, Mianyang, Sichuan Province, China

Correspondence should be addressed to Ying Luo; yluo@swust.edu.cn

Received 23 June 2020; Revised 12 July 2020; Accepted 18 July 2020; Published 1 September 2020

Academic Editor: Bin Gao

Copyright © 2020 Ying Luo et al. This is an open access article distributed under the Creative Commons Attribution License, which permits unrestricted use, distribution, and reproduction in any medium, provided the original work is properly cited.

Energy Harvesting- (EH-) powered Device-to-Device (D2D) Communication underlying Cellular Network (EH-DCCN) has been deemed as one of the basic building blocks of Internet of Things due to its green energy efficiency and adjacent communication. But available energy will be one of the biggest obstacles when implementing EH-DCCN due to the immaturity of EH technology and the volatility of environmental energy resources. To improve energy utilization, this study investigates an efficient scheduling and power allocation scheme about transmission load equilibrium in the time domain. Accordingly, a short-term Sum Energy Efficiency (stSEE) maximization problem for EH-powered D2D communication is modelled, while ensuring a fundamental transmission rate requirement of cellular users. Consequently, the optimization problem is a nonconvex mixed integer nonlinear programming problem. Thus, we propose a two-layer convex approximation iteration algorithm which can obtain a feasible quasioptimal solution for the stSEE problem. Simultaneously, a two-step heuristic algorithm in a slot-by-slot fashion is also developed to acquire a suboptimal solution without requiring statistical knowledge of channel and energy arrival processes. Simulated analysis indicates that the short-term scheduling strategy can obtain better performances in terms of energy efficiency and transmission rate than conventional real-time scheduling scheme. Besides, the maximum scheduled number of EH-D2D pairs underlying one cellular user under different EH efficiency is analysed, which can give us a theoretical reference about the deployment of future EH-DCCN.

1. Introduction

The dawn of Internet of Things (IoT) installed for industry production, smart housing, and environmental monitoring has given birth to billions of mobile wireless devices [1]. Ericsson predicts that there will be about 15 billion mobile devices in 2021, and most of them will be low-power devices with short-range communication [2]. The ever-increasing proliferation of wireless devices, together with an exponential rise in users' data demand, is already creating an urgent need for wireless cellular networks to design some new technologies that can attain desired transmission rates and, meanwhile, can achieve green communications [3, 4]. Recent emphasis on green communications has generated great interest in the investigations of energy harvesting- (EH-)

powered wireless networks [5–7]. EH technique can harvest energy from environmental energy resources to prolong the lifetime of wireless communication devices with low power consumption and limited battery life. On the other hand, Device-to-Device (D2D) communication has been viewed as a promising paradigm that can offload traffic from cellular networks by communicating directly with each other in close proximity via multiplexing the spectrum resources being assigned to cellular users (CUs) [8, 9]. Accordingly, EH-powered D2D Communication underlying Cellular Network (EH-DCCN), which combines the characteristics of short-range transmission and green communication, will be an attractive way to keep a better transmission service quality with green energy resources. Nevertheless, this sustainable energy support technique will result in intermittent energy

supply issue, which do not exist in the conventional D2D communication systems with fixed energy sources. Consequently, how to efficiently utilize and manage unreliable energy so as to satisfy different transmission demand is the most urgent challenge to achieve the green D2D communication paradigm.

1.1. Related Works. A lot of research has paid their attentions to the challenges caused by the uncertain energy supply technique from different aspects, such as access control and resource management, for the EH-DCCN.

In view of access control, Darak et al. design an online learning handover scheme between D2D mode and Radio Frequency EH (RFEH) mode based on subband statistics in D2D-RFEH communication [10]. For cognitive and EH-based D2D transmission, Sakr and Hossain propose two spectrum access policies for the cellular network, namely, random and prioritized access policies, to evaluate transmission and outage probability for D2D and cellular users [11]. The authors of [12] develop a D2D communication provided by EH Heterogeneous cellular Network (D2D-EHFN), where User Equipment Relays (UERs) harvest energy from an access point to support D2D communication. This paper derives the proper distribution of RFEH-powered UER and proposes an efficient UER selection method.

To adapt the uncertainty in energy supply, researchers have also devoted their efforts to the design of efficient resource management schemes in terms of power allocation, spectrum matching, and time sharing for EH-DCCN. Tutuncuoglu and Yener study the power allocation policies for EH-supported transmitters by optimizing the sum rate [13], which is similar to a one-to-one spectrum sharing model in D2D communication underlying cellular network [14]. Yet, the Quality of Service (QoS) requirement, which mainly refers to transmission rate demand, is not involved in the proposed policy. Similarly, the sum rate maximization problem for D2D communication under a downlink resource multiplex system in the presence of multiple CUs and EH-powered D2D links is studied in [15]. To ensure energy-efficient spectrum resource assignment, Ding et al. investigate the energy cost minimization problem [16]. Considering the power allocation and time-sharing spectrum occupation management, Hadzi-Velkov et al. maximize the overall cellular network transmission rate based on the statistical average of the harvested energy [17].

The above research works have addressed many challenges caused by the unstable and unreliable power supply of EH from different aspects. Nevertheless, those works are mainly based on a one-to-one spectrum sharing mode where one CU's radio resource is multiplexed by one D2D pair. In this sharing mode, the CU's spectrum will be vacant when the available energy of the EH-powered D2D pair (EH-DP) cannot meet the energy consumption requirement. Hence, by taking the high spectrum efficiency demand into account, one-to-multiple sharing mode, namely, one CU and multiple EH-DPs sharing one radio spectrum, is needed. In this way, the cellular spectrum gap caused by the energy deficiency of the single EH-DP can be filled up. In practice, multiple D2D pairs can be allowed to share the same resource with

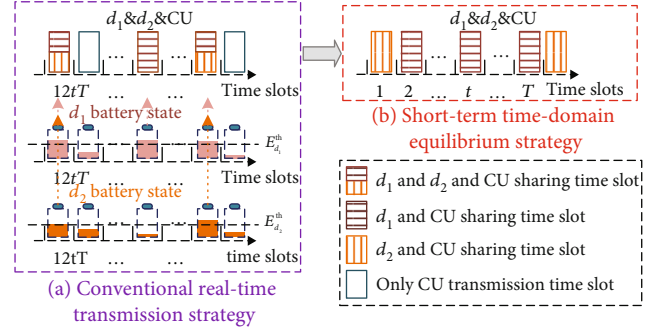


FIGURE 1: An example of motivations.

the cellular users as long as the interference of D2D communications is not harmful to the cellular links [18–20]. However, under the one-to-multiple sharing mode, due to the variation of EH efficiency, environmental energy resources, and channel status, the transmission requests, which are relied on available energy, among EH-DPs at different time slots may be unbalanced. Since the traffic is delay-tolerant, the mutual interference among users can be efficiently decreased by balancing the transmission requests among time slots and finally improve energy efficiency. The following section will take two EH-powered D2D pairs underlying cellular network as a simple example to illustrate our main motivations.

1.2. Motivations. Before describing our motivations, we must make some important statements. We only consider that the D2D user (DU) has EH capability [21]. Meanwhile, for simplicity, suppose that the traffic pattern of each user is full buffer, and all users operate in a time-slotted fashion and are synchronous.

When multiple EH-DPs multiplex the same spectrum resource, the transmission request of EH-DPs at the different time slots may be unbalanced. As illustrated by Figure 1, two EH-DPs d_1 and d_2 are permitted to share a radio spectrum with one CU. From Figure 1(a), the available energy of users is different due to various channel interference conditions and energy conversion efficiency. When the available energy of EH-DP reaches its transmission power threshold $E_{d_u}^{\text{th}}$ ($u \in \{1, 2\}$), EH-DPs will launch the transmission request. Thus, when the two EH-DPs d_1 and d_2 initiate the transmission request at the same time slots, such as time slot 1, the conventional real-time transmission strategy will let them transmit data at the same time by the corresponding power allocation scheme under the interference constraint. However, each of them may not multiplex the spectrum resource in the next time slot (e.g., time slot 2) because of energy supply or energy consumption. However, in the short-term time-domain equilibrium strategy, as depicted in Figure 1(b), either of the two EH-powered D2D pairs can be assigned to multiplex the spectrum resource of CU in the time slot 2. As a result, the interference between the two D2D links in the time slot 1 will be eliminated. Hence, to avoid unnecessary consumption of the harvested energy, the interference among users is required to be appropriately managed in one-to-multiple sharing scenarios [5].

As mentioned above, by fully considering the available energy and channel status (channel status mainly refers to mutual interference conditions among users (including CU and EH-DPs) in this study), how to balance the transmission loads among different time slots under EH-DCCN with one-to-multiple sharing mode so as to improve the performance of EH-DCCN is the key concern of this study. As far as we know, the considered short-term time-domain energy-efficient equilibrium program is the first attempt to do so in EH-DCCN.

1.3. Contributions and Organizations. As previously described, this study focuses on designing an energy-efficient transmission scheduling and power allocation scheme so as to increase the performance of the EH-DCCN with the one-to-multiple radio resource sharing mode. Thus, our main contributions can be divided into three main areas:

- (i) Firstly, this study optimizes a short-term Sum Energy Efficiency (stSEE) problem about EH-powered D2D communication to realize the energy-efficient scheduling scheme. Simultaneously, the available energy and transmission rate constraints of both CUs and EH-DPs are also considered in the optimization problem
- (ii) Subsequently, a two-layer convex approximation iteration algorithm (CAIA), which consists of an outer-layer iteration algorithm (OLIA) and an inner-layer convex approximation (ILCA) algorithm, is proposed to obtain a feasible quasioptimal solution for the modelled stSEE maximization problem which is a nonconvex mixed integer nonlinear programming (MINLP) problem
- (iii) Thirdly, a two-step heuristic algorithm, the time-division scheduling scheme (TDSS), is also developed to acquire a suboptimal solution without requiring statistical knowledge of channel and EH processes. Remarkably, TDSS not only can acquire a suboptimal solution for the stSEE problem but also has a lower computational complexity

The rest of this study is organized as follows. In Section 2, we describe the system model in detail and formulate the stSEE maximization problem. The two feasible algorithms, CAIA and TDSS, are elaborated by Sections 3 and 4, respectively. The numerical simulation performance results and the computational complexity of the proposed algorithms are presented and analysed in Section 5. In Section 6, we conclude this study.

2. System Description and Problem Formulation

This section introduces the system model and formulates the considered resource scheduling problem. To facilitate the understanding, some important notations in this study are listed in Table 1.

2.1. System Model. In what follows, we assume that spectrum matching has already finished. This is to say that multiple EH-DPs have already been allocated to one dedicated CU in some particular optimization conditions, e.g., EE maximization [22]. Thus, as shown in Figure 2, a typical single cellular network consisting of a Base Station (BS) and K EH-DP/CU groups is considered. Suppose that the system utilizes a certain number of orthogonal spectra, then we can divide the spectra into the same number of EH-DP/CU groups. Namely, the communication links in the same group transmit on the same spectrum, and the communication links in different groups use the orthogonal one. Let B represent BS, c_k ($k = \{1, 2, \dots, K\}$) denote CU in the k th EH-DP/CU group, and $d_{k,i}$ be a pair of D2D users in the EH-DP set $|\Phi_{D_k}| = N_k$ of the k th EH-DP/CU group. In the k th EH-DP/CU group, N_k EH-DPs share the uplink transmission link of the c_k th CU ($c_k \in \Phi_C, \{|\Phi_C| = K\}$) to transmit. According to the energy assumption in Section 1.2, the transmitter of each EH-DP is supplied by EH technique and has a battery to store harvested energy. Meanwhile, the available power of the receiver of each EH-DP is deemed as unlimited due to the low-power property of the decoding process.

Generally speaking, as illustrated by the EH-DP/CU group 2 of Figure 2, each EH-DP transmission will simultaneously cause interference to receivers of cellular and EH-DP links. Likewise, cellular transmission will generate interference to the EH-DP receivers. Assume that the entire system executes on a slot-by-slot basis. Accordingly, in any time slot, the instantaneous transmission rate of the cellular and EH-DP links can be given by $r_{c_k}^t$ and $r_{d_{k,i}}^t$, respectively,

$$\begin{aligned} r_{c_k}^t &= \log \left(1 + \frac{p_{c_k}^t \cdot g_{c_k B}}{\sum_{d_{k,j} \in \Phi_{D_k}} x_{d_{k,i}}^t \cdot p_{d_{k,i}}^t \cdot g_{d_{k,i} B} + n_0} \right), \\ r_{d_{k,i}}^t &= \log \left(1 + \frac{p_{d_{k,i}}^t \cdot g_{d_{k,i}}}{p_{c_k}^t \cdot g_{c_k d_{k,i}} + \sum_{\substack{d_{k,j} \in \Phi_{D_k} \\ d_{k,j} \neq d_{k,i}}} x_{d_{k,j}}^t \cdot p_{d_{k,j}}^t \cdot g_{d_{k,i} d_{k,j}} + n_0} \right), \end{aligned} \quad (1)$$

where $x_{d_{k,i}}^t$ ($d_{k,i} \in \Phi_{D_k}$) is the indicator parameter, 1 indicates the $d_{k,i}$ th D2D pair chosen to transmit in time slot t , and 0 indicates the $d_{k,i}$ th D2D pair not chosen. $p_{c_k}^t$ and $p_{d_{k,i}}^t$ are the corresponding transmission power of CUs and EH-DPs in time slot t , respectively. $g_{i,j}$ denotes the channel gain between nodes i and j . n_0 means the noise power and equals to $B_W \cdot \beta_n$, where β_n is the density of noise power and B_W is the uplink channel bandwidth of each group.

2.2. Energy Model. As demonstrated in Figure 3, at time slot t , the transmitter of each EH-DP needs to harvest energy from the environmental energy resources, to store the energy in a battery, and to use the available energy to finish transmission. We study the condition that the energy arrival process in each EH-DP is i.i.d. For the $d_{k,i}$ th EH-DP, $E_{d_{k,i}}^t$ units of energy can be harvested in time slot t , where $E_{d_{k,i}}^t \geq 0$. $\{E_{d_{k,i}}^1, E_{d_{k,i}}^2, \dots,$

TABLE 1: Important notations.

Symbol	Definition
k	EH-DP/CU group number, which belongs to $[1, K]$
c_k	Cellular user in k th EH-DP/CU group
$d_{k,i}$	EH-DP user in k th EH-DP/CU group
Φ_C	Cellular user set, where $ \Phi_C = K$
Φ_{D_k}	EH-DP user set in k th EH-DP/CU group, where $ \Phi_{D_k} = N_k$
r_u^t	Transmission rate of user u ($u \in (\Phi_C, \Phi_{D_k})$) in an instantaneous time slot
r_u^{\max}	Minimum transmission rate of each user in each time slot
t	Time slot, where $t \in [0, T]$
p_u^t	Transmission power of user u in an instantaneous time slot
p_u^{\max}	Maximum transmission power of each user in each time slot
$x_{d_{k,i}}^t$	Transmission indicator parameter, 1 indicates that the $d_{k,i}$ th D2D pair is chosen to transmit in time slot t , otherwise
$g_{i,j}$	Channel gain between nodes i and j
n_0	Noise power
B_W	Channel bandwidth of each cellular user
ρ_n	Density of noise power
$E_{d_{k,i}}^t$	Harvested energy of $d_{k,i}$ th D2D user in an instantaneous time slot
$\lambda_{d_{k,i}}^t$	Energy harvesting efficiency of $d_{k,i}$ th D2D user

$\{E_{d_{k,i}}^t, \dots, E_{d_{k,i}}^T\}$ is the time sequence of harvested energy in T time slots and obeys an i.i.d. *Bernoulli* process:

$$E_{d_{k,i}}^t (\text{watt/timeslot}) = \begin{cases} E, & \text{with probability of } (\lambda_{d_{k,i}} \in [0, 1]), \\ 0, & \text{with probability of } (1 - \lambda_{d_{k,i}}). \end{cases} \quad (2)$$

$\lambda_{d_{k,i}}$ and E are called EH efficiency of the $d_{k,i}$ th EH-DP. Notably, the concepts of terms of energy and power in this study are equivalent in the unit time slot.

In Figure 3, $E_{d_{k,i}}^t$ units of energy are harvested by EH technique and added to the battery at each time slot. Accordingly, $p_{d_{k,i}}^t$ units of energy will be consumed for data transmission of the $d_{k,i}$ th device. The existing energy of the $d_{k,i}$ th EH-DP in a battery is defined as $B_{d_{k,i}}^t$ ($t \in \{1, 2, \dots, T\}$). Thus, a cumulative power constraint can be expressed as follows:

$$\sum_{n=1}^t p_{d_{k,i}}^n \leq \sum_{n=1}^t E_{d_{k,i}}^n + B_{d_{k,i}}^0, \forall d_{k,i} \in \Phi_{D_k}, t = \{1, 2, \dots, T\}. \quad (3)$$

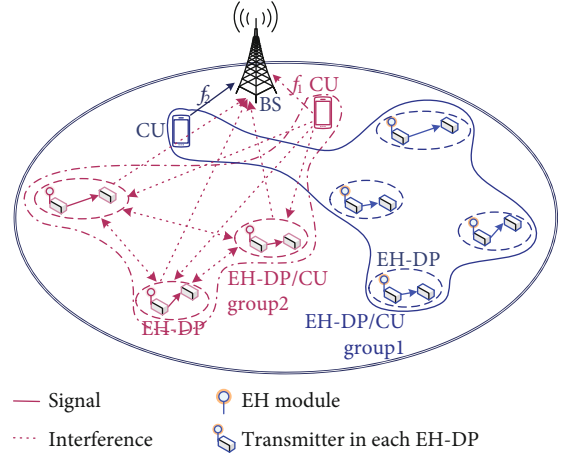


FIGURE 2: System model when CUs and EH-DPs share the uplink spectrum resource.

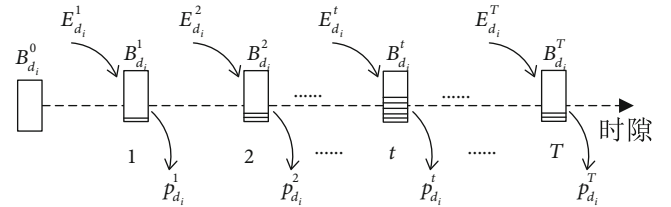


FIGURE 3: Energy condition in discrete time slots of the $d_{k,i}$ th D2D pair.

Suppose that the harvested energy can be stored without any loss and used for only communication purposes from the battery. Meanwhile, the battery capacity is large enough to hold every quanta of harvested energy. This assumption is especially valid for the current state of technology in which batteries have very large capacities compared to the energy harvesting efficiency [23]. Furthermore, assume that all state information including Channel State Information (CSI) and Energy State Information (ESI) can be obtained by BS so that BS has the control capability in terms of transmission scheduling and power allocation [24, 25].

2.3. Mathematical Model. The short-term Sum Energy Efficiency (stSEE) for EH-powered D2D communication optimization problem is formulated as \mathbf{P}_{EE} :

$$(\mathbf{P}_{EE}) \max_{X, P_C, P_D} \text{imize} : \frac{\sum_{k=1}^K \sum_{t=1}^T \sum_{d_{k,i} \in \Phi_D} x_{d_{k,i}}^t \cdot r_{d_{k,i}}^t}{\sum_{k=1}^K \sum_{t=1}^T \sum_{d_{k,i} \in \Phi_D} x_{d_{k,i}}^t \cdot p_{d_{k,i}}^t}, \quad (4)$$

$$\text{s.t. } 0 \leq p_{c_k}^t \leq p_{c_k}^{\max} \quad (t = \{1, 2, \dots, T\}, \forall c_k \in \Phi_C), \quad (4a)$$

$$r_{c_k}^t \geq r_{c_k}^{\text{th}}, \quad (4b)$$

$$\sum_{n=1}^t p_{d_{k,i}}^n \leq \sum_{n=1}^t E_{d_{k,i}}^n + B_{d_{k,i}}^0 \quad (t = \{1, 2, \dots, T\}, \forall d_{k,i} \in \Phi_D), \quad (4c)$$

$$0 \leq p_{d_{k,i}}^t \leq p_{d_{k,i}}^{\max}, \quad (4d)$$

$$r_{d_{k,i}}^t \geq r_{d_{k,i}}^{th} \left(\forall x_{d_{k,i}}^t = 1 \right), \quad (4e)$$

$$x_{d_{k,i}}^t \in \{0, 1\}, \quad (4f)$$

where $X = \{x_{d_{k,i}}^t (d_{k,i} \in \Phi_D, t = \{1, 2, \dots, T\})\}$ is the indicator parameter set about whether the $d_{k,i}$ th EH-DP is allowed to transmit or not in an instantaneous time slot t . $\mathbb{P}_C = \{p_{c_k}^t (c_k \in \Phi_C, k = \{1, 2, \dots, K\}, t = \{1, 2, \dots, T\})\}$ and $\mathbb{P}_D = \{p_{d_{k,i}}^t (d_{k,i} \in \Phi_D, t = \{1, 2, \dots, T\})\}$ are the sets of transmission power of CU and EH-DPs, respectively. To avoid serious mutual interference, as represented by (4a) and (4d), the maximal transmission power in each time slot should be limited at the CU and EH-DP side, respectively. In this study, multiple EH-DPs can share the CU's uplink channel resource to transmit. Thus, the mathematical model should guarantee the minimum QoS of CU. So, (4b) defines a threshold about transmission rate demand for CU. Similarly, as (4e) shows, the chosen EH-DPs allowed to transmit in the t th time slot must have a minimum transmission rate requirement. At last, (4c) denotes the available energy constraint of EH-DP.

2.4. Problem Decoupling. The maximization problem \mathbf{P}_{EE} can be decoupled into K subproblems according to the spectrum orthogonality. Hence, for any of EH-DP/CU groups $k (k = \{1, 2, \dots, K\})$, we have following optimization problem \mathbf{P}_{EE}^k :

$$\left(\mathbf{P}_{EE}^k \right) \max_{X_k, P_{C_k}, P_{D_k}} \text{imize} : \frac{\sum_{t=1}^T \sum_{d_{k,i} \in \Phi_{D_k}} x_{d_{k,i}}^t \cdot r_{d_{k,i}}^t}{\sum_{t=1}^T \sum_{d_{k,i} \in \Phi_{D_k}} x_{d_{k,i}}^t \cdot p_{d_{k,i}}^t}, \quad (5)$$

$$\text{s.t. (5a) - (5f)}, \quad (5a)$$

where $X_k = \{x_{d_{k,i}}^t (d_{k,i} \in \Phi_{D_k}, t = \{1, 2, \dots, T\})\}$, $P_{C_k} = \{p_{c_k}^t (t = \{1, 2, \dots, T\})\}$, and $P_{D_k} = \{p_{d_{k,i}}^t\}$.

3. Two-Layer Convex Approximation Algorithm (TLCA)

As described in \mathbf{P}_{EE}^k , some of the variables (the components of P_{C_k} and P_{D_k}) can be real-valued, whereas the other variables (the components of X_k) are binary-valued. Furthermore, the optimization utility function (5) and restraints (4b) and (4e) depend on $r_{c_k}^t$ and $r_{d_{k,i}}^t$, which have nonconvex feature (the simple proof of the nonconvex of $r_{c_k}^t$ and $r_{d_{k,i}}^t$ can be seen in Appendix A). So, (5) is a nonconvex MINLP problem, by which computational complexity is NP-hard. An intuitive proof of NP-hardness is that MINLP includes ILP problem (Formula (5) can be reduced to an ILP problem when the power allocation variables P_{C_k} and P_{D_k} are fixed), which has been proved to be NP-hard [26, 27]. Based on the above discussion, we design a two-layer convex approximation iteration algorithm (CAIA), which contains an outer-layer iteration algorithm (OLIA) and an inner-layer convex approximation (ILCA) algorithm, to obtain a feasible quasi-optimal solution. The OLIA first equivalently transform the fractional programming problem. Secondly, the ILCA is

implemented to approximately convert the nonconvex MINLP optimization into a convex one.

3.1. Outer-Layer Iteration Algorithm (OLIA). First of all, the target of \mathbf{P}_{EE}^k (5), is a nonlinear fractional programming paradigm [28], which can be transformed into an equivalent multiobjective program by the Dinkelbach method. For easier description, we use Ω to represent the feasible solution set of problem (5). Let q_k^* denote the maximum stSEE of EH-DP communication in the k th EH-DP/CU group. Then, we have the following definition:

$$q_k^* = \max_{\{X_k, P_{C_k}, P_{D_k}\} \in \Omega} \text{imize} : \frac{\sum_{t=1}^T \sum_{d_{k,i} \in \Phi_{D_k}} x_{d_{k,i}}^t \cdot r_{d_{k,i}}^t}{\sum_{t=1}^T \sum_{d_{k,i} \in \Phi_{D_k}} x_{d_{k,i}}^t \cdot p_{d_{k,i}}^t}. \quad (6)$$

Accordingly, the following theorem can be ready to present.

Theorem 1. The maximum stSEE q_k^* can be achieved if and only if

$$\max_{\{X_k, P_{C_k}, P_{D_k}\} \in \Omega} \text{imize} : \left\{ \sum_{t=1}^T \sum_{d_{k,i} \in \Phi_{D_k}} x_{d_{k,i}}^t \cdot r_{d_{k,i}}^t - q_k^* \cdot \sum_{t=1}^T \sum_{d_{k,i} \in \Phi_{D_k}} x_{d_{k,i}}^t \cdot p_{d_{k,i}}^t \right\} = 0. \quad (7)$$

Proof. The proof is similar to the proof in [28].

Hence, formula (7) can be addressed by an iterative process, which is demonstrated by Algorithm 1. Define m as the number of iterations, q_k^m as the instantaneous EE for the k th EH-DP/CU group in the m th iteration, and ε as the convergence threshold.

Although problem (Algorithm 1) is equivalent to problem (5), which is mainly transferred by Dinkelbach's theorem, problem (Algorithm 1) is also a nonconvex MINLP formulation. Hence, to handle this situation, we propose an inner-layer convex approximation algorithm to convert (Algorithm 1) into a convex one.

3.2. Inner-Layer Convex Approximation (ILCA). For convenience, let q_k represent q_k^m in each iteration of OLIA. ILCA should perform the following three steps to convert the nonconvex MINLP problem (Algorithm 1) into a convex one. For the first step, the value of $x_{d_{k,i}}^t$ is relaxed into a continuous interval $[0, 1]$, and $(x_{d_{k,i}}^t \cdot p_{d_{k,i}}^t)$ is substituted by $S_{d_{k,i}}^t$:

$$\max_{X_k, P_{C_k}, P_{D_k}} \text{imize} : \left\{ \sum_{t=1}^T \sum_{d_{k,i} \in \Phi_{D_k}} R_{d_{k,i}}^t (p_{c_k}^t, S_{d_{k,i}}^t) - q_k \cdot \sum_{t=1}^T \sum_{d_{k,i} \in \Phi_{D_k}} S_{d_{k,i}}^t \right\}, \quad (8)$$

$$\text{s.t. (5a)}, \quad (8a)$$

$$R_{c_k}^t (p_{c_k}^t, S_{d_{k,i}}^t) \geq r_{c_k}^{th}, \quad (8b)$$

$$\sum_{n=1}^t S_{d_{k,i}}^n \leq \sum_{n=1}^t E_{d_{k,i}}^n + B_{d_{k,i}}^0, \quad (8c)$$

$$0 \leq S_{d_{k,i}}^t \leq p_{d_{k,i}}^{\max}, \quad (8d)$$

$$R_{d_{k,i}}^t(p_{c_k}^t, S_{d_{k,i}}^t) \geq x_{d_{k,i}}^t \cdot r_{d_{k,i}}^{\text{th}}, \quad (8e)$$

$$x_{d_{k,i}}^t \in [0, 1], \quad (8f)$$

where $R_{c_k}^t$ and $R_{d_{k,i}}^t$ shown by (9) and (10) are the equivalent transformation functions of $r_{c_k}^t$ and $r_{d_{k,i}}^t$ according to $S_{d_{k,i}}^t = x_{d_{k,i}}^t \cdot p_{d_{k,i}}^t$, respectively, and are related to $p_{c_k}^t$ and $S_{d_{k,i}}^t$:

$$R_{c_k}^t(p_{c_k}^t, S_{d_{k,i}}^t) = \log \left(1 + \frac{p_{c_k}^t \cdot g_{c_k B}}{\sum_{d_{k,j} \in \Phi_{D_k}} S_{d_{k,i}}^t \cdot g_{d_{k,i} B} + n_0} \right), \quad (9)$$

$$R_{d_{k,i}}^t(p_{c_k}^t, S_{d_{k,i}}^t) = \log \left(1 + \frac{S_{d_{k,i}}^t \cdot g_{d_{k,i}}}{p_{c_k}^t \cdot g_{c_k d_{k,i}} + \sum_{\substack{d_{k,j} \in \Phi_{D_k} \\ d_{k,j} \neq d_{k,i}}} S_{d_{k,i}}^t \cdot g_{d_{k,i} d_{k,j}} + n_0} \right). \quad (10)$$

According to the above equivalent substitution, the optimization problem (Algorithm 1) can be equivalently solved by finding solutions about variables of X_k , P_{c_k} , and S_{D_k} .

For the second step, as inequality (11) expresses, ILCA introduces the same convex approximation formula as [29] used to acquire an approximate transmission rate about the original one:

$$\alpha \log n + \beta \leq \log(1 + n). \quad (11)$$

The bound of approximation rate is proven to be tight and has low complexity in a high-SINR regime (i.e., $n \gg 1$). At this moment, $n = n_0$ and $\alpha = n_0/(1 + n_0)$, $\beta = \log(1 + n_0) - \alpha \log n_0$ [29]. To obtain the tightened lower bound, we need an iteration algorithm (such as step 2~step 6 in p.3751 of [29]) to make the approximation reach a high-SINR one.

For the third step, we perform some equivalent substitution of variables by equations of $p_{c_k}^t = e^{p_{c_k}^t}$, $S_{d_{k,i}}^t = e^{S_{d_{k,i}}^t}$. Consequently, according to the above three steps, problem (Algorithm 1) can be approximately transformed into the following convex optimization formulation:

$$\max_{X_k, \tilde{P}_{c_k}, \tilde{S}_{D_k}} \text{imize} : \left\{ \sum_{t=1}^T \sum_{d_{k,i} \in \Phi_{D_k}} \tilde{R}_{d_{k,i}}^t - q_k \cdot \sum_{t=1}^T \sum_{d_{k,i} \in \Phi_{D_k}} e^{\tilde{S}_{d_{k,i}}^t} \right\}, \quad (12)$$

$$\text{s.t. } \tilde{p}_{c_k}^t \leq \log(p_{c_k}^{\max}), \quad (12a)$$

$$r_{c_k}^{\text{th}} - \tilde{R}_{c_k}^t(\tilde{p}_{c_k}^t, \tilde{S}_{d_{k,i}}^t) \leq 0, \quad (12b)$$

$$\sum_{n=1}^t e^{\tilde{S}_{d_{k,i}}^n} - \sum_{n=1}^t E_{d_{k,i}}^n - B_{d_{k,i}}^0 \leq 0, \quad (12c)$$

$$\tilde{p}_{d_{k,i}}^t \leq \log(p_{d_{k,i}}^{\max}), \quad (12d)$$

$$x_{d_{k,i}}^t \cdot r_{d_{k,i}}^{\text{th}} - \tilde{R}_{d_{k,i}}^t(\tilde{p}_{c_k}^t, \tilde{S}_{d_{k,i}}^t) \leq 0, \quad (12f)$$

$$x_{d_{k,i}}^t \in [0, 1], \quad (12e)$$

where $R_{c_k}^t \sim (\tilde{p}_{c_k}^t, \tilde{S}_{d_{k,i}}^t)$ and $R_{d_{k,i}}^t \sim (\tilde{p}_{c_k}^t, \tilde{S}_{d_{k,i}}^t)$ are the tight approximation about $R_{c_k}^t$ and $R_{d_{k,i}}^t$ after the second and third steps and denoted by (13) and (14), respectively,

$$\tilde{R}_{c_k}^t(\tilde{p}_{c_k}^t, \tilde{S}_{d_{k,i}}^t) = \alpha_{c_k}^t \left(\log(g_{c_k B}) + \tilde{p}_{c_k}^t - \log \left(\sum_{d_{k,i} \in \Phi_{D_k}} e^{\tilde{S}_{d_{k,i}}^t} \cdot g_{d_{k,i} B} + n_0 \right) \right) + \beta_{c_k}^t, \quad (13)$$

$$\tilde{R}_{d_{k,i}}^t(\tilde{p}_{c_k}^t, \tilde{S}_{d_{k,i}}^t) = \alpha_{d_{k,i}}^t \left(\log(g_{d_{k,i}}) + \tilde{S}_{d_{k,i}}^t - \log \left(e^{\tilde{p}_{c_k}^t} \cdot g_{c_k d_{k,i}} + \sum_{\substack{d_{k,j} \in \Phi_{D_k} \\ d_{k,j} \neq d_{k,i}}} e^{\tilde{S}_{d_{k,i}}^t} \cdot g_{d_{k,i} d_{k,j}} + n_0 \right) \right) + \beta_{d_{k,i}}^t, \quad (14)$$

where the updating of $\alpha_{c_k}^t$, $\alpha_{d_{k,i}}^t$ and $\beta_{c_k}^t$, $\beta_{d_{k,i}}^t$ is the same. Obviously, according to the convexity of log-sum-exp [29, 30], problem (12) can easily proof to be a convex one. As a result, we can utilize one of the typical convex optimization algorithms to solve it easily and efficiently. When the solutions of problem (12) are obtained, we can convert the solving variables of original problem (5) back by using equations $p_{c_k}^t = e^{\tilde{p}_{c_k}^t}$, $S_{d_{k,i}}^t = e^{\tilde{S}_{d_{k,i}}^t}$, $x_{d_{k,i}}^t = 1$ when $\tilde{p}_{d_{k,i}}^t$ is no less than zero, and otherwise, $x_{d_{k,i}}^t = 0$.

Even though CAIA can obtain a quasioptimal solution for the original problem, there are two key obstacles to practically implement the proposed algorithm. Firstly, the iteration complexity of CAIA is one of the key obstacles to implement in the LTE (Long-Term Evolution) system which requires the scheduling period in milliseconds [31]. Secondly, the overall CSI and ESI during a period of time are hard to obtain practically. Thus, we propose a heuristic algorithm, which is named time-division scheduling scheme

Initialization: $m=1, q_k^m=0; \varepsilon=10^{-2};$
 step 1: For a given q_k^m , obtain X_k', P_{C_k}' and P_{D_k}' by solving the following optimization problem:

$$F(q_k^m) = \max_{\{X_k, P_{C_k}, P_{D_k}\} \in \Omega} : \{ \sum_{t=1}^T \sum_{d_{k,i} \in \Phi_{D_k}} x_{d_{k,i}}^t \cdot r_{d_{k,i}}^t - q_k^m \cdot \sum_{t=1}^T \sum_{d_{k,i} \in \Phi_{D_k}} x_{d_{k,i}}^t \cdot p_{d_{k,i}}^t \},$$

 step 2: Set $q_k^{m+1} = \sum_{t=1}^T \sum_{d_{k,i} \in \Phi_{D_k}} x_{d_{k,i}}^t \cdot [r_{d_{k,i}}^t (P_{C_k}', P_{D_k}') / p_{d_{k,i}}^t]$; If $|F(q_k^m)| > \varepsilon, m = m + 1;$
 step 3: Repeat the steps 1~2 until $|F(q_k^m)| \leq \varepsilon.$
Update: return $X = X_k', P_{C_k} = P_{C_k}'$ and $P_{D_k} = P_{D_k}'.$

ALGORITHM 1: Outer-layer iteration algorithm (OLIA).

(TDSS), to obtain a suboptimal solution with low computational complexity.

4. The Time-Division Scheduling Scheme (TDSS)

The complexity of CAIA and the difficulty obtained in the overall ESI and CSI promote us to design a heuristic algorithm to solve the stSEE problem. Although the ESI of all D2D pairs and the CSI of all involved communication links during a period of time are hard to obtain, the latest CSI and ESI (such as the next time slot) can be acquired through some prediction algorithms. For example, some environmental sources' (e.g., solar and wind) behavior can be predicted through the expected availability at a given time within some error margin [32]. Similarly, channel prediction is feasible and accurate if the predicted frequency is much higher than the channel changing time [33]. It is important to note that the prediction algorithms are not in our consideration.

With the CSI and ESI of the latest time slot, we can simply balance the transmission requirements between two adjacent time slots and hence increase the network performance. Accordingly, a heuristic algorithm, which is called TDSS, is proposed. TDSS can decouple the stSEE problem into two steps: D2D Pairs Choosing Strategy (DPCS) and power allocation strategy (PAS). As the pseudocode of Algorithm 2 shows, firstly, DPCS determines the corresponding EH-DPs in the set of Φ_{D_k} to multiplex the channel resource in each time slot for the k th EH-DP/CU group, where $k = \{1, 2, \dots, K\}$. After that, PAS allocates the corresponding power for

the CU and the chosen EH-DPs. In other words, in each time slot, the two-step scheme firstly determines the indicative factor $x_{d_{k,i}}^t$ for EH-DPs in the k th group and then allocates $p_{c_k}^t$ and $p_{d_{k,i}}^t$ for the CU and the chosen EH-DPs. In the following two subsections, the detailed algorithm steps of DPCS and PAS will be described.

4.1. D2D Pairs Choosing Strategy (DPCS). The DPCS is the first procedure in TDSS and aimed at choosing the proper EH-DPs to multiplex the channel resource of CU at each time slot with the intention of load balance. The purpose of load balance is to schedule the transmission requirements between two adjacent time slots so as to decrease the interference between EH-DPs.

The design of DPCS is inspired by a basic characteristic of the optimization problem, which comes from the transmission rate restraints of CU and EH-DP. It means that those chosen EH-DPs in each time slot should satisfy a basic available energy threshold $p_{d_{k,i}}^{\text{th}}$. If not, the EH-DP cannot be a candidate to multiplex the channel resource. Based on this, $p_{d_{k,i}}^{\text{th}}$ is expressed by Corollary 4 and is derived in Appendix A.

Corollary 4. *In order to ensure the PAS has a feasible solution set, the available power of the chosen EH-DP $d_{k,i}$ battery must satisfy a minimum value:*

$$B_{d_{k,i}}^t \geq p_{d_{k,i}}^{\text{th}}, \quad (15)$$

where

$$p_{d_{k,i}}^{\text{th}} = \frac{\sum_{d_{k,j} \in \Phi_{D_k}, d_{k,j} \neq d_{k,i}} p_{d_{k,j}}^{\text{max}} (\mathcal{M}_{d_{k,i}} \cdot g_{d_{k,j}B} + \mathcal{N}_{d_{k,i}} \cdot g_{d_{k,j}d_{k,i}}) + n_0 (\mathcal{M}_{d_{k,i}} + \mathcal{N}_{d_{k,i}})}{g_{c_k B} \cdot g_{d_{k,i}} - g_{d_{k,i}B} \cdot \mathcal{M}_{d_{k,i}}}, \quad (16)$$

where $\mathcal{M}_{d_{k,i}} = r_{c_k}^{\text{th}} \cdot r_{d_{k,i}}^{\text{th}} \cdot g_{c_k d_{k,i}}, \mathcal{N}_{d_{k,i}} = r_{d_{k,i}}^{\text{th}} \cdot g_{c_k B}.$

Proof. The proof of this corollary is provided in Appendix B.

Therefore, based on the minimum energy threshold $p_{D_k}^{\text{th}}$ ($p_{D_k}^{\text{th}} = \{p_{d_{k,i}}^{\text{th}}, d_{k,i} \in \Phi_{D_k}\}$) and the latest ESI prediction value

$E_{D_k}^t \sim (E_{D_k}^t = \{E_{d_{k,i}}^t\}, d_{k,i} \in \Phi_{D_k})$, the proposed DPCS has three key steps to determine the candidate EH-DPs for each EH-DP/CU group as illustrated in Figure 4 and Algorithm 3.

Step 1. With the current available energy $B_{d_{k,i}}^t$ and minimum energy consumption threshold $p_{d_{k,i}}^{\text{th}}$, we can pick out m_k^t

Input: Set $t=1$;
Output: X, P_C, P_D ;
While $t \leq T$ **do**
 for each k EH-DPs/CU group **do**
 step 1: the D2D Pairs Choosing Strategy (DPCS) determines the binary variables $\{x_{d_{k,i}}^t, (d_{k,i} \in \Phi_{D_k})\}$ according to the CSI and ESI of the time slot t and $t+1$;
 step 2: the Power Allocation Strategy (PAS) allocates the power control parameters $\{p_{c_k}^t, p_{d_{k,i}}^t\}$ after step one.

ALGORITHM 2: Time-division scheduling scheme (TDSS).

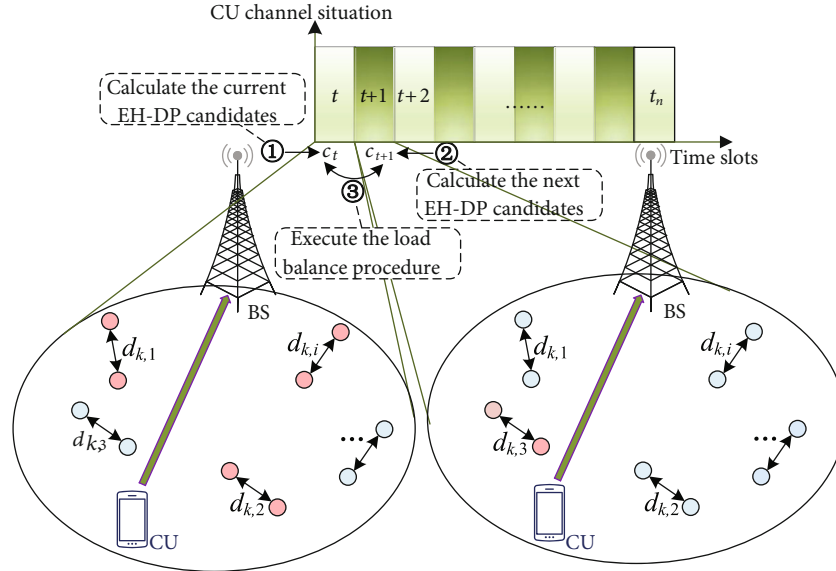


FIGURE 4: D2D Pairs Choosing Strategy (DPCS) in the t th time slot for the k th EH-DP/CU group.

Input: Set $t, B_{d_{k,i}}^t, p_{d_{k,i}}^{th}$, and $E_{d_{k,i}}^{t+1\sim}, d_{k,i} \in \Phi_D$;
Output: $x_{d_{k,i}}^t$;
Initialize: m_k^t and $m_k^{t+1} = 0$;
 step 1: pick out the current EH-DP candidates: if $B_{d_{k,i}}^t \geq p_{d_{k,i}}^{th}$, ($\forall d_{k,i} \in \Phi_{D_k}$), then $m_k^t = m_k^t + 1$;
 step 2: pick out the next EH-DP candidates: based on the energy arrival prediction value $E_{d_{k,i}}^{t+1\sim}$, calculate the next available energy according to equation $B_{d_{k,i}}^{t+1} = B_{d_{k,i}}^t - p_{d_{k,i}}^{th} + E_{d_{k,i}}^{t+1\sim}$. Similarly, let $m_k^{t+1} = m_k^{t+1} + 1$ when $B_{d_{k,i}}^{t+1} \geq p_{d_{k,i}}^{th}$ for all EH-DP in Φ_{D_k} .
 step 3: load balance procedure: consider the feature that energy cannot be used in advance. So, only when $m_k^t - m_k^{t+1} \geq 2$, the transmission load between two adjacent time slots can be balanced, and the current allowed transmission load c_t equals to $\lceil (m_k^t + m_k^{t+1})/2 \rceil$. After that, pick out m_k^t EH-DPs in the current candidate list to multiplex the current channel resource of c_t -th CU.

ALGORITHM 3: Time-division scheduling scheme (TDSS).

candidate EH-DPs from the set Φ_{D_k} in an instantaneous time slot t for the k th EH-DP/CU group. As Figure 4 illustrates, the EH-DPs with the red color are candidates which meet the above basic energy demand.

Step 2. If m_k^t candidate EH-DPs can multiplex the channel resource to transmit at the t th time slot, $p_{d_{k,i}}^{th}$ unit power will be consumed at least. According to the power update rule $B_{d_{k,i}}^{t+1} = B_{d_{k,i}}^t - p_{d_{k,i}}^{th} + E_{d_{k,i}}^{t+1\sim}$, m_k^{t+1} candidate EH-DPs can also

be picked out from the set Φ_{D_k} at time slot $t+1$ according to $B_{d_{k,i}}^{t+1}$ and $p_{d_{k,i}}^{th}$.

Step 3. The number of candidate D2D pairs between the two time slots can be balanced for the purpose of decreasing the interference among D2D pairs. For example, in Figure 4, the current and next EH-DP candidates are 3 and 1, respectively. Thus, the number of transmitted D2D pairs of the two adjacent time slots can be evenly assigned to 2. In other

words, if the number difference of candidate D2D pairs between the current time slot and the adjacent next time slot is larger than or equal to 2, we can execute the load balance procedure. Notably, we can only schedule the condition that the service requirements in the current time is larger than the next due to the store-and-use characteristic of energy harvesting [34]. After that, in time slot t , DPCS will choose the average assignment number of D2D candidates $\lceil (m_k^t + m_k^{t+1})/2 \rceil$ to multiplex CU channel according to the principles of lower interference and larger transmission rate.

After the DPCS, m_k^t EH-DPs can be selected from Φ_{D_k} to multiplex the channel resource of CU c_k in k th EH-DP/CU group. Therefore, $x_{d_{k,i}}^t (d_{k,i} \in \Phi_{D_k^s})$, where $\Phi_{D_k^s}$ is the set of the selected EH-DPs in Φ_{D_k} , is set to 1. In the same way, $x_{d_{k,i}}^t (d_{k,i} \in \{\Phi_{D_k} - \Phi_{D_k^s}\})$ is set to 0.

4.2. Power Allocation Strategy (PAS). After determining the binary indicator variables $x_{d_{k,i}}^t$, the optimal power should be allocated for each transmission node (CUs and chosen EH-DPs) by maximizing the EE of the D2D communication, while guaranteeing the CUs' transmission service quality. Thus, the optimization problem \mathbf{P}_{EE}^k will become an EE maximization problem as stated in s_P1:

$$(s_P1) \text{ maximize : } \frac{\sum_{d_{k,i} \in \Phi_{D_k^s}} R_{d_{k,i}}^t(p_{c_k}^t, p_{d_{k,i}}^t)}{\sum_{d_{k,i} \in \Phi_{D_k^s}} p_{d_{k,i}}^t}, \quad (17)$$

$$\text{s.t. } 0 \leq p_{c_k}^t \leq p_{c_k}^{\max}, \quad (17a)$$

$$R_{c_k}^t(p_{c_k}^t, p_{d_{k,i}}^t) \geq r_{c_k}^{\text{th}}, \quad (17b)$$

$$p_{d_{k,i}}^t \leq E_{d_{k,i}}^t + B_{d_{k,i}}^t - p_{d_{k,i}}^{t-1}, \quad (17c)$$

$$0 \leq p_{d_{k,i}}^t \leq p_{d_{k,i}}^{\text{th}}, \quad (17d)$$

$$R_{d_{k,i}}^t(p_{c_k}^t, p_{d_{k,i}}^t) \geq r_{d_{k,i}}^{\text{th}}, \quad (17e)$$

where $R_{c_k}^t$ and $R_{d_{k,i}}^t$ are the relative transmission rate equations about $p_{c_k}^t$ and $p_{d_{k,i}}^t$, respectively, and can be obtained by (9) and (10). Notably, the EH-DPs belong to the set of $\Phi_{D_k^s}$ at this time. The constraint (17c) is the available energy of each chosen D2D pair in battery. (17d) and (17e) are the constraints of maximum transmission power and minimum transmission rate of the relative choosing EH-DPs, respectively. The similar restraints for CU are (17a) and (17b).

Remarkably, the objective function is a fractional non-convex optimization problem because the numerator of objective function of s_P1 and the constraints (17b) and (17e) are nonconvex. Thus, it is difficult to find a solution for the objective optimization problem. However, we can utilize the same convex approximation approach as CAIA used to obtain a tight lower-bound convex approximation of the numerator in the nonconcave formula (17). Hence, inequal-

ity (11) and equality substitution $p_{c_k}^t = e^{p_{c_k}^{\tilde{t}}}$, $p_{d_{k,i}}^t = e^{p_{d_{k,i}}^{\tilde{t}}}$ can convert s_P1 to a lower bound which is illustrated by fs_P1:

$$(fs_P1): \text{ maximize : } \frac{f(p_{c_k}^{\tilde{t}}, p_{d_{k,i}}^{\tilde{t}})}{\{p_{c_k}^{\tilde{t}}, p_{d_{k,i}}^{\tilde{t}}\} g(p_{c_k}^{\tilde{t}}, p_{d_{k,i}}^{\tilde{t}})}, \quad (18)$$

$$\text{s.t. } p_{c_k}^{\tilde{t}} \leq \log(p_{c_k}^{\max}), \quad (18a)$$

$$R_{c_k}^{\tilde{t}}(p_{c_k}^{\tilde{t}}, p_{d_{k,i}}^{\tilde{t}}) \geq r_{c_k}^{\text{th}}, \quad (18b)$$

$$p_{d_{k,i}}^{\tilde{t}} \leq \log(E_{d_{k,i}}^t + B_{d_{k,i}}^t - p_{d_{k,i}}^{t-1}), \quad (18c)$$

$$p_{d_{k,i}}^{\tilde{t}} \leq \log(p_{d_{k,i}}^{\max}), \quad (18d)$$

$$R_{d_{k,i}}^{\tilde{t}}(p_{c_k}^{\tilde{t}}, p_{d_{k,i}}^{\tilde{t}}) \geq r_{d_{k,i}}^{\text{th}}, \quad (18e)$$

where $f(p_{c_k}^{\tilde{t}}, p_{d_{k,i}}^{\tilde{t}})$ and $g(p_{c_k}^{\tilde{t}}, p_{d_{k,i}}^{\tilde{t}})$ are shown by (19) and (20), respectively. Similarly, $R_{c_k}^{\tilde{t}}(p_{c_k}^{\tilde{t}}, p_{d_{k,i}}^{\tilde{t}})$ and $R_{d_{k,i}}^{\tilde{t}}(p_{c_k}^{\tilde{t}}, p_{d_{k,i}}^{\tilde{t}})$ can be seen in (13) and (14), respectively. As fs_P1 shows, it is a fractional optimization problem. As we know, log-sum-exp is convex. So, the function $f(p_{c_k}^{\tilde{t}}, p_{d_{k,i}}^{\tilde{t}})$ is jointly concave about parameters $p_{c_k}^{\tilde{t}}$ and $p_{d_{k,i}}^{\tilde{t}}$. Besides, the function $g(p_{c_k}^{\tilde{t}}, p_{d_{k,i}}^{\tilde{t}})$ can be easily proved to be jointly convex about parameters $p_{c_k}^{\tilde{t}}$ and $p_{d_{k,i}}^{\tilde{t}}$. Likewise, the constraints (18b) and (18e) are also jointly convex functions. Thus, fs_P1 is a typical fractional optimization problem and can be solved by the Dinkelbach algorithm [35]. So, the main power allocation algorithm flow of PAS can be summarized by Algorithm 4.

$$f(p_{c_k}^{\tilde{t}}, p_{d_{k,i}}^{\tilde{t}}) = \sum_{d_{k,i} \in \Phi_{D_k^s}} R_{d_{k,i}}^{\tilde{t}}(p_{c_k}^{\tilde{t}}, p_{d_{k,i}}^{\tilde{t}}), \quad (19)$$

$$g(p_{c_k}^{\tilde{t}}, p_{d_{k,i}}^{\tilde{t}}) = \sum_{d_{k,i} \in \Phi_{D_k}} e^{p_{d_{k,i}}^{\tilde{t}}}. \quad (20)$$

5. Simulation Results

In this section, our goals are to verify the effectiveness of our proposed algorithms and study the impact of EH efficiency factors on system performance. Consequently, we will present numerical results to evaluate the proposed algorithm (CAIA) and the suboptimal heuristic algorithm (TDSS) in aspects of average (avg.) achievable EE and transmission rate of EH-DP. Furthermore, to assess the proposed algorithms, we will compare the proposed algorithms with the real-time transmission strategy (RTS), the Exhaustive Searching Scheme (ESS), and the Q-Learning Approach (QLA).

Input: $\{x_i^t (i \in \{\Phi_{D_k}\})\}$ for k -th group at time slot t ;
Output: $\{p_i^t (i \in \{c_k, \Phi_{D_k}\})\}$;
Initialization: $m = 0, \lambda_k^m = 0, \varepsilon = 10^{-2}$; set the fs_P1 as the power allocation optimization target;
While $F(\lambda_k^m) > \varepsilon \mathbf{do}$
 $\{p_{c_k}^{t*}, p_{d_{k,i}}^{t*}\} = \arg \max \{f(p_{c_k}^{t*}, p_{d_{k,i}}^{t*}) - \lambda_k^m \cdot g(p_{c_k}^{t*}, p_{d_{k,i}}^{t*})\}$ with constraints of (18a)~(18e);
 $\lambda_k^m = f(p_{c_k}^{t*}, p_{d_{k,i}}^{t*}) / g(p_{c_k}^{t*}, p_{d_{k,i}}^{t*})$;
 Update $F(\lambda_k^m) = f(p_{c_k}^{t*}, p_{d_{k,i}}^{t*}) - \lambda_k^m \cdot g(p_{c_k}^{t*}, p_{d_{k,i}}^{t*})$;
 $m = m + 1$;
End
Update: $p_i^t = \begin{cases} e^{p_i^{t*}}, & i \in \{c_k\} \cup \Phi_{D_k}^i \\ 0, & i \in \Phi_{D_k} - \Phi_{D_k}^i \end{cases}$

ALGORITHM 4: Power allocation strategy (PAS).

TABLE 2: Parameter setting in EH-DCCN simulation environment.

Parameter	Value
Path loss, CU link	$128.1 + 37.6 \log(\text{dck}[\text{Km}])$ dB
Path loss, DU link	$148 + 40 \log([\text{Km}])$ dB
CU max Tx power ($p_{c_k}^{\max}$)	20 dBm
D2D max Tx power ($p_{d_{k,i}}^{\max}$)	17 dBm
Possible harvested energy for each EH-DP (E)	$5 * 10^{-4}$ Watts
Initial battery power ($B_{d_{k,i}}^0$)	0 Watt
The arrival energy probability for each EH-DP ($\lambda_{d_{k,i}}$)	Randomly choose from 0.1 to δ , $\delta \in (0, 1]$
Channel bandwidth (B_W)	180 kHz
Noise power density (ρ_n)	-174 dBm/Hz
Number of D2D links (N_k)	Randomly choose from 2 to 8
Min trans. rate, CU link ($r_{c_k}^{\text{th}}$)	2 bps/Hz
Min trans. rate, DU link ($r_{d_{k,i}}^{\text{th}}$)	4 bps/Hz
Sum time slots (T)	200
Discount factor of QLA (γ)	0.8

In each time slot, once the EH-DP has enough energy to satisfy its transmission power demand, the RTS scheme will let EH-DP transmit directly by executing the power allocation algorithm for the CUs and the chosen EH-DPs. ESS can enumerate all possible solutions during the short-term time horizon and thus attain an optimal solution. QLA, a well-known reinforcement learning program, is widely used to solve some long-term or short-term utilities [36, 37]. To better assess the effectiveness of the proposed algorithms, we implement QLA as a centralized one.

5.1. Simulation Setup. The performance of the compared methods and the proposed algorithms in this study is evaluated via simulations. Above all, the considered cellular network with radius of 800 meters is demonstrated in Figure 1. The central controller, BS, has the capability of acquiring all users' position, and it is always located at the centre of this

cellular area. Suppose that there exists K ($K = 20$) EH-DP/CU groups. For the k th group ($k = \{1, 2, \dots, K\}$), N_k EH-DPs can multiplex the uplink channel radio resource of CU c_k , where N_k is randomly selected from 2 to 8. All users are randomly deployed in the cellular zone. And meanwhile, the distance between transmitter and receiver of each EH-DP pair is randomly selected between [20, 50] meters [21]. Remarkably, to avoid serious mutual interference between each other, a minimum distance threshold, which equals to 200 meters, should be obeyed between CU and EH-DPs [38, 39]. Similarly, the distance among EH-DPs in each group must be larger than 100 meters. The energy arrival process for every EH-DP is assumed to be i.i.d. *Bernoulli* sample, which conforms to formula (2). The other network parameters used in this study are listed in Table 2.

We repeat each simulation scenario with different energy arrival probabilities; for example, δ is 0.3 among EH-DPs, 100 times and average the results.

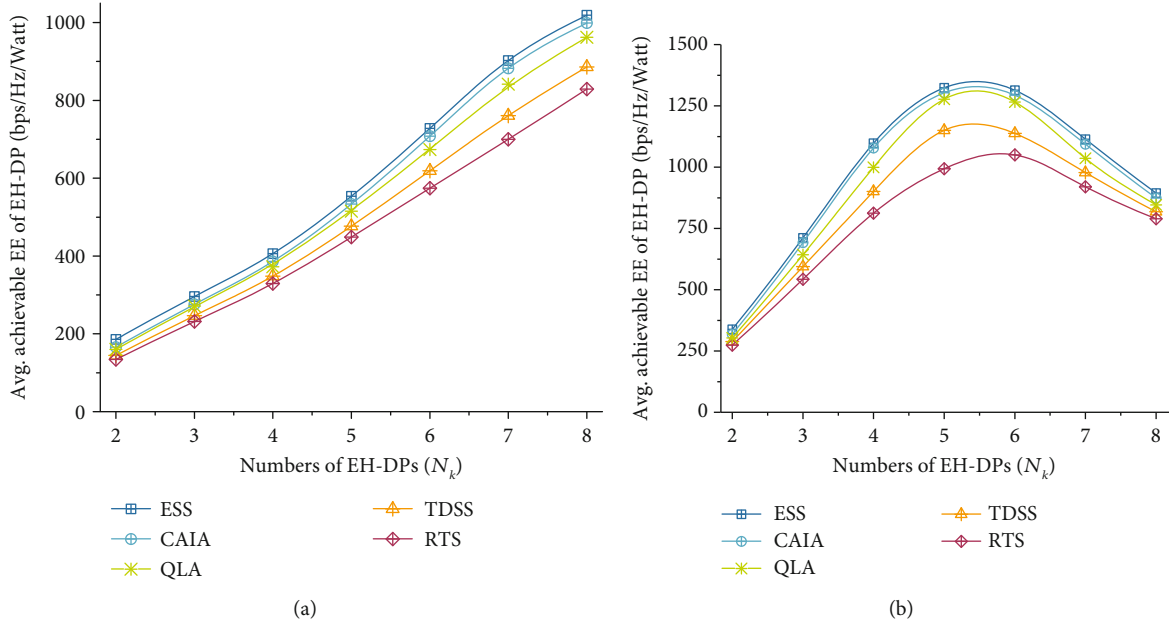
5.2. Complexity Comparison. The computational complexity is an important aspect to better assess the effectiveness of the above algorithms. First of all, there are two important things that should be mentioned.

- (i) The procedure of algorithms (CAIA, TDSS, and RTS) includes convex optimization of nonlinear programming. So, we use the ε -approximate solution to measure the computational complexity. It means that the computational complexity of algorithms (CAIA, TDSS, and RTS) is the needed iteration times when the solution reaches ε condition, such as Algorithms 1 and 4
- (ii) We calculate and express the worst-case computational complexity of all algorithms for a fair comparison

It is hard to have a thorough and correct analysis of complexity of convex nonlinear programming problems. However, generally speaking, the complexity is related to the space required to store input data and to the running time of the algorithm until a solution is found [40]. Besides, Vidal et al. [41] produced that the complexity of an ε -approximate

TABLE 3: The computational complexity of CAIA, TDSS, RTS, ESS, and QLA.

Algorithms	Complexity	Simulation time (seconds)
ESS	$\mathcal{O}\left(\left(p_c^{\max} \cdot (p_d^{\max})^D\right)^T\right)$	955.74
CAIA	$\mathcal{O}((2D+1) \cdot T \cdot \log((2D+1) \cdot T) \cdot \log((2D+1) \cdot T \cdot B/\epsilon))$	106.52
QLA	$\mathcal{O}(T \cdot \mathbb{S} \times \mathbb{A} /\epsilon^2(1-\gamma)^5) = \mathcal{O}\left(T \left[(D+1) \cdot 2^D \cdot p_c^{\max} \cdot (p_d^{\max})^D\right]/\epsilon^2(1-\gamma)^5\right)$	293.11
TDSS	$\mathcal{O}(D \cdot T + (D+1) \cdot T \cdot \log((2D+1)) \cdot \log((D+1) \cdot B/\epsilon))$	16.79
RTS	$\mathcal{O}((D+1) \cdot T \cdot \log((2D+1)) \cdot \log((D+1) \cdot B/\epsilon))$	15.76

FIGURE 5: Average achievable EE of EH-DP: (a) $\delta = 0.3$; (b) $\delta = 0.7$.

solution for the continuous convex problem is $\mathcal{O}(n \log m \log(nB/\epsilon))$, where n is the number of variables, m is the number of constraints, and B is the constraint bound. Moreover, as we all know, the complexity of QLA is related to the size of state-action space $|\mathbb{S} \times \mathbb{A}|$ [42]. Thus, the complexity of the above-mentioned algorithms can be depicted in Table 3.

In Table 3, D means the number of D2D pairs, i.e., $D = N_k = |\Phi_{D_k}|$. B represents the maximal resource threshold. γ denotes the discount factor of QLA. The simulation time is the average result of the algorithms being executed about 100 times under a simulation scenario with $N_k = 5$, $\delta = 0.3$. Thus, we can draw a valid conclusion that ESS has the highest complexity while TDSS and RTS have the similar complexity, which is the lowest one. And then, QLA exhibits a little bit lower complexity than ESS, and CAIA is lower than QLA.

5.3. Performance Results and Analysis

5.3.1. The EE Performance Comparison. Figure 5 shows the simulation results of avg. achievable EE of EH-DP. It is worth noting that the results of QLA shown are steady-state perfor-

mance. The simulation results of avg. achievable EE exhibit three significant conclusions:

- (i) By comparing with RTS, the EE performance of CAIA and TDSS shows that our proposed short-term transmission scheduling strategy obtains better EE than RTS whatever the numbers of EH-DP. In other words, the short-term energy-efficient scheduling strategy is more suitable for the EH-DCCN. Moreover, due to the approximate rules of CAIA, CAIA can acquire a tight lower bound of the stSEE problem by comparing with the optimal algorithm ESS. The heuristic algorithm TDSS can obtain a sub-optimal solution for the stSEE problem with the lowest computational complexity. With lots of trial and error, QLA owns the similar EE performance with ESS. However, the computational complexity is the biggest obstacle about the implementation of ESS and QLA
- (ii) With the rise of the harvested energy or the number of EH-DPs, the growth rate of EE between the short-term scheduling scheme and the real-time

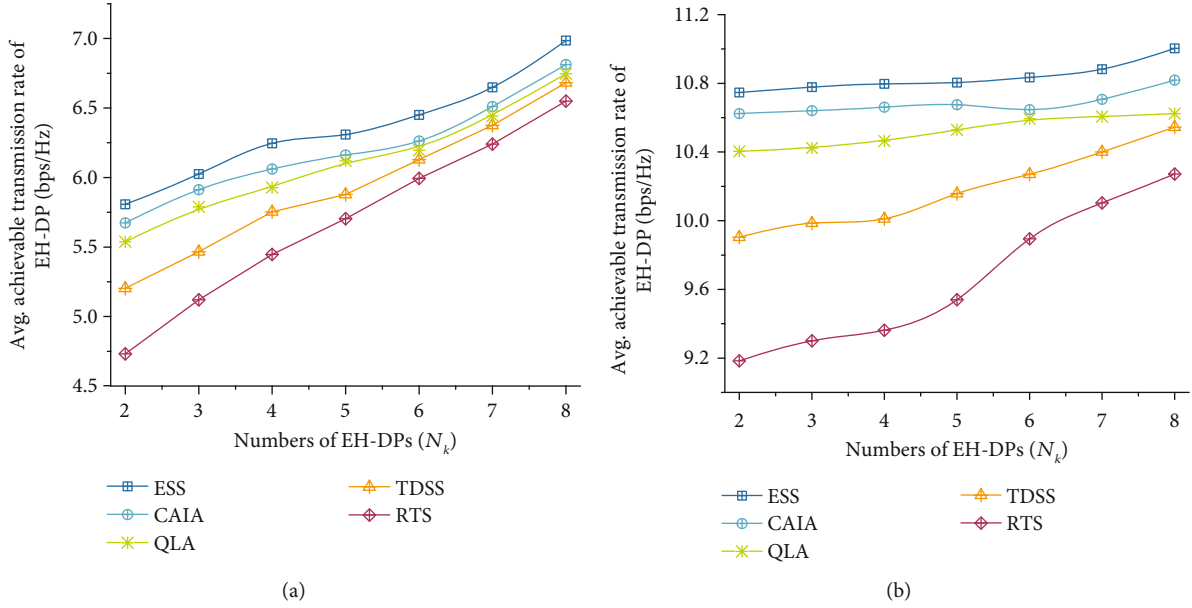


FIGURE 6: Average achievable transmission rate of EH-DP: (a) $\delta = 0.3$; (b) $\delta = 0.7$.

transmission gradually becomes smaller. For instance, as shown in Figure 5(b), the increasing rate of avg. EE between CAIA and RTS is about 35% under the number of EH-DP which is 5. However, the increasing rate of avg. EE is declined to 13% under the number of EH-DP which is 8. That is due to the fact that as the energy arrival probability or number of EH-DPs increases, the time slots available to be scheduled will be decreased

- (iii) Additionally, please note that under δ equals 0.7 of Figure 5(b), the avg. EE slowly declines when the EH-DP's number is no less than 5. This is because the more numbers of EH-DPs there are, the more transmission requests there are. As a result, more energy must be consumed to endure the mutual interference so as to satisfy the target transmission rate. In the end, the average EE will decline. This phenomenon means that the maximal available scheduled number of EH-DPs is 5 under the energy arrival probability of 0.7. From this, the maximum sustainable numbers of EH-DP can be easily obtained under different EH probability. In this way, we can give a theoretical development reference for future EH-DCCN

5.3.2. The Transmission Rate Performance Comparison. For purpose of better revealing the different reactions of the above algorithms in the modelled stSEE optimization under different EH-DCCN scenarios, the mean and variance of transmission rate of EH-DPs are exhibited in Figures 6 and 7, respectively. The variance of transmission rate, which can express the equilibrium level among users, means the degree of deviation from its mean. The smaller the value of variance, the higher the equilibrium level. Two crucial phenomena can be concluded from Figures 6 and 7:

- (i) Obviously, as demonstrated by Figure 6, along with the increasing of numbers of EH-DPs, or energy arrival probabilities, the avg. transmission rate of EH-DPs will increase accordingly. However, the growth rate of the avg. transmission rate of EH-DPs, just like the trend of EE performance, is going to be very slow when the harvested energy or the number of EH-DPs grows a certain extent
- (ii) From Figure 7, the variance of transmission rate of CAIA, ESS, and QLA is always lower than that of RTS and TDSS under any situations. It means that CAIA, ESS, and QLA will make the EH-DPs achieve better balanced effect. So, stSEE programming can be better executed by CAIA, ESS, and QLA. This is because of the fact that CAIA, ESS, and QLA can make better decision by fully considering short-term resource equilibrium according to channel interference (i.e., number of EH-DPs) and energy level (i.e., energy arrival probability). Moreover, the poorer equilibrium of the slot-by-slot programming schemes, i.e., TDSS and RTS, also perfectly explains that the short-term energy-efficient scheduling strategy is more suitable for improving the performance of EH-DCCN

6. Conclusions

In this study, we investigate energy-efficient time-domain transmission equilibrium scheduling and power allocation scheme for improving the performance of the EH-powered D2D communication underlying cellular network, where cellular users (CUs) and EH-powered D2D pairs (EH-DPs) transmit data over a shared uplink channel. According to the volatility of energy availability and the channel conditions of users, a short-term Sum Energy Efficiency (stSEE)

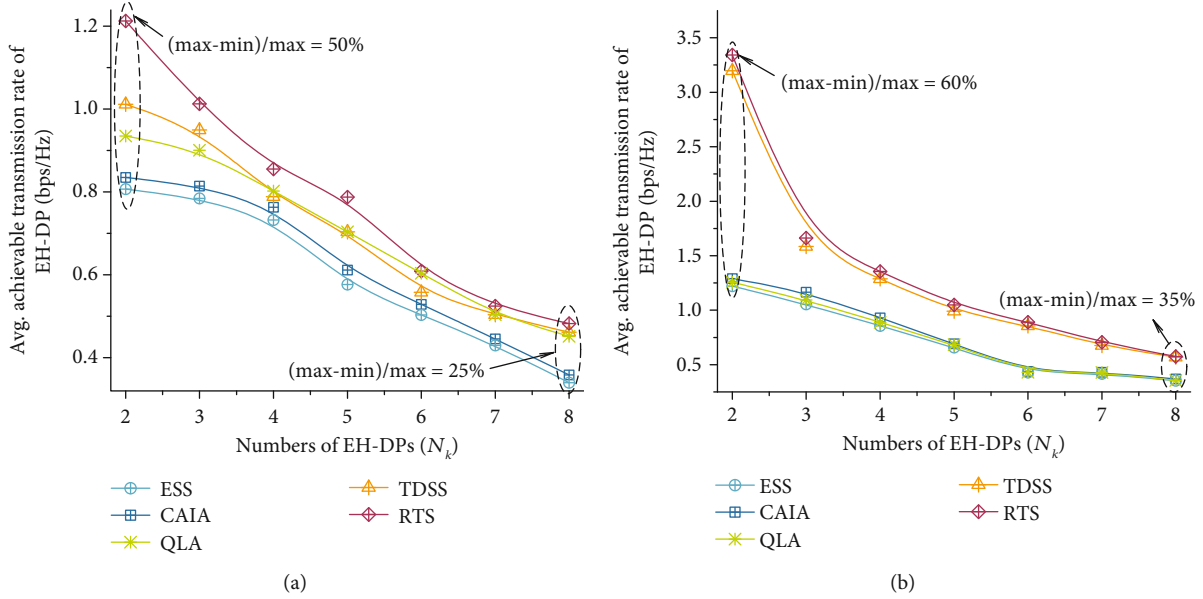


FIGURE 7: Average variance of transmission rate of EH-DPs: (a) $\delta = 0.3$; (b) $\delta = 0.7$.

maximization problem of EH-powered D2D communication is modelled, while ensuring the transmission rate requirements of CUs. However, the optimization problem, including transmission scheduling of EH-DPs and power allocation for CUs and chosen EH-DPs during a finite time horizon, is difficult and time-consuming. So, we propose a two-layer convex approximation iteration algorithm (CAIA) which can obtain a feasible quasioptimal solution for the modelled stSEE maximization problem. Simultaneously, a two-step heuristic algorithm in a slot-by-slot fashion is also developed to acquire a suboptimal solution without requiring statistical knowledge of channel and EH processes. By numerical analysis, the results show that the short-term time-domain equilibrium scheduling strategy can obtain better performances in terms of energy efficiency and transmission rate than the real-time scheduling algorithm for different EH settings. Besides, we also study the maximum scheduled number of D2D pairs underlying one CU under different energy harvesting efficiency, which can give us the insight needed to design EH-powered D2D communications.

Appendix

A. Proof of the Nonconvex Feature of $r_{c_k}^t$ and $r_{d_{k,i}}^t$

For the sake of presentation, we can use a general form (A.1) to describe $r_{c_k}^t$ and $r_{d_{k,i}}^t$:

$$r_i(P) = \log \left(1 + \frac{P_i \cdot a_i}{\sum_{j=1, j \neq i}^N P_j \cdot a_j + n_0} \right), \quad (\text{A.1})$$

where i belongs to set $\{\Phi_C, \Phi_D\}$, N equals to the sum number of all users reusing one spectrum resource, P is the set of transmission power, and a_i denotes the corresponding channel gain when user i is at the current channel. The necessary

and sufficient condition to prove the convexity of a function is to see whether the Hessian matrix of the function is positive definite for all variables. Consequently, the first-order partial derivative of (A.1) with respect to variable P can be denoted as follows:

$$\frac{\partial r_i}{\partial p_i} = \frac{a_i}{\mathcal{M}}, \quad (\text{A.2a})$$

$$\frac{\partial r_i}{\partial p_j} = \frac{a_j(\mathcal{N} - \mathcal{M})}{\mathcal{M} \cdot \mathcal{N}}, \quad (\text{A.2b})$$

where $\mathcal{M} = \sum_{i=1}^N p_i \cdot a_i$, $\mathcal{N} = \sum_{j=1, j \neq i}^N p_j \cdot a_j$. Due to the indicator parameters x , we must discuss different interference situations, i.e., various N . So, we will describe the interference situation and the corresponding Hessian matrix expression under various scenarios with different numbers of users.

- (1) When N equals to 1, r_i can be expressed as formula (A.3a). Accordingly, the second-order condition of (A.3a) with regard to $P = \{p_1\}$, i.e., Hessian matrix $H_N = 1$, can be represented as formula (A.3b). Obviously, the transmission rate is concave under $N = 1$:

$$r_1(P) = \log \left(1 + \frac{P_1 \cdot a_1}{n_0} \right), \quad (\text{A.3a})$$

$$H_{N=1} = \frac{\partial^2 r_1}{\partial p_1^2} = \frac{-a_1^2}{\mathcal{M}^2} < 0 \quad (\text{A.3b})$$

- (2) In the same way, when N equals to 2, the general transmission rate form (A.1) and its Hessian matrix expression can be written as equations (A.4a) and (A.4b), respectively. According to formula (A.4b)

and the second derivative test (as in [42], p. 971), the transmission rate is neither convex nor concave under $N = 2$:

$$r_i(P) = \log \left(1 + \frac{p_i \cdot a_i}{\sum_{j=1, j \neq i}^2 p_j \cdot a_j + n_0} \right), \quad (\text{A.4a})$$

$$H_{N=2}^{r_i} = \begin{vmatrix} \frac{\partial^2 r_i}{\partial p_i^2} & \frac{\partial^2 r_i}{\partial p_i \partial p_j} \\ \frac{\partial^2 r_i}{\partial p_i \partial p_j} & \frac{\partial^2 r_i}{\partial p_j^2} \end{vmatrix} \quad (\text{A.4b})$$

$$= \begin{vmatrix} \frac{-a_i^2}{\mathcal{M}^2} & \frac{-a_i a_j}{\mathcal{M}^2} \\ \frac{-a_i a_j}{\mathcal{M}^2} & \frac{-a_j^2 (\mathcal{N}^2 - \mathcal{M}^2)}{\mathcal{M}^2 \mathcal{N}^2} \end{vmatrix} = \frac{-a_i^2 a_j^2}{\mathcal{M}^2 \mathcal{N}^2} < 0$$

(3) Under $N = 3$, we can also obtain the relative transmission rate form and Hessian matrix expression as shown in equations (A.5a) and (A.5b). Thus, the convexity of the transmission rate cannot be judged:

$$r_i(P) = \log \left(1 + \frac{p_i \cdot a_i}{\sum_{j=1, j \neq i}^3 p_j \cdot a_j + n_0} \right), \quad (\text{A.5a})$$

$$H_{N=3}^{r_i} = \begin{vmatrix} \frac{\partial^2 r_i}{\partial p_i^2} & \frac{\partial^2 r_i}{\partial p_i \partial p_j} & \frac{\partial^2 r_i}{\partial p_i \partial p_k} \\ \frac{\partial^2 r_i}{\partial p_j \partial p_i} & \frac{\partial^2 r_i}{\partial p_j^2} & \frac{\partial^2 r_i}{\partial p_j \partial p_k} \\ \frac{\partial^2 r_i}{\partial p_k \partial p_i} & \frac{\partial^2 r_i}{\partial p_k \partial p_j} & \frac{\partial^2 r_i}{\partial p_k^2} \end{vmatrix}$$

$$= \begin{vmatrix} \frac{-a_i^2}{\mathcal{M}^2} & \frac{-a_i a_j}{\mathcal{M}^2} & \frac{-a_i a_k}{\mathcal{M}^2} \\ \frac{-a_i a_j}{\mathcal{M}^2} & \frac{-a_j^2 (\mathcal{N}^2 - \mathcal{M}^2)}{\mathcal{M}^2 \mathcal{N}^2} & \frac{-a_j a_k (\mathcal{N}^2 - \mathcal{M}^2)}{\mathcal{M}^2 \mathcal{N}^2} \\ \frac{-a_k a_i}{\mathcal{M}^2} & \frac{-a_k a_j (\mathcal{N}^2 - \mathcal{M}^2)}{\mathcal{M}^2 \mathcal{N}^2} & \frac{-a_k^2 (\mathcal{N}^2 - \mathcal{M}^2)}{\mathcal{M}^2 \mathcal{N}^2} \end{vmatrix} = 0 \quad (\text{A.5b})$$

(4) Similarly, the Hessian matrix expression when $N \geq 4$ equals to zero. Therefore, the concavity and convexity of r_i cannot be estimated

From the above discussion, the form of r_i cannot be confirmed due to the indicator parameters x . Thus, the concavity and convexity of r_i cannot be always estimated. As a result, the sum rate, i.e., $\sum_i r_i$ is neither convex nor concave.

B. Proof of the Minimal Energy Threshold

From the transmission rate requirements of CU and D2D pairs in equations (6b) and (6e), we can easily obtain the transmission power constraints of CU as follows if $d_{k,i}$ belongs to $\Phi_{D_k^t}$:

$$\begin{cases} p_{c_k}^t \geq \left\{ \frac{\tilde{r}_{d_{k,i}}^t \left(\sum_{d_{k,i} \in \Phi_{D_k^t}} p_{d_{k,i}}^t g_{d_{k,i},B} + n_0 \right)}{g_{cB}} \right\}, \\ p_{c_k}^t \leq \left\{ \frac{\left(p_{d_{k,i}}^t g_{d_{k,i}} / r_{c_k}^{\text{th}} - \sum_{\substack{d_{k,j} \in \Phi_{D_k} \\ d_{k,j} \neq d_{k,i}}} p_{d_{k,i}}^t g_{d_{k,i},B} - n_0 \right)}{g_{cd_{k,i}}} \right\}, \end{cases} \quad (\text{B.1})$$

where $r_{c_k}^{\text{th}} = (\exp(r_{c_k}^{\text{th}}) - 1)$, $r_{d_{k,i}}^{\text{th}} = (\exp(r_{d_{k,i}}^{\text{th}}) - 1)$. If the solution of $p_{c_k}^t$ of the optimization problem exists, the lower and upper power bound of CU in (B.1) should satisfy the following relationship:

$$\frac{\tilde{r}_{d_{k,i}}^t \left(\sum_{d_{k,i} \in \Phi_{D_k^t}} p_{d_{k,i}}^t g_{d_{k,i},B} + n_0 \right)}{g_{cB}} < \frac{\left(p_{d_{k,i}}^t g_{d_{k,i}} / r_{c_k}^{\text{th}} - \sum_{\substack{d_{k,j} \in \Phi_{D_k} \\ d_{k,j} \neq d_{k,i}}} p_{d_{k,i}}^t g_{d_{k,i},B} - n_0 \right)}{g_{cd_{k,i}}}. \quad (\text{B.2})$$

Thus, the minimal energy requirement, which ensures the minimal transmission rate requirements of EH-DPs and CUs, can be converted by (B.2) and represented as follows:

$$p_{d_{k,i}}^{\text{th}} > \frac{\sum_{\substack{d_{k,j} \in \Phi_{D_k^t} \\ d_{k,j} \neq d_{k,i}}} p_{d_{k,j}}^t \left(\mathcal{M}_{d_{k,i}} \cdot g_{d_{k,j},B} + \mathcal{N}_{d_{k,i}} \cdot g_{d_{k,j},d_{k,i}} \right) + n_0 \left(\mathcal{M}_{d_{k,i}} + \mathcal{N}_{d_{k,i}} \right)}{g_{c_k B} \cdot g_{d_{k,i}} - g_{d_{k,i},B} \cdot \mathcal{M}_{d_{k,i}}}, \quad (\text{B.3})$$

where $\mathcal{M}_{d_{k,i}} = r_{c_k}^{\text{th}} \cdot r_{d_{k,i}}^{\text{th}} \cdot g_{c_k d_{k,i}}$, $\mathcal{N}_{d_{k,i}} = r_{d_{k,i}}^{\text{th}} \cdot g_{c_k B}$. In the worst case, the receiver of each D2D pair will receive the interference from all other D2D pairs. It means that the set

of $\Phi_{D_k^s} = \Phi_{D_k}$. Thus, the minimal requirement power can be calculated by (B.4) when $p_{c_k}^t = p_{c_k}^{\text{max}}$ and $p_{d_{k,j}}^t = p_{d_{k,j}}^{\text{max}}$:

$$p_{d_{k,i}}^{\text{th}} > \frac{\sum_{\substack{d_{k,j} \in \Phi_{D_k} \\ d_{k,j} \neq d_{k,i}}} p_{d_{k,j}}^{\text{max}} \left(\mathcal{M}_{d_{k,i}} \cdot g_{d_{k,j} B} + \mathcal{N}_{d_{k,i}} \cdot g_{d_{k,j} d_{k,i}} \right) + n_0 \left(\mathcal{M}_{d_{k,i}} + \mathcal{N}_{d_{k,i}} \right)}{g_{c_k B} \cdot g_{d_{k,i}} - g_{d_{k,i} B} \cdot \mathcal{M}_{d_{k,i}}}. \quad (\text{B.4})$$

Data Availability

Please contact the corresponding author to acquire the underlying data if necessary.

Conflicts of Interest

The authors declare that there is no conflict of interest regarding the publication of this paper.

Acknowledgments

The authors would like to thank the supports of the National Natural Science Foundation of China under Grant 61771410 and 61601383, the Sichuan Science and Technology Program 2018GZ0095, the Southwest University of Science and Technology research fund 18zx7144, and the Postgraduate Innovation Fund Project by Southwest University of Science and Technology 20ycx0059.

References

- [1] F. Jameel, M. A. Javed, and D. N. K. Jayakody, "Physical layer security of energy harvesting machine-to-machine communication system," in *5G Enabled Secure Wireless Networks*, pp. 123–153, Springer, 2019.
- [2] V. Vijayaraghavan and R. Agarwal, "Security and privacy across connected environments," in *Connected Environments for the Internet of Things*, pp. 19–39, Springer, 2017.
- [3] Z. Hasan, H. Boostanimehr, and V. K. Bhargava, "Green cellular networks: a survey, some research issues and challenges," *IEEE Communications Surveys & Tutorials*, vol. 13, no. 4, pp. 524–540, 2011.
- [4] I. Chih-Lin, C. Rowell, S. Han, Z. Xu, G. Li, and Z. Pan, "Toward green and soft: a 5G perspective," *IEEE Communications Magazine*, vol. 52, no. 2, pp. 66–73, 2014.
- [5] M.-L. Ku, W. Li, Y. Chen, and K. J. R. Liu, "Advances in energy harvesting communications: past, present, and future challenges," *IEEE Communications Surveys & Tutorials*, vol. 18, no. 2, pp. 1384–1412, 2016.
- [6] S. Peng and C. P. Low, "Energy neutral directed diffusion for energy harvesting wireless sensor networks," *Computer Communications*, vol. 63, pp. 40–52, 2015.
- [7] Y. Huang, J. Wang, P. Zhang, and Q. Wu, "Performance analysis of energy harvesting multi-antenna relay networks with different antenna selection schemes," *IEEE Access*, vol. 6, pp. 5654–5665, 2018.
- [8] M. Noura and R. Nordin, "A survey on interference management for device-to-device (D2D) communication and its challenges in 5G networks," *Journal of Network and Computer Applications*, vol. 71, pp. 130–150, 2016.
- [9] D. T. Huynh, X. Wang, T. Q. Duong, N. S. Vo, and M. Chen, "Social-aware energy efficiency optimization for device-to-device communications in 5G networks," *Computer Communications*, vol. 120, pp. 102–111, 2018.
- [10] S. J. Darak, H. Zhang, J. Palicot, and C. Moy, "An efficient policy for D2D communications and energy harvesting in cognitive radios: Go Bayesian!," in *23rd European Signal Processing Conference (EUSIPCO)*, pp. 1231–1235, Nice, France, 2015.
- [11] A. H. Sakr and E. Hossain, "Cognitive and energy harvesting-based D2D communication in cellular networks: stochastic geometry modeling and analysis," *IEEE Transactions on Communications*, vol. 63, pp. 1867–1880, 2015.
- [12] H. H. Yang, J. Lee, and T. Q. S. Quek, "Heterogeneous cellular network with energy harvesting based D2D communication," *IEEE Transactions on Wireless Communications*, vol. 15, no. 2, pp. 1406–1419, 2016.
- [13] K. Tutuncuoglu and A. Yener, "Sum-rate optimal power policies for energy harvesting transmitters in an interference channel," *Journal of Communications and Networks*, vol. 14, no. 2, pp. 151–161, 2012.
- [14] L. Sun, Q. Du, P. Ren, and Y. Wang, "Two birds with one stone: towards secure and interference-free D2D transmissions via constellation rotation," *IEEE Transactions on Vehicular Technology*, vol. 65, no. 10, pp. 8767–8774, 2016.
- [15] S. Gupta, R. Zhang, and L. Hanzo, "Energy harvesting aided device-to-device communication underlaying the cellular downlink," *IEEE Access*, vol. 5, pp. 7405–7413, 2017.
- [16] Z. Ding, S. M. Perlaza, I. Esnaola, and H. V. Poor, "Power allocation strategies in energy harvesting wireless cooperative networks," *IEEE Transactions on Wireless Communications*, vol. 13, no. 2, pp. 846–860, 2014.
- [17] Z. Hadzi-Velkov, I. Nikoloska, G. K. Karagiannidis, and T. Q. Duong, "Wireless networks with energy harvesting and power transfer: joint power and time allocation," *IEEE Signal Processing Letters*, vol. 23, no. 1, pp. 50–54, 2016.
- [18] P. Phunchongharn, E. Hossain, and D. I. Kim, "Resource allocation for device-to-device communications underlaying LTE-advanced networks," *IEEE Wireless Communications*, vol. 20, no. 4, pp. 91–100, 2013.
- [19] N. Golrezaei, P. Mansourifard, A. F. Molisch, and A. G. Dimakis, "Base-station assisted device-to-device communications for high-throughput wireless video networks," *IEEE Transactions on Wireless Communications*, vol. 13, no. 7, pp. 3665–3676, 2014.

- [20] N. Lee, X. Lin, J. G. Andrews, and R. W. Heath, "Power control for D2D underlaid cellular networks: modeling, algorithms, and analysis," *IEEE Journal on Selected Areas in Communications*, vol. 33, no. 1, pp. 1–13, 2015.
- [21] Y. Luo, P. Hong, R. Su, and K. Xue, "Resource allocation for energy harvesting-powered D2D communication underlying cellular networks," *IEEE Transactions on Vehicular Technology*, vol. 66, no. 11, pp. 10486–10498, 2017.
- [22] Z. Zhou, G. Ma, M. Dong, K. Ota, C. Xu, and Y. Jia, "Iterative energy-efficient stable matching approach for context-aware resource allocation in D2D communications," *IEEE Access*, vol. 4, pp. 6181–6196, 2016.
- [23] V. Sharma, U. Mukherji, V. Joseph, and S. Gupta, "Optimal energy management policies for energy harvesting sensor nodes," *IEEE Transactions on Wireless Communications*, vol. 9, no. 4, pp. 1326–1336, 2010.
- [24] A. Tang, X. Wang, and C. Zhang, "Cooperative full duplex device to device communication underlying cellular networks," *IEEE Transactions on Wireless Communications*, vol. 16, no. 12, pp. 7800–7815, 2017.
- [25] P. Aquilina, A. C. Cirik, and T. Ratnarajah, "Weighted sum rate maximization in full-duplex multi-user multi-cell MIMO networks," *IEEE Transactions on Communications*, vol. 65, no. 4, pp. 1590–1608, 2017.
- [26] M. R. Garey and D. S. Johnson, *Computers and intractability*, vol. 174, San Francisco: freeman, 1979.
- [27] C. Li, L. Toni, J. Zou, H. Xiong, and P. Frossard, "QoE-driven mobile edge caching placement for adaptive video streaming," *IEEE Transactions on Multimedia*, vol. 20, pp. 965–984, 2018.
- [28] W. Dinkelbach, "On nonlinear fractional programming," *Management Science*, vol. 13, no. 7, pp. 492–498, 1967.
- [29] J. Papandriopoulos and J. S. Evans, "SCALE: a low-complexity distributed protocol for spectrum balancing in multiuser DSL networks," *IEEE Transactions on Information Theory*, vol. 55, no. 8, pp. 3711–3724, 2009.
- [30] S. Boyd and L. Vandenberghe, *Convex Optimization*, Cambridge university press, 2004.
- [31] M. T. Islam, A. E. M. Taha, S. Akl, and S. Choudhury, "A two-phase auction-based fair resource allocation for underlying D2D communications," in *IEEE International Conference on Communications (ICC)*, pp. 1–6, Kuala Lumpur, Malaysia, 2016.
- [32] A. Kansal, J. Hsu, S. Zahedi, and M. B. Srivastava, "Power management in energy harvesting sensor networks," *ACM Transactions on Embedded Computing Systems*, vol. 6, no. 4, p. 32, 2007.
- [33] H. Jiang, W. Zhuang, X. Shen, and Q. Bi, "Quality-of-service provisioning and efficient resource utilization in CDMA cellular communications," *IEEE Journal on Selected Areas in Communications*, vol. 24, no. 1, pp. 4–15, 2006.
- [34] Y. Dong, J. Wang, B. Shim, and D. I. Kim, "DEARER: a distance-and-energy-aware routing with energy reservation for energy harvesting wireless sensor networks," *IEEE Journal on Selected Areas in Communications*, vol. 34, no. 12, pp. 3798–3813, 2016.
- [35] A. Zappone and E. Jorswieck, "Energy efficiency in wireless networks via fractional programming theory," *Foundations and Trends® in Communications and Information Theory*, vol. 11, no. 3-4, pp. 185–396, 2014.
- [36] K. Wu, C. Tellambura, and H. Jiang, "Optimal transmission policy in energy harvesting wireless communications: a learning approach," in *2017 IEEE International Conference on Communications (ICC)*, pp. 1–6, Paris, France, 2017.
- [37] S. Bahrami, V. W. S. Wong, and J. Huang, "An online learning algorithm for demand response in smart grid," *IEEE Transactions on Smart Grid*, vol. 9, no. 5, pp. 4712–4725, 2018.
- [38] M. Zeng, Y. Luo, Q. Guo, and H. Jiang, "Power allocation for energy harvesting-based D2D communication underlying cellular network," in *2017 36th Chinese Control Conference (CCC)*, pp. 7605–7610, Dalian, China, 2017.
- [39] Y. Luo, P. Hong, and R. Su, "Energy-efficient scheduling and power allocation for energy harvesting-based D2D communication," in *GLOBECOM 2017 - 2017 IEEE Global Communications Conference*, pp. 1–6, Singapore, Singapore, 2017.
- [40] D. Ilie, "Optimization algorithms with applications to unicast QoS routing in overlay networks," Blekinge Institute of Technology Research Report, 2007, <http://urn.kb.se/resolve?urn=urn:nbn:se:bth-00370>.
- [41] T. Vidal, D. Gribel, and P. Jaillet, "Separable convex optimization with nested lower and upper constraints," *INFORMS Journal on Optimization*, vol. 1, no. 1, pp. 71–90, 2019.
- [42] M. G. Azar, R. Munos, M. Ghavamzadeh, and H. Kappen, "Speedy Q-learning," in *Advances in Neural Information Processing Systems*, Spain, 2011.

Research Article

Parameter Recognition of Mode-Converted Wave in Single-Source Ultrasound Using Gabor Transform for Bolt Axial Stress Evaluation

Ping Chen ¹, Xingliang He,¹ and Wei Song²

¹College of Mechanical Engineering, Chongqing University, Chongqing 400044, China

²Southwest Oil and Gas Field Company, Chongqing 400021, China

Correspondence should be addressed to Ping Chen; champion@126.com

Received 17 June 2020; Revised 21 July 2020; Accepted 5 August 2020; Published 20 August 2020

Academic Editor: Bin Gao

Copyright © 2020 Ping Chen et al. This is an open access article distributed under the Creative Commons Attribution License, which permits unrestricted use, distribution, and reproduction in any medium, provided the original work is properly cited.

In this paper, a novel parameter recognition method of mode-converted wave in single-source ultrasound is put forward and applied to the estimation of axial stresses in bolts. To overcome the distortion and aliasing of the mode-converted wave in single-source ultrasonic signal, a time-frequency parameter recognition method based on the Gabor transform is introduced to recognize the accurate time of flight (TOF) of the mode-converted wave. Based on the mode conversion of the single-source longitudinal ultrasound, a new nonlinear evaluation model based on acoustoelastic equation is derived to determine the axial stress of bolt. The performance of the proposed method is evaluated by comparing it with the commonly used TOF ratio method of longitudinal wave and shear wave (L-S). The experiment result shows that the proposed method is more effective in detecting the connection status of bolted joints than the traditional L-S method.

1. Introduction

Loosening is one kind of failure that can markedly impact the stiffness and reliability of bolted joints. Insufficient preload of bolt will significantly increase the risk of overall mechanical structural disintegration. One way to address the critical issues in maintaining the strength of the structure and ensuring the safety of engineers is to apply appropriate pretightening force to the bolted joints and conduct long-term online monitoring of their axial stress. The most frequently used nondestructive estimation methods of stress include the photoelasticity method [1], resistance strain gauge method [2], piezoresistance method [3], active sensing method [4, 5], and ultrasonic testing method [6–9]. Among all these methods, the ultrasonic testing method is considered as a potential alternative technique due to its convenience to measure bolt tension with better accuracy.

Among the ultrasonic testing technologies, the acoustoelastic method by using TOF [6–12] is a typical stress measurement method. In the method, the TOF difference before and after bolt loading is calculated and multiplied with an

acoustic-stress factor to achieve the axial stress. Whereas one shortcoming of this method is that it cannot be utilized to measure the stress of a fastened bolt. Yasui et al. [13] proposed the L-S method based on multisource ultrasound to solve this problem, in which the stress is measured according to the TOF ratio of longitudinal wave (L-wave) and shear wave (S-wave) by two separate transducers mounted on the two ends of the bolt with great care and precision. And the TOF ratio was proved to be independent of the original length of the bolt or the initial TOF. However, the coupling conditions (e.g., installation position, pressure, and coupling agent concentration) of the L-wave and S-wave transducers must be repeatable to ensure accuracy. Hence, this method is difficult to achieve reliable measurement results under practical conditions. Kim and Hong [14] proposed a stress measurement method using mode conversion of longitudinal waves to reduce the experimental error caused by different contact condition. However, compared with the multi-source method, owing to aliasing and distortion in the mode-converted wave signal used in Kim's method, it's difficult to obtain accurate TOF directly. They used a special designed probe with an acoustic lens to

generate the mode-converted wave with high SNR (signal-noise ratio). In addition, it is necessary to provide enough space to install the specially designed probe, and the length of the workpiece cannot exceed the focal length of the lens. Therefore, a new parameter recognition method of the mode-converted wave in single-source ultrasound must be studied to promote the measurement efficiency of the bolt.

In this paper, a novel axial stress evaluation method using the mode-converted wave generated by single-source ultrasound based on the Gabor transform is proposed. Firstly, the distortion and aliasing of mode-converted process in single-source ultrasonic longitudinal signal are analyzed. Then, the parameter recognition method based on the Gabor transform and Gaussian empirical model to obtain the accurate TOF of the mode-converted signal is introduced and its effectiveness is proved by simulation. Next, a new nonlinear model for evaluating the axial stress of bolt is derived based on the acoustoelastic equation. Finally, the performance of the proposed method is evaluated by comparing it with the commonly used TOF ratio method of longitudinal wave and shear wave. And the experiment result shows that the proposed method is more effective in detecting the connection status of bolted joints than the traditional L-S method.

2. TOF Recognition Method in Single-Source Ultrasound

2.1. Mode-Converted Wave in Ultrasonic Testing. The velocities and polarization directions of the S-wave and the L-wave are related to the elastic properties, anisotropy, and current stress state of materials. Both the L-wave and the S-wave can be transmitted in solid medium, while only the L-wave can be transmitted in fluid medium. When a longitudinal wave beam enters the solid medium from the fluid medium, it will not only be reflected at the interface but will also derive an orthogonal bipolarized transverse wave and some other waveforms near the interface, such as the Rayleigh wave and the Love wave. Similarly, when there exist ultrasound incidents from the solid medium to the fluid medium, reflection wave and orthogonal bipolarized transverse wave will occur. This phenomenon is called mode conversion. Figure 1 shows a typical mode conversion process in a monostatic pulse-echo experiment, in which the red beam represents a longitudinal wave and the green beam represents a shear wave.

In Figure 1, L_{inc} represents the incident single-source longitudinal wave generated by the transducer. At the liquid-solid interface, L_{inc} derives a reflection wave L_{refl} , a transmission L-wave (LL), and a transmission shear wave (LT). Suppose that the reflection angle of the longitudinal wave is α and the angle of shear wave is β , the relationship between them can be described by Snell's law:

$$\frac{\sin \alpha}{C_L} = \frac{\sin \beta}{C_T}. \quad (1)$$

In equation (1), C_L and C_T refer to the acoustical velocities of L-wave and S-wave in the solid medium, respectively. When LL and LT reach the other end of the mounted solid, the mode conversion occurs again. The LL generates the LLL wave and

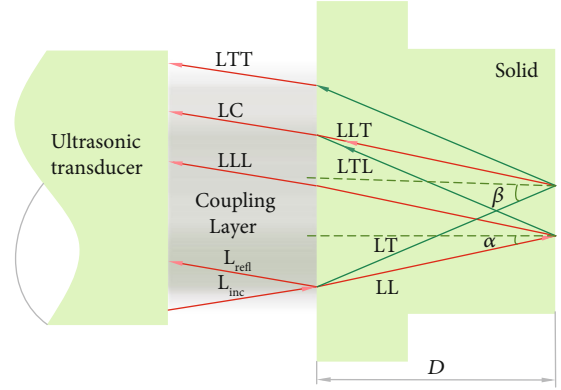


FIGURE 1: Mode conversion in a pulse-echo experiment.

the LLT wave, and the LT generates the LTL wave and the LTT wave. At last, all the waves undergo mode conversion again after arriving at the left solid interface, and the part transmitted into the coupling layer will all be converted to longitudinal waves and captured by the transducer. It should be noted that the propagation distance of the LLT and the LTL is exactly the same theoretically.

The transit time of acoustical wave can be rephrased as TOF, and TOF_L and TOF_T denote the transit time of L-wave and S-wave, respectively, in this paper. The relationship between the TOF and the sound velocity can be expressed as

$$\begin{cases} C_L \approx \frac{2D}{TOF_L}, \\ C_T \approx \frac{2D}{TOF_T}, \end{cases} \quad (2)$$

where D is the length of the solid medium. And the TOF of the converted waves (T_{LLL} , T_{LLT} , T_{LTL} , and T_{LTT}) in solid can be expressed as

$$\begin{cases} T_{LLL} = \frac{2D/\cos \alpha}{2D/TOF_L}, \\ T_{LLT} = \frac{D/\cos \alpha}{2D/TOF_L} + \frac{D/\cos \beta}{2D/TOF_T}, \\ T_{LTL} = \frac{D/\cos \alpha}{2D/TOF_L} + \frac{D/\cos \beta}{2D/TOF_T}, \\ T_{LTT} = \frac{2D/\cos \beta}{2D/TOF_T}. \end{cases} \quad (3)$$

When the incident direction is vertical to the interface, the angles α and β are approximately equal to zero. So, their relationship can be described as

$$T_{LLL} < T_{LLT} = T_{LTL} < T_{LTT}. \quad (4)$$

Equations (3) and (4) can determine the positions of the converted waves in a time-domain signal approximately. In general, the LTT wave has serious attenuation in amplitude and falls in the vicinity of the second echo of LLL (because

the travel speed of the L-wave is nearly two times than that of the S-wave). Therefore, the LTT wave is not suitable for stress evaluation. Owing to the relatively low attenuation, it is possible for the remaining LLT wave and the LTL wave to be adopted in stress evaluation. However, their waveforms are completely overlapped in the time domain because the LLT and LTL have exactly the same TOF in theory (here we use LC to represent the overlapped mode-converted waveforms). Moreover, LC often exhibits varying degrees of nonlinear distortion and aliasing caused by coupling conditions and multiple mode conversion. As a result, the direct acquisition of the LC TOF through the original signal is almost infeasible.

2.2. Parameter Recognition Method Using the Gabor Transform. The cross-correlation method is the most commonly used parameter recognition method to obtain the TOF of an ultrasonic signal, which can achieve high estimation accuracy under the condition of high signal-to-noise ratio (SNR). However, due to the nonlinear distortion and aliasing in LC, applying the cross-correlation method to this situation may cause extra error [15]. This paper introduces an ultrasonic signal processing method based on an empirical model [15, 16] and the Gabor transform [17] to recognize the parameter of the LC. The Gabor transform is a time-frequency transform method and widely used in signal parameter estimation for the ability of revealing the local frequency distribution of a signal or an image. From the perspective of time-frequency analysis, this paper applies the Gabor transform to estimate the parameter of the empirical model of LC. The authors use $X_{LC}(t)$ to express the signal of LC in time domain, and $X_{LC}(t)$ can be rephrased as a two-dimensional time-frequency expansion by applying the Gabor transform:

$$X_{LC}(t) = \sum_{\tau=-\infty}^{+\infty} \sum_{\omega=-\infty}^{+\infty} C_{\tau,\omega} h_{\tau,\omega} = \sum_{\tau=-\infty}^{+\infty} \sum_{\omega=-\infty}^{+\infty} C_{\tau,\omega} h(t - \tau a) e^{-j2\pi b \omega t}. \quad (5)$$

In equation (5), τ and ω represent the time and frequency coordinates of the two-dimensional plane, a and b are the width of the time and frequency grid of the plane, respectively, $C_{\tau,\omega}$ is the Gabor expansion coefficient, and $h_{\tau,\omega}$ is the Gabor generating function. What is more, $C_{\tau,\omega}$ is also defined as the Gabor transform (GT) of $X_{LC}(t)$:

$$C_{\tau,\omega} = \text{GT}(X_{LC}) = \int_{-\infty}^{\infty} X_{LC}(\delta) h^*(\delta - \tau a) e^{-j2\pi \omega b \delta} d\delta. \quad (6)$$

According to the physical characteristics of the ultrasonic transducer commonly used in bolt stress detection technology, the Gauss attenuation signal [18] is selected as the empirical model to describe LC:

$$S_{LC}(t) = A_0 e^{(-d(t-\tau))^2} \sin 2\pi \omega (t - \tau). \quad (7)$$

In equation (7), A_0 is the amplitude and d is the shape factor. Since the Gaussian function is still a Gaussian kernel function after Fourier transformation, its energy distribution is concentrated in both the frequency domain and the time

domain, which can clearly reveal the local details of the signal. Considering that $S_{LC}(t)$ is a Gaussian model, an analysis window function with a Gaussian kernel is selected as the Gabor generating function:

$$h_{\tau,\omega} = \eta e^{-r_0(t-a\tau)^2 + j\omega_0[(t-a\tau)/b\omega]}. \quad (8)$$

To ensure the energy uniformity of the window function, let

$$\eta = \left(\frac{2r_0}{\pi} \right)^{1/4}. \quad (9)$$

Then, the Euclidean distance of Gabor generating function and the empirical model is adopted to characterize the similarity between $S_{LC}(t)$ and $h_{\tau,\omega}(t)$, which can be expressed as

$$\|S_{LC}(t) - h_{\tau,\omega}(t)\|^2 = S_{LC}^2(t) + h_{\tau,\omega}^2(t) - 2|\text{GT}(S_{LC})|. \quad (10)$$

In fact, the purpose of finding the maximum similarity between the Gabor generating function and the empirical model is equivalent to obtaining the minimum value of equation (10). Since $S_{LC}^2(t)$ and $h_{\tau,\omega}^2(t)$ are both nonnegative and unrelated to τ and ω , the minimum value of equation (10) is transformed into the maximum value of $|\text{GT}(S_{LC})|$. And $|\text{GT}(S_{LC})|$ can be further written as

$$|\text{GT}(S_{LC})| = f(\tau, \omega) = \eta A_0 \sqrt{\frac{\pi}{d+r_0}} e^{-((4dr_0(\tau-\text{TOF})^2 + (\omega_c - (\omega_0/\omega))^2)/(4(d+r_0)))}. \quad (11)$$

In conclusion, the parameter recognition of the empirical model of LC can be described as

$$\{\text{TOF}, \omega_C\} = \arg \max_{\tau, \omega} |\text{GT}(S_{LC})|. \quad (12)$$

2.3. Parameter Recognition Using Particle Filter. Absolutely, the solution of equation (12) is a typical two-dimensional optimization problem. Taking both estimation accuracy and convergence speed into account, the particle filter method is selected as the solver of equation (12). The basic idea of the particle filter algorithm is the Monte Carlo method, which approximates and replaces the probability density function of the system through a large number of random samples and selects a subset of particles for sequential importance sampling according to the posterior probability in order to shrink the scope of estimation [19–22]. Assume the target vector V_{LC} :

$$V_{LC} = (\text{TOF}, \omega_C). \quad (13)$$

The parameter recognition process of the empirical model of LC based on the particle filter method is as follows:

- (1) Suppose the lengths of the time and the frequency axials of the Gabor expansion plane is M and N , respectively. Establish the initial particle set according to the number of particles K :

$$P({}^0V_{LC}) = \left\{ {}^0V_{LC}^i, W_0^i \right\}_{i=0}^K, \quad (14)$$

$$\sum_{i=0}^N W_0^i = 1.$$

In equation (14), ${}^0V_{LC}^i$ refers to the target vector of each particle in the initial set and W_0^i is the probability of each particle in the initial set. They can be expressed as

$$\begin{cases} {}^0V_{LC}^i = (\text{TOF}_0^i, \omega_{C0}^i), \\ \text{TOF}_0^i \in [0, M], \omega_{C0}^i \in [0, N]. \end{cases} \quad (15)$$

To ensure generality, the uniform distribution is selected as the initial importance distribution:

$$W_0^i = \left(\frac{1}{M}, \frac{1}{N} \right). \quad (16)$$

- (2) Substituting the value of TOF_0^i and ω_{C0}^i into equation (11) for each particle in the set, then the expression of $|\text{GT}_i(S_{LC})|$ can be derived. Next, we can calculate the state transition probability according to the likelihood between $|\text{GT}(S_{LC})|$ and $|\text{GT}_i(X_{LC})|$. The normalized weight corresponding to the state transition probability of each particle is given by

$$w_i = \frac{|\text{GT}_i(S_{LC})| - |\text{GT}(X_{LC})|}{\sum_{i=1}^K |\text{GT}_i(S_{LC})| - |\text{GT}(X_{LC})|}. \quad (17)$$

- (3) Perform sequential importance resample according to the elimination threshold which equals to the average of w_i . The particles with low weight are eliminated and those with high weight are retained and copied. After resample, the new particle set can be derived as

$$P({}^jV_{LC}) = \left\{ {}^jV_{LC}^i, W_j^i \right\}_{i=0}^K, \quad (18)$$

$$\sum_{i=0}^N W_j^i = 1.$$

- (4) Repeat procedures (1) to (3) until the values of every particle are exactly the same as each other, and the target vector of the last set is expressed as

$$V_{LC}^{\text{est}} = (\text{TOF}^{\text{est}}, \omega_C^{\text{est}}). \quad (19)$$

TABLE 1: Parameters of the simulation signals.

Number	f_{c_1} (MHz)	f_{c_2} (MHz)	τ_1 (s)	τ_2 (s)
1	4.000	3.000	1.900×10^{-6}	2.100×10^{-6}
2	4.500	3.500	2.000×10^{-6}	2.200×10^{-6}
3	5.002	4.000	2.100×10^{-6}	2.300×10^{-6}
4	5.500	4.500	2.200×10^{-6}	2.400×10^{-6}
5	6.000	5.000	2.300×10^{-6}	2.500×10^{-6}
6	6.500	5.500	2.400×10^{-6}	2.600×10^{-6}
7	7.000	6.000	2.500×10^{-6}	2.700×10^{-6}
8	7.500	6.500	2.600×10^{-6}	2.800×10^{-6}

TOF^{est} and ω_C^{est} are corresponding to the TOF and the central frequency of mode-converted wave LC.

2.4. Simulation. To evaluate the performance of the proposed method, a group of double Gaussian echo signals with different TOF and central frequency are introduced to simulate the mode-converted wave LC. The general expression of the signals is

$$S(t) = A_1 e^{-d_1(t-\tau_1)^2} \sin f_{c_1}(t - \tau_1) + A_2 e^{-d_2(t-\tau_2)^2} \sin f_{c_2}(t - \tau_2), \quad (20)$$

where A_1 and A_2 represent the amplitude of the echo envelope, τ_1 and τ_2 are the TOF, f_{c_1} and f_{c_2} are the central frequencies, and d_1 and d_2 are the shape factors. In each signal, $A_1 = 1$ V, $A_2 = 0.8$ V, $d_1 = 1.5 \times 10^{-7}$ s, and $d_2 = 1.4 \times 10^{-7}$ s. The values of the TOF and the central frequency of these signals are shown in Table 1. The initial set is made up of 10000 random chosen particles within the range of $\pm 2 \times 10^{-7}$ sec and ± 0.5 MHz around the preset values. After -10 dB~10 dB Gaussian white noise is applied to the signals to simulate different SNR conditions, the TOFs and the central frequencies of No. 1~No. 8 signals are recognized and each signal is calculated over 100 times. The No. 1 signal with 5 dB noise is shown in Figure 2(a), and its Gabor expansion is shown in Figure 2(b). It can be observed in Figure 2(a) that the time-domain signal is severely distorted and the echoes are submerged in clutter, while the echoes can be clearly recognized in the diagram of Gabor expansion (Figure 2(b)) and the recognized results are shown in Table 2.

The TOF difference caused by the acoustoelastic effect in an actual measurement is generally about 1%, while for the proposed method the measurement error of TOF is about 0.5% in average under the condition of low SNR, as shown in Table 2. Therefore, the parameter recognition using the Gabor transform is efficient and can be applied to the TOF recognition of mode-converted wave in single-source ultrasound.

3. Nonlinear Evaluation Model of Bolt Axial Stress

3.1. Nonlinear Evaluation Model Based on Mode-Converted Ultrasound. The existing evaluation models [6–14] of bolt

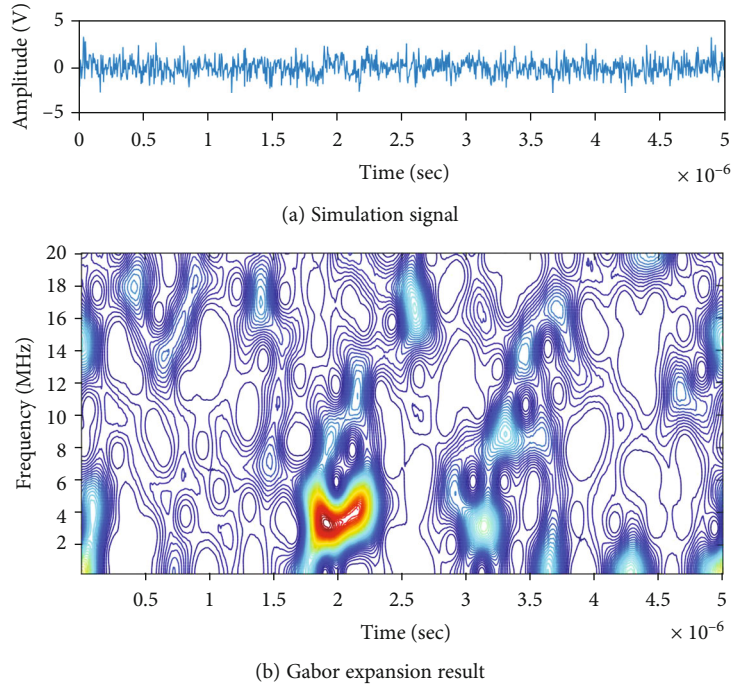


FIGURE 2: Simulation results.

TABLE 2: Recognized results of the simulation signals.

Number	f_{c_1} (MHz)	f_{c_2} (MHz)	Average frequency error	τ_1 (s)	τ_2 (s)	Average TOF error
1	4.082	2.939	2.04%	1.901×10^{-6}	2.106×10^{-6}	0.17%
2	4.495	3.507	0.15%	1.987×10^{-6}	2.198×10^{-6}	0.76%
3	5.012	3.978	0.37%	2.102×10^{-6}	2.308×10^{-6}	0.22%
4	5.498	4.487	0.24%	2.204×10^{-6}	2.389×10^{-6}	0.32%
5	5.991	5.012	0.19%	2.297×10^{-6}	2.486×10^{-6}	0.35%
6	6.504	5.612	0.89%	2.406×10^{-6}	2.587×10^{-6}	0.38%
7	6.993	6.124	1.00%	2.507×10^{-6}	2.712×10^{-6}	0.36%
8	7.522	6.514	0.25%	2.602×10^{-6}	2.791×10^{-6}	0.20%

axial stress are simplified and linear. And it is inevitable for them to induce extra fitting error. In this part, a new nonlinear evaluation model of bolt axial stress is proposed, its nonlinear feature is much better to meet the characteristic of acoustic elastic effect in theory. According to the theory of elasticity and nonlinear acoustic [23],

$$\begin{cases} C_L^2 = C_{L0}^2 - \sigma \left[\frac{(\lambda + 2\mu)(4\lambda + 10\mu + 4m)/(\mu + \lambda + 2j)}{\rho_0(3\lambda + 2\mu)} \right], \\ C_T^2 = C_{T0}^2 - \sigma \left[\frac{(2j - 2(m + \lambda + 2\mu))/\mu}{\rho_0(3\lambda + 2\mu)} \right], \end{cases} \quad (21)$$

where C_L and C_T are the velocities of longitudinal wave and shear wave in a solid medium under stress, respectively; C_{L0} and C_{T0} are their velocities in the stress-free state; λ and μ are the Lamé coefficients; j and m are the third-order elastic

constants and ρ_0 is the density of the solid. Equation (21) can be rewritten as

$$\begin{cases} C_L = C_{L0}(1 - k_L\sigma)^{1/2}, \\ C_T = C_{T0}(1 - k_T\sigma)^{1/2}, \end{cases} \quad (22)$$

where

$$\begin{aligned} k_L &= \frac{(\lambda + 2\mu)(4\lambda + 10\mu + 4m)/(\mu + \lambda + 2j)}{[\rho_0(3\lambda + 2\mu)]^{1/2}/C_{L0}}, \\ k_T &= \frac{(2j - 2(m + \lambda + 2\mu))/\mu}{[\rho_0(3\lambda + 2\mu)]^{1/2}/C_{T0}}. \end{aligned} \quad (23)$$

The propagation speed of elastic waves will change along with the stress status of the medium on the basis of equation (22), while in practical measurement, because the change of

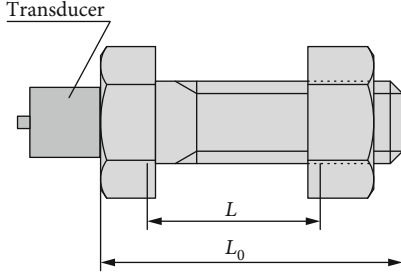


FIGURE 3: Bolt connection structure.

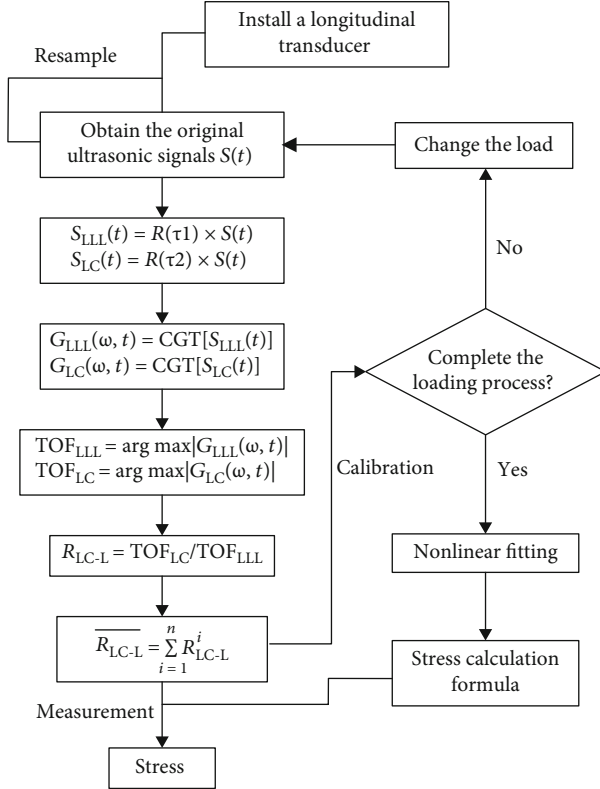


FIGURE 4: Flowchart of the stress evaluation.

sound velocity is too weak to detect, TOF is often frequently used instead of velocity. Figure 3 shows a typical bolt connection structure, in which L and L_0 are the equivalent stress length and overall length of the bolt, respectively. Since the stress distribution in a loaded bolt is inhomogeneous, the bolt can be simplified to an axisymmetric cylinder with uniform stress distribution, in which L represents the length of the cylinder. Then, the TOF can be expressed as

$$\begin{cases} T_L = \frac{2[(1 + \sigma E^{-1})L + L_0 - L]}{C_L}, \\ T_T = \frac{2[(1 + \sigma E^{-1})L + L_0 - L]}{C_S}, \end{cases} \quad (24)$$

where T_L and T_T are the TOF of L-wave and S-wave, respectively. Squaring the quotient of T_L by T_T , we can obtain

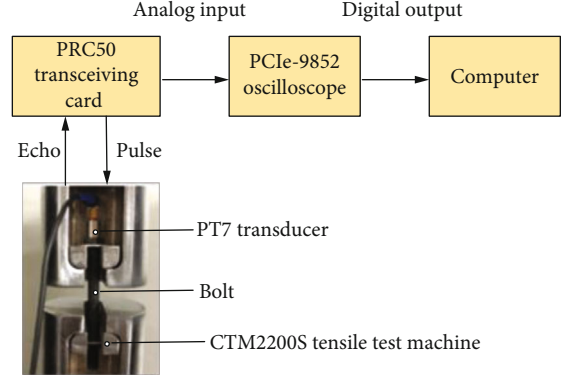


FIGURE 5: Experiment device.

$$R_{L-S}^2 = \frac{C_{L0}^2 K_L}{C_{T0}^2 K_T} \frac{(C_{T0}^2 K_T / C_{L0}^2 K_L) - (C_{T0}^2 / C_{L0}^2)}{(C_{T0}^2 K_T / C_{L0}^2 K_L) ((C_{T0}^2 / C_{L0}^2) - (C_{T0}^2 / C_{L0}^2) K_T \sigma)}. \quad (25)$$

Let

$$\begin{aligned} a &= \frac{C_{T0}^2 K_T}{C_{L0}^2 K_L}, \\ b &= \frac{C_{T0}^2}{C_{L0}^2}, \\ c &= K_T. \end{aligned} \quad (26)$$

Then, equation (25) can be simplified as

$$R_{L-S}^2 = \frac{1}{a} + \frac{a-b}{a(b-bc\sigma)}. \quad (27)$$

Since the TOF of LC can be expressed as

$$T_{LC} = \frac{T_T + T_L}{2} = \frac{T_L/x + T}{2}, \quad (28)$$

the TOF ratio R_{LC-L} of LC wave to LLL wave (LC-L method) is derived as

$$R_{LC-L} = \frac{1}{2R_{L-S}} + \frac{1}{2}. \quad (29)$$

Finally, the axial stress σ can be calculated by the following nonlinear model:

$$\sigma = \frac{b-a}{abcR_{L-S}^2 - bc} + \frac{1}{c} = \frac{b-a}{abc[1/(2R_{LC-L} - 1)]^2 - bc} + \frac{1}{c}. \quad (30)$$

Based on the derivations above, as long as the coefficients related to material properties and the TOF ratio R_{LC-L} are known, the axial stress of the bolt can be determined.

TABLE 3: Details of the samples.

Type	Specification	Guaranteed load	Section area	Material
Hexagon head half thread bolt	M8 × 104	2160 kg	36.6mm ²	C45
	M12 × 200	3200 kg	84.3mm ²	C35

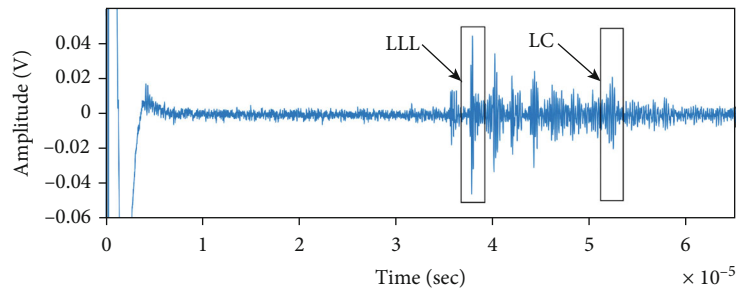
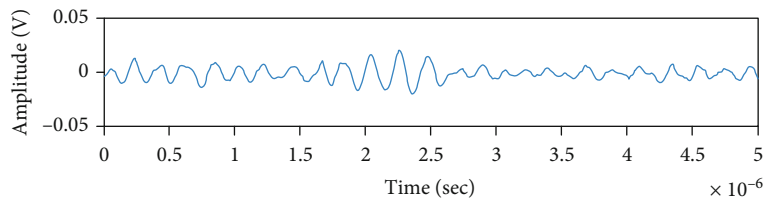
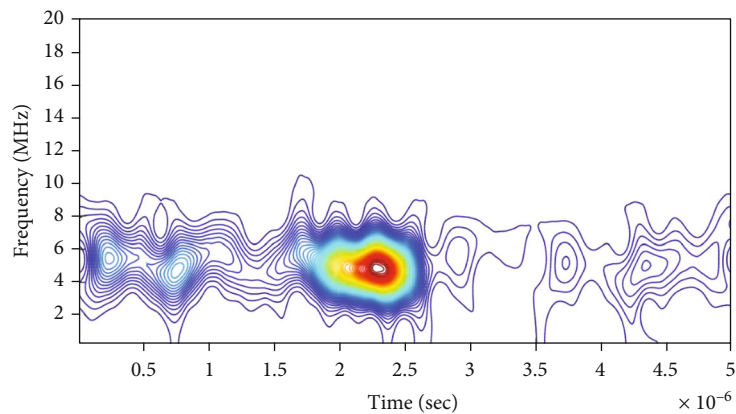


FIGURE 6: Ultrasound in a M8 × 104 bolt.



(a) LC waveform



(b) Gabor expansion of LC

FIGURE 7: LC and its Gabor expansion.

3.2. *Flowchart of Stress Evaluation.* The process of the measurement and calibration methods of bolt axial stress using single-source mode-converted ultrasound is shown in Figure 4.

- (1) Mill the head of the tested bolt flat and mount a longitudinal transducer on it properly to ensure stable coupling status
- (2) Obtain the original signal by conducting a monostatic pulse-echo experiment, and then resample the signal for at least 100 times to get the statistical data of the signal
- (3) Extract waveform of LLL ($S_{LLL}(t)$) and LC ($S_{LC}(t)$) of each signal by a rectangular window $R(\tau)$
- (4) Utilize the Gabor transform to get the Gabor expansion of $S_{LLL}(t)$ and $S_{LC}(t)$
- (5) Calculate the TOF of LC and LLL by the particle filter optimization method
- (6) Obtain the value of R_{LC-L} of each signal by dividing the TOF of LC to the TOF of LLL
- (7) Average the statistical R_{LC-L} and get the best estimate value to reduce the random errors

TABLE 4: Estimated TOF of sample M8 × 104.

Axial stress (MPa)	TOF of L (μ S)	TOF of LC(μ S)	TOF of S(μ S)	R_{LC-L}	R_{L-S}
0	37.763	52.271	65.417	1.38419	0.57727
10	37.770	52.279	65.427	1.38414	0.57728
20	37.778	52.289	65.435	1.38411	0.57734
30	37.785	52.298	65.449	1.38409	0.57732
40	37.793	52.308	65.460	1.38407	0.57734
50	37.799	52.316	65.471	1.38406	0.57734
60	37.808	52.327	65.480	1.38402	0.57740
70	37.815	52.336	65.491	1.38400	0.57741
80	37.822	52.344	65.502	1.38396	0.57742
90	37.829	52.353	65.513	1.38394	0.57743
100	37.836	52.362	65.524	1.38392	0.57744
110	37.842	52.370	65.534	1.38391	0.57744
120	37.849	52.379	65.545	1.38389	0.57745
130	37.856	52.387	65.556	1.38385	0.57746
140	37.866	52.399	65.566	1.38380	0.57752
150	37.874	52.408	65.577	1.38375	0.57755
160	37.881	52.416	65.587	1.38370	0.57757
170	37.887	52.424	65.598	1.38369	0.57756
180	37.893	52.431	65.603	1.38366	0.57761
190	37.901	52.439	65.621	1.38358	0.57757

TABLE 5: Estimated TOF of sample M12 × 200.

Axial stress (MPa)	TOF of L (μ S)	TOF of LC(μ S)	TOF of S(μ S)	R_{LC-L}	R_{L-S}
0	76.194	105.170	133.346	1.38029	0.57140
10	76.207	105.186	133.365	1.38027	0.57142
20	76.222	105.204	133.386	1.38023	0.57144
30	76.236	105.221	133.415	1.38020	0.57142
40	76.250	105.238	133.428	1.38017	0.57147
50	76.265	105.256	133.450	1.38014	0.57149
60	76.279	105.274	133.475	1.38012	0.57149
70	76.292	105.289	133.489	1.38008	0.57152
80	76.305	105.305	133.510	1.38005	0.57153
90	76.315	105.317	133.530	1.38003	0.57152
100	76.328	105.333	133.545	1.38000	0.57155
110	76.343	105.351	133.573	1.37997	0.57155
120	76.358	105.368	133.591	1.37992	0.57158
130	76.373	105.386	133.621	1.37989	0.57156
140	76.387	105.403	133.639	1.37986	0.57159
150	76.402	105.421	133.658	1.37982	0.57162
160	76.416	105.438	133.685	1.37979	0.57161
170	76.430	105.456	133.701	1.37977	0.57165
180	76.443	105.471	133.721	1.37973	0.57166
190	76.452	105.481	133.738	1.37970	0.57166

- (8) Change the load of the tested bolt and repeat operations 2–6 for at least 10 times to complete the calibration process of the tested bolt

- (9) Correlate the stress and R_{LC-L} to get the calibration data. Then, nonlinear fitting is conducted to estimate the value of a , b , and c in equation (30) to get the evaluation model of axial stress of the bolt

- (10) Evaluate the axial stress by the nonlinear evaluation model

4. Experiment

4.1. Setup. The JSR PRC50 ultrasonic transceiving card with gain range from -14 dB to 60 dB is selected as the actuator for the ultrasonic transducers. And the AD-link PCIe-9852 oscilloscope with sampling rates upper to 200 MHz is selected as the data acquisition hardware. They are integrated into a portable industrial computer, as shown in Figure 5. Then, the ultrasonic calibration/measurement software to implement excitation, acquisition, and processing of ultrasonic signals is programmed based on LABVIEW. The Dakota PT7 magnetic longitudinal ultrasonic transducer is chosen as the L-wave source and an Olympus V-156RM transverse ultrasonic transducer is chosen as the S-wave source. The central frequency of both probes is 5 MHz. Two types of bolts with different specifications and materials are selected as the test samples. The specification of the specimens is listed in Table 3. The CTM2200S tensile testing machine is utilized to simulate the loading condition with the maximum load 2000 kg and load accuracy $\pm 0.1\%$.

4.2. TOF Estimation. Figure 6 shows the ultrasonic signal collected in sample M8 × 104 excited by the PT7 L-wave transducer. According to equations (3) and (4), the waveforms of LLL and LC can be recognized obviously, as shown in Figure 6. And the TOF of LLL can almost be obtained directly because its waveform is clearly a single sharp pulse. While the waveform of LC is consisted of several peaks with similar amplitudes and different phases, its TOF cannot be directly determined. Figure 7 shows the waveform of LC intercepted from the original signal and its Gabor expansion. From Figure 7(b), it can be observed that there is a sharp peak in the diagram of Gabor expansion, and the TOF of the intercepted waveform can be obtained by the proposed particle filter method.

In order to eliminate the influence of temperature on the sound velocity, the whole experiment is carried out under constant temperature (20°C). The loading range is 0–190 MPa and the loading step is 10 MPa. The elongation of TOF caused by the acoustoelastic effect is around 1 nanosecond per MPa, but the minimum sampling period of PCIe-9852 is 5 ns. There is a certain probability that the change of the signal cannot be collected intact, so the one-dimensional fast Fourier interpolation method is introduced to enhance the sample rate. After being processed by ten-time upsampling, the time resolution of the system is upgraded to 0.5 ns. The estimated TOFs under different stress status using the proposed method are shown in Tables 4 and 5, in which R_{L-S} is the time ratio of longitudinal wave (L) to shear wave (S) and R_{LC-L} is the time ratio of converted wave (LC) to longitudinal wave.

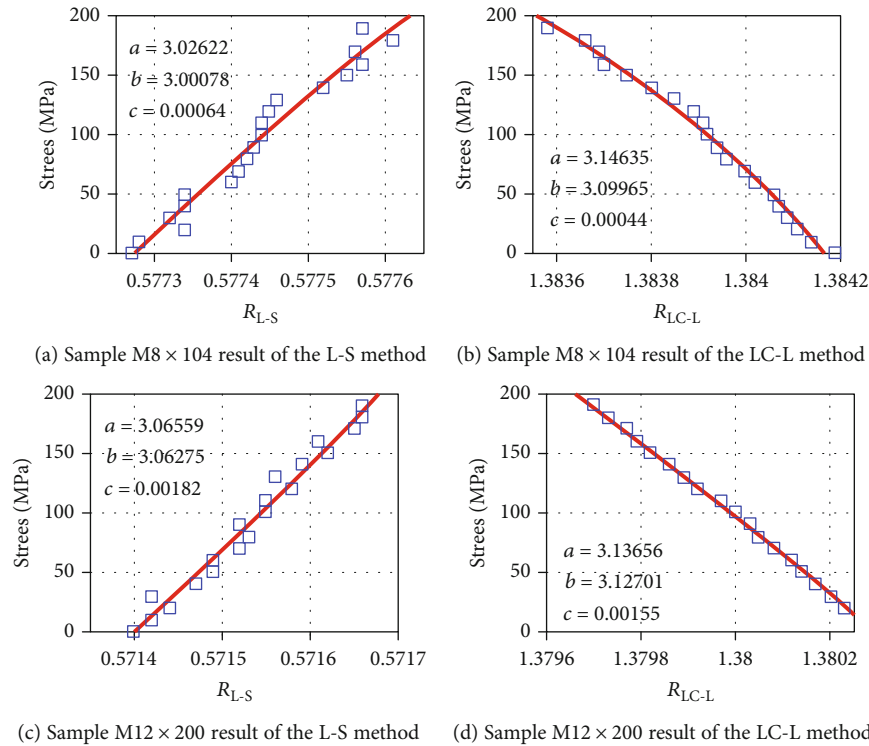


FIGURE 8: Calibration results.

TABLE 6: Measurement result of sample $M8 \times 104$.

Preset stress (MPa)	R_{LC-L}	R_{L-S}	Result of LC-L (MPa)	Error of LC-L	Result of L-S (MPa)	Error of L-S
20	1.38410	0.57731	21.012	5.06%	23.531	17.65%
40	1.38407	0.57733	38.975	-2.56%	41.891	4.72%
60	1.38403	0.57741	61.211	2.02%	62.301	3.83%
80	1.38397	0.57742	82.007	2.50%	82.990	3.73%
100	1.38394	0.57744	101.250	1.25%	95.699	-4.30%
120	1.38388	0.57748	118.271	-1.43%	122.256	1.88%
140	1.38379	0.57751	142.571	0.11%	134.368	-3.88%
160	1.38372	0.57757	163.254	2.03%	163.021	1.88%
180	1.38363	0.57760	180.201	0.11%	181.336	0.74%
200	1.38357	0.57763	198.367	-0.82%	208.214	4.10%

TABLE 7: Measurement result of sample $M12 \times 200$.

Preset stress (MPa)	R_{LC-L}	R_{L-S}	Result of LC-L (MPa)	Error of LC-L	Result of L-S (MPa)	Error of L-S
20	1.38022	0.57145	22.103	10.51%	17.655	-11.72%
40	1.38017	0.57147	38.127	-4.68%	40.239	0.59%
60	1.38013	0.57148	58.699	-2.16%	55.627	-7.28%
80	1.38004	0.57154	81.475	1.84%	88.044	10.05%
100	1.38001	0.57157	96.583	-3.42%	105.215	5.21%
120	1.37992	0.57159	119.338	-0.55%	123.144	2.62%
140	1.37985	0.57161	140.152	-0.10%	144.878	3.48%
160	1.37979	0.57162	163.254	2.03%	157.716	-1.42%
180	1.37974	0.57165	179.563	-0.24%	182.771	1.53%
200	1.37969	0.57164	199.361	-0.32%	204.885	2.44%

4.3. Calibration/Measurement. The axial stress calibration tests of bolts are carried out using the L-S method and the LC-L method, respectively. Figure 8 shows the calibration curves obtained from nonlinear fitting by Levenberg-Marquardt method. It can be clearly observed that the results of the LC-L method are significantly better than the results of the L-S method from Figure 8. The correlation coefficients between the fitting model and original data of the LC-L method are 0.9957 for sample $M8 \times 104$ and 0.9994 for sample $M12 \times 200$. The correlation coefficients of the L-S method are 0.9487 for sample $M8 \times 104$ and 0.94664 for sample $M12 \times 200$.

Another two bolts exactly the same as the samples are chosen to test the validity of the proposed method. After

loading by the tensile testing machine at the step of 20 MPa, the TOFs under different stress status using the proposed method are recognized. And then, the Levenberg-Marquardt models of calibration results are utilized to evaluate the stress of bolts. The evaluation results are shown in Tables 6 and 7 and Figure 9. In Figure 9, the yellow bar represents the absolute error using the proposed method and the blue bar refers to the absolute error of the L-S method. According to the results, the average evaluation errors of the LC-L method and the L-S method for sample $M8 \times 104$ are 1.789% and 4.671%, respectively. And the average errors of sample $M12 \times 200$ are 2.582% and 4.634%. As a result, the proposed method has a higher

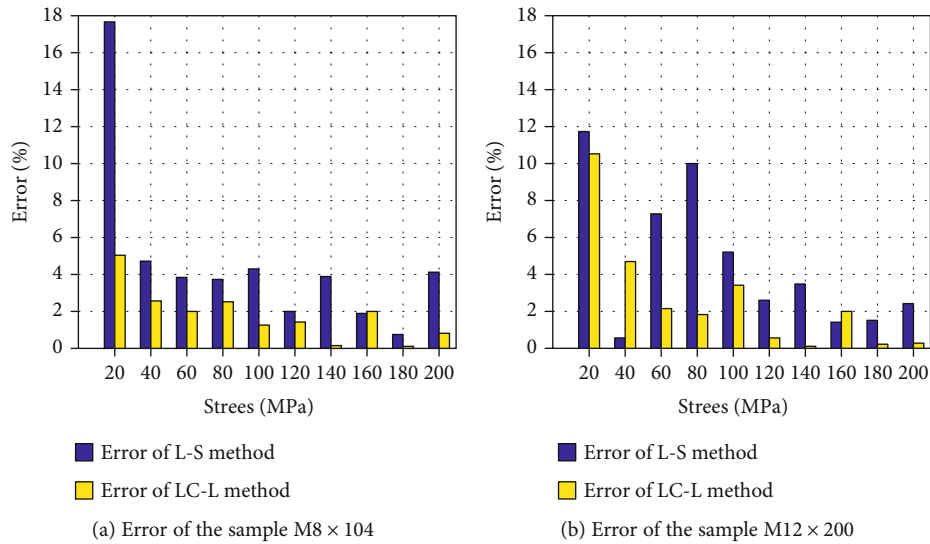


FIGURE 9: Measurement error.

accuracy as it utilizes a single longitudinal ultrasound. However, the accuracy of the L-S method is relatively low for the difference of the coupling conditions of L-wave and S-wave transducers.

5. Conclusions

In order to determine the parameters of mode-converted wave in single-source ultrasound for bolt stress evaluation, a time-frequency parameter recognition method based on the Gabor transform and a new bolt axial stress evaluation model are proposed in this paper. After analyzing the propagation and the mode conversion process of ultrasonic longitudinal wave in mounted solid, a parameter recognition method based on the Gabor transform to achieve the accurate TOF of the mode-converted wave is introduced to overcome the distortion and aliasing in single-source ultrasonic signal and its effectiveness is proved by simulation. Based on the mode conversion of single-source ultrasound and the acoustoelastic effect, a nonlinear evaluation model of the axial stress is put forward. The proposed method is compared with the commonly used L-S method by a series of calibrations and experiments. And the experiment results show that the proposed method can effectively detect the bolt axial stress ranging from 20 MPa to 200 MPa with a higher accuracy. As a result, the proposed method is more efficient and applicable in detecting the connection status of bolted joints than the traditional L-S method.

Data Availability

The measurement data used to support the findings of this study are included within the article.

Conflicts of Interest

The authors declare no conflict of interest.

Acknowledgments

This research was funded by the National Natural Science Foundation of China (grant number 51374264) and the Science and Technology Major Project of Chongqing (grant number cstc2018jszx-cyztzxX0032).

References

- [1] L. U. Peng, Y. U. Le, L. Hua et al., "Research on screw bolt's pre-tightening force by coating photoelasticity," *Chinese quarterly of mechanics*, vol. 2, pp. 275–278, 2013.
- [2] X. Wang, Q. Sun, F. Zhang, J. Duan, H. Liang, and H. Wang, "Design on static resistance strain gauge of mine roof bolt based on ATmega16L," *Journal of Liaoning Technical University (Natural Science)*, vol. 2, pp. 288–292, 2011.
- [3] Z. G. Guo and Z. Sun, "Piezoelectric impedance based prestress force monitoring for PSC beam," *Advanced Materials Research*, vol. 255-260, pp. 742–746, 2011.
- [4] J. Xu, C. Wang, H. Li, C. Zhang, J. Hao, and S. Fan, "Health monitoring of bolted spherical joint connection based on active sensing technique using piezoceramic transducers," *Sensors*, vol. 18, no. 6, p. 1727, 2018.
- [5] F. Wang, Y. J. Xu, L. Wu, L. Li, D. Liu, and L. Zhu, "A PEFKS- and CP-ABE-based distributed security scheme in interest-centric opportunistic networks," *International Journal of Distributed Sensor Networks*, vol. 2013, 10 pages, 2013.
- [6] S. G. Joshi and R. G. Pathare, "Ultrasonic instrument for measuring bolt stress," *Ultrasonics*, vol. 22, no. 6, pp. 261–269, 1984.
- [7] J. S. Heyman and E. Churn, "Ultrasonic measurement of axial stress," *Journal of Testing and Evaluation*, vol. 10, no. 5, pp. 202–211, 1992.
- [8] D. I. Crecraft, "The measurement of applied and residual stresses in metals using ultrasonic waves," *Journal of Sound and Vibration*, vol. 5, no. 1, pp. 173–192, 1967.
- [9] N. Y. Nikitina and L. A. Ostrovsky, "An ultrasonic method for measuring stresses in engineering materials," *Ultrasonics*, vol. 35, no. 8, pp. 605–610, 1998.

- [10] A. C. Holt, B. Cunningham, G. C. Johnson, and D. Auslander, "An ultrasonic technique for axial bolt-stress determination," *Review of Progress in Quantitative Nondestructive Evaluation*, pp. 1549–1557, 1987.
- [11] D. E. Bray, "Application of ultrasonic stress measurement to engineering components," *Journal of the Acoustical Society of America*, vol. 102, no. 5, pp. 3082–3082, 1997.
- [12] H. U. Youbin, X. U. Yong, and Z. Jianmin, "Application of ultrasonic measurement technique for bolt stress to tightening of mill shell," *Mining & Processing Equipment*, vol. 8, pp. 112–116, 2012.
- [13] H. Yasui, H. Tanaka, I. Fujii, and K. Kawashima, "Ultrasonic measurement of axial stress in short Bolts with consideration of nonlinear deformation," *JSM International Journal Series A Solid Mechanics and Material Engineering*, vol. 42, no. 1, pp. 111–118, 1999.
- [14] N. Kim and M. Hong, "Measurement of axial stress using mode-converted ultrasound," *NDT & E International*, vol. 42, no. 3, pp. 164–169, 2009.
- [15] R. Demirli and J. Saniie, "Model-based estimation of ultrasonic echoes part I: analysis and algorithms," *IEEE Transaction Ultrasonic, Ferro Electrics and Frequency Control*, vol. 48, no. 3, pp. 787–802, 2001.
- [16] L. Angrisani, A. Baccigalupi, and R. SchianoLoMoriello, "A measurement method based on Kalman filtering for ultrasonic time-of-flight estimation," *IEEE Transactions on Instrumentation and Measurement*, vol. 55, no. 2, pp. 442–448, 2006.
- [17] Z. K. Lu, C. Yang, and J. W. Wang, "Gabor transform based time-frequency estimation of ultrasonic echo signal," *Journal of Electronics & Information Technology*, vol. 3, pp. 652–657, 2013.
- [18] D. W. Wang, Z. B. Wang, Y. X. Chen et al., "Ultrasonic echo processing method based on dual-Gaussian attenuating model," *Acta Physica Sinica*, vol. 8, pp. 168–176, 2019.
- [19] H. Huang, W. Li, D. A. Luo, D. W. Qiu, and Y. Gao, "An improved particle filter algorithm for geomagnetic indoor positioning," *Journal of Sensors*, vol. 2018, 9 pages, 2018.
- [20] M. Mishra, J. Odelius, A. Thaduri, A. Nissen, and M. Rantatalo, "Particle filter-based prognostic approach for railway track geometry," *Mechanical systems and signal processing*, vol. 96, pp. 226–238, 2017.
- [21] K. Li and L. Chang, "Robust Gaussian particle filter based on modified likelihood function," *IET Science, Measurement & Technology*, vol. 12, no. 1, pp. 132–137, 2018.
- [22] Y. Kim, W. Chung, and D. Hong, "Indoor parking localization based on dual weighted particle filter," *International Journal of Precision Engineering & Manufacturing*, vol. 19, no. 2, pp. 293–298, 2018.
- [23] J. L. Rose and P. B. Nagy, "Ultrasonic waves in solid media," *Journal of the Acoustical Society of America*, vol. 107, no. 4, pp. 1807–1808, 2000.

Research Article

Active Vibration Control of PID Based on Receptance Method

Lijuan Peng,¹ Jian Wang¹,² Guicheng Yu,³ Zuoxue Wang,² Aijun Yin,² and Hongji Ren²

¹Department of Computer Science and Technology, Southwest University of Science and Technology, Mianyang 621010, China

²College of Mechanical Engineering, Chongqing University, Chongqing 400044, China

³Gas Storage Management Department, PetroChina Southwest Oil & Gas Field Company, Chongqing 401147, China

Correspondence should be addressed to Jian Wang; vi@cqu.edu.cn

Received 19 June 2020; Revised 10 July 2020; Accepted 10 July 2020; Published 14 August 2020

Academic Editor: Bin Gao

Copyright © 2020 Lijuan Peng et al. This is an open access article distributed under the Creative Commons Attribution License, which permits unrestricted use, distribution, and reproduction in any medium, provided the original work is properly cited.

Active vibration control approaches have been widely applied on improving reliability of robotic systems. For linear vibratory systems, the vibration features can be altered by modifying poles and zeros. To realize the arbitrary assignment of the closed-loop system poles and zeros of a linear vibratory system, in this paper, an active PID input feedback vibration control method is proposed based on the receptance method. The establishment and verification of the proposed method are demonstrated. The assignable poles during feedback control are calculated and attached with importance to expand the application of the integral control. Numerical simulations are conducted to verify the validity of the proposed method in terms of the assignment of closed-loop poles, zeros, and both. The results indicate that the proposed method can be used to realize the active vibration control of closed-loop system and obtain the desired damping ratio, modal frequency, and dynamic response.

1. Introduction

Nowadays, the demand for lower vibration and higher reliability in robotic systems is increasing [1]. Extensive studies have been conducted to optimize the controlling of various nonlinear systems [2–6]. A common vibration control approach is to modify system dynamics using controllers [7]. PID-based approaches have been widely applied on motion control of robotic systems [8, 9]. Generally, the vibration characteristics of a linear vibratory system are determined by its zeros and poles, and the assignment of eigenvalues in a system is of great importance in improving system reliability.

Traditionally, the solutions of pole assignment are solved by using the information of mass, damping, and stiffness matrices acquired from the finite element (FE) models [10]. However, FE models are generally limited by the incapability in obtaining precise damping models of real structures. Ram and Mottershead [11] developed an active vibration control method for linear system based on receptance method to accurately assign the system poles and zeros to specified values. One considerable advantage of this method is that it is entirely based on data from modal testing rather than the exact mass, damping, and stiffness matrices. Mottershead

et al. assigned part of the system poles to the predetermined values while keeping nonimportant poles unchanged by making the nonimportant poles uncontrollable or unobservable [12]. Zhang et al. presented the theory of applying acceleration feedback and position feedback to the nondamping system to assign part of poles [13]. Ouyang proposed a method of using acceleration feedback and velocity feedback in active vibration control [14]. Recently, neural network- (NN-) based pole-zero assignment methods have gained a lot of attention [15–18]. However, NN-based approaches may fail to yield desired results on practice due to the black-box nature of NN and the requirement of NN parameter optimization skills.

Previous studies indicate that various combinations of acceleration, velocity, and position make it flexible and applicable to select the type of feedback when implementing active vibration control. However, a vibration system will inevitably become a singular system when the acceleration feedback is applied, which leads to the unavailability of the receptance method. In this paper, integral control is introduced to overcome this limitation. The contributions of this paper are summarized as follows: (1) A PID input feedback active vibration control method is proposed based on the receptance method. (2) The numerical solutions for assignment

of closed-loop poles and zeros by applying the proposed method are demonstrated.

The rest of the paper is organized as follows: The assignments of poles and zeros in PID control systems are demonstrated in Section 2 and Section 3, respectively. Then, numerical simulations are conducted to verify the validity of the proposed method in Section 4. Finally, Section 5 concludes the paper.

2. Pole Assignment of PID Control Systems

2.1. Formulation of Pole Assignment. The equation of a n degree freedom linear system can be described in second-order form as follows according to [19]:

$$M\ddot{x}(t) + C\dot{x}(t) + Kx(t) = 0, \quad (1)$$

where $M, C, K \in R^{n \times n}$ are mass, damping, and stiffness matrices, respectively; $x(t) \in R^{n \times 1}$ is the displacement vector. $M = M^T, C = C^T, K = K^T$, and for any nonzero vector $v \in R^{n \times 1}$, there is $v^T M v \geq 0, v^T C v \geq 0$, and $v^T K v \geq 0$.

Integrate PID feedback control to the system and the closed-loop system can be written as follows:

$$M\ddot{x}(t) + C\dot{x}(t) + Kx(t) = bu(t), \quad (2)$$

where $b \in R^{n \times 1}$ is the force distribution vector and $u(t)$ is the input control vector:

$$u(t) = g_1^T x(t) + g_2^T \int_0^t x(\tau) d\tau + g_3^T \dot{x}(t), \quad (3)$$

where $g_1, g_2, g_3 \in R^{n \times 1}$ are input control gain vectors for displacement, differential, and velocity, respectively.

Express Equation (2) in the Laplace space:

$$[Ms^2 + Cs + K]x(s) = b \left(g_1^T + \frac{g_2^T}{s} + sg_3^T \right) x(s). \quad (4)$$

Then,

$$\left[Ms^2 + Cs + K - b \left(g_1^T + \frac{g_2^T}{s} + sg_3^T \right) \right] x(s) = 0. \quad (5)$$

Equation (5) shows that the highest order of the system stiffness matrix is a positive definite matrix, so the closed-loop system must be a nonsingular system. Therefore, the system receptance matrix exists.

The receptance matrix can be obtained by applying the Sherman–Morrison formula for Equation (5):

$$\hat{H}(s) = H(s) + \frac{H(s)b(g_1 + (g_2/s) + sg_3)^T H(s)}{1 - (g_1 + (g_2/s) + sg_3)^T H(s)b}, \quad (6)$$

where $H(s) = [Ms^2 + Cs + K]^{-1}$ is the receptance matrix of the open-loop system, which can be obtained in practice by mea-

suring the receptance $H(i\omega)$ [20]. The characteristic polynomial $p(s)$ can be derived from Equation (6) at the same time:

$$p(s) = 1 - \left(g_1 + \frac{g_2}{s} + sg_3 \right)^T H(s)b. \quad (7)$$

Thus, the roots of Equation (8) are the pole of the closed-loop system:

$$p(s) = 0. \quad (8)$$

Given $H(s)$, b , and Equation (9):

$$p(\mu_i) = 0. \quad (9)$$

The problem of assigning the poles of a closed-loop system to setpoints $\{\mu_1, \mu_2, \dots, \mu_N\}$ can be transformed to the solution of input control gain vectors g_1, g_2 , and g_3 . Where $\mu_i \in \{\mu_i\}_{i=1}^N, \mu_i \neq 0, \{\mu_i\}_{i=1}^N$ is closed under conjugation, N is the number of closed-loop system poles that can be assigned.

2.2. Minimum Number of Assignable Poles N . Given a positive definite system with closed-loop conjugate poles $\{\mu_i\}_{i=1}^N$, suppose that the adjoint matrix of $H(s)$ is $A(s)$ and the determinant is $D(s)$. $p(s) = 0$ can be expressed as follows:

$$1 - \left(g_1 + \frac{g_2}{s} + sg_3 \right)^T \frac{A(s)}{D(s)} b = 0. \quad (10)$$

Since for any $\mu_i \in \{\mu_i\}_{i=1}^N, D(\mu_i) \neq 0$, Equation (10) can be written as follows:

$$sD(s) - (sg_1 + g_2 + s^2g_3)^T A(s)b = 0. \quad (11)$$

Set

$$q(s) = (sg_1 + g_2 + s^2g_3)^T A(s)b. \quad (12)$$

The highest degree of s in $q(s)$ is $(2n - 2) + 2 = 2n$ and the highest degree of s in $D(s)$ is $2n$. Since the number of closed-loop poles N is equal to the degree of Equation (10) and the highest degree of s in Equation (10) is $2n + 1$, the number of characteristic polynomial root is $N = 2n + 1$. It should be noted that due to the introduction of integral control, the closed-loop system will produce an extra nonzero pole.

In fact, the introduction of integral control into closed-loop system will lead to a nonregular and generalized system. The closed-loop system is stable if (1) it is regular and (2) all of its assigned poles have negative real components [21]. The regularity of the closed-loop system in this method is guaranteed by the positive definiteness of the mass matrix. The values of the assigned poles can be arranged to stabilize the closed-loop system given that their real components are negative and $\{\mu_i\}_{i=1}^N$ is self-conjugate.

2.3. Calculate Vectors g_1, g_2, g_3 and Minimum Sensor Layout Method. The solution of g_1, g_2, g_3 can be realized by the following equation:

$$Gg = \gamma, \quad (13)$$

where

$$G = \begin{bmatrix} \Psi_1^T & \frac{\Psi_1^T}{\mu_1} & \mu_1 \Psi_1^T \\ \Psi_2^T & \frac{\Psi_2^T}{\mu_2} & \mu_2 \Psi_2^T \\ \vdots & \vdots & \vdots \\ \Psi_N^T & \frac{\Psi_N^T}{\mu_N} & \mu_N \Psi_N^T \end{bmatrix}, \Psi_i = H(\mu_i)b, \quad (14)$$

$$g^T = [g_1^T \quad g_2^T \quad g_3^T]$$

$$\gamma^T = [1 \ 1 \ \dots \ 1]$$

and $G \in R^{N \times 3n}$, $g \in R^{3n \times 1}$, and $\gamma \in R^{N \times 1}$.

The pole assignment problem raised by Equation (2) can be solved by applying Equation (13) and Equation (14). One solution for Equation (13) is as follows:

$$g = G^+ \gamma, \quad (15)$$

where G^+ is the Moore–Penrose generalized inverse of G . When the assigned closed-loop poles are self-conjugate, $g_1, g_2,$ and g_3 can be calculated according to Equations (13)–(15).

Considering the limitation of the additional mass in the actual control system, the number of sensors used to measure the motion parameters of the system should be as small as possible. Therefore, the value of some items in g_1, g_2, g_3 can be assigned to zero by setting the values of the corresponding columns of the G to be zero. In practice, the solution means that fewer sensors are involved. Due to the integration of PID input feedback control and $N = 2n + 1$, the number that can be allocated to zero in G has at most $3n - N = n - 1$ columns. Therefore, the number of sensors can be reduced accordingly in practice to minimize the effect of the additional mass on the system.

2.4. Validity Analysis. When the value of the preset poles $\{\mu_i\}_{i=1}^N$ and the optional k ($0 \leq k \leq n - 1$) column vector to be replaced by the 0 in the G are determined, a specific PID input feedback solution is derived, identified as W_k . From Equations (13)–(15), g_1, g_2, g_3 can be calculated in this specific PID input feedback solution. Below we will show how to verify whether W_k is valid or not.

The closed-loop receptance matrix $\hat{H}(s)$ can be derived from Equation (5) as follows:

$$\hat{H}(s) = \Omega(s)^{-1}, \quad (16)$$

where $\Omega(s)$ is as follows:

$$\Omega(s) = Ms^2 + Cs + K - b \left(g_1^T + \frac{g_2^T}{s} + sg_3^T \right). \quad (17)$$

The problem of verifying whether a particular W_k is valid is equivalent to verifying whether $\Omega(s)$ is a nonsingular matrix for any $s \notin \{\mu_i\}_{i=1}^N$ under the determined case. The verification process of W_k is as follows: Firstly, the real vectors g_1, g_2, g_3 are calculated according to Equations (13)–(15). Then, substitute g_1, g_2, g_3 into Equation (17) and obtain the determinant $w(s)$ of $\Omega(s)$. For any $s \notin \{\mu_i\}_{i=1}^N$, if $w(s)$ is zero, the closed-loop system poles cannot be assigned to the designated values, meaning that W_k is invalid. Otherwise, the closed-loop system poles can be assigned to the specified desired values, indicating that W_k is valid.

3. Zero Assignment of PID Control Systems

3.1. Formulation of Zero Assignment. The characteristic polynomial for the zeros of receptance \hat{H}_{ij} can be realized when the denominator matrix (i, j) of Equation (6) is zero:

$$\hat{H}_{ij}(s) = e_i^T \left(H(s) + \frac{H(s)b(g_1 + (g_2/s) + sg_3)^T H(s)}{1 - (g_1 + (g_2/s) + sg_3)^T H(s)b} \right) e_j, \quad (18)$$

where e_i, e_j are the unit vectors obtained from the corresponding columns of the identity matrix.

Therefore, the problem of assigning zeros of the closed-loop system receptance \hat{H}_{ij} to the setpoints $\{\xi_1, \xi_1, \dots, \xi_r\}$ can be realized as follows:

Given $H(s), b, i, j,$ and

$$e_i^T \left\{ \left[1 - \left(g_1 + \frac{g_2}{\xi_k} + \xi_k g_3 \right)^T H(\xi_k) b \right. \right. \\ \left. \left. + H(\xi_k) b \left(g_1 + \frac{g_2}{\xi_k} + \xi_k g_3 \right)^T \right] H(\xi_k) \right\} e_j = 0 \quad (19)$$

Calculate the input control gain vectors g_1, g_2, g_3 . Where $\xi_k \notin \{\xi_i\}_{i=1}^r$, $r \leq 2n - 1$, r is the number of poles in a closed-loop system that can be assigned.

Equation (19) can be written in the following form:

$$H_{ij}(\xi_k) \left[\left(g_1 + \frac{g_2}{\xi_k} + \xi_k g_3 \right)^T H(\xi_k) b \right] \\ - e_i^T H(\xi_k) b \left(g_1 + \frac{g_2}{\xi_k} + \xi_k g_3 \right)^T H(\xi_k) e_j = H_{ij}(\xi_k), \quad (20)$$

where $H_{ij}(s)$ is the open-loop receptance value at the open-loop system coordinate of (i, j). Transform Equation

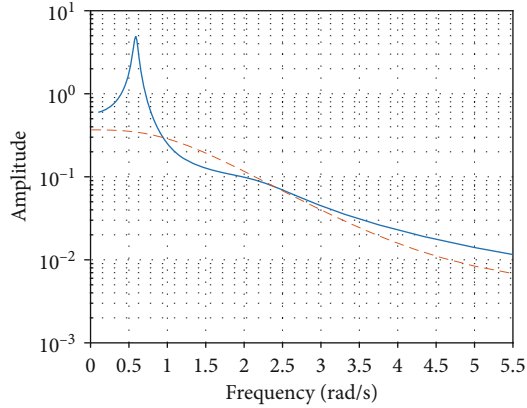


FIGURE 1: The frequency response for the original system $H_{3,3}$ (solid line) and the modified system $H_{3,3}$ (dotted line).

(20) to $(g_1 + (g_2/\xi_k) + \xi_k g_3)^T (H_{ij}(\xi_k)H(\xi_k)b - e_i^T H(\xi_k)bH(\xi_k)e_j) = H_{ij}(\xi_k)$. Since $e_i^T H(\xi_k)b$ is a scalar, set

$$t_k = H_{ij}(\xi_k)H(\xi_k)b - e_i^T H(\xi_k)bH(\xi_k)e_j. \quad (21)$$

We have $(g_1 + (g_2/\xi_k) + \xi_k g_3)^T t_k = H_{ij}(\xi_k)$. Since $H_{ij}(\xi_k)$ is scalar, after transposing we get $t_k^T g_1 + (t_k^T g_2/\xi_k) + \xi_k t_k^T g_3 = H_{ij}(\xi_k)$, i.e., $(t_k^T \quad t_k^T/\xi_k \quad \xi_k t_k^T) \begin{pmatrix} g_1 \\ g_2 \\ g_3 \end{pmatrix} = H_{ij}(\xi_k)$.

Therefore, for preset closed-loop system zeros $\{\xi_1, \xi_1, \dots, \xi_r\}$, we have

$$T \begin{pmatrix} g_1 \\ g_2 \\ g_3 \end{pmatrix} = \begin{pmatrix} H_{ij}(\xi_1) \\ H_{ij}(\xi_2) \\ \vdots \\ H_{ij}(\xi_r) \end{pmatrix}, \quad (22)$$

where

$$T = \begin{bmatrix} t_1^T & \frac{t_1^T}{\mu_1} & t_1^T \xi_1 \\ t_2^T & \frac{t_2^T}{\mu_2} & t_2^T \xi_2 \\ & & \vdots \\ t_r^T & \frac{t_r^T}{\mu_r} & t_r^T \xi_r \end{bmatrix}. \quad (23)$$

It can be seen from Equation (22) that the inverse of the matrix T can be obtained when the preset zeros $\{\xi_1, \xi_1, \dots, \xi_r\}$ are given, and then the real vectors g_1, g_2, g_3 can also be obtained. In particular, when i and j are overlapped, the distribution of zeros will affect the closed-loop pole assignment of the system, which is significant [22].

3.2. Pole and Zero Assignment. We can assign the zeros and poles in the closed-loop system at the same time according to Equation (13) and Equation (22). In this case, the total number of zeros and poles follows $r + N \leq 2n + 1$. Similarly, by assigning k ($0 \leq k \leq n - 1$) columns in Equation (13) and Equation (22) to zero, we can get the optimized allocation scheme.

4. Numerical Simulations

4.1. Pole Assignment Simulation. Consider a three-degree-of-freedom system with matrices:

$$M = \begin{bmatrix} 2 & & \\ & 2 & \\ & & 3 \end{bmatrix}, \quad C = \begin{bmatrix} 2.5 & -2 & 0 \\ -2 & 3 & -1 \\ 0 & -1 & 1 \end{bmatrix}, \quad (24)$$

$$K = \begin{bmatrix} 10 & -3 & -4 \\ -3 & 3 & 0 \\ -4 & 0 & 4 \end{bmatrix}.$$

The open-loop poles are $-0.0305 \pm 0.5894i$, $-0.8503 \pm 1.0119i$, and $-0.6609 \pm 2.1200i$.

Now use pole assignment method proposed in this paper to modify the closed-loop response of the system. Set $b = [1 \quad 1 \quad 1]^T$. For $n = 3$, $N = 7$ according to Section 2.2. Since the original system has a lower characteristic frequency and a smaller damping ratio, the closed-loop system characteristic values are assigned as $\mu_{1,2} = -1 \pm 0.5i$, $\mu_{3,4} = -1 \pm i$, $\mu_{5,6} = -2 \pm i$, and $\mu_7 = -3$ to increase the damping of the system and enhance the stability.

Obtain g_1, g_2, g_3 according to Equations (13)–(15):

$$\begin{cases} g_1 = [-38.1817 & -6.7810 & 11.3765]^T, \\ g_2 = [3.7396 & -14.4487 & 2.4203]^T, \\ g_3 = [-4.1357 & -4.5904 & -10.6608]^T. \end{cases} \quad (25)$$

The above PID input feedback solution is valid according to Section 2.4. In order to visualize the effect of this method, the frequency response curve, zero-pole distribution, and Nyquist plot of the $H_{3,3}$ of original system and the modified system are given, shown in Figures 1–5. Figures 2 and 3 show that the poles of the modified system are assigned to the specified positions, and an additional pole is added to the modified system due to the integration of integral feedback. The introduction of the extra pole improves the flexibility to handle the closed-loop systems in engineering applications. We can see from Figure 1, Figure 4, and Figure 5 that after pole

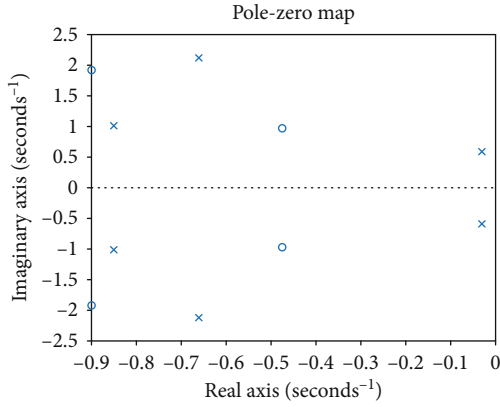


FIGURE 2: The zero-pole map for the original system $H_{3,3}$.

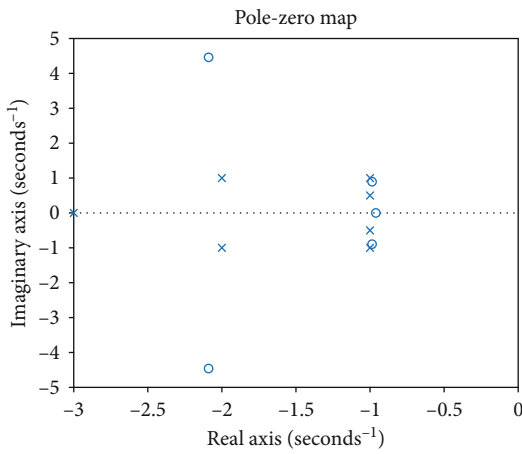


FIGURE 3: The zero-pole map for the modified system $H_{3,3}$.

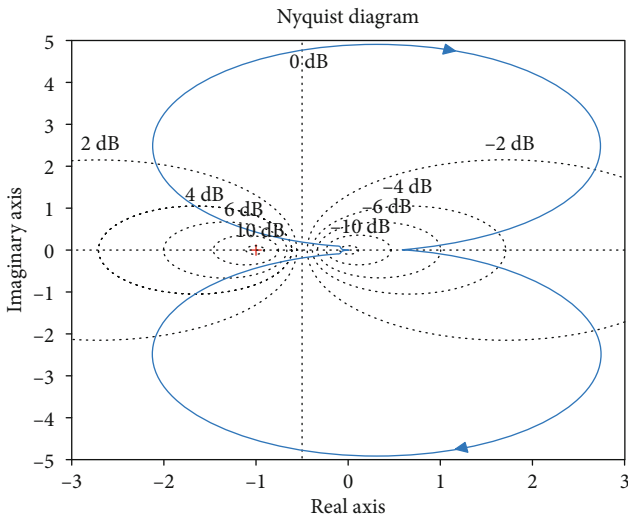


FIGURE 4: The Nyquist curve for the original system $H_{3,3}$.

reassignment, system features such characteristic frequency, damping, and stability have been changed, and the overall performances have been improved.

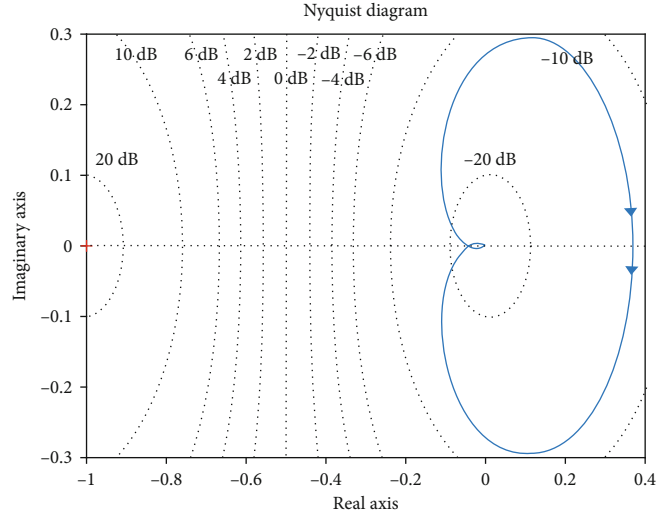


FIGURE 5: The Nyquist curve for the modified system $H_{3,3}$.

TABLE 1: Pole assignment solutions.

Plan	Column replaced by a zero vector in G
W_1	{1}, {2}, {3}, {4}, {5}, {6}, {7}, {8}, {9}
W_2	{1,2}, {1,3}, {2,3}, {1,4}, {2,4}, {3,4}, {1,5}, {2,5}, {3,5}, {4,5}, {1,6}, {2,6}, {3,6}, {4,6}, {5,6}, {1,7}, {2,7}, {3,7}, {4,7}, {5,7}, {6,7}, {1,8}, {2,8}, {3,8}, {4,8}, {5,8}, {6,8}, {7,8}, {1,9}, {2,9}, {3,9}, {4,9}, {5,9}, {6,9}, {7,9}, {8,9}

TABLE 2: The control gains that correspond to Table 1.

Plan	Control gain
W_1	$g_1 = [0 \quad -64.6499 \quad 33.3755]^T$ $g_2 = [55.1590 \quad -68.2535 \quad 18.7660]^T$ $g_3 = [5.1115 \quad -31.2131 \quad 15.4023]^T$
W_2	$g_1 = [0 \quad 0 \quad -23.1931]^T$ $g_2 = [301.6367 \quad -56.1317 \quad -191.4356]^T$ $g_3 = [37.4365 \quad 9.1931 \quad -93.6944]^T$

4.2. Minimum Sensor Configuration for Pole Assignment.

Based on the pole assignment in Section 4.1 and the minimum sensor layout in Section 2.3, a minimum sensor configuration scheme for pole assignment simulation is developed and verified according to Section 2.4. Table 1 shows all solutions that can assign the poles of the closed-loop system to preset values $\mu_{1,2} = -1 \pm 0.5i$, $\mu_{3,4} = -1 \pm i$, and $\mu_{5,6} = -2 \pm i$, while keeping the closed-loop system stable at the same time for the case in Section 4.1. The PID feedback gains for the 2 solutions are given in Table 2 (only the control gains of the first method in each W_k are given). The system performance may destabilize when the number of assigned poles is less than N (i.e., when the lacked poles are assigned, the number of assigned poles in Table 3 is $2n$). This highlights the importance of determining the number of assignments. The specific results are demonstrated in Tables 1–3.

TABLE 3: Results under lacked poles.

Preset poles	Control gain	Actual poles
$\{\mu_i\}_{i=1}^{2n} = \begin{cases} -1 \pm 0.5i \\ -1 \pm i \\ -2 \pm i \end{cases}$	$g_1 = [-8.8455 \quad 0.9987 \quad -11.5646]^T$ $g_2 = [4.9075 \quad 1.1948 \quad -1.5619]^T$ $g_3 = [-13.0963 \quad 1.7248 \quad 5.5819]^T$	$\begin{cases} -1 \pm 0.5i \\ -1 \pm i \\ -2 \pm i \\ 1.0915 \end{cases}$

4.3. *Zero Assignment Simulation.* Considering the three-degree-of-freedom system in Section 4.1, we use zero assignment method in Section 3 to modify the closed-loop system zeros and the closed-loop response of the system.

Set $b = [1 \quad 1 \quad 1]^T$ and the closed-loop system $H_{3,3}(s)$ zeros as $\xi_{1,2} = -1 \pm 0.5i$, $\xi_{3,4} = -2 \pm 0.5i$. Obtain g_1, g_2, g_3 according to Equation (22):

$$\begin{cases} g_1 = [1.9623 & -3.0448 & 0]^T, \\ g_2 = [-1.3215 & -0.4912 & 0]^T, \\ g_3 = [-6.3791 & -1.4682 & 0]^T. \end{cases} \quad (26)$$

The closed-loop poles calculated are $-0.1439 \pm 0.5047i$, $-0.6195 \pm 1.6824i$, $-1.0199 \pm 0.9522i$, and -3.4404 . The poles are distributed in the left half plane of the imaginary axis and the closed-loop system is stable. The frequency response curve, the zero-pole distribution diagram, and the Nyquist diagram of the modified system $H_{3,3}$ are illustrated in Figure 6, Figure 7, and Figure 8, respectively. Comparing Figure 2 with Figure 7, we can see that the zeros of the system are accurately assigned to the desired values. Figure 4, Figure 6, and Figure 8 indicate that, after the assignment of zeros, the system stability increases.

4.4. *Pole and Zero Assignment Simulation.* Based on the three-degree-of-freedom system in Section 4.1, set $b = [1 \quad 1 \quad 1]^T$, the closed-loop system $H_{3,3}(s)$ zeros as $\xi_{1,2} = -1 \pm 0.5i$, and the closed-loop system poles as $\mu_{1,2} = -1 \pm 0.5i$. Obtain g_1, g_2, g_3 according to Equations (13)–(15) and Equation (22):

$$\begin{cases} g_1 = [1.9623 & -3.0448 & 0]^T, \\ g_2 = [-1.3215 & -0.4912 & 0]^T, \\ g_3 = [-6.3791 & -1.4682 & 0]^T. \end{cases} \quad (27)$$

The closed-loop poles calculated at this time are $-0.3563 \pm 1.6213i$, $-0.9778 \pm 0.9769i$, $-1 \pm 0.5i$, and -3 . The poles are distributed in the left half plane of the imaginary axis and the closed-loop system is stable. The frequency response curve, the zero-pole distribution diagram, and the Nyquist diagram of the modified system $H_{3,3}$ are illustrated in Figure 9, Figure 10, and Figure 11, respectively. Figure 2 and Figure 10 indicate that the system zeros and poles are accurately assigned to the desired values. After the assignment, an increased system stability is observed according to Figure 4, Figure 9, and Figure 11. The validity of the proposed method is verified by the simulation results.

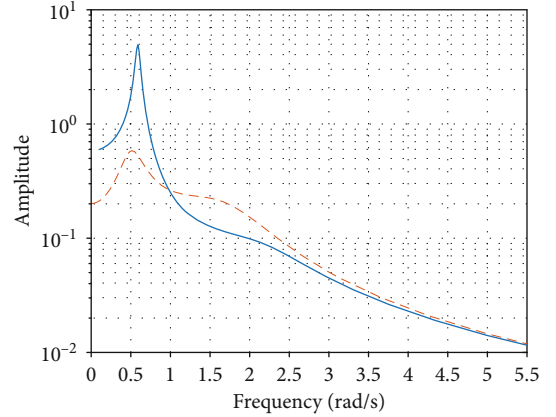


FIGURE 6: The frequency response for the original system $H_{3,3}$ (solid line) and the modified system $H_{3,3}$ (dotted line).

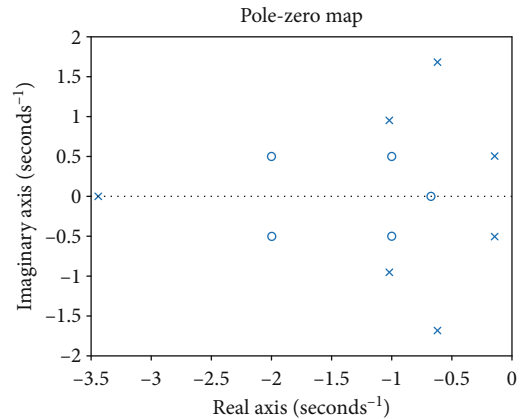


FIGURE 7: The pole-zero map for the modified system $H_{3,3}$.

5. Conclusions

In this paper, a PID-active vibration control method is proposed based on the receptance method. The proposed method can be utilized to assign the poles and zeros of closed-loop systems in order to improve the performances. Due to the integration of integral control, the proposed method guarantees the positive definiteness of the system and avoids the appearance of a nonsingular system. The proposed method also extends the application of the dynamic flexibility method. The procedures of assigning poles and zeros to a system are demonstrated. Numerical simulations for pole and zero assignments are conducted. Simulation

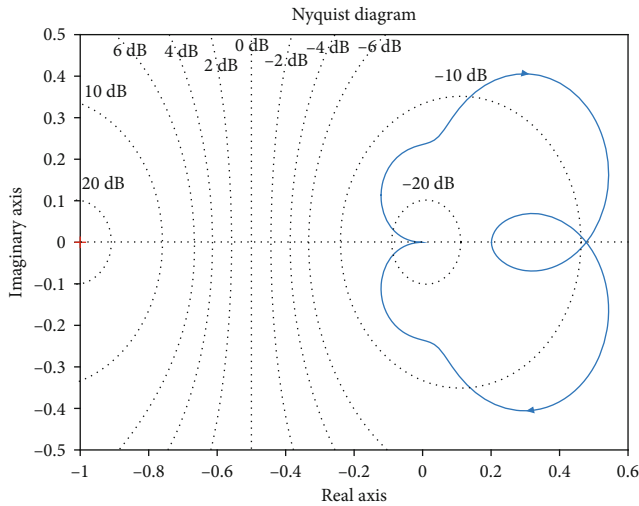


FIGURE 8: The Nyquist curve for the modified system $H_{3,3}$.

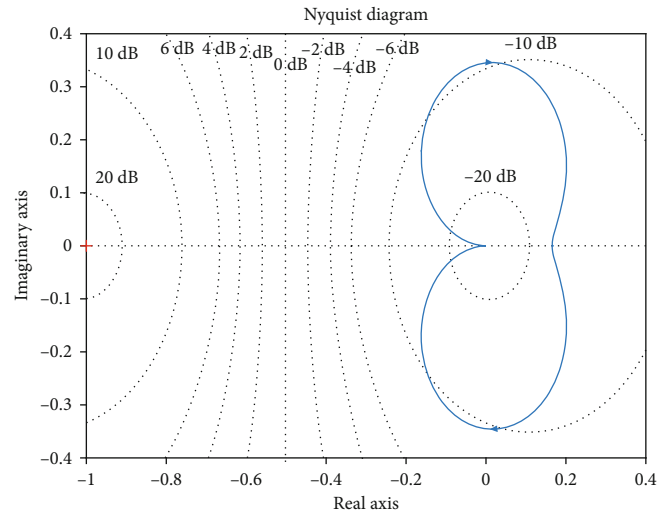


FIGURE 11: The Nyquist curve for the modified system $H_{3,3}$.

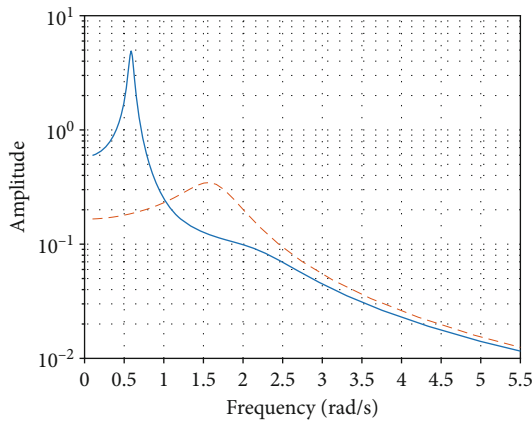


FIGURE 9: The frequency response for the original system $H_{3,3}$ (solid line) and modified system $H_{3,3}$ (dotted line).

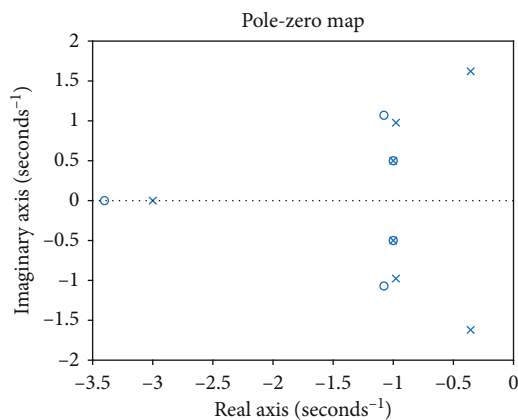


FIGURE 10: The pole-zero map for the modified system $H_{3,3}$.

results indicate that the proposed method is generally effective. The proposed method in this paper can be utilized to improve performance and reliability on robotic systems such

as flexible robots, robot arms, and intelligent vehicles. In future work, the proposed method will be expanded to handle vibration control tasks for nonlinear systems with multi inputs and outputs.

Data Availability

No data was used to support this study.

Conflicts of Interest

The authors declare that there is no conflict of interest regarding the publication of this paper.

Acknowledgments

This work is supported by the Key Science and Technology Research Project of Chongqing (cstc2018jszx-cyztzxX0032).

References

- [1] J. J. Lima, J. M. Balthazar, R. T. Rocha et al., "On positioning and vibration control application to robotic manipulators with a nonideal load carrying," *Shock and Vibration*, vol. 2019, Article ID 5408519, 14 pages, 2019.
- [2] Y. Chang, Y. Wang, F. E. Alsaadi, and G. Zong, "Adaptive fuzzy output-feedback tracking control for switched stochastic pure-feedback nonlinear systems," *International Journal of Adaptive Control and Signal Processing*, vol. 33, no. 10, pp. 1567–1582, 2019.
- [3] Y. Wang, Y. Chang, A. F. Alkhateeb, and N. D. Alotaibi, "Adaptive fuzzy output-feedback tracking control for switched nonstrict-feedback nonlinear systems with prescribed performance," *Circuits, Systems, and Signal Processing*, vol. 39, 2020.
- [4] L. Ma, N. Xu, X. Huo, and X. Zhao, "Adaptive finite-time output-feedback control design for switched pure-feedback nonlinear systems with average dwell time," *Nonlinear Analysis: Hybrid Systems*, vol. 37, p. 100908, 2020.
- [5] X. H. Chang, Y. Liu, and M. Shen, "Resilient control design for lateral motion regulation of intelligent vehicle," *IEEE/ASME*

- Transactions on Mechatronics*, vol. 24, no. 6, pp. 2488–2497, 2019.
- [6] L. Ma, G. Zong, X. Zhao, and X. Huo, “Observed-based adaptive finite-time tracking control for a class of nonstrict-feedback nonlinear systems with input saturation,” *Journal of the Franklin Institute*, 2019.
- [7] R. Mou, L. Hou, Y. Jiang, Y. Zhao, and Y. Wei, “Study of automobile suspension system vibration characteristics based on the adaptive control method,” *International Journal of Acoustics & Vibration*, vol. 20, no. 2, pp. 101–106, 2015.
- [8] J. de Jesus Rubio, P. Cruz, L. A. Paramo, J. A. Meda, D. Mujica, and R. S. Ortigoza, “PID anti-vibration control of a robotic arm,” *IEEE Latin America Transactions*, vol. 14, no. 7, pp. 3144–3150, 2016.
- [9] Y. Sekhar and C. Vinothkumar, *Ieee. Development of a Lab View Based Controller for Active Vibration Control of Panel Structures Using Piezo-Electric Wafers*, Ieee, New York, 2016.
- [10] M. L. Xia and S. Li, “A combined approach for active vibration control of fluid-loaded structures using the receptance method,” *Archive of Applied Mechanics*, vol. 88, no. 10, pp. 1683–1694, 2018.
- [11] Y. M. Ram and J. E. Mottershead, “Receptance method in active vibration control,” *AIAA Journal*, vol. 45, no. 3, pp. 562–567, 2007.
- [12] J. E. Mottershead, M. G. Tehrani, and Y. M. Ram, “Assignment of eigenvalue sensitivities from receptance measurements,” *Mechanical Systems and Signal Processing*, vol. 23, no. 6, pp. 1931–1939, 2009.
- [13] J. F. Zhang, H. J. Ouyang, and J. Yang, “Partial eigenstructure assignment for undamped vibration systems using acceleration and displacement feedback,” *Journal of Sound and Vibration*, vol. 333, no. 1, pp. 1–12, 2014.
- [14] H. Ouyang, “Pole assignment of friction-induced vibration for stabilisation through state-feedback control,” *Journal of Sound and Vibration*, vol. 329, no. 11, pp. 1985–1991, 2010.
- [15] S. M. Gharghory and A. E. Ebrahim, “Self-adaptive firefly algorithm with pole zero cancellation method for controlling SMIB power system,” *International Journal of Computational Intelligence and Applications*, vol. 18, no. 2, p. 1950013, 2019.
- [16] A. S. Chopade, S. W. Khubalkar, A. S. Junghare, M. V. Aware, and S. Das, “Design and implementation of digital fractional order PID controller using optimal pole-zero approximation method for magnetic levitation system,” *IEEE/CAA Journal of Automatica Sinica*, vol. 5, no. 5, pp. 977–989, 2018.
- [17] X. Fengxia, Z. Xuejie, S. Xiaohui, and W. Shanshan, “Composite control of RBF neural network and PD for nonlinear dynamic plants using U-model,” *Journal of Intelligent Fuzzy Systems*, vol. 35, no. 1, pp. 565–575, 2018.
- [18] R. Song and S. Chen, “A self-tuning proportional-integral-derivative-based temperature control method for draw-texturing-yarn machine,” *Mathematical Problems in Engineering*, vol. 2017, Article ID 1864321, 17 pages, 2017.
- [19] L. E. Ciotirca, O. Bernal, J. Enjalbert et al., “New stability method of a multirate controller for a three-axis high-Q MEMS accelerometer with simultaneous electrostatic damping,” *IEEE Sensors Journal*, vol. 18, no. 15, pp. 6106–6114, 2018.
- [20] R. Samin, M. G. Tehrani, and J. E. Mottershead, “Active vibration suppression by the receptance method: partial pole placement, robustness and experiments,” in *Vibration Problems Icovp 2011*, J. Naprstek, J. Horacek, M. Okrouhlik, B. Marvalova, F. Verhulst, and J. T. Sawicki, Eds., vol. 139 of Springer Proceedings in Physics, pp. 371–377, Springer-Verlag Berlin, Berlin, 2011.
- [21] J. Y. Ishihara and M. H. Terra, “On the Lyapunov theorem for singular systems,” *IEEE Transactions on Automatic Control*, vol. 47, no. 11, pp. 1926–1930, 2002.
- [22] Y. M. Ram, “Pole-zero assignment of vibratory systems by state feedback control,” *Journal of Vibration and Control*, vol. 4, no. 2, pp. 145–165, 2016.

Research Article

A Multifrequency Heterodyne Phase Error Compensation Method for 3D Reconstruction

Zihao Yu ¹, Jin Liu ¹, Haima Yang ², Bo Huang,¹ and Yumei Jian¹

¹School of Electronic and Electrical Engineering, Shanghai University of Engineering Science, Shanghai, China 201600

²School of Optical-Electrical and Computer Engineering, University of Shanghai for Science and Technology, Shanghai, China 200093

Correspondence should be addressed to Jin Liu; flyingpine@sina.com and Haima Yang; snowyhm@sina.com

Received 29 May 2020; Revised 18 June 2020; Accepted 19 June 2020; Published 8 August 2020

Academic Editor: Bin Gao

Copyright © 2020 Zihao Yu et al. This is an open access article distributed under the Creative Commons Attribution License, which permits unrestricted use, distribution, and reproduction in any medium, provided the original work is properly cited.

In view of the problem of “jumping points” in the phase unwrapping of the multifrequency heterodyne principle, this paper proposes a novel method to improve the multifrequency heterodyne. By solving the root-mean-square error of the original frequency function, it includes the relationship between the error and the adjacent phase in the condition of constrained phase unwrapping, and it compensates phase $\pm 2\pi$ of the skip point. To ensure the accuracy of phase unwrapping, the function with a “jump point” after each phase unwrapping and the absolute phase curve of the principal value function are used to establish the threshold judgment model of the least square method, and the initial phase unwrapping of the principal value function with different frequencies is carried out continuously. The simulation analysis of phase compensation with the four-step phase-shifting method shows that the error is reduced to 36% under the set environment. The experimental result of 3D reconstruction by measuring the flatness of the plate shows that the error decreases by 41% after phase compensation compared with before phase compensation. The three-dimensional reconstruction experiment of pitch measurement with a nut shows that the nut after phase compensation is smooth without noise, and the pitch error is 0.033 mm, which verified the method is workable and effective.

1. Introduction

Based on triangulation, the structured light three-dimensional measurement method has been widely used in various fields due to its high-precision and noncontact measurement [1–3]. For example, the measurement of three-dimensional morphology is applied to reverse engineering, biomedical treatment, heritage acquisition, architecture and computer animation, etc. [4–6]. To get a high-precision three-dimensional profile, we need to unwrap the phase accurately. The four-step phase-shifting method is adopted in the 3D reconstruction process. The arctangent function is involved in the derivation process, so the phase is wrapped between $[-\pi, \pi]$. Therefore, the wrapped phase needs to be unwrapped continuously in the global field [7].

At present, the principle of multifrequency heterodyne is one of the widely used methods. Multifrequency heterodyne is a time phase unwrapping method [8, 9]. The calculation of phase unwrapping at different frequencies is independent in

the process of phase unwrapping. Therefore, the algorithm can better suppress interference. However, there are some problems in phase unwrapping of multifrequency heterodyne, such as jumping error [10]. Jiang et al. [11] proposed a series of constraints to compensate the phase of multifrequency heterodyne. Zhang et al. proposed a look-up table method to build a preestablished storage table between the input gray and the output gray to compensate for the nonlinear phase error in the projection and acquisition system, but this method took a lot of time to calculate [12]. Cai et al. used the Hilbert algorithm to compensate the reverse error, but this method was unable to measure the profile of complex objects, and the measurement speed was slow [13].

In order to solve the problem of jumping error in the principle of multifrequency heterodyne, this paper proposes a novel method to improve multifrequency heterodyne [14–16]. The innovation of this paper is described below. The root-mean-square error of the principal value function with different frequencies is solved, and the phase unwrapping is

carried out with this error as the corresponding constraint condition. Finally, the least square threshold judgment model is established for the function with a “jump point” after each phase unwrapping and the absolute phase curve of the principal value function. According to the threshold value, whether to enter the next iteration is judged. If the error is greater than the set value, then the error is taken as the constraint condition for phase unwrapping again until the threshold condition is met.

In this way, the jumping error is eliminated when the phase of the initial principal value function of different frequencies is unwrapped. Through the simulation of phase unwrapping of sinusoidal gratings with three different frequencies of noise, there is a “jump point” in phase unwrapping before phase compensation, and a continuous phase is got after phase compensation; in the experimental part, the method is applied to 3D profile reconstruction, and the experimental results show that the 3D profile after phase compensation is more smooth without a jump point.

In this paper, the contributions of the phase error compensation method are as follows. Firstly, the constraints of the phase error compensation method in this paper are more concise and easy to calculate. Secondly, this paper compensates the wrapping phase of various frequencies, respectively, and the phase becomes more continuous after phase unwrapping. Thirdly, compared with single-frequency wrapping phase error compensation, the multifrequency heterodyne method is more fault-tolerant and accurate in 3D reconstruction of objects because of the independent phase unwrapping process of various frequencies. The second part of this paper involves the description of the principle of multifrequency heterodyne phase unwrapping; the third part is a novel method of phase compensation; we divide the fourth part into simulation verification of this method and experimental verification of the feasibility of this method; the fifth part is the summary.

2. The Principle of the Multifrequency Heterodyne Method

The principle of the heterodyne method is to stack the principal values of sine grating functions with different frequencies and finally get the entire image with the frequency of 1 Hz, where absolute phase $\phi(x, y)$ of its expression is [17]

$$\phi(x, y) = 2\pi k(x, y) + \varphi(x, y), \quad (1)$$

where $k(x, y)$ is an integer. $\varphi(x, y)$ is the principal value function of the phase of the sine grating functions. The key to phase unwrapping is to find the value of $k(x, y)$.

Different frequencies of λ_1 and λ_2 correspond to phase function $\varphi_1(x, y)$ and $\varphi_2(x, y)$, respectively. The wrapped phase maps of φ_1 and $\varphi_2(x, y)$ will be unwrapped, where the expression of absolute phase is [18]

$$\begin{cases} \phi_1 = 2\pi k_1 + \varphi_1, \\ \phi_2 = 2\pi k_2 + \varphi_2. \end{cases} \quad (2)$$

The schematic diagram of multifrequency heterodyne shows phase unwrapping in Figure 1.

The fringe series n satisfy

$$\begin{cases} \lambda_1 n_1 = \lambda_2 n_2, \\ \begin{cases} n_i = k_i + \Delta n_i, \\ \Delta n_i = \frac{\varphi_i}{2\pi}. \end{cases} \end{cases} \quad (3)$$

The integer fringe numbers of the fringe patterns of different frequencies on the same point satisfy

$$\begin{cases} k_1 = k_2, & \varphi_1 \geq \varphi_2, \\ k_1 = k_2 + 1, & \varphi_1 < \varphi_2. \end{cases} \quad (4)$$

The heterodyne phase value is

$$\varphi_{12} = \Delta\varphi = \phi_1 - \phi_2 = \begin{cases} \varphi_1 - \varphi_2, & \varphi_1 \geq \varphi_2, \\ 2\pi + \varphi_1 - \varphi_2, & \varphi_1 < \varphi_2. \end{cases} \quad (5)$$

From Equations (2)–(5), we get

$$\frac{\phi_1}{2\pi} \lambda_1 = \frac{\phi_2}{2\pi} \lambda_2 = \frac{\phi_{12}}{2\pi} \lambda_{12}. \quad (6)$$

The frequency value after superposition of different frequencies is

$$\lambda_{12} = \frac{\lambda_1 \lambda_2}{\lambda_2 - \lambda_1}. \quad (7)$$

From Equations (6) and (7), the absolute phase value of fringe gratings with different frequencies is

$$\phi_1 = \frac{\lambda_2}{\lambda_2 - \lambda_1} \Delta\varphi. \quad (8)$$

From Equations (2) and (8), the key value $k(x, y)$ is

$$k_1 = \text{floor} \left[\frac{(\Delta\varphi \lambda_2 / (\lambda_2 - \lambda_1)) - \varphi_1}{2\pi} \right] = \text{floor} \left[\frac{(\varphi_{12} \lambda_{12} / \lambda_1) - \varphi_1}{2\pi} \right]. \quad (9)$$

Finally, the absolute phase value ϕ_1 can be got [19]:

$$\phi_1 = 2\pi * \text{floor} \left[\frac{(\varphi_{12} \lambda_{12} / \lambda_1) - \varphi_1}{2\pi} \right] + \varphi_1. \quad (10)$$

In fact, there will be some “jumping points” in the process of multifrequency heterodyne phase unwrapping. Therefore, it is necessary to compensate the errors to improve the precision of phase unwrapping.

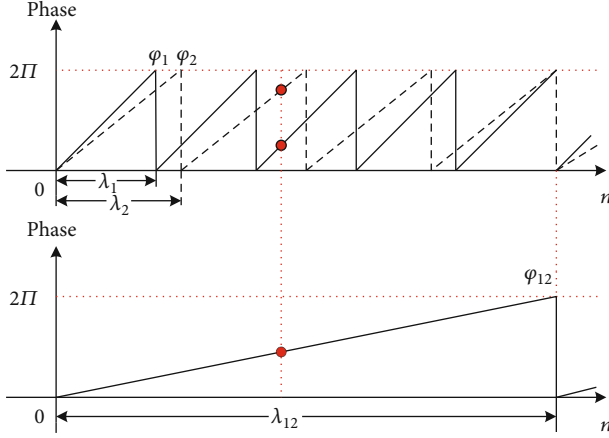


FIGURE 1: Multifrequency heterodyne phase unwrapping principle.

3. Multifrequency Heterodyne Phase Error Compensation

There are three kinds of gratings with different frequencies. The projector projects the gratings with fringe periods of 70, 64, and 59. After collecting by a CCD camera, they carry the phase unwrapping processing out. Finally, the noise problem shown in the red circle area in Figure 2 will appear in the result of global phase unwrapping. After analysis, it is a jump error. Therefore, it is necessary to compensate the phase error before 3D reconstruction of the object, so as to avoid “jumping points” in the reconstructed model.

With the multifrequency heterodyne method, there are some problems such as jumping error. First, calculate the root-mean-square error (RMSE) after the phase unwrapping of sine grating functions with different frequencies. According to the principle of multifrequency heterodyne in the upper section and the formula below, the root-mean-square error (RMSE) can be got:

$$\text{RMSE} = \sqrt{\frac{\sum_{i=1}^i (\phi_i - \lambda_i * X)^2}{i}}, \quad (11)$$

where $\phi'_{12}(x, y)$ is the wrapped phase after dual-frequency correction, computing σ_{ϕ_1} and σ_{ϕ_2} over $\phi_1(x, y)$ and $\phi_2(x, y)$, and select $\sigma_{\phi} = \max\{\sigma_{\phi_1}, \sigma_{\phi_2}\}$. In this way, avoid the jumping error caused by the noise in the wrapped phase. The phase unwrapping function after correction is

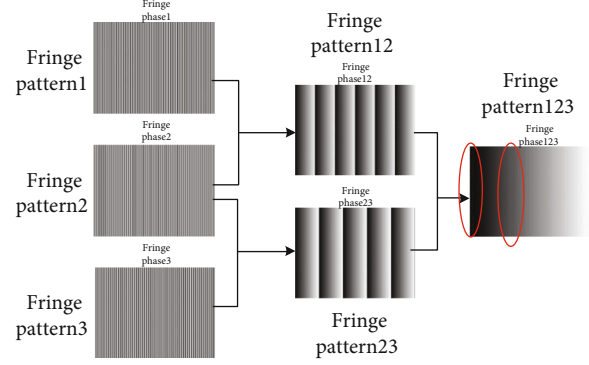


FIGURE 2: Schematic diagram of multifrequency heterodyne.

where X defined as

$$X = \frac{\left(\sum_{i=1}^i \phi_i * \lambda_i\right)}{\sum_{i=1}^i \lambda_i^2},$$

$$\text{RMSE} = \sqrt{\frac{\sum_{i=1}^i \left(\phi_i - \lambda_i * \left(\frac{\left(\sum_{i=1}^i \phi_i * \lambda_i\right)}{\sum_{i=1}^i \lambda_i^2}\right)\right)^2}{i}}, \quad (12)$$

where ϕ_i is the absolute phase value of a certain frequency grating, i.e., the value after phase unwrapping of fringes; λ_i is the frequency of the fringes; and i is the total frequency. The wrapped phase error is analyzed, and the error is a Gaussian distribution, and the root-mean-square error (RMSE) is calculated as σ_{ϕ} , where σ_{ϕ_1} , σ_{ϕ_2} , σ_{ϕ_3} are the principal value function ϕ_1 , ϕ_2 , and ϕ_3 Gaussian standard deviations. To deal with the “jump point” error, add the constraint conditions to the original algorithm. The constraints are

$$\phi'_{12}(x, y) = \begin{cases} \phi_{12}(x, y) - 2\pi & -2\sigma_{\phi} < \phi_1(x, y) - \phi_2(x, y) < 0, \quad \phi_1(x, y), \phi_2(x, y) < 0, \\ 2\pi + \phi_{12}(x, y) & 0 < \phi_1(x, y) - \phi_2(x, y) < 2\sigma_{\phi}, \quad \phi_1(x, y), \phi_2(x, y) > 0, \\ \phi_{12}(x, y), & \text{otherwise,} \end{cases} \quad (13)$$

$$\phi'_{12}(x, y) = 2\pi * \text{floor} \left[\frac{\left(\left(\phi'_{12}(x, y) \lambda_{12}\right) / \lambda_1\right) - \phi_1(x, y)}{2\pi} \right] + \phi_1(x, y). \quad (14)$$

For the heterodyne function $\phi_{23}(x, y)$, the constraints are

$$\varphi'_{23}(x, y) = \begin{cases} \varphi_{23}(x, y) - 2\pi & -2\sigma_\varphi < \varphi_2(x, y) - \varphi_3(x, y) < 0, \quad \varphi_2(x, y), \varphi_3(x, y) < 0, \\ 2\pi + \varphi_{23}(x, y) & 0 < \varphi_2(x, y) - \varphi_3(x, y) < 2\sigma_\varphi, \quad \varphi_2(x, y), \varphi_3(x, y) > 0, \\ \varphi_{23}(x, y), & \text{otherwise,} \end{cases} \quad (15)$$

where $\varphi'_{23}(x, y)$ is the wrapped phase after dual-frequency correction. Two wrapped phase maps of $\varphi_2(x, y)$ and $\varphi_3(x, y)$ have Gaussian standard deviation σ_{φ_2} and σ_{φ_3} , respectively, computing σ_{φ_2} and σ_{φ_3} over $\varphi_2(x, y)$ and $\varphi_3(x, y)$,

and select $\sigma_\varphi = \max\{\sigma_{\varphi_2}, \sigma_{\varphi_3}\}$. $\varphi'_{123}(x, y)$ is using a similar method. Compensation for jumping errors in the wrapped phase map $\varphi_{123}(x, y)$ is computed by

$$\varphi'_{123}(x, y) = \begin{cases} \varphi_{123}(x, y) - 2\pi & -2\sigma_\varphi < \varphi'_{12}(x, y) - \varphi'_{23}(x, y) < 0, \quad \varphi'_{12}(x, y), \varphi'_{23}(x, y) < 0, \\ 2\pi + \varphi_{123}(x, y) & 0 < \varphi'_{12}(x, y) - \varphi'_{23}(x, y) < 2\sigma_\varphi, \quad \varphi'_{12}(x, y), \varphi'_{23}(x, y) > 0, \\ \varphi_{123}(x, y), & \text{otherwise,} \end{cases} \quad (16)$$

where $\varphi'_{123}(x, y)$ is the wrapped phase after compensation. At this moment, the value of σ_φ is determined by $\sigma_\varphi = \max\{\sqrt{2} \max\{\sigma_{\varphi_1}, \sigma_{\varphi_2}\}, \sqrt{2} \max\{\sigma_{\varphi_2}, \sigma_{\varphi_3}\}\}$.

$$\begin{cases} \phi'_{12}(x, y) = 2\pi * \text{floor} \left[\frac{\left(\left(\varphi'_{123}(x, y) \lambda_{123} \right) / \lambda_{12} \right) - \varphi'_{12}(x, y)}{2\pi} \right] + \varphi'_{12}(x, y), \\ \phi'_{23}(x, y) = 2\pi * \text{floor} \left[\frac{\left(\left(\varphi'_{123}(x, y) \lambda_{123} \right) / \lambda_{23} \right) - \varphi'_{23}(x, y)}{2\pi} \right] + \varphi'_{23}(x, y), \end{cases} \quad (17)$$

where $\phi'_{12}(x, y)$ and $\phi'_{23}(x, y)$ are the phase unwrapping function after correction. After phase compensation is completed, the model relationship between the compensated phase unwrapping mean $X' * \lambda$ and the compensated frequency phase unwinding phase function value ϕ'_i is established. The model relation is given by formula (18). After phase compensation, there may be a “jump point” function and its absolute phase curve of its principal value function to establish the least square method threshold judgment model and determine whether the error is less than the set threshold value. If not, return the error to Equations (13)–(17) as the condition of constrained phase unwrapping and then carry out phase compensation until the threshold condition is met. The judgment equation is

$$\text{error} = \sum_{i=1}^i \left(X' * \lambda_i - \phi'_i \right)^2, \quad (18)$$

$$X' = \frac{\left(\sum_{i=1}^i \phi'_i * \lambda_i \right)}{\sum_{i=1}^i \lambda_i^2}. \quad (19)$$

The multifrequency heterodyne completes phase compensation.

4. Simulation and Experimental Analysis

4.1. Simulation Analysis of 3D Reconstruction before and after Phase Error Compensation. Three sinusoidal gratings with different frequencies are selected for phase compensation. The three frequencies are 70, 64, and 59, respectively. The simulation environment is a nonideal sinusoidal grating with a resolution of 1024 * 768. In Figure 3, it can be seen that the environment noise before compensation will cause the “jump points” of the last phase unwrapping. First, the root-mean-square error (RMSE) of the noise is calculated as σ_φ , which is the constraint condition of Equations (13) and (15) in this

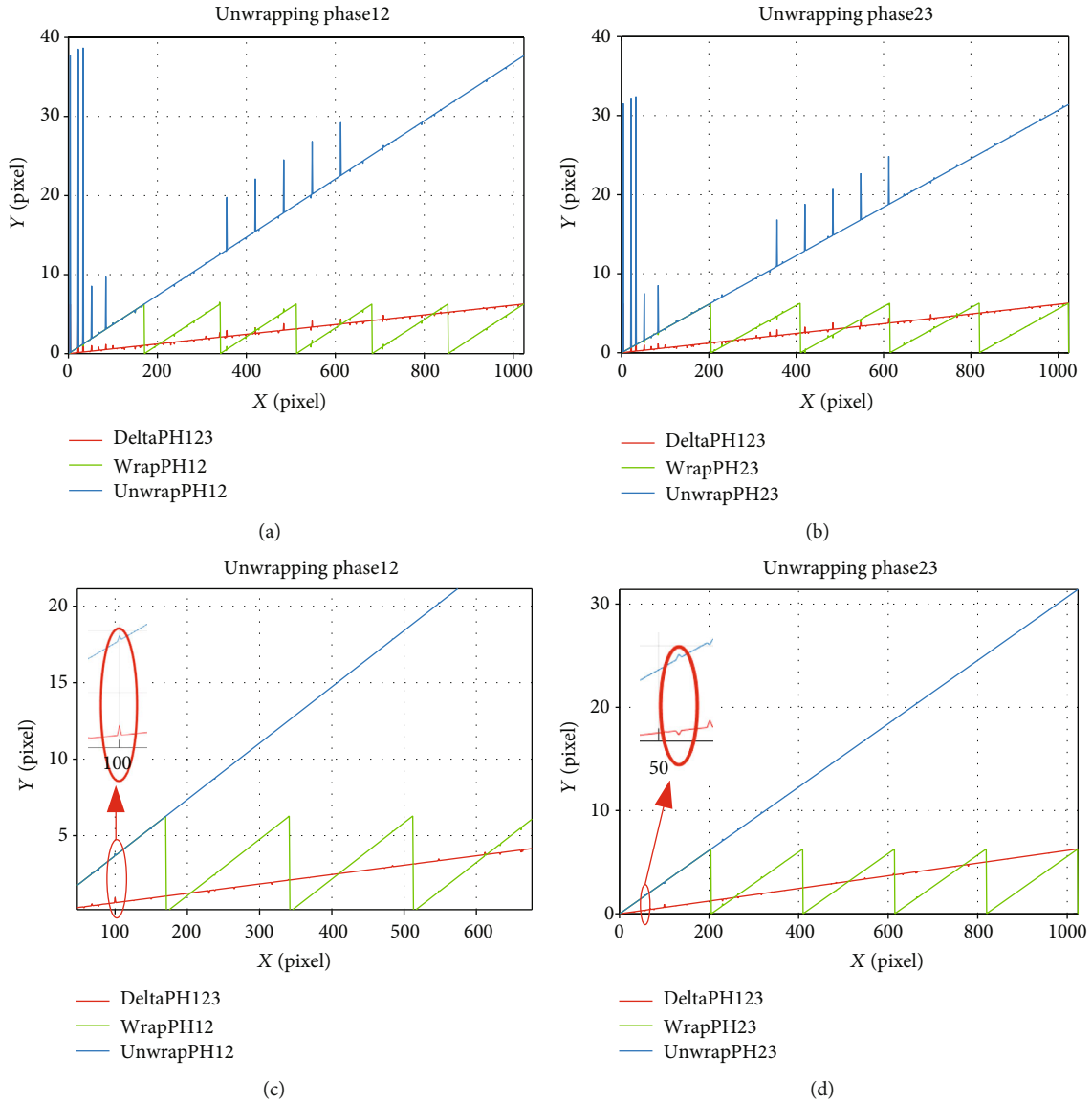


FIGURE 3: The phase wrap and unwrap curve of the heterodyne function (a, b) before compensation and (c, d) after compensation.

paper. Functions φ_{12} and φ_{23} , through judging the σ_φ and $\varphi_1(x, y) - \varphi_2(x, y)$ relationship, determine whether a jump occurs, and finally, the phase of the jump point is carried out to add or subtract 2π . The green curves in Figures 3(a) and 3(b) represent the principal value functions $\varphi_{12}(x, y)$ and $\varphi_{23}(x, y)$ of the wrapped phase, respectively; the red curves are $\Delta\varphi_{12}$ and $\Delta\varphi_{23}$; the blue curves are φ_{12} and φ_{23} after the phase unwrapping. It can be seen that the function shows “jumping points” because of noise, and the pixel jump reaches 30-40 pixels at the beginning and end. After the algorithm proposed in this paper is used for compensation, as shown in Figures 3(c) and 3(d), the pixel jump drops to 5 pixels after the phase of the blue curve is unwrapped, indicating that the phase is compensated.

Figures 4(a), 4(b), and 4(c), respectively, correspond to the phase compensation front curve of functions φ_1 , φ_2 , and φ_3 . The initial noise also exists in these three principal

value functions. It is transferred to the principal value function after superposition frequency by the heterodyne method. The basic steps of the heterodyne method are as follows: step 1: get the phase value of the principal value function first; step 2: get an entire image with the phase frequency of 1 Hz by using the principle of the heterodyne method; and step 3: reverse $\varphi_i = 2\pi k_i + \varphi_i$. According to the heterodyne method, the frequency is got by superposition, and the sequence of phase unwrapping is the principal value functions φ_{12} , φ_{23} , φ_1 , φ_2 , and φ_3 , while the final purpose is to obtain the last three different frequency principal value functions, the continuous phase unwrapping of φ_1 , φ_2 , and φ_3 . In the process of phase unwrapping, when the errors of Figures 3(c) and 3(d) pass through the next phase unwrapping, because the errors of the jumping points of the principal value functions φ_{12} and φ_{23} are already tiny, the relationship of constraint conditions σ_φ and $\varphi_1(x, y) - \varphi_2(x, y)$ may not meet

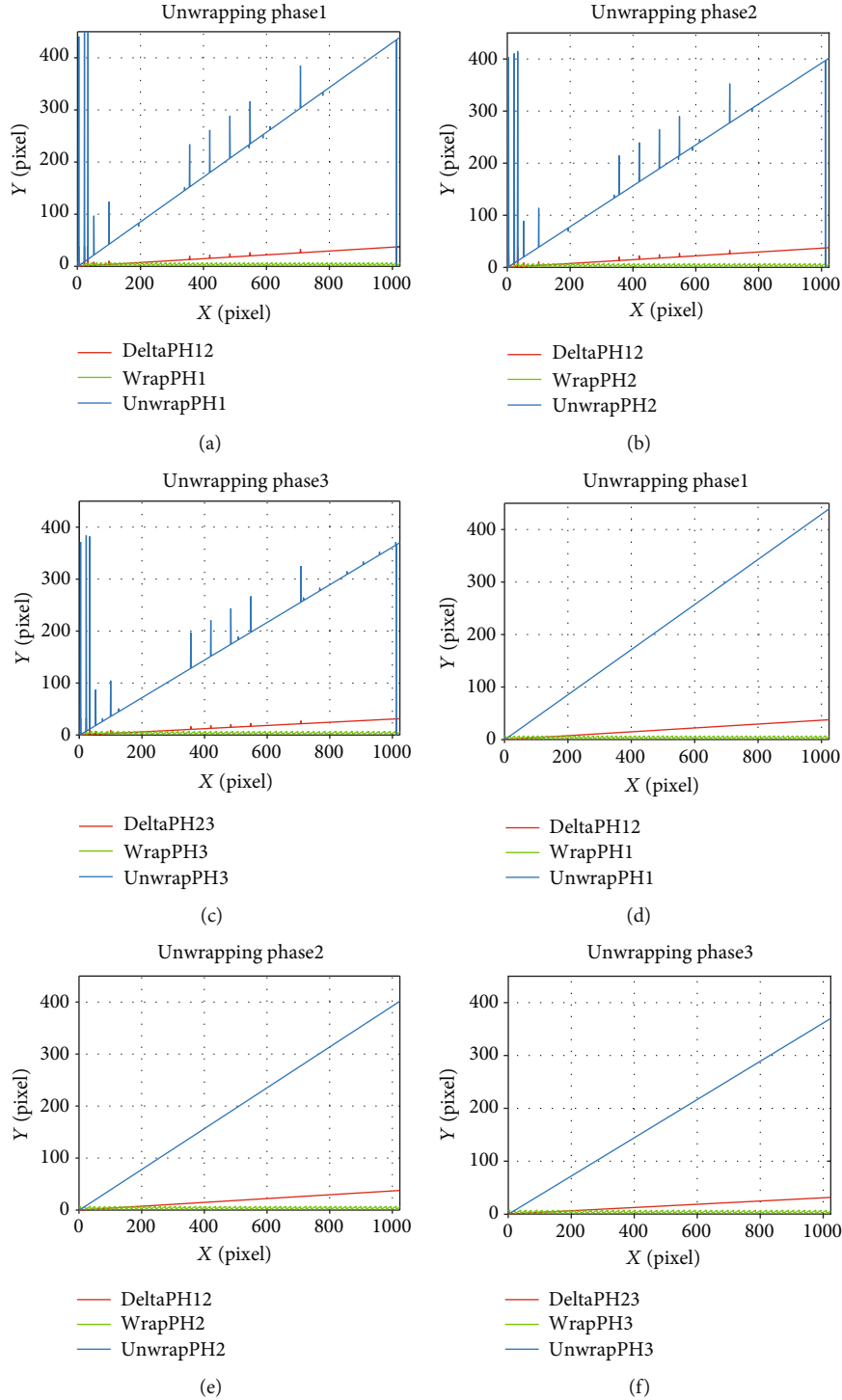


FIGURE 4: The phase wrap and unwrap curve of the function (a–c) before compensation and (d–f) after compensation.

the conditions of $-2\sigma_\varphi < \varphi_1(x, y) - \varphi_2(x, y) < 0$ or $0 < \varphi_1(x, y) - \varphi_2(x, y) < 2\sigma_\varphi$, which is not enough to affect the phase unwrapping of φ_1 , φ_2 , and φ_3 , so the phase unwrapping no longer has a jump. In this paper, a decision condition of the least square method is added to the method. The error is still large, but after many iterations, it is found that the phase unwrapping of φ_1 , φ_2 , and φ_3 in Figures 4(d), 4(e), 4(f), respectively, does not have jumping points.

The experimental results show that the errors of the principal value function before phase compensation (phase wrapping) and after phase compensation (phase unwrapping) can be ignored, and the errors of the principal value function of heterodyne can be reduced by 36%. Table 1 shows the calculated standard deviation before and after the phase compensation, which shows that the algorithm in this paper has a significant improvement on the accuracy.

TABLE 1: Error analysis before and after phase compensation during phase unwrapping.

Phase unwrapping	Phase12	Phase23	Phase1	Phase2	Phase3
Standard deviation before phase compensation	0.00372	0.00387	0.0630	0.0591	0.0654
Standard deviation after phase compensation	0.00237	0.00253	/	/	/

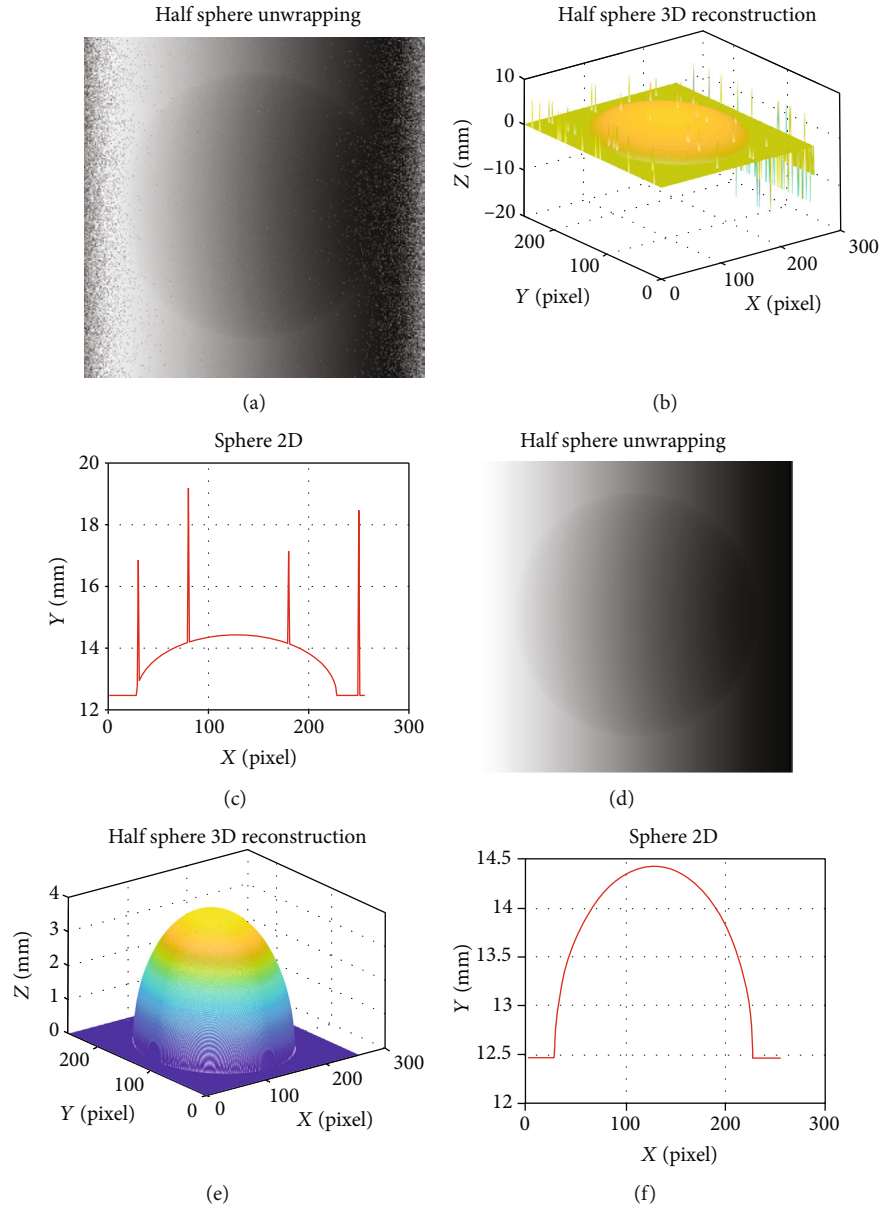


FIGURE 5: (a–c) Phase unwrapping before phase compensation and 3D and 2D visualization of data. (d–f) Phase unwrapping after phase compensation and 3D and 2D visualization of data.

In order to further prove the accuracy and better visualization effect of the method proposed in this paper, combined with MATLAB, the hemispherical $R = 50$ radius is simulated by the four-step phase-shifting method, and the grating resolution ratio is 256×256 . Gaussian noise with standard deviation of 0.01 is added. Figures 5(a–f) display the three-dimensional and two-dimensional images of the phase unwrapping, respectively. Through the comparison of the

two sets of data, we can see the recovery morphology of the hemisphere after the phase compensation, which shows that the compensation method proposed in this paper is accurate and workable.

4.2. Experimental Analysis of 3D Reconstruction before and after Phase Error Compensation. In the experiment, the flat plate and nut are scanned for verification. Figure 6(a) is for

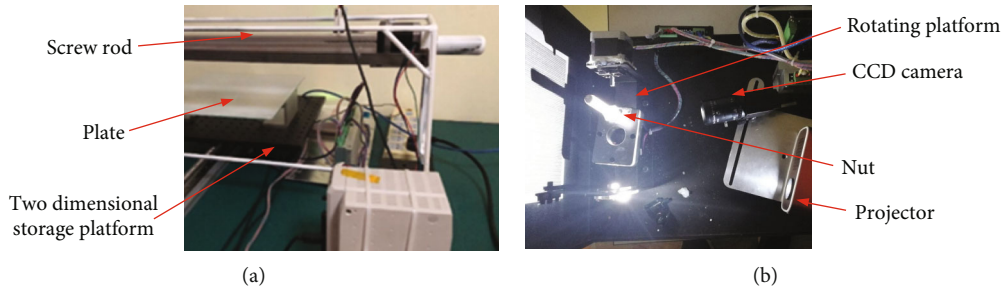


FIGURE 6: Experiment platform. (a) Plate. (b) Nut.

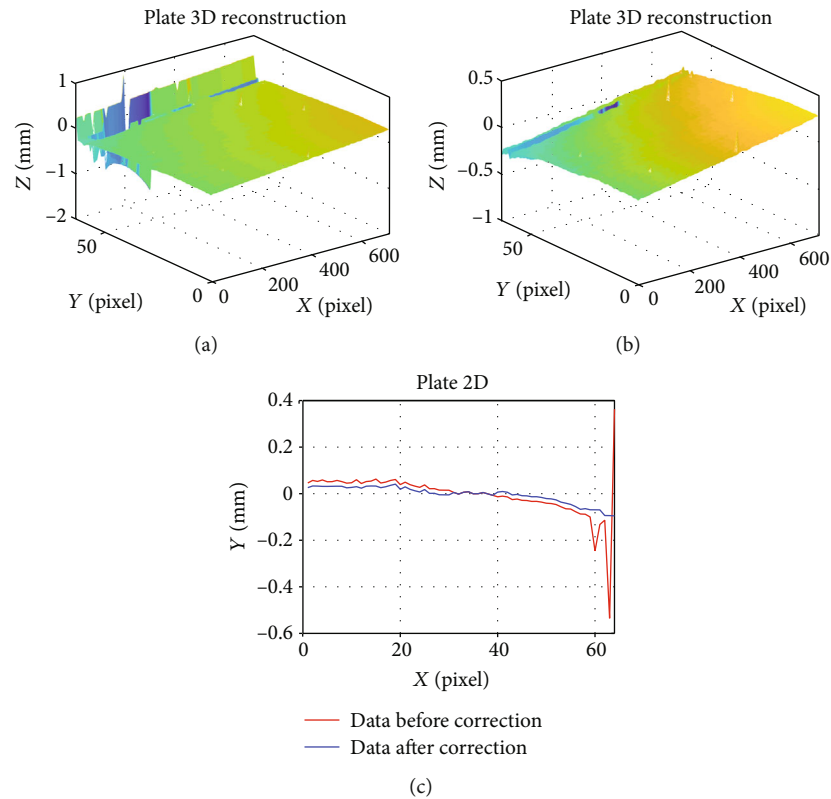


FIGURE 7: Wave of flatness and error. (a) Flatness before phase compensation. (b) Flatness after phase compensation. (c) Plate section error data.

scanning and collecting the plate data. The experimental platform mainly includes a screw rod, a two-dimensional storage platform, a projector and camera installed on the screw rod, and a two-dimensional storage platform controlled by a step motor, which can move along the horizontal X -axis and Y -axis. Figure 6(b) is to collect the nut data. The place where the nut of the experimental platform is placed is a two-freedom-degree rotating platform, which can swing the arm forward and backward, and the fixed axis can rotate in a circle. In the experiment, the projector resolution ratio is 1024×768 pixels, the camera resolution ratio is 3078×2048 pixels, and the number of fringe periods is 64, 60, and 57. The upper computer of the two platforms is a Windows 10 system, and the CPU is Intel i5. The camera collects the data

of the flat plate and the nut, respectively, gets the data, and compares the effect of phase compensation and noncompensation for the data.

First, collect the plate data, and the number of effective points collected is 64×716 . In this paper, 3D reconstruction is carried out by the four-step phase-shifting method. Figure 7(a) shows the three-dimensional image before phase compensation, in which there are jump points when the pixel is close to 64 pixels. Figure 7(b) carries out phase compensation in this method, and it can be seen that it eliminates the "jump points." To show the more obvious change, Figure 7(c) shows the variation of the cross-section data, data before phase compensation (red), and data after phase compensation (blue); the front and back

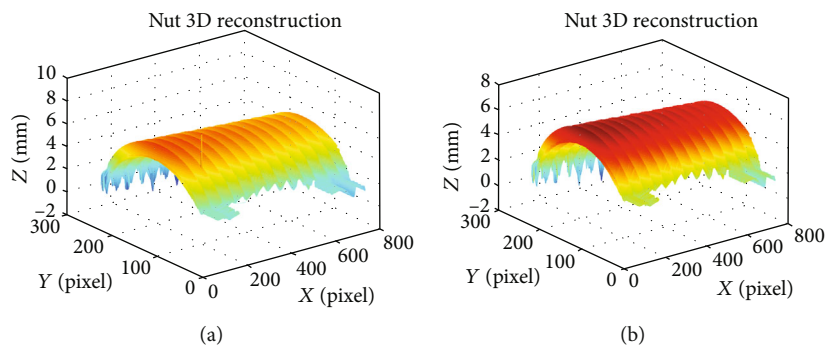


FIGURE 8: Three-dimensional reconstructions of the partial thread of the nut (a) before phase compensation and (b) after phase compensation.

TABLE 2: Measurement of pitch.

Pitch	1	2	3	4	5	6	7	8	9	10
Measurement	1.78	1.79	1.78	1.78	1.78	1.78	1.78	1.79	1.79	1.78
Error	0.03	0.04	0.03	0.03	0.03	0.03	0.03	0.04	0.04	0.03

error is reduced from the maximum error of 0.5 mm to 0.1 mm; and the error is reduced by 40%, verifying the feasibility of the phase compensation method.

To analyze the accuracy of the phase error compensation method proposed in this paper, the nuts which are widely used in industry are used for reconstruction. The pitch standard is easy to query and can be analyzed quantitatively. Therefore, the pitch value is taken as another standard to evaluate the accuracy of the phase error compensation method in this paper. The four-step phase-shifting method is used to collect nut data for 3D reconstruction. Figure 8 shows the reconstruction model of the nut before and after phase compensation.

By calculating the thread pitch of the nut (unit: mm) as the measurement standard, analyze the distance between ten adjacent threads of the screw, among which the specification of the screw is M12, and the standard pitch is 1.75 mm. For the acquired data, the distance between adjacent ten threads is recorded as shown in Table 2.

According to the table, Figures 8(a) and 8(b) show that the surface of the nut after compensation is flat and there is no jumping error. It shows that the novel method of multifrequency heterodyne phase error compensation proposed in this paper can effectively eliminate the “jump point” in the actual 3D reconstruction and ensure the high reconstruction accuracy.

5. Conclusion

To eliminate the jumping error in the process of phase unwrapping, this paper proposes a novel method of multifrequency heterodyne phase compensation, which solves the problem of “jumping points” in the actual situation. In this paper, the root-mean-square error (RMSE) of the principal value function with different frequencies after phase unwrap-

ping is calculated first, and they include it in the constraint condition of phase compensation, to suppress the jump error. The least square threshold judgment condition is added to verify whether there is still a “jump point” with large error after compensation, which affects the global unwrapping of the last phase. If it is greater than the threshold value, it will carry a simple reiteration to meet the threshold requirements. In this paper, the simulation analysis shows that the error is reduced by 36% in the set environment, and the phase unwrapping after the error compensation can effectively eliminate the “jumping points” and get the continuous phase. The experimental verification of flatness measurement shows that the error after phase compensation is reduced by 41% compared with that before compensation, and the three-dimensional reconstruction of the nut can also achieve high accuracy. After the error compensation, the 3D reconstruction object surface becomes smoother and more continuous. Simulation and experiment show that the improved multifrequency heterodyne phase compensation method is workable.

The future direction of the work in the paper can be divided into the following points. First, it can be seen from the experimental data before and after the compensation of the plate that there is still room for correction of the error of the plate, and it is not clear whether the formula proposed in this paper is the best for the reconstruction error compensation. Second, this paper is to carry out 3D reconstruction of objects without mirror reflection. How to achieve high-precision 3D reconstruction of mirror reflection objects is still a problem to be solved.

Data Availability

The data used to support the findings of this study are available from the corresponding authors upon request.

Conflicts of Interest

The authors declare that there is no conflict of interest regarding the publication of this paper.

Acknowledgments


This work was supported in part by the National Natural Science Foundation of China under Grant 61701296 and Grant U1831133, in part by the Natural Science Foundation of Shanghai under Grant 17ZR1443500, and in part by the Shanghai Aerospace Science and Engineering Fund under Grant SAST2017-062.

References

- [1] C. Zuo, L. Huang, M. Zhang, Q. Chen, and A. Asundi, "Temporal phase unwrapping algorithms for fringe projection profilometry: a comparative review," *Optics and Lasers in Engineering*, vol. 85, pp. 84–103, 2016.
- [2] B. Pan, Q. Kema, L. Huang, and A. Asundi, "Phase error analysis and compensation for nonsinusoidal waveforms in phase-shifting digital fringe projection profilometry," *Optics Letters*, vol. 34, no. 4, pp. 416–418, 2009.
- [3] M. Dai, F. Yang, C. Liu, and X. He, "A dual-frequency fringe projection three-dimensional shape measurement system using a DLP 3D projector," *Optics Communications*, vol. 382, pp. 294–301, 2017.
- [4] S. Zhang and S.-T. Yau, "High-resolution, real-time 3D absolute coordinate measurement based on a phase-shifting method," *Optics Express*, vol. 14, no. 7, pp. 2644–2649, 2006.
- [5] S. Yu, J. Zhang, X. Yu, X. Sun, H. Wu, and X. Liu, "3D measurement using combined Gray code and dual-frequency phase-shifting approach," *Optics Communications*, vol. 413, pp. 283–290, 2018.
- [6] H. Wang, W. Song, E. Zio, A. Kudreyko, and Y. Zhang, "Remaining useful life prediction for lithium-ion batteries using fractional brownian motion and fruit-fly optimization algorithm," *Measurement*, vol. 161, article 107904, 2020.
- [7] E. B. Li, X. Peng, J. Xi, J. F. Chicharo, J. Q. Yao, and D. W. Zhang, "Multi-frequency and multiple phase-shift sinusoidal fringe projection for 3D profilometry," *Optics Express*, vol. 13, no. 5, pp. 1561–1569, 2005.
- [8] H. Wang, F. Liu, and Q. Zhu, "Improvement of phase unwrapping algorithm based on image segmentation and merging," *Optics Communications*, vol. 308, pp. 218–223, 2013.
- [9] C. S. Cho and J. Han, "Phase error reduction for multi-frequency fringe projection profilometry using adaptive compensation," *Current Optics and Photonics*, vol. 2, pp. 332–339, 2018.
- [10] S. Xing and H. Guo, "Correction of projector nonlinearity in multi-frequency phase-shifting fringe projection profilometry," *Optics Express*, vol. 26, no. 13, pp. 16277–16291, 2018.
- [11] C. Jiang, S. Xing, and H. Guo, "Fringe harmonics elimination in multi-frequency phase-shifting fringe projection profilometry," *Optics Express*, vol. 28, no. 3, pp. 2838–2856, 2020.
- [12] C. Zhang, H. Zhao, L. Zhang, and X. Wang, "Full-field phase error detection and compensation method for digital phase-shifting fringe projection profilometry," *Measurement Science and Technology*, vol. 26, no. 3, p. 035201, 2015.
- [13] Z. Cai, X. Liu, H. Jiang et al., "Flexible phase error compensation based on Hilbert transform in phase shifting profilometry," *Optics Express*, vol. 23, no. 19, pp. 25171–25181, 2015.
- [14] H. Zhao, Z. Wang, H. Jiang, Y. Xu, and C. Dong, "Calibration for stereo vision system based on phase matching and bundle adjustment algorithm," *Optics & Lasers in Engineering*, vol. 68, pp. 203–213, 2015.
- [15] C. Mao, R. Lu, and Z. Liu, "A multi-frequency inverse-phase error compensation method for projector nonlinear in 3D shape measurement," *Optics Communications*, vol. 419, pp. 75–82, 2018.
- [16] W. Song, H. Liu, and E. Zio, "Generalized cauchy process: difference iterative forecasting model," *Chaos, Solitons & Fractals*, 2020, In press.
- [17] L. Wang, L. Song, L. J. Zhong, P. Xin, S. Li, and H. Qi, "Multi-frequency heterodyne phase shift technology in 3-D measurement," *Advanced Materials Research*, vol. 774-776, pp. 1582–1585, 2013.
- [18] Z. Zhang, Y. Xu, and Y. Liu, "Crosstalk reduction of a color fringe projection system based on multi-frequency heterodyne principle," in *2013 International Conference on Optical Instruments and Technology*, p. 904607, Optoelectronic Measurement Technology and Systems, Beijing, China, 2013.
- [19] S. Zhang and S.-T. Yau, "Generic nonsinusoidal phase error correction for three-dimensional shape measurement using a digital video projector," *Applied Optics*, vol. 46, no. 1, pp. 36–43, 2007.

Research Article

Feedback-Dubins-RRT Recovery Path Planning of UUV in an Underwater Obstacle Environment

Bing Hao ¹, Zheping Yan,² Xuefeng Dai,¹ and Qi Yuan³

¹College of Computer and Control Engineering, Qiqihar University, Qiqihar, Heilongjiang Province, China

²College of Automation, Harbin Engineering University, Harbin, Heilongjiang Province, China

³College of Telecommunication and Electronic Engineering, Qiqihar University, Heilongjiang Province, China

Correspondence should be addressed to Bing Hao; haobing_learning@163.com

Received 29 March 2020; Revised 24 June 2020; Accepted 1 July 2020; Published 1 August 2020

Academic Editor: Bin Gao

Copyright © 2020 Bing Hao et al. This is an open access article distributed under the Creative Commons Attribution License, which permits unrestricted use, distribution, and reproduction in any medium, provided the original work is properly cited.

In this paper, a UUV (Unmanned Underwater Vehicle) recovery path planning method of a known starting vector and end vector is studied. The local structure diagram is designed depending on the distance and orientation information about the obstacles. According to the local structure diagram, a Rapidly exploring Random Tree (RRT) method with feedback is used to generate a 3D Dubins path that approaches the target area gradually, and the environmental characteristic of UUV reaching a specific target area is discussed. The simulation results demonstrate that this method can effectively reduce the calculation time and the amount of data storage required for planning. Meanwhile, the smooth spatial path generated can be used further to improve the feasibility of the practical application of UUV.

1. Introduction

With the development and advancement of science and technology, more and more underwater special tasks require UUV to complete. After more than ten or twenty hours of work, the recovery of UUV can be carried out on an underwater platform or a surface ship. At this time, both underwater and surface recovery will face the problem of three-dimensional autonomous motion planning for UUV [1–2]. The content of this paper is to assume that UUV and the recovery platform are not in the same plane. UUV can independently plan the path from the initial point to the target point, and it needs to make sure that the attitude angle at the target point is consistent with the recovery platform.

If the environment where UUV recovery is carried out is complicated with dense obstacles, many various obstacle avoidance methods can be used. However, most obstacle avoidance methods require local replanning, which will generate several subpaths. Repeated iterations of subpaths will

increase the time spent in planning recovery paths, and the movement time of UUV and the data storage capacity will also be increased.

In [3], path planning is divided into two types: global path planning and local path planning. A graph search method is one of the global path planning methods. One of the graph search methods is Rapidly exploring Dense Tree (RDT) [4]. By supposing that there is a dense sequence of sample points in the C space, the new configuration points of the shortest distance from the current configuration source point are selected iteratively and connected to form a tree structure. An RDT algorithm is called Rapidly exploring Random Trees (RRT) when using a random method to select new configuration points [5]. Frazzoli et al. proposed an algorithm for constructing a two-dimensional random incremental road map [6]. It is assumed that there is a non-collision guidance loop to guide the vehicle from any state (including configuration point and speed) to any desired configuration point. In [7], Griffiths et al. proposed a RRT algorithm for constructing traversable paths by modeling

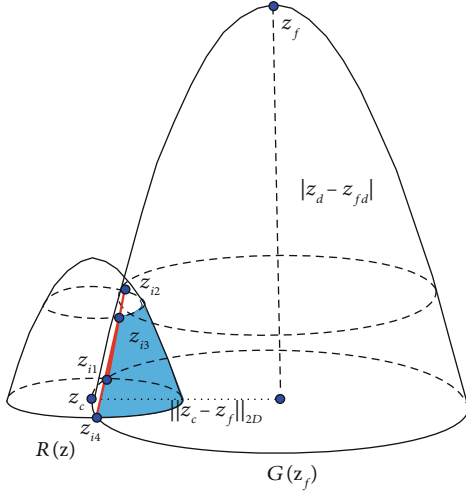


FIGURE 1: The geometry of relative positions of the local-level frame map centered at the current vector and the target vector.

prior environmental data. Examine the branches of the tree as it grows to ensure that the vehicle's turning radius and climb rate constraints are met. The previous research results have fully confirmed that the RRT algorithm [8–10] has a very important value both in theory and in application. However, many previous studies cannot find the most solution to this algorithm theory based on the given cost function [11, 12].

Local path planning algorithms can be divided into heuristic-based path planning algorithms and trajectory generation algorithms [13, 14]. Trajectory generation technology is considered to be a part of the local path planning process, which mainly realizes the construction of a traversal path between two or more path points. The Dubins curve is a type of trajectory generation technology [15]. In order to move the control object from the initial position to the target position, the optimal plane path is constructed in the form of the Dubins curve, and the heading at the initial position and the target position is fixed. The path is a combination of a curve that satisfies the maximum curvature constraint of the control object and a straight line tangent to it.

2. Feedback-Dubins-RRT Recovery Path Planning of UUV

In this paper, the RRT algorithm of global planning and the Dubins curve generation technology of local planning are combined, and the two technologies are extended to a three-dimensional space, taking into account the constraints of UUV, and the autonomous path planning method is given, so as to complete the precise docking of UUV and the recovery platform moves in a three-dimensional environment. The previous path planning method relies on the current sensor data, which can be called the forward path planning method here. The accuracy of forward path planning depends on the accuracy of sensor data and the UUV state model, but these are often difficult to guarantee in long-distance navigation [16].

This paper will imitate the idea of a feedback control loop in control theory, plan the path and feedback the current location information, at the same time compensate the feedback location information, and carry out the next planning according to the feedback position information, which can improve the success rate and accuracy of path planning to a certain extent. The total length of the whole Dubins path can be obtained by the planning algorithm. Since the speed of UUV is seen as a constant, the time at which the UUV reaches the original target point can be calculated.

2.1. Spatial Obstacle Model. Based on the sensors carried by UUV, the range and shape size of the obstacles can be recognized. In this paper, the obstacle that may occur in a recovery environment is described as a spatial ellipsoid model. Let the i th space obstacle model be R_{obi} and the coordinate of the center point of the obstacle model be $R_{obi}(R_{obin}, R_{obie}, R_{obid})$. The radius and height of the obstacle model are a_{obi} , b_{obi} , and c_{obi} , respectively. In most cases, the data of the obstacle shape is detected by carrying sensors. However, after long-term underwater navigation, its navigation error has accumulated to a value that cannot be ignored. In order to avoid obstacles accurately, the obstacle model size is expanded according to navigation errors. By assuming that the error coefficient of navigation is ξ , the obstacle ellipsoid model is defined as

$$R_{obi}(\mathbf{z}) \triangleq \left\{ \mathbf{z} \in Z : \sqrt{\frac{(z_n - z_{obin})^2}{(\xi a_{obi})^2} + \frac{(z_e - z_{obie})^2}{(\xi b_{obi})^2}} \leq 1, \right. \\ \left. |z_d - z_{obid}| \leq \frac{1}{\xi c_{obi}} \sqrt{\frac{z_{obin}^2}{(\xi a_{obi})^2} + \frac{z_{obie}^2}{(\xi b_{obi})^2}} \right\}. \quad (1)$$

Let φ_{\max} represent the maximum rotation angle of UUV, γ_{\max} represent the maximum navigation angle of UUV, and V represent the speed of UUV. The minimum turning radius of UUV can be calculated as

$$r_{\min} = \frac{V^2 \cos \gamma_{\max}}{g \tan \varphi_{\max}}. \quad (2)$$

2.2. Feedback-Dubins-RRT Path Planning

2.2.1. Spatial Model of a Current Vector and Target Vector. Figure 1 shows the local structure of the current vector model and the target vector model of UUV in a recovery path.

Definitions $R(z_c(t))$ and $R(z_f)$, respectively, represent the ellipsoidal regions with the current vector point $\mathbf{z}_c(t) = [z_{cn}, z_{ce}, z_{cd}, z_{c\phi}]$ and the target vector point $\mathbf{z}_f = [z_{fn}, z_{fe}, z_{fd}, z_{f\phi}]$ as the center point of the model. The four elements of the vector represent the north-east earth coordinate and the heading angle of UUV at this point, respectively.

$$\begin{aligned}
R(\mathbf{z}_c(t)) &\triangleq \left\{ \mathbf{z} \in \mathbf{Z} : \sqrt{\frac{(z_n - z_{cn})^2}{a^2} + \frac{(z_e - z_{ce})^2}{b^2}} \right. \\
&\leq 1, |z_d - z_{cd}| \leq \frac{1}{c} \sqrt{\frac{z_{cn}^2}{a^2} + \frac{z_{ce}^2}{b^2}} \left. \right\}, \\
R(\mathbf{z}_f) &\triangleq \left\{ \mathbf{z} \in \mathbf{Z}_{\text{free}} : \sqrt{\frac{(z_n - z_{fn})^2}{a^2} + \frac{(z_e - z_{fe})^2}{b^2}} \right. \\
&\leq 1, |z_d - z_{fd}| \leq \frac{1}{c} \sqrt{\frac{z_{fn}^2}{a^2} + \frac{z_{fe}^2}{b^2}} \left. \right\}. \tag{3}
\end{aligned}$$

Here, \mathbf{Z} represents the set of all space vectors. \mathbf{Z}_{obs} represents the set of position vectors where UUV is located which inevitably intersect with obstacles. Let $\mathbf{Z}_{\text{free}} = \mathbf{Z} \setminus \mathbf{Z}_{\text{obs}}$.

Then, the goal of the planning is tried to find a path so that all vectors on the path are in the set and satisfy the kinematic constraints of UUV. a , b , and c are the parameters of the ellipsoid model, and its value can be designed according to the navigation environment.

Construct another spatial ellipsoid based on the current vector and the target vector $G(\mathbf{z}_f(t))$, the geometric positional relationship is shown in Figure 1, and the expressed area is calculated as the following equation.

$$\begin{aligned}
G(\mathbf{z}_f(t)) &\triangleq \left\{ \mathbf{z} \in \mathbf{Z} : \sqrt{\frac{(z_n - z_{fn})^2}{A^2} + \frac{(z_e - z_{fe})^2}{B^2}} \right. \\
&= 1, |z_d - z_{fd}| \leq \frac{1}{C} \sqrt{\frac{z_{fn}^2}{A^2} + \frac{z_{fe}^2}{B^2}} \left. \right\}, \tag{4}
\end{aligned}$$

where A , B , and C are the parameters of the ellipsoid, $\max(A, B) = \|z_c(t) - z_f\|_{2D}$.

$\partial R(\mathbf{z}_c(t))$ represents the boundary of the current vector region model $R(\mathbf{z}_c(t))$.

$$\begin{aligned}
\partial R(\mathbf{z}_c(t)) &\triangleq \left\{ \mathbf{z} \in \mathbf{Z} : \sqrt{\frac{(z_n - z_{cn})^2}{a^2} + \frac{(z_e - z_{ce})^2}{b^2}} \right. \\
&= 1, |z_d - z_{cd}| \leq \frac{1}{c} \sqrt{\frac{z_{cn}^2}{a^2} + \frac{z_{ce}^2}{b^2}} \left. \right\}. \tag{5}
\end{aligned}$$

$z_{i1}z_{i2}$ and $z_{i3}z_{i4}$ are at the intersection of ellipsoid $G(\mathbf{z}_f)$ and $R(\mathbf{z}_c(t))$.

$C(\mathbf{z})$ represents the vector on the boundary $\partial R(\mathbf{z}_c(t))$, which is also located in $G(\mathbf{z}_f)$. Next, the problem of recovery path planning can be converted to find a collision-free path on $\partial R(\mathbf{z}_c(t))$, so that the distance between UUV and ellipsoid $G(\mathbf{z}_f)$ gradually reduces until UUV can reach the target vector \mathbf{z}_f .

Definition 1. If $\sqrt{((z_{cn} - z_{fn})^2/a^2) + ((z_{ce} - z_{fe})^2/b^2)} > 1$ and $|z_{cd} - z_{fd}| > 1/c \sqrt{(z_{fn}^2/a^2) + (z_{fe}^2/b^2)}$, then $\mathbf{z} \notin R(\mathbf{z}_f)$.

Definition 2. If $\sqrt{((z'_n - z'_{fn})^2/a^2) + ((z'_e - z'_{fe})^2/b^2)} \leq \sqrt{((z_{cn} - z_{fn})^2/a^2) + ((z_{ce} - z_{fe})^2/b^2)}$ and $|z'_d - z_{fd}| \leq |z_d - z_{fd}|$, then $\mathbf{z}' \in C(\mathbf{z})$.

Definition 3. Two integers ρ_r and ρ_d satisfy

$$\begin{aligned}
\rho_r &< \min(a, b), \\
\rho_d &< \frac{1}{c} \sqrt{\frac{z_{fn}^2}{a^2} + \frac{z_{fe}^2}{b^2}}. \tag{6}
\end{aligned}$$

$O(\mathbf{z})$ is a subset of $C(\mathbf{z})$.

$$\begin{aligned}
O(\mathbf{z}) &\triangleq \left\{ \sqrt{(z_{cn} - z_{fn})^2 + (z_{ce} - z_{fe})^2} \right. \\
&\quad \left. - \sqrt{(z'_n - z'_{fn})^2 + (z'_e - z'_{fe})^2} \right. \\
&\quad \left. \geq \rho_r, \mathbf{z}' \in C(\mathbf{z}) : (|z_{cd} - z_{fd}| - |z'_d - z_{fd}| \geq \rho_d) \right\}. \tag{7}
\end{aligned}$$

The distance of the vector to the target vector is less than the distance from the current point $\mathbf{z}_c(t)$ to the target vector.

2.2.2. The Basic Idea to Generate a Recovery Path. This section describes the Feedback-Dubins-RRT algorithm which produces a collision-free path from the current vector $\mathbf{z}_c(t)$ to the target model region in $O(\mathbf{z})$, such that the distance between the current vector $\mathbf{z}_c(t)$ and the target vector \mathbf{z}_f is progressively shortened.

Step 1. Initialize the set of vectors $\{\mathbf{z}\}$. Let the current vector $\mathbf{z}_c(t)$ be the only vector in the tree structure $\{\mathbf{z}\}$.

Step 2. Progressive growth of random trees:

Step 2.1. Random node vectors \mathbf{z}_{rand} are generated in set $R(\mathbf{z})O(\mathbf{z})$ and set $O(\mathbf{z})$ with a fixed probability P and $1 - P$, respectively.

Step 2.2. Find the node vector \mathbf{z}_{near} closest to the randomly generated vector \mathbf{z}_{rand} in the structure of the existing tree.

Step 2.3. Connect the node vector \mathbf{z}_{near} and the random vector \mathbf{z}_{rand} with the Dubins curve.

Step 2.4. Check whether the generated Dubins curve is collision-free and meets the kinematic constraints of UUV.

Step 2.5. If the result of Step 2.4 is collision-free, the random vector \mathbf{z}_{rand} is added to the tree structure to become the node vector of the tree and the Dubins curve path is used as the branch of the tree.

Step 3. Iteration of complete growth of random trees:

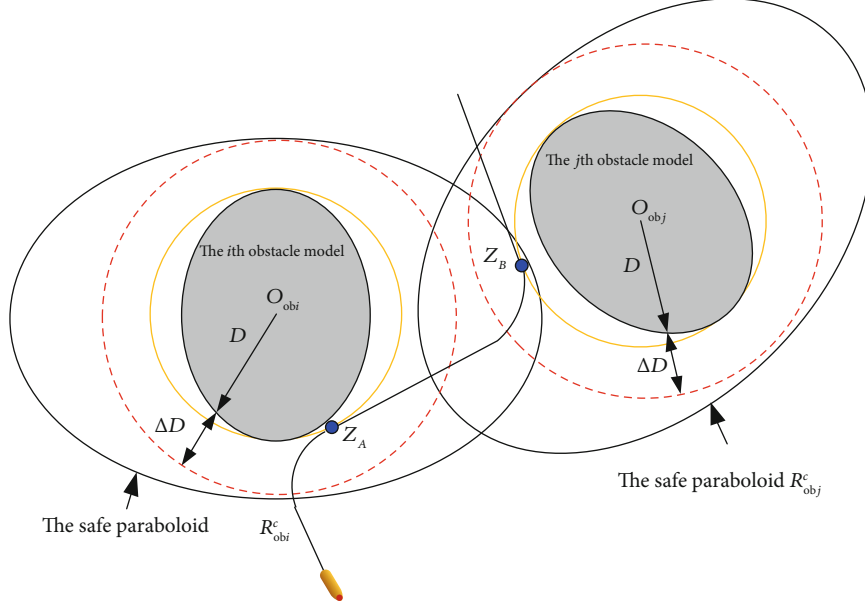


FIGURE 2: The distance between obstacles meets the traversable condition.

TABLE 1: Center point coordinates and parameters of obstacles.

Obstacle number	Coordinate (m)	a_{obi} (m)	b_{obi} (m)	c_{obi} (m)
1	(100, 200, 435)	30	40	13
2	(440, 300, 425)	50	30	15
3	(440, 740, 300)	40	30	40
4	(900, 600, 430)	40	30	14
5	(550, 550, 325)	32	40	25
6	(750, 150, 450)	20	20	10
7	(900, 900, 325)	60	50	35

Step 3.1. Check if there is a vector in $O(\mathbf{z})$ that has been connected to the structure of the tree.

Step 3.2. If the condition in Step 3.1 is met, the path from the current node vector to this vector is extracted. If the condition in Step 3.1 is not satisfied, a node vector is randomly generated and connected to the current node vector and the Dubins path between them is extracted.

Step 4. Determine whether the growth of random trees ends: the algorithm ends when the vector in $O(\mathbf{z})$ becomes the structure of the tree or the preset number of cycles is reached.

2.2.3. *Existence Condition of a Collision-Free Path.* For the environment with dense obstacles, it is needed to give the existence conditions of collision paths. Let $(R_{ob1}, R_{ob2}, \dots, R_{obn})$, $n \in N$ represent the set of all obstacles. R_{obi}, R_{obj} , $i \neq j$, $i, j \in N$ are two arbitrarily adjacent obstacles. The shortest distance from the i th obstacle to the j th obstacle is defined as

$$d_{ij} = \min_{p_i \in \partial R_{obi}, p_j \in \partial R_{obj}} \sqrt{(p_{in} - p_{jn})^2 + (p_{ie} - p_{je})^2}. \quad (8)$$

Here, $p_i = (p_{in}, p_{ie}, p_{id})$ and $p_j = (p_{jn}, p_{je}, p_{jd})$ represent any point on the boundary of the i th obstacle and the j th obstacle.

According to the aforementioned method, a threatening circle is set on the outside of each obstacle. If there is a collision-free path through a dense obstacle, the distance between two obstacles should be greater than the difference between the radius of the threatening circle and the minimum turning radius. In other words, if there is a collision-free path through obstacles in a dense-obstacle environment, no point on the threaten circle can be covered by other obstacle areas.

Definition 4. A dense-obstacle environment is traversable if and only if the distance between the i th obstacle and the j th obstacle satisfies

$$d_{ij} > \max \left\{ \left[\min(a_{obi}^c, b_{obi}^c) - \max(a_{obi}, b_{obi}) \right], \left[\min(a_{obj}^c, b_{obj}^c) - \max(a_{obj}, b_{obj}) \right] \right\}. \quad (9)$$

$a_{obi}^c, b_{obi}^c, a_{obj}^c, b_{obj}^c$ are the parameters of threatening zones R_{obi}^c and R_{obj}^c , respectively. $\min(a_{obi}^c, b_{obi}^c)$, $\min(a_{obj}^c, b_{obj}^c)$ are the radius of the threatening circle of the i th obstacle and the j th obstacle, respectively. $a_{obi}, b_{obi}, a_{obj}, b_{obj}$ are the parameters of the i th obstacle and the j th obstacle, respectively.

Theorem 5. It is assumed that obstacle-intensive environments are traversable. The current node vector is $\mathbf{z}_c(t) = [z_{cn}(t), z_{ce}(t), z_{cd}(t), z_{c\phi}(t)]$. The minimum turning radius of UAV is r_{\min} . $R_{obi} \in (R_{ob1}, R_{ob2}, \dots, R_{obn})$ represents any obstacle model, and its radius and height are a_{obi}, b_{obi} and c_{obi} , respectively. Ellipsoid R_{obi}^c is a model expanded according to the obstacle model R_{obi} , and its parameters are a_{obi}^c, b_{obi}^c and c_{obi}^c and

TABLE 2: Distance between different obstacles.

Spacing (m)	Obstacle 1	Obstacle 2	Obstacle 3	Obstacle 4	Obstacle 5	Obstacle 6	Obstacle 7
Obstacle 1	*	308.06	559.25	Not adjacent	521.21	Not adjacent	Not adjacent
Obstacle 2	308.06	*	Not adjacent	450.08	241.05 Not passable	315.49	Not adjacent
Obstacle 3	559.25	Not adjacent	*	Not adjacent	171.26 Not passable	Not adjacent	427.20
Obstacle 4	Not adjacent	450.08	Not adjacent	*	314.36	441.61	264.71
Obstacle 5	521.21	241.05 Not passable	171.26 Not passable	314.36	*	402.52	430.63
Obstacle 6	Not adjacent	315.49	Not adjacent	441.61	402.52	*	Not adjacent
Obstacle 7	Not adjacent	Not adjacent	427.20	264.71	430.63	Not adjacent	*

satisfied $\min(a_{obi}^c, b_{obi}^c) = \sqrt{[\max(a_{obi}, b_{obi}) + r_{\min}]^2 - r_{\min}^2}$ and $c_{obi}^c = c_{obi}$. If the current node vector $\mathbf{z}_c(t)$ is not included in ellipsoid R_{obi}^c , then a collision-free path can be found by the Feedback-Dubins-RRT algorithm.

Proof. As shown in Figure 2, the obstacle circle is generated with the radius of $D = \max(a_{obi}, b_{obi})$ and a threatening circle is set to the radius of $D + \Delta D$, where $D + \Delta D = \min(a_{obi}^c, b_{obi}^c)$. This radius is the minimum distance between UUV and obstacles when UUV navigates with the maximum rotation angle and maximum navigation angle. Z' is the tangent point between the circle generated with the minimum turning radius and the obstacle circle. By projecting their geometric positions in the x - y plane, the geometric relationship is expressed as follows:

$$\begin{aligned} (D + \Delta D + r_{\min} \sin \alpha_i)^2 + (r_{\min} \cos \alpha_i)^2 &= (D + r_{\min})^2, \\ (D + r_{\min} \sin \alpha_i)^2 + \Delta D^2 + 2\Delta D(D + r_{\min} \sin \alpha_i) \\ + (r_{\min} \cos \alpha_i)^2 &= D^2 + r_{\min}^2 + 2Dr_{\min}. \end{aligned} \quad (10)$$

Merge and get the following form:

$$\begin{aligned} D^2 + 2\Delta D(D + r_{\min} \sin \alpha_i) + 2Dr_{\min} \sin \alpha_i - 2Dr_{\min} &= 0, \\ \Delta &= 4(D + r_{\min} \sin \alpha_i)^2 - 4 \times 2Dr_{\min}(\sin \alpha_i - 1) \\ &= 4[D^2 + (r_{\min} \sin \alpha_i)^2 + 2Dr_{\min} \sin \alpha_i - 2Dr_{\min}(\sin \alpha_i - 1)] \\ &= 4[D^2 + (r_{\min} \sin \alpha_i)^2 + 2Dr_{\min}], \\ \Delta D &= \frac{-2(D + r_{\min} \sin \alpha_i) \pm \sqrt{4[D^2 + (r_{\min} \sin \alpha_i)^2 + 2Dr_{\min}]}}{2} \\ &= -(D + r_{\min} \sin \alpha_i) \pm \sqrt{D^2 + (r_{\min} \sin \alpha_i)^2 + 2Dr_{\min}}. \end{aligned} \quad (11)$$

ΔD is positive, so there is

$$\Delta D = -(D + r_{\min} \sin \alpha_i) + \sqrt{D^2 + (r_{\min} \sin \alpha_i)^2 + 2Dr_{\min}}. \quad (12)$$

When $\alpha_i = 0$,

$$\Delta D_{\max} = -D + \sqrt{(D + r_{\min})^2 - r_{\min}^2}, \quad (13)$$

$$D + \Delta D_{\max} = \sqrt{(D + r_{\min})^2 - r_{\min}^2}.$$

Therefore, if the current vector is not contained by the ellipsoid R_{obi}^c , UUV is navigating with the direction angle $\pi/2$ or $-\pi/2$ and the collision-free path can be obtained by the planning algorithm.

If the current vector $\mathbf{z}_c(t)$ is not included in the ellipsoid R_{obi}^c , then there is an arbitrary node vector \mathbf{Z}_A that approaches the boundary of the obstacle R_{obi} with the direction angle $\pi/2$ or $-\pi/2$ and makes the path of the current node vector $\mathbf{z}_c(t)$ to the vector \mathbf{Z}_A collision-free.

In addition, the obstacle environment is assumed to be traversable, indicating that \mathbf{Z}_A must be outside the ellipsoid R_{obj}^c . In other words, the next node vector \mathbf{Z}_B can also be found to approach the boundary of the obstacle R_{obj} with direction angle $\pi/2$ or $-\pi/2$ and make \mathbf{Z}_A to \mathbf{Z}_B a collision-free path. This process is repeated multiple times until a collision-free path from the current vector to the target vector is obtained.

2.3. Feedback-Dubins-RRT Path Pruning. Although it is efficient and feasible to use the proposed algorithm for path planning, the results of the algorithm are still not optimal due to the random growth of spatial trees. In order to reduce unnecessary navigation and rotation of UUV, some unnecessary path node vectors need to be deleted. In this paper, a simple and effective method is used to remove the unnecessary path node vectors so that the recovery path can be quickly generated. The generated Feedback-Dubins-RRT vector set is trimmed as follows:

Step 1. All vectors from the start vector to the target vector generated by the foregoing method are placed into the set $(\mathbf{z}_1, \dots, \mathbf{z}_N)$, where \mathbf{z}_1 represents the starting vector and \mathbf{z}_N represents the target vector.

Step 2. Let the set of node vectors of the recovery path be an empty set. Then, let $j = N$ and add vector \mathbf{z}_j to the trimmed set of recovery path vectors.

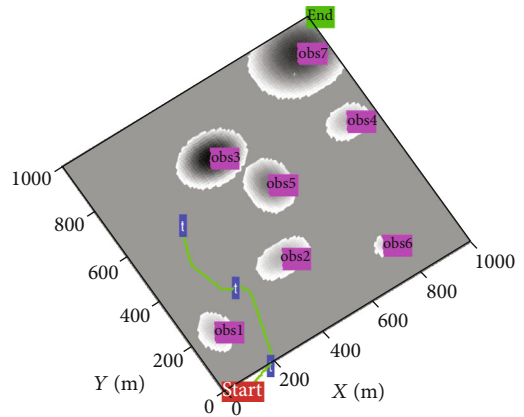
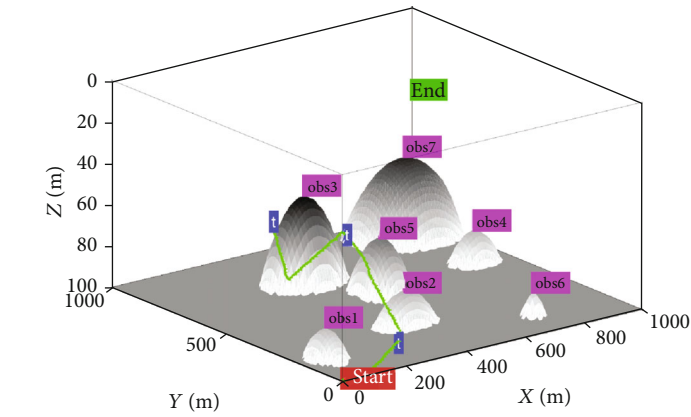
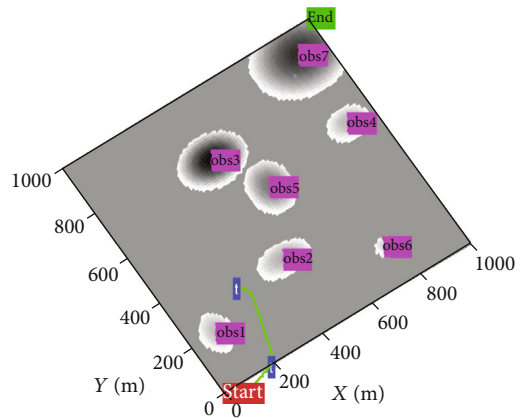
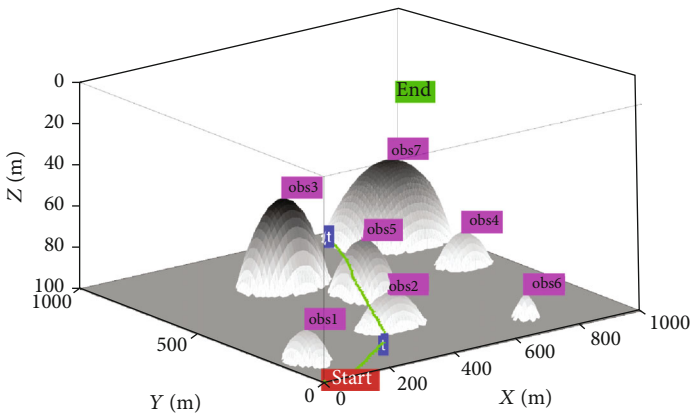
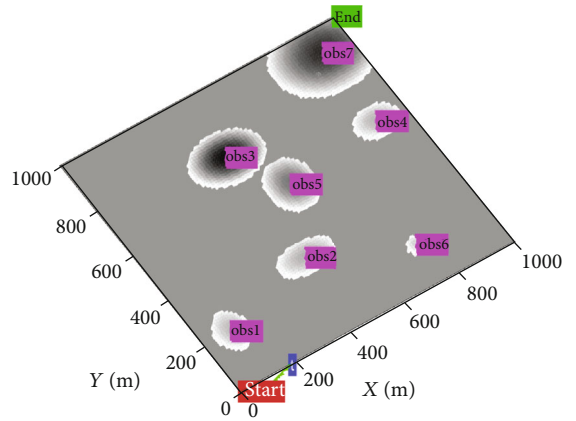
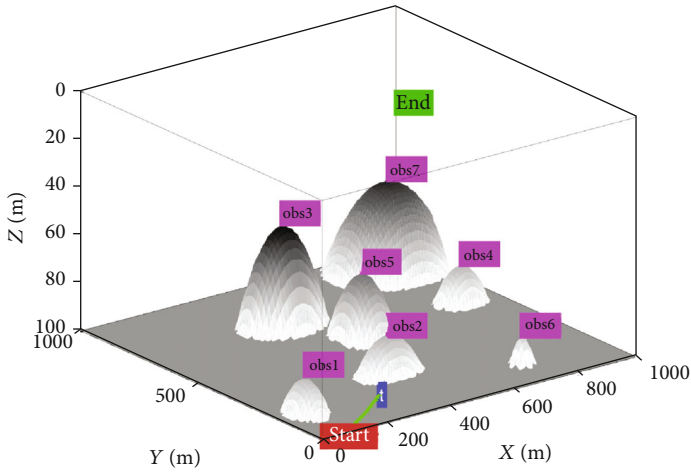


FIGURE 3: Continued.

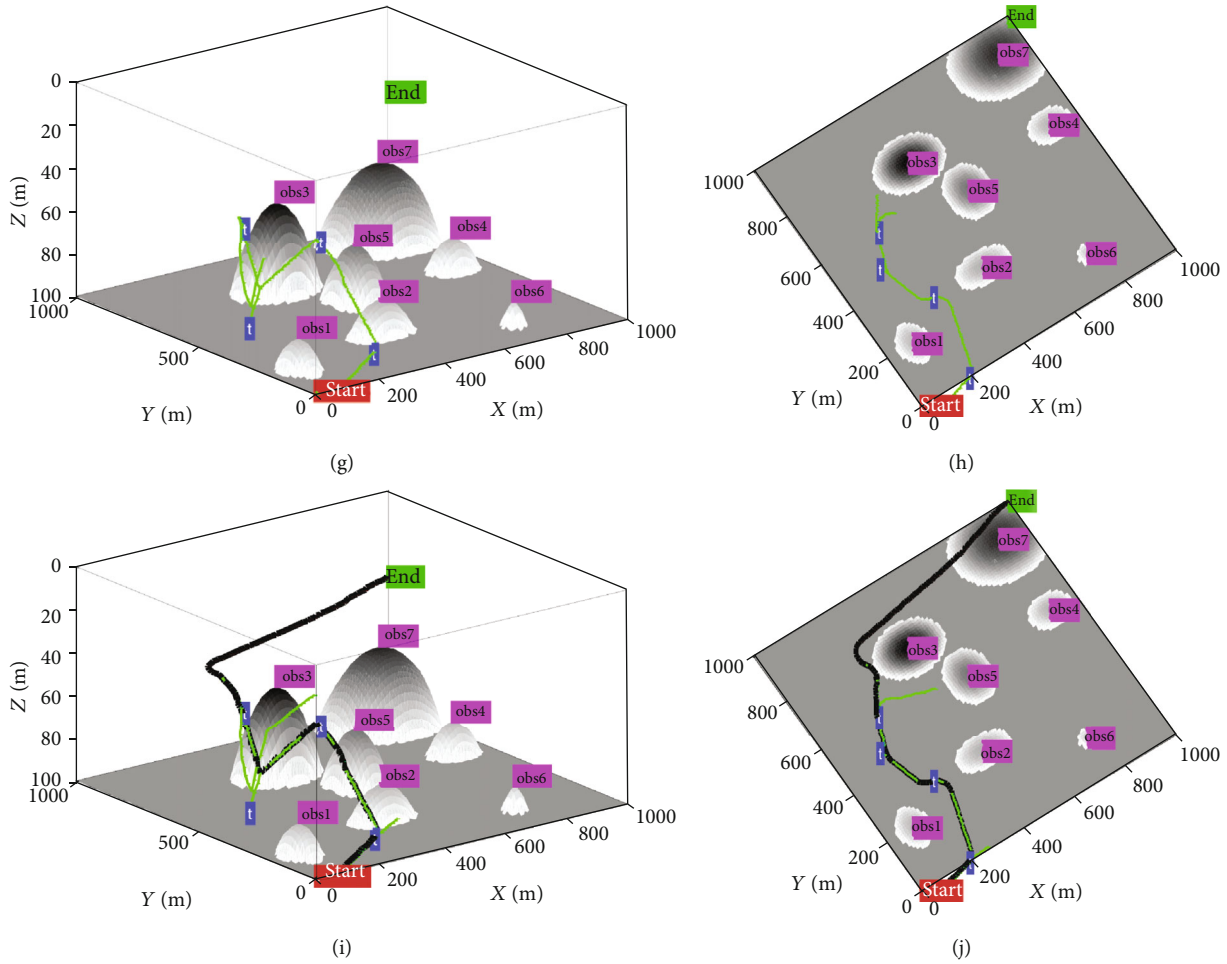


FIGURE 3: The recovery path generated by the Feedback-Dubins-RRT algorithm: (a) three-dimensional graph of the second node generated, (b) top view of the second node generated, (c) three-dimensional graph of the fourth node generated, (d) top view of the fourth node generated, (e) three-dimensional graph of the sixth node generated, (f) top view of the sixth node generated, (g) three-dimensional graph of the eighth node generated, (h) top view of the eighth node generated, (i) three-dimensional graph of all the nodes generated, and (j) top view of all the nodes generated.

Step 3. Check whether there is a collision-free Dubins path between the node vector \mathbf{z}_i and other node vectors in the order of the foot labels, $i \in [1, \dots, j-1]$.

Step 4. When a node vector is found and the Dubins path between it and other node vectors is collision-free, let $j = i$ and add vector \mathbf{z}_i to the set of trimmed path points. Repeat this process until a complete collision-free path is generated from the starting vector to the target vector.

By trimming the path node vector generated by the Feedback-Dubins-RRT algorithm, some unnecessary path node vectors are deleted, so that the original path can be optimized.

3. Simulation

In this section, a set of cases will be given to verify the effectiveness of the proposed recovery path planning algorithm.

In the three-dimensional geodetic coordinate system, the range of length, width, and height of a space is 1000 m,

1000 m, and 100 m. The initial point position is set at (0, 0, 98), and the target point position is set at (1000, 1000, 40). In order to prove the generality of the algorithm, the heading angle and pitch angle of UAV at the initial position and the target position are randomly generated. Suppose that there are seven intensive obstacles in the environment. The coordinates of the center point and its parameters of the obstacles are shown in Table 1. The distance between adjacent obstacles is shown in Table 2, in which the second and fifth obstacles, as well as the third and fifth obstacles, do not satisfy the conditions adopted in Theorem 5. The program has been running many times, and the results of the two versions are given in Figures 3 and 4. The radius of the Dubins path depends on the scope of the area. $r_{\min} = 0.05 * dx$, where dx is the maximum value of the length, width, and height of the area.

In Figure 3, the growth of the random tree and the process of obtaining the final path can be seen in detail at dynamically intercepting the output of the second, fourth, sixth, and eighth path nodes generated.

Figure 4 shows the result of the rerun of the same initial conditions as Figure 3. It can be seen from Figure 4 that the

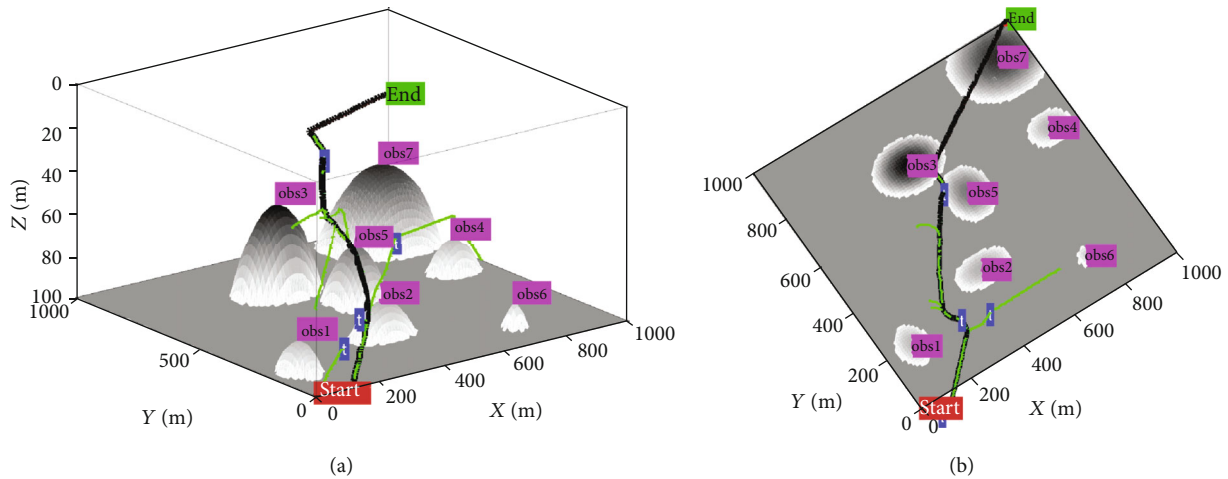


FIGURE 4: The second recovery path generated by the Feedback-Dubins-RRT algorithm: (a) three-dimensional graph of all the nodes generated and (b) top view of all the nodes generated.

path passes through two obstacles ob1 and ob2 which are determined to be inaccessible in Theorem 5, and the path does not intersect the obstacle. The path satisfies the constraints and reaches the target point. The length of the path is 1933 m. Thus, it can be seen that Theorem 5 gives a sufficient condition to ensure traversability rather than a necessary condition.

4. Conclusion

In this paper, the planning method of a spatial path is given for the known recovery starting point vector and target point vector in a 3D environment. For the obstacle-intensive environment, a method which constructs a local structure map between the obstacle and the target vector based on the distance and orientation information is proposed. The three-dimensional Dubins planning path is generated by Feedback-Dubins-RRT according to the local structure map, and the obstacle can be avoided infinitely and reach the target area. The simulation results show that the proposed algorithm can solve the problem of path planning and obstacle avoidance in a three-dimensional environment.

The Feedback-Dubins-RRT recovery path planning algorithm still needs to be improved in the following two aspects. (1) In a three-dimensional environment, when the environment is unknown or there are dynamic obstacles, the path planning algorithm in this paper needs to be improved to add a dynamic obstacle avoidance strategy to generate a real-time planned path. (2) The path generated by Feedback-Dubins-RRT can only be asymptotically optimal, and the algorithm idea needs to be improved to generate the optimal path under the current initial conditions.

Data Availability

The data used to support the findings of this study are available from the corresponding author upon request.

Conflicts of Interest

The authors declare that there is no conflict of interests regarding the publication of this paper.

Acknowledgments

This work is partially supported by the Basic Scientific Research Business Cost Scientific Research Project of Heilongjiang Provincial University (135209236 and 135309453) and the Joint Guiding Project of Natural Science Foundation of Heilongjiang Province under Grant LH2019F038.

References

- [1] M. D. Feezor, F. Yates Sorrell, P. R. Blankinship, and J. G. Bellingham, "Autonomous underwater vehicle homing/docking via electromagnetic guidance," *IEEE Journal of Oceanic Engineering*, vol. 26, no. 4, pp. 515–521, 2001.
- [2] J.-Y. Park, B.-H. Jun, P.-M. Lee, Y.-K. Lim, and J.-H. Oh, "Modified linear terminal guidance for docking and a time-varying ocean current observer," in *2011 IEEE Symposium on Underwater Technology and Workshop on Scientific Use of Submarine Cables and Related Technologies*, pp. 1–6, Tokyo, Japan, April 2011.
- [3] D. Ferguson and A. Stentz, "Using interpolation to improve path planning: the field D* algorithm," *Journal of Field Robotics*, vol. 23, no. 2, pp. 79–101, 2006.
- [4] L. E. Kavraki, P. Svestka, J. C. Latombe, and M. H. Overmars, "Probabilistic roadmaps for path planning in high-dimensional configuration spaces," *IEEE Transactions on Robotics and Automation*, vol. 12, no. 4, pp. 566–580, 1996.
- [5] S. G. Faal and C. D. Onal, "Regionally growing random trees: a synergistic motion planning and control algorithm for dynamic systems," in *Proceedings of 2016 IEEE International Conference on Automation Science and Engineering*, pp. 141–147, Fort Worth, USA, 2016.
- [6] E. Frazzoli, M. A. Dahleh, and E. Feron, "Real-time motion planning for agile autonomous vehicles," *Journal of Guidance, Control, and Dynamics*, vol. 25, no. 1, pp. 116–129, 2002.

- [7] S. Griffiths, J. Saunders, A. Curtis, B. Barber, T. McLain, and R. Beard, "Maximizing miniature aerial vehicles," *IEEE Robotics and Automation Magazine*, vol. 13, no. 3, pp. 34–43, 2006.
- [8] W. Aguilar and S. Morales, "3D environment mapping using the Kinect V2 and path planning based on RRT algorithms," *Electronics*, vol. 5, no. 4, p. 70, 2016.
- [9] D. Connell and H. M. La, "Dynamic path planning and replanning for mobile robots using RRT," in *2017 IEEE International Conference on Systems, Man, and Cybernetics (SMC)*, pp. 1429–1434, Banff, AB, Canada, October 2017.
- [10] Y. Wang, P. Pandit, A. Kandhari, Z. Liu, and K. A. Daltorio, "Rapidly exploring random tree algorithm-based path planning for worm-like robot," *Biomimetics*, vol. 5, no. 2, p. 26, 2020.
- [11] A. Pandey, V. S. Panwar, M. E. Hasan, and D. R. Parhi, "V-REP-based navigation of automated wheeled robot between obstacles using PSO-tuned feedforward neural network," *Journal of Computational Design and Engineering*, vol. 7, 2020.
- [12] A. Pandey, A. K. Kashyap, D. R. Parhi, and B. K. Patle, "Autonomous mobile robot navigation between static and dynamic obstacles using multiple ANFIS architecture," *World Journal of Engineering*, vol. 16, no. 2, pp. 275–286, 2019.
- [13] L. Singh and J. Fuller, "Trajectory generation for a UAV in urban terrain, using nonlinear MPC," in *Proceedings of the 2001 American Control Conference. (Cat. No.01CH37148)*, pp. 2301–2308, Arlington, VA, June 2001.
- [14] D. H. Shim, Hoam Chung, and S. S. Sastry, "Conflict-free navigation in unknown urban environments," *IEEE Robotics and Automation Magazine*, vol. 13, no. 3, pp. 27–33, 2006.
- [15] L. E. Dubins, "On curves of minimal length with a constraint on average curvature with prescribed initial and terminal positions and tangents," *American Journal of Mathematics*, vol. 79, no. 3, pp. 497–516, 1957.
- [16] H. Yu and R. Beard, "A vision-based collision avoidance technique for micro air vehicles using local-level frame mapping and path planning," *Autonomous Robots*, vol. 34, no. 1-2, pp. 93–109, 2013.

Research Article

Research on an Improved Metal Surface Defect Detection Sensor Based on a 3D RFID Tag Antenna

Qiang Li , Jianbin Chen , and Liang Zhao

School of Information Engineering, Southwest University of Science and Technology, Mianyang, Sichuan 621010, China

Correspondence should be addressed to Qiang Li; liqiangsir@swust.edu.cn

Received 9 March 2020; Revised 9 May 2020; Accepted 15 May 2020; Published 8 July 2020

Academic Editor: Bin Gao

Copyright © 2020 Qiang Li et al. This is an open access article distributed under the Creative Commons Attribution License, which permits unrestricted use, distribution, and reproduction in any medium, provided the original work is properly cited.

Structural health monitoring (SHM) technology is a monitoring process and early warning method for the health status or damage of special workpiece structures by deploying sensors. In recent years, there have been many studies on SHM, such as ultrasonic, pulsed eddy current, optical fiber, magnetic powder, and other nondestructive testing technologies. Due to their sensor deployment, testing environment, power supply, and transmission line wiring mechanism, they bring problems such as detection efficiency, long-term monitoring, and unreliable systems. The combination of wireless sensing technology and intelligent detection technology is used to solve the above problems. Therefore, this paper studies the tag antenna smart sensor, which is used to characterize the extension of metal defects in SHM. Then, it presents a wireless passive three-dimensional sensing antenna, and simulations verify the feasibility of the antenna. The simulation results show that the antenna can characterize the two extension directions of depth and width of the metal surface structure smooth defect. At the same time, the antenna can characterize the position of smooth defects on the surface of metal structures relative to the antenna and then realize the smooth defect positioning.

1. Introduction

It is necessary that civil infrastructure applications must possess the necessary reliability and safety [1]. The development of civil building structure indicates that metal will be increasingly invested in infrastructure such as large buildings, bridges, and landmark buildings. The important load-bearing parts in this kind of engineering structure show structural fatigue caused by periodic load pressure and structural corrosion caused by harsh environments, especially those in long-term service and exposed environments. Those will lead to serious accidents. Hence, SHM technology monitors the components' degree of structural damage regularly. The aim is to achieve an effective online assessment of structural healthy life. It has become an extremely important safety prediction measure for catastrophic failures caused by failure of important components. Among many structural defects, the initial defect expansion mode is mainly transverse expansion in all strain paths [2]. The most dangerous defect is the transverse defect of structure [3], which will cause the bearing capacity of the structural frame to decrease rapidly. As a

result, the structural frame will be easily broken during usage. Thus, it is particularly important to detect the transverse defect of the component structure. Structural defect monitoring is used to intuitively characterize structural damage. This is used as an essential indicator for structural health and service life assessment.

SHM is achieved by nondestructive testing methods without damaging the components being inspected, in industry, such as common visual inspection [4], ultrasonic inspection [5], eddy current inspection [6], and fiber optic inspection [7]. Visual inspection is a method by which a person periodically detects the degree of structural damage using auxiliary equipment [8], which has high labor costs, low detection efficiency, and environmental constraints. On the other hand, due to the low resolution of the artificial naked eye for microscopic changes in defects, this is prone to misjudgment and omission. Compared with visual inspection, ultrasonic detection, eddy current detection, and fiber detection technology have higher sensitivity and resolution. The test results are more reliability. However, these three types of tests also require manual inspection. Besides, the three

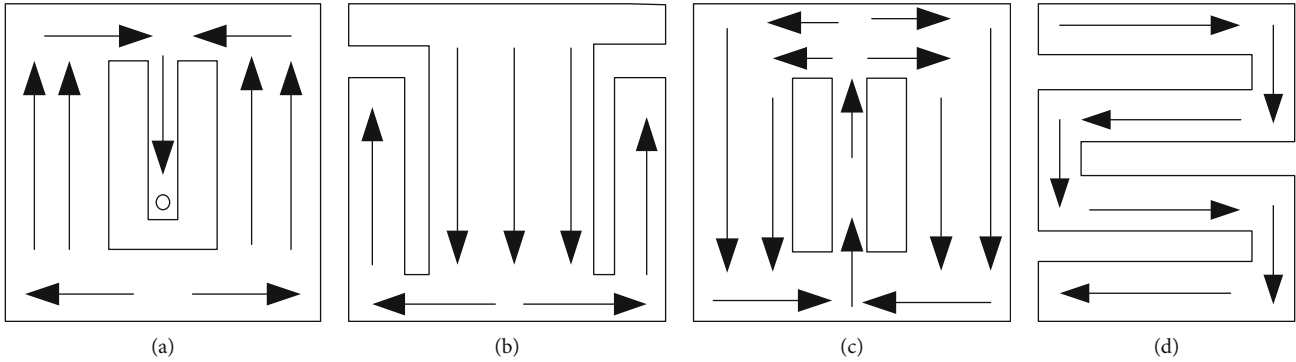


FIGURE 1: Schematic diagram of the meandering slot for the microstrip patch antenna. (a) U-slot current path. (b) L-slot current path. (c) H-slot current path. (d) Rectangular slotted current path.

methods are not only complicated in the detection process but also limited by large-scale structural inspection and large-area monitoring. In distributed detection systems, large-scale wiring is required to provide then power and signal transmission lines for sensors in the system. With the expansion of the detection range and increase in the number of sensor deployments, large-scale power lines and signal transmission lines need to be installed. If the system is worked for a long time, there will be many problems on the cables. Accordingly, more manpower and material resources will be invested in the inspection and maintenance system [9].

Wireless sensor networks can solve the wiring problems and reduce the cost investment of traditional embedded sensor detection systems [10]. Although there are many research studies on reducing wireless sensor networks' energy consumption [11], it is still unavoidable to use batteries with limited energy to power sensors. Furthermore, replacing a large number of batteries requires more workers and time. Investment of battery will also limit the sensor deployment granularity [12], and it will not meet the energy conservation and environmental protection measures [13]. Introducing the sensing capability into the radio frequency identification (RFID) system [14] and combining it with the Internet of Things technology [15], a wireless passive sensor detection system can be realized. So far, there have been many research studies on RFID sensor tag antennas, such as temperature detection [16], humidity detection [17], gas detection [18] in the environmental field, wireless displacement detection [19], and level detection in the field of industrial detection [20]. Based on the RFID sensor system, this paper studies and simulates a kind of tag antenna sensor, which can characterize extended information of metal defects.

2. Literature Review

Nondestructive testing based on RFID sensing technology, in the field of SHM, mainly focused on researching tag antennas for strain and defect sensing of test pieces. For strain antenna sensors, Kobayashi et al. manufactured an ultrathin piezoelectric strain sensor, which used a 5×5 array of monitors to make a reliable test for large equipment through different working voltages on the defective part, but this is an active

RFID sensor network [21]. Daliri et al. carried out research on wireless passive strain measurement applications using circular microstrip patch antenna (CMPA) sensors, proposed a CMPA operation at 1.5 GHz, and studied different materials for tag antennas [22]. Using high-quality dielectric materials as the tag antenna substrate can measure strain at a distance of 20 cm from the reader, while the strain at 5 cm can only be measured with RF4 dielectric materials [23].

For a defect sensing antenna, Shishir et al. designed a chipless passive structural health monitoring sensor based on a frequency selective surface array and a wireless microwave metamaterial sensor with a flexible substrate, whose electromagnetic characteristics are related to the antenna geometry; the antenna can detect the damage location [24]. Caizzone and Giampaolo studied and designed a pair of passive PIFA tag sensing antennas and placed two PIFA tags on each side of the defect, which can detect the width of the concrete structure defect [25]. Zhang and Tian proposed a specific three-dimensional antenna sensor for the detection and characterization of early metal corrosion; its size was $20 \text{ mm} \times 20 \text{ mm} \times 16 \text{ mm}$, which inherits pulsed eddy current nondestructive testing advantages and provides a distributed monitoring cost-effective method [26]. Martinez-Castro et al. detected longer defect changes by using the composite sensor array [27]. Marindra et al. proposed a chipless RFID sensor tag, which integrates 4 end-loaded dipole resonators as a 4-bit ID encoder and a circular microstrip patch antenna resonator, and its size was $60 \text{ mm} \times 60 \text{ mm} \times 2 \text{ mm}$. Sub-millimeter-level defects can be detected through experiments on natural fatigue defects [28]. Subsequently, a sensor tag with a size of $35 \text{ mm} \times 35 \text{ mm}$ was raised. It was composed of cross-dipole patches and L-shaped patches with different lengths [29]. And then, they used the principal component analysis (PCA) method to detect metal surface cracks, corrosion, and other defects. Padmavathy and others studied microstrip patch antennas with the circular and rectangular slots. By using the 3D electromagnetic simulation software, the simulation results show that the antenna can detect the direction information of defects [30]. Xue et al. used the Rogers RT/duriod 5880 material as the substrate and dielectric board material to build a two-vertical capacitive microstrip line defect sensor antenna $45.4 \text{ mm} \times 39 \text{ mm} \times 0.5 \text{ mm}$, which can detect defect widths within one hundredth of a millimeter, while affected by

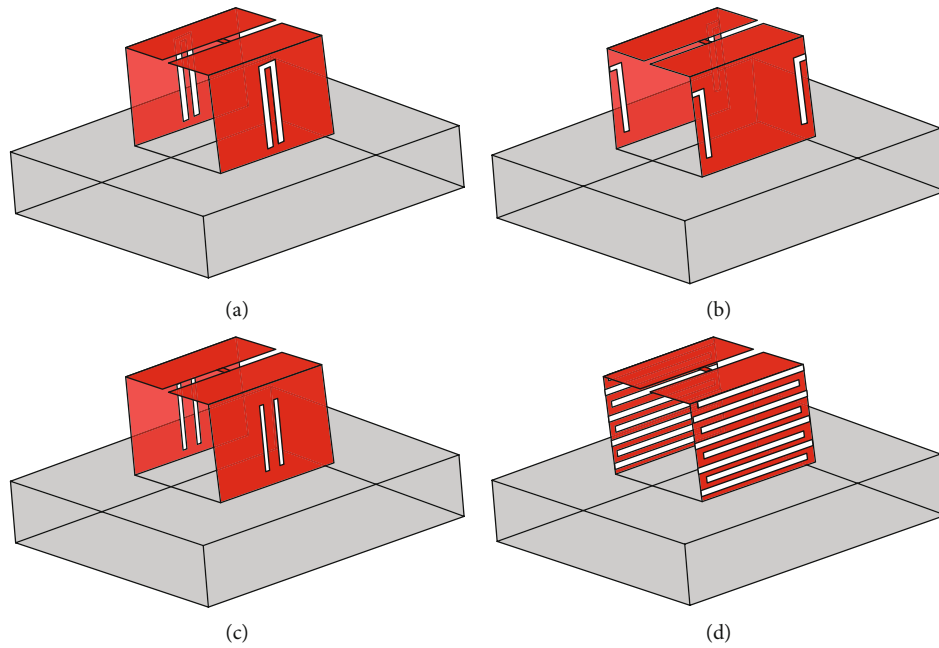


FIGURE 2: Bending dipole antenna with increased substrate thickness (slotted). (a) U-shaped slotted model. (b) L-shaped slotted model. (c) H-shaped slotted model. (d) Rectangular slotted model.

the environmental and manufacturing errors; the sensitivity coefficient obtained by the test is very different from the numerical simulation value [31].

The above research includes the use of special materials for tag antenna substrates and the use of array antennas to detect the metal or nonmetal defects. The important problem is that the above research can only detect the defect expansion in a single direction.

3. Influence of the Metal Surface on a UHF RFID Dipole Tag Antenna

3.1. Influence of the Metal Surface on Incident Electromagnetic Waves. From the perspective of energy collection, according to the principle of electromagnetic induction, when the antenna is close to the metal surface, the electromagnetic waves emitted by the reader will “distort” near the metal surface, resulting in a large tangential component and a small normal component [32]. Therefore, the antenna cannot obtain working energy by cutting a magnetic induction line to generate an induced current, which causes the passive antenna to fail to work normally. Meanwhile, parasitic capacitance will be generated inside the metal, causing electromagnetic friction, energy loss, and detuning of the antenna and reader; overall, system performance will decline [26].

From the perspective of communication capability, the antenna generates eddy current inside the whole. When the antenna is close to the metal surface, it will absorb the electromagnetic wave energy and convert it into its own electric field energy, which causes electromagnetic wave energy to decrease sharply. Finally, a part of the energy lost is in the form of heat [33]. An induced magnetic field will be produced by eddy current, and its lines will be perpendicular

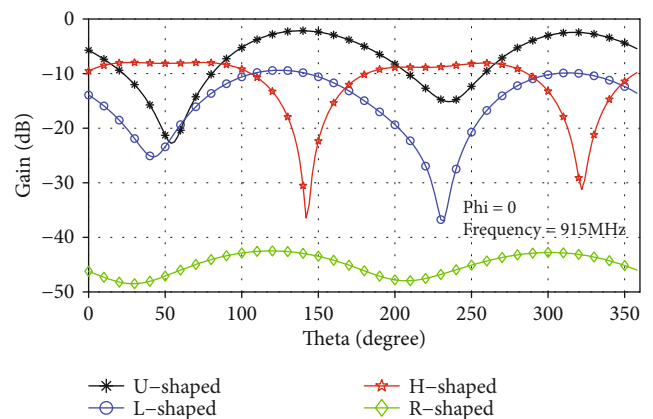


FIGURE 3: Two-dimensional gain graph with different slotting methods.

to the metal surface and opposite to the direction of electromagnetic waves, which will cause the magnetic field strength to be greatly attenuated near the metal surface [32], and the communication ability between the reader and the antenna will be hindered.

3.2. Influence of the Metal Surface on Performance Parameters of a Tag Antenna. Metal has a large impact on antenna impedance. Due to the radiation of metal boundary conditions, antenna reactance is reduced. Absorbing materials can be used to overcome this problem. A capacitance is also formed between the metal surface and the antenna, which will affect capacitive reactance of the antenna itself, and even worse, this influence cannot be eliminated. The field strength is close to zero near the metal surface, and the radiation efficiency of the antenna is seriously attenuated. Only

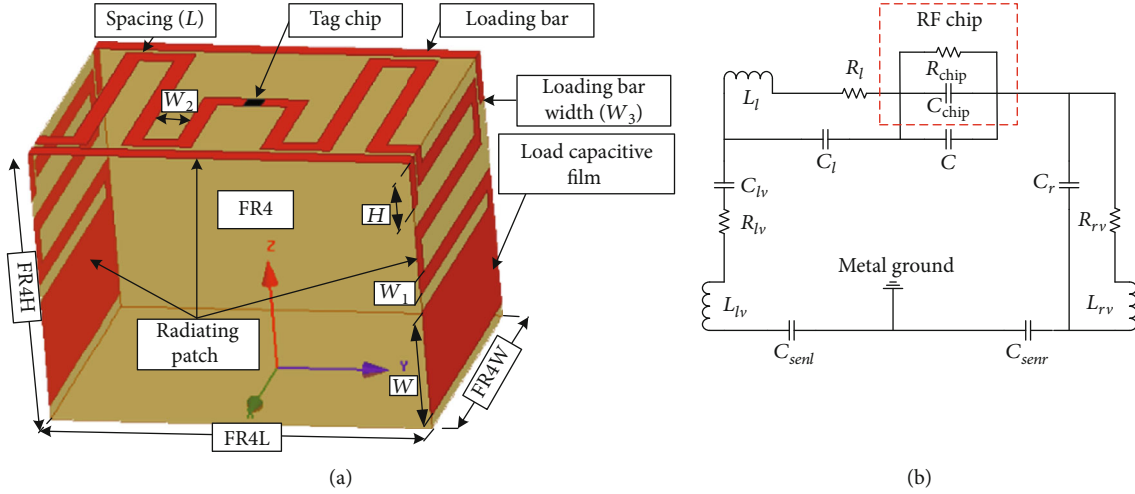
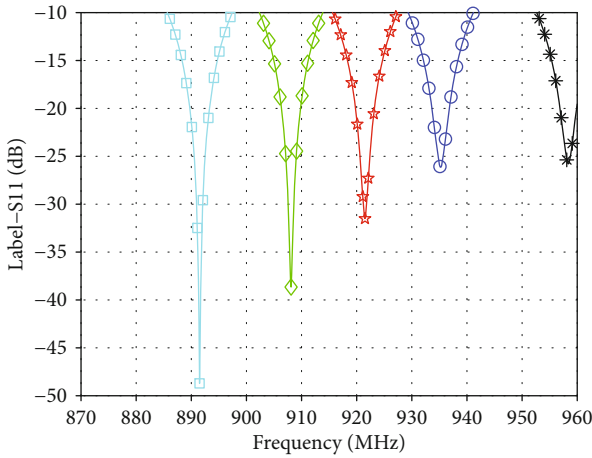


FIGURE 4: 3D patch bending dipole antenna model and equivalent circuit diagram. (a) 3D patch bending dipole antenna model. (b) Equivalent circuit diagram of the 3D patch bending dipole antenna.



- * FR4H = 15mm
- ◇ FR4H = 18mm
- FR4H = 16mm
- FR4H = 19mm
- ★ FR4H = 17mm

FIGURE 5: Simulation and verification of tag structure parameters.

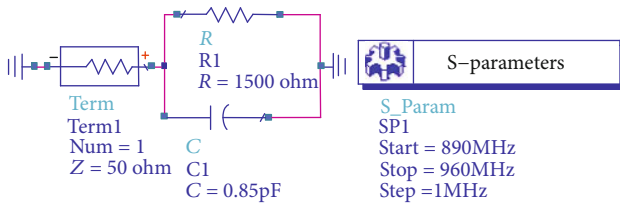


FIGURE 6: Chip equivalent circuit diagram.

when the antenna is 0.25λ away from the metal surface [27] will it obtain the largest energy.

4. Modeling and Analysis of a 3D Bent Patch Dipole Antenna

In response to the problems discussed in Section 3, since the magnetic induction lines near the metal plane only have tan-

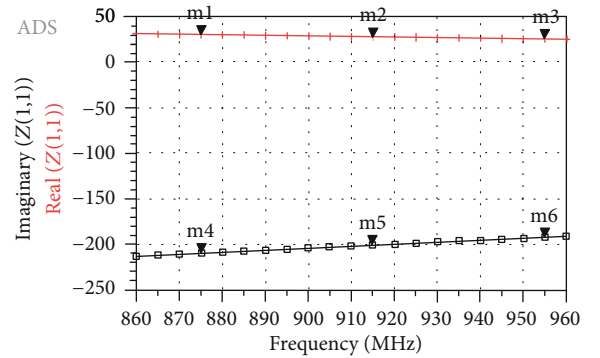


FIGURE 7: Impedance change of the chip at different operating frequencies.

TABLE 1: Chip impedance at three operating frequencies.

m1 (875 MHz)	m2 (915 MHz)	m3 (955 MHz)
$Z_1 = 29.9 - j209.7$	$Z_2 = 27.4 - j200.9$	$Z_3 = 25.2 - j192.8$

gent vectors and the normal vector component is close to zero, the planar label antenna cuts the magnetic field lines to obtain low energy. Considering that antenna radiation efficiency is directly proportional to the electrical size of the antenna, the available space is used as much as possible [34]. Suppose that the label antenna is designed by increasing the thickness of the label dielectric substrate. The antenna can be properly away from the device metal surface under test, and it can be bent on the side of the substrate. By doing so, the magnetic field lines can be cut by the antenna arm on the side to obtain the driving energy, and also, the size of the tag can be reduced. According to the radiation principle of the rectangular microstrip patch antenna, it can be known that the path length of the excitation current is inversely proportional to the resonant frequency of the entire tag antenna by using two gaps at the two open ends for radiation. Consequently, the patch antenna uses a slot method to make the current on the antenna surface tortuously flow so as to

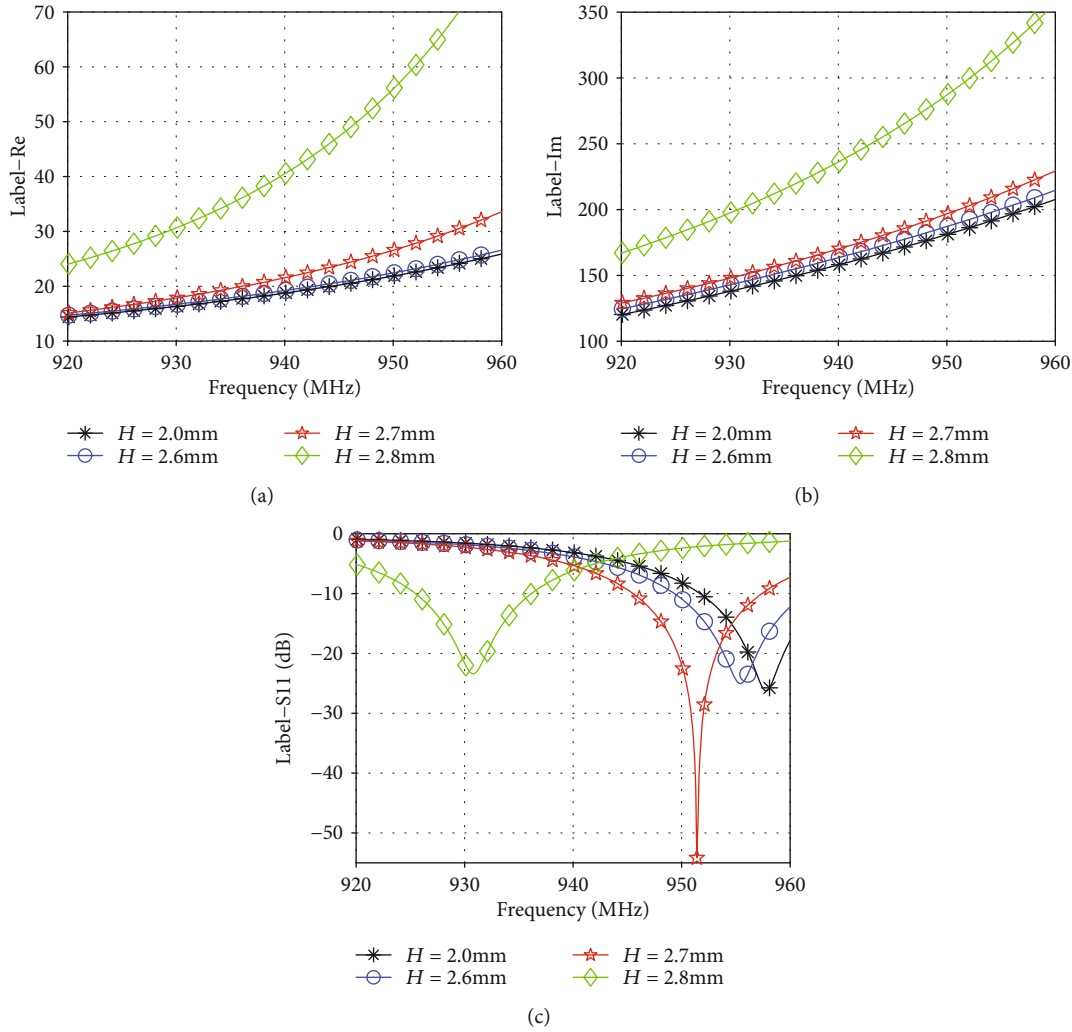


FIGURE 8: Effect of vertical depth H of the loading horizontal strip on the antenna impedance and resonance frequency. (a) Antenna impedance real part. (b) Antenna impedance imaginary part. (c) Antenna resonance frequency.

increase the effective path of the current. At the same operating frequency, antenna size can be reduced to achieve miniaturization. There are many ways with slotting, such as U-shaped groove, L-shaped groove, H-shaped groove, and rectangular groove. The slotted current paths are shown in Figure 1.

As shown in Figure 2, while increasing the thickness of the tag antenna base, the end of the tag antenna is bent to the base side and different slotting techniques are used under the same model. The two-dimensional gain curves with different slotting methods are shown in Figure 3. Through rectangular slotting, the antenna gain is higher in most of the directions, and the omnidirectionality is better in the xoz plane ($\phi = 0$).

The tag antenna is used for characterizing metal structure defects. The base material of this research object is the FR4 epoxy board with high heat resistance and moisture resistance. Its dielectric constant is 4.4, and its loss tangent angle is 0.02. In order to adjust antenna impedance to match tag chip impedance, horizontal bars are provided on both sides of the antenna, and capacitor pieces are provided at antenna

ends, and then, the rectangular slot method is used to establish the antenna model. Finally, a three-dimensional model of a curved dipole tag antenna is proposed. The antenna structure model and parameters are shown in Figure 4(a). Figure 4(b) shows the equivalent circuit model of the tag model on the metal surface, where C represents the capacitance formed at the near end of the feed, and C_1 , R_1 , and L_1 represent the capacitance, resistance, and inductance of antenna structure on the upper left, respectively. R_{1v} and L_{1v} represent the resistance and inductance of the antenna structure on the left side of the tag. C_{1v} indicates the capacitance between the upper structures of the left antenna structure domain. The left side of the antenna is separated from the top and right sides only for impedance adjustment. C_r , R_{rv} , and L_{rv} indicate the capacitance, resistance, and inductance of the upper right and right structures of the tag, respectively. C_{senl} and C_{senr} indicate the capacitance formed between the metal ground and the tag. The changes in the metal ground will affect C_{senl} and C_{senr} , which will affect antenna impedance changes, which indirectly cause the impedance mismatch between the antenna and the tag chip. Then, the

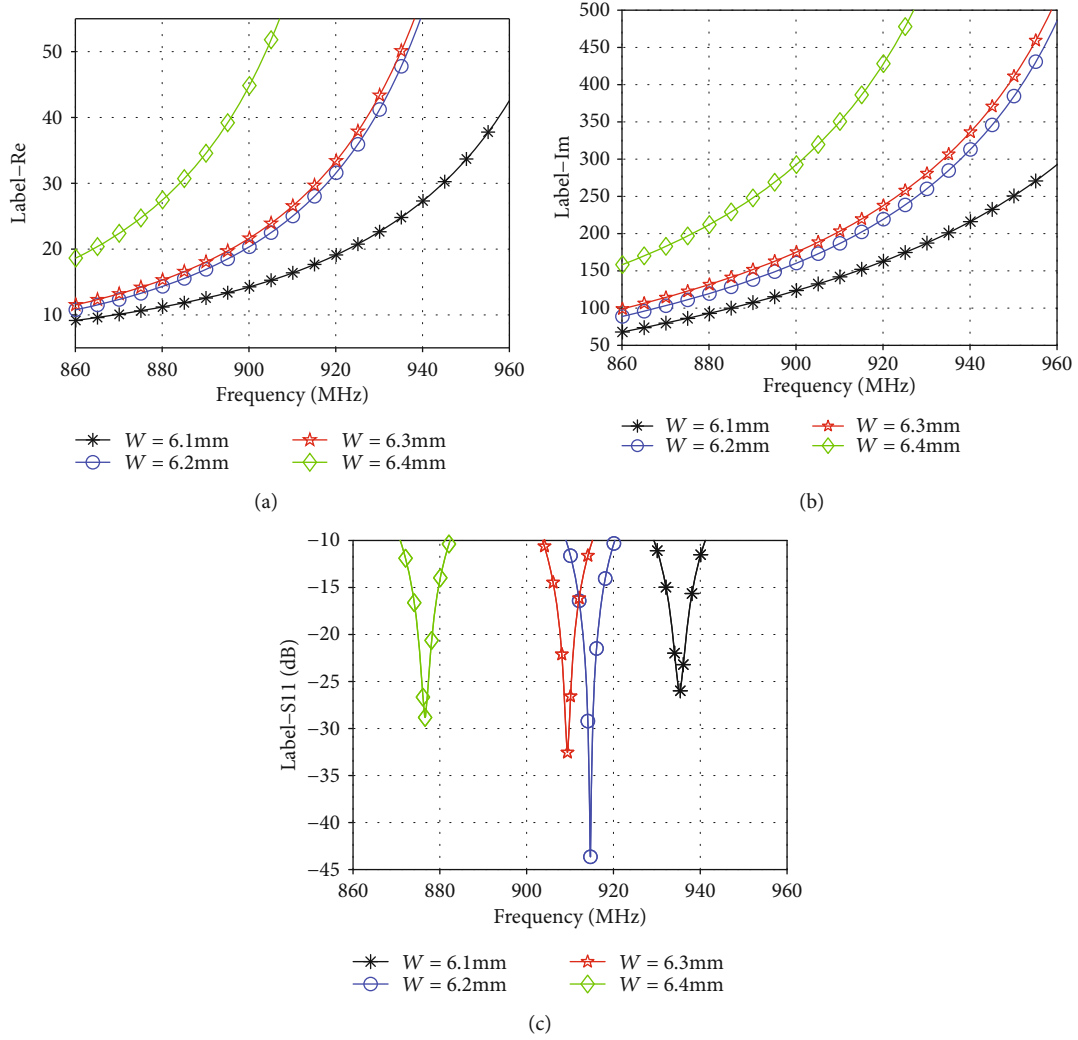


FIGURE 9: Effect of vertical depth W of the capacitive piece at both ends of the antenna on the antenna impedance and resonance frequency. (a) Antenna impedance real part. (b) Antenna impedance imaginary part. (c) Antenna resonance frequency.

resonance frequency will change. This enables monitoring of metal defect expansion.

At present, readers in commercial ultra-high-frequency (UHF) RFID systems can recognize frequency bands from 860 MHz to 960 MHz, and the antenna frequency is 915 MHz. Structural parameters need to be adjusted to optimize the impedance matching between the chip and the antenna when optimizing design, which will result in a decreased harmonic frequency. So, if the antenna resonance frequency is 930 MHz, the general rectangular microstrip antenna length (l) and width (w) are calculated as follows [35]:

$$l = \frac{c \times (\epsilon_{fr4e})^{-1/2}}{2f} - 2\Delta l, \quad (1)$$

$$w = \left(\frac{2}{\epsilon_{fr4e} + 1} \right)^{1/2} \times \frac{c}{4 \times f}.$$

The equivalent dielectric constant (ϵ_{fr4e}) of the antenna dielectric substrate for the rectangular patch and the equivalent extension length (Δl) caused by the fringe field of the microstrip antenna are as follows:

$$\epsilon_{fr4e} = \frac{\epsilon_{fr4} + 1}{2} + \frac{\epsilon_{fr4} - 1}{2} \times \left(\frac{w}{w + 12h} \right)^{1/2}, \quad (2)$$

$$\Delta l = 0.412 \times \frac{(\epsilon_{fr4e} + 0.3) \times ((w/h) + 0.264)}{(\epsilon_{fr4e} - 0.258) \times ((w/h) + 0.8)} \times h.$$

The dielectric thickness h of the preset tag antenna is 16 mm; then, the calculated l is 72 mm and w is 48 mm. In this paper, the two ends of the tag antenna are folded on both sides to reduce the size. Therefore, the equivalent antenna width should be set to 16 mm, which is one-third of w . The opposite antenna ends can increase antenna capacitive reactance and impedance. It is beneficial for getting energy when the antenna arms cut the tangential

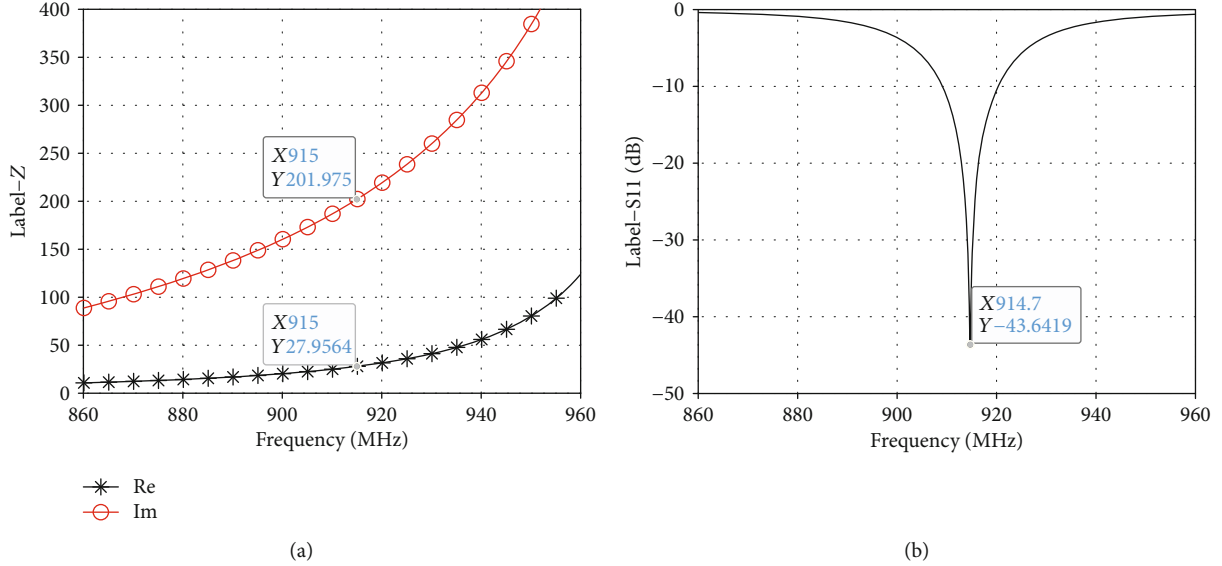


FIGURE 10: Antenna impedance and resonance frequency after parameter optimization. (a) Antenna impedance. (b) Antenna resonance frequency (return loss).

TABLE 2: Antenna structure parameter size (unit: mm).

Parameter	FR4L	FR4W	FR4H	W	W ₁	W ₂	W ₃	L	H
Size	22	16	16	6.2	1	2	1	0.5	2.8

magnetic field lines. The base height (FR4H) of the antenna is set to 16 mm, the width (FR4W) is set to 16 mm, and the length (FR4L) is set to 22 mm. The parameters are determined by simulation, as shown in Figure 5; when the FR4H is 16 mm, the antenna resonant frequency is slightly greater than 930 MHz, so parameters are set reasonably.

5. Design of a 3D Bent Patch Dipole Antenna

The RFID sensor tag is composed of a chip and an antenna. Passive RFID sensor tag impedance matching is particularly important. Impedance matching can reduce the scattering effects caused by echoes formed inside the tag. The energy utilization rate is high, which can increase the sensor tag antenna and the reader distance. According to the Alien Higgs-3 passive RF chip data sheet, ADS software is used to establish a chip equivalent circuit simulation diagram, as shown in Figure 6.

Simulation results show that Alien Higgs-3 chip impedance changes with the operating frequency as shown in Figure 7. As the operating frequency increases, the equivalent reactance of the radio frequency chip decreases and the capacitive reactance increases. The impedances are shown in Table 1 at 875 MHz, 915 MHz, and 955 MHz operating frequencies for reference.

If the antenna operating frequency considers the mid-frequency 915 MHz between 860 MHz and 960 MHz, the antenna impedance should be designed as $Z_2^* = 27.4 + j200.9$.

The basic antenna model and impedance have been determined. When the working frequency is 915 MHz, the

distance between the antenna surface and the radiation boundary should be greater than 0.25λ ; then, the ideal boundary condition is set to $180 \text{ mm} \times 180 \text{ mm} \times 118 \text{ mm}$. The antenna is mainly used to characterize metal defects. So an aluminum block with a size of $130 \text{ mm} \times 50 \text{ mm} \times 20 \text{ mm}$ is placed under the antenna. Through Ansys high-frequency structure simulator (HFSS) 15.0 modeling and antenna parameter tuning, its structural parameters are shown in Figure 4. Figures 8 and 9 show that the simulation results of the vertical depth (H) of the antenna loading horizontal strip and the vertical depth (W) of the capacitive piece at both antenna ends vary, respectively. The frequency moves to a low frequency, and the vertical depth of the capacitive plate has a great influence on the resonance frequency.

As shown in Figure 10, when $H = 2.8 \text{ mm}$ and $W = 6.2 \text{ mm}$, the tag antenna impedance is $Z_2' = 27.9564 + j201.975$ and its return loss is as low as -43.6419 dB , which achieves good conjugate matching with the tag chip. The structural parameters of the optimized antenna are shown in Table 2.

Figure 11 shows the 2D directional gain pattern and 3D radiation pattern of the tag antenna on the metal surface. The label has better omnidirectionality in the space area above the metal plate, and the radiation area is wide. The RFID reader in a large space can recognize the tag.

6. Analysis of Metal Defect Extended Induction Capability

This paper mainly studies that antenna performance parameters change, which are caused by defects on the surface of metal structures. Defect depth is an important indicator for judging the carrying capacity of metal. The deeper the defect, the lower the metal's compression resistance and the higher the risk factor. The defect width can simulate the expansion trend of the defect on the metal surface, and then, we can

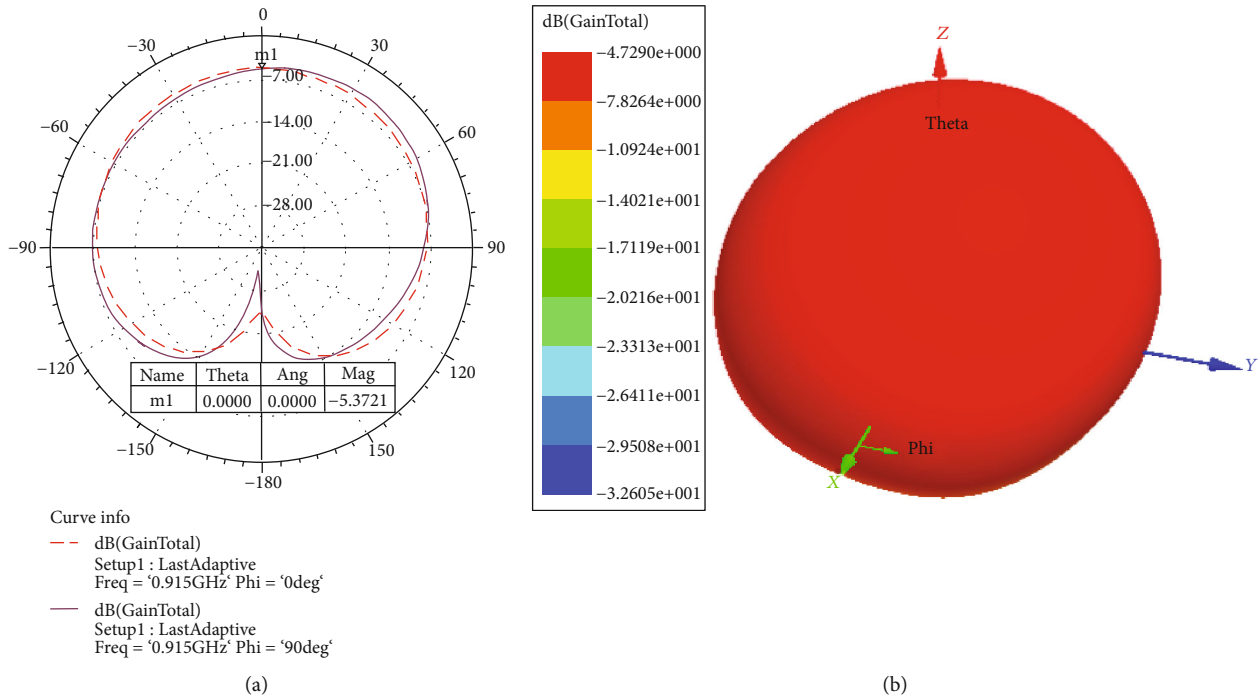


FIGURE 11: Full pattern of antenna directivity gain and radiation. (a) Antenna 2D directional gain diagram. (b) Antenna 3D radiation diagram.

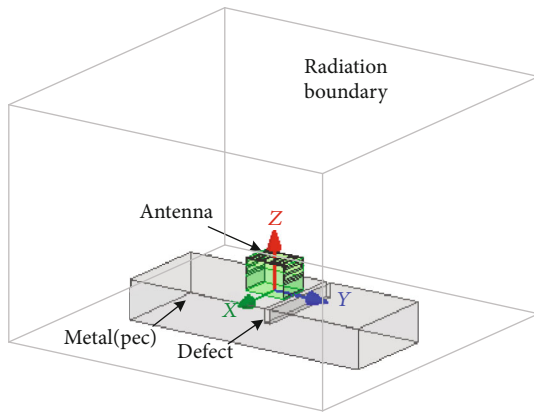


FIGURE 12: Simulation of surface defects on metal structures.

study the relative position of the defect and label to locate the position where the defect occurs on the surface of metal structures.

6.1. Analysis of the Defect Depth of Metal Structure Surfaces.

A smooth defect is simulated on the metal structure surface, as shown in Figure 12. When the defect is 12 mm to the right of the antenna and its width is 3 mm, its depth changes. The results show that when the metal surface depth deepens, the real and imaginary parts of antenna impedance decrease (same frequency), the antenna resonance frequency moves toward a high frequency, and the return loss coefficient increases, as shown in Figure 13.

In the field of antenna design, the radiation pattern indicates the radio wave strength in different directions of the antenna. Figure 14 shows the two-dimensional gain of the antenna at various defect depths. The simulation result shows that as the metal surface structural defect depth expands, it has little effect on the radiation effect of the tag antenna and the directional gain, which indicates that under normal operating conditions, defect depth expansion within a certain range will not cause the reader to fail to recognize the label.

6.2. Analysis of the Surface Defect Width of Metal Structures.

The defect position is 12 mm away from the antenna center, and its depth is 5 mm; then, its width expands to the right. The antenna impedance and resonance frequency with width change are shown in Figure 15. The results show that as the surface defect width of the metal structure expands, the real and imaginary parts of antenna impedance decrease (same frequency), and its resonance frequency moves to a high frequency.

Similarly, Figure 16 shows the two-dimensional gain of the tag antenna at various defect widths. As the defect width generated on the metal surface structure changes, the radiation surface and gain of the tag antenna change less.

6.3. Analysis of the Relative Distance between the Surface Defects of Metal Structures and the Antenna.

The defect width and depth are set to 1 mm. The relative distance between the surface defect of the simulated metal structure and the antenna center is changed, and the defect depth and width remain unchanged. Antenna impedance and resonance frequency results are shown in Figure 17. As the

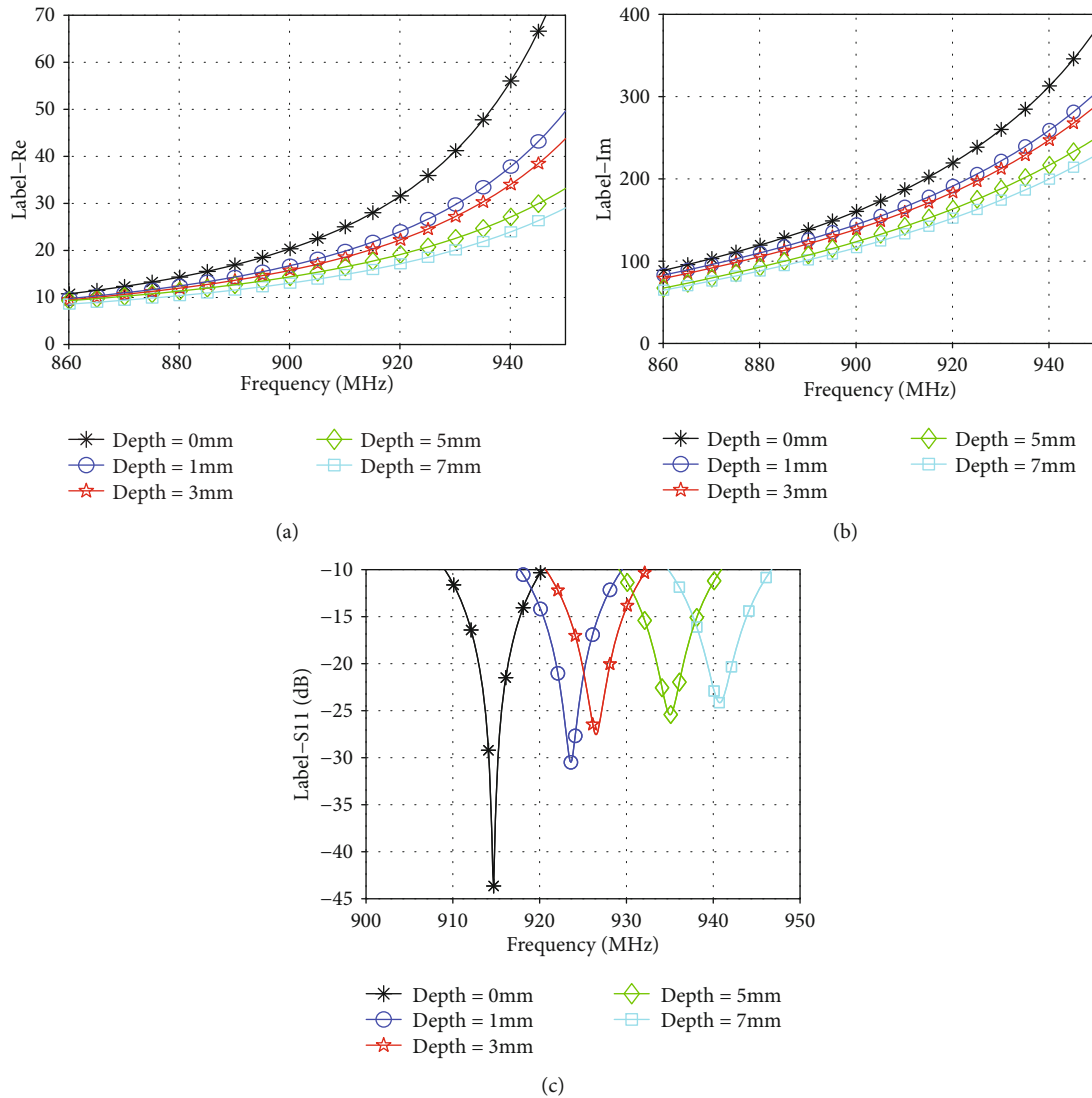


FIGURE 13: Simulation results of antenna performance parameters changing with increasing defect depth. (a) Real part of the antenna. (b) Imaginary part of the antenna. (c) Antenna resonance frequency.

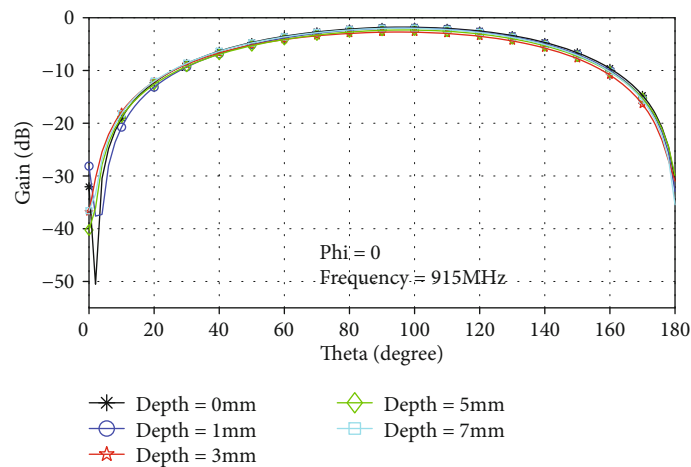


FIGURE 14: The two-dimensional gain of the tag antenna at various defect depths.

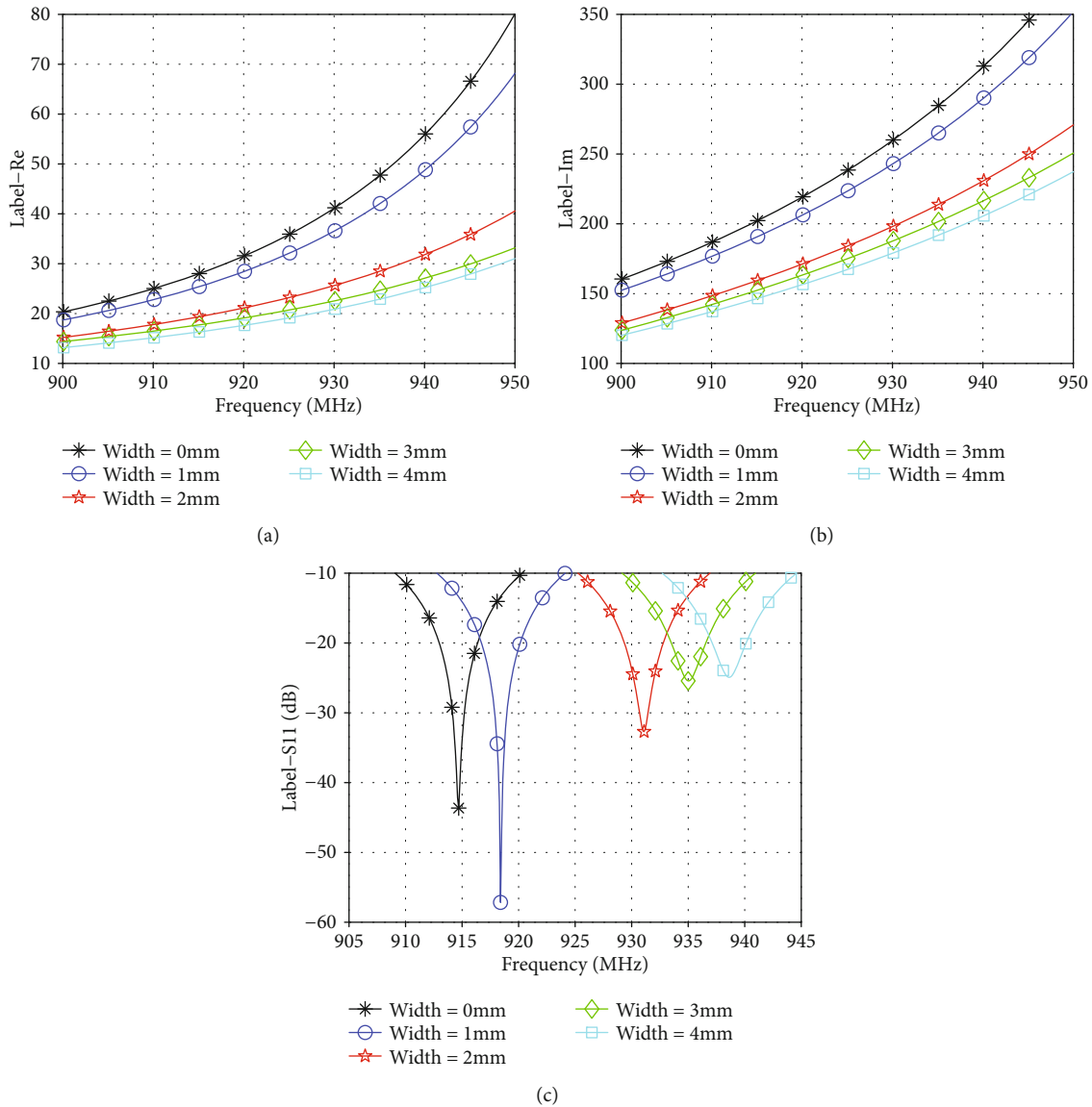


FIGURE 15: Simulation results of antenna performance parameters as defect width increases. (a) Real part of the antenna. (b) Imaginary part of the antenna. (c) Antenna resonance frequency.

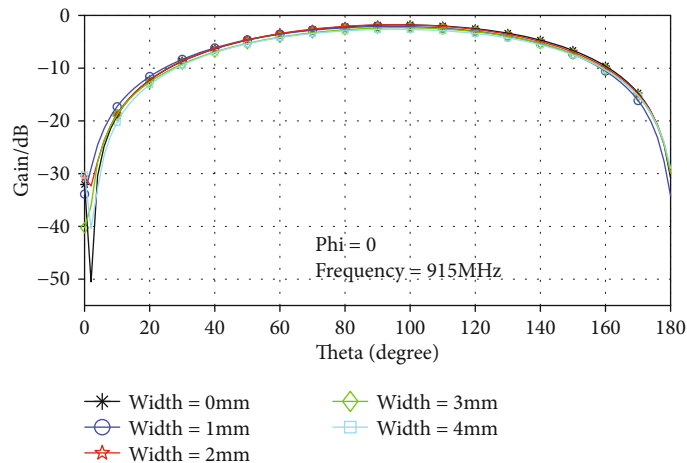


FIGURE 16: The two-dimensional gain of the tag antenna at various defect widths.

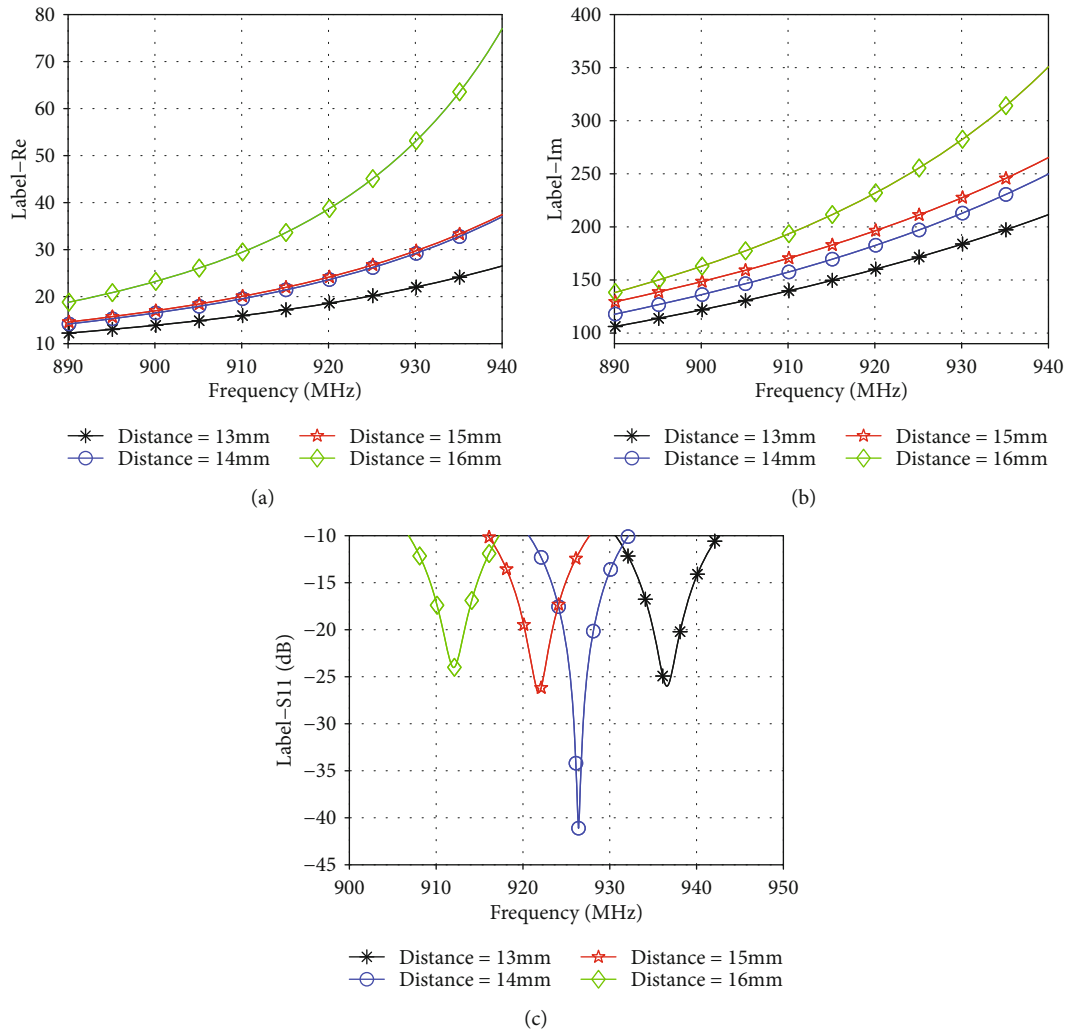


FIGURE 17: Simulation results of antenna performance parameters as a function of the relative distance between the defect and the tag antenna. (a) Real part of the antenna. (b) Imaginary part of the antenna. (c) Antenna resonance frequency.

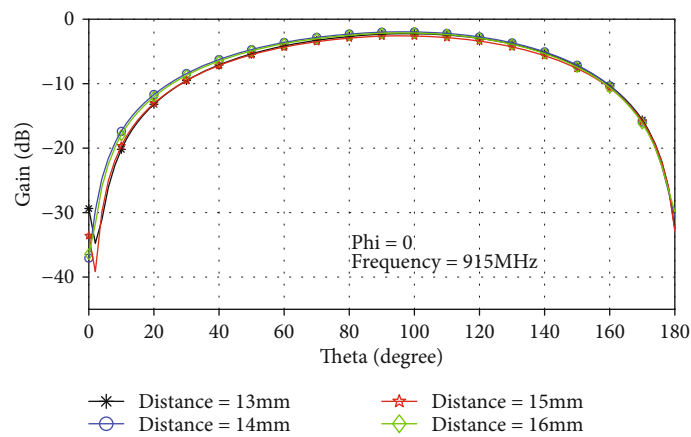


FIGURE 18: The two-dimensional gain diagram of the tag antenna when the relative distance between the defect and the tag antenna is different.

relative distance between the metal structure defect and the sensing antenna increases, the real and imaginary antenna impedance values show an increasing trend (same frequency), and its resonance frequency moves to a low frequency, which is different from the results of defect depth and width changes.

The two-dimensional polar coordinate gain of the antenna at different distances is shown in Figure 18. When the precision is 1 mm, the antenna gain changes little with the position of the defect on the metal structure surface. The gain in all directions will not be greatly affected by the distance change.

7. Conclusion

The purpose of this paper was to study the multi-directional expansion of metal defects by antennas. A 3D patch-bend dipole antenna with an operating frequency of 915 MHz was simulated using FR-4 epoxy substrate and analyzed by Ansys HFSS 15.0. The simulation results show that the antenna can detect the depth (2 mm accuracy) and width (1 mm accuracy) of smooth defects (1 mm accuracy) on the metal structure surface and the locations of smooth defects on the metal surface, which is relative to the sensor tag antenna. Neither the radiation direction nor the radiation direction gain has a large effect. Although this antenna is only suitable for the detection of surface smooth defects on metal structures on the right side of the antenna, this article provides a new design reference model for tag antennas. At the same time, the 3D antenna simulation model can characterize the specific smooth defect multiple expansion directions by a single antenna. This tag antenna has huge potential in nondestructive testing and SHM.

Data Availability

No specific dataset is required.

Conflicts of Interest

The authors declare that there are no conflicts of interest regarding the publication of this paper.

Acknowledgments

This work is supported by Sichuan Science and Technology Program (No. 2019JDTD0019).

References

- [1] K. M. Abbas, G. Manogaran, C. Thota, D. Lopez, V. Vijayakumar, and R. Sundarasekar, *Studies in big data series: internet of things and big data technologies for next generation healthcare*, Springer International Publishing, 2017.
- [2] A. Gryguć, S. B. Behraves, S. K. Shaha et al., "Multiaxial cyclic behaviour of extruded and forged AZ80 Mg alloy," *International Journal of Fatigue*, vol. 127, pp. 324–337, 2019.
- [3] Y. Yao, S. T. E. Tung, and B. Glisic, "Crack detection and characterization techniques—an overview," *Structural Control & Health Monitoring*, vol. 21, no. 12, pp. 1387–1413, 2014.
- [4] U. D. Gandhi, P. M. Kumar, R. Varatharajan, G. Manogaran, R. Sundarasekar, and S. Kadu, "Hiotpot: surveillance on IoT devices against recent threats," *Wireless Personal Communications*, vol. 103, no. 2, pp. 1179–1194, 2018.
- [5] M. Pathak, S. Alahakoon, M. Spiriyagin, and C. Cole, "Rail foot flaw detection based on a laser induced ultrasonic guided wave method," *Measurement*, vol. 148, article 106922, 2019.
- [6] S. Ahmed, C. Reboud, P. E. Lhuillier, P. Calmon, and R. Miorelli, "An adaptive sampling strategy for quasi real time crack characterization on eddy current testing signals," *NDT & E International*, vol. 103, pp. 154–165, 2019.
- [7] J. Li, T. Yu, M. Zhang, J. Zhang, L. Qiao, and T. Wang, "Temperature and crack measurement using distributed optic-fiber sensor based on raman loop configuration and fiber loss," *IEEE Photonics Journal*, vol. 11, no. 4, article 6802113, pp. 1–13, 2019.
- [8] G. Manogaran, D. Lopez, C. Thota, K. M. Abbas, S. Pyne, and R. Sundarasekar, "Big data analytics in healthcare internet of things," in *Innovative Healthcare Systems for the 21st Century. Understanding Complex Systems*, H. Qudrat-Ullah and P. Tsasis, Eds., Springer, Cham, 2017.
- [9] J. P. Lynch and K. J. Loh, "A summary review of wireless sensors and sensor networks for structural health monitoring," *The Shock and Vibration Digest*, vol. 38, no. 2, pp. 91–128, 2006.
- [10] Y. L. Guo, Q. P. Wang, H. Huang, W. Tan, and G. X. Zhang, "The research and design of routing protocols of a wireless sensor network in the coal mine data acquisition," in *2007 International Conference on Information Acquisition*, pp. 25–28, Seogwipo-si, South Korea, July 2007.
- [11] S. J. Ashaj and E. Erçelebi, "Energy saving data aggregation algorithms in building automation for health and security monitoring and privacy in medical internet of things," *Journal of Medical Imaging and Health Informatics*, vol. 10, no. 1, pp. 204–210, 2020.
- [12] R. Bhattacharyya, C. Floerkemeier, and S. Sarma, "Low-cost, ubiquitous RFID-tag-antenna-based sensing," *Proceedings of the IEEE*, vol. 98, no. 9, pp. 1593–1600, 2010.
- [13] M. M. Tentzeris, A. Georgiadis, and L. Roselli, "Energy harvesting and scavenging scanning the issue," *Proceedings of the IEEE*, vol. 102, no. 11, pp. 1644–1648, 2014.
- [14] M. Mayer and N. Goertz, "RFID tag acquisition via compressed sensing: fixed vs. random signature assignment," *IEEE Transactions on Wireless Communications*, vol. 15, no. 3, pp. 2118–2129, 2016.
- [15] R. Lodato and G. Marrocco, "Close integration of a UHF-RFID transponder into a limb prosthesis for tracking and sensing," *IEEE Sensors Journal*, vol. 16, no. 6, pp. 1806–1813, 2016.
- [16] F. Costa, A. Gentile, S. Genovesi et al., "A depolarizing chipless RF label for dielectric permittivity sensing," *IEEE Microwave and Wireless Components Letters*, vol. 28, no. 5, pp. 371–373, 2018.
- [17] D. Alonso, Q. Y. Zhang, Y. Gao, and D. Valderas, "UHF passive RFID-based sensor-less system to detect humidity for irrigation monitoring," *Microwave and Optical Technology Letters*, vol. 59, no. 7, pp. 1709–1715, 2017.
- [18] J. S. Lee, J. Oh, J. Jun, and J. Jang, "Wireless hydrogen smart sensor based on Pt/graphene-immobilized radio-frequency

- identification tag,” *ACS Nano*, vol. 9, no. 8, pp. 7783–7790, 2015.
- [19] X. Lai, Z. Cai, Z. Xie, and H. Zhu, “A novel displacement and tilt detection method using passive UHF RFID technology,” *Sensors*, vol. 18, no. 5, article 1644, 2018.
- [20] H. Huang, P. Y. Chen, C. H. Hung, R. Gharpurey, and D. Akinwande, “A zero power harmonic transponder sensor for ubiquitous wireless μ L liquid- volume monitoring,” *Scientific Reports*, vol. 6, no. 1, 2016.
- [21] T. Kobayashi, T. Yamashita, N. Makimoto, S. Takamatsu, and T. Itoh, “Ultra-thin piezoelectric strain sensor 5 x 5 array integrated on flexible printed circuit for structural health monitoring by 2D dynamic strain sensing,” in *2016 IEEE 29th International Conference on Micro Electro Mechanical Systems (MEMS)*, pp. 1030–1033, Shanghai, China, January 2016.
- [22] A. Daliri, A. Galehdar, S. John, C. H. Wang, W. S. T. Rowe, and K. Ghorbani, “Wireless strain measurement using circular microstrip patch antennas,” *Sensors and Actuators*, vol. 184, pp. 86–92, 2012.
- [23] A. Daliri, A. Galehdar, W. S. T. Rowe, S. John, and C. H. Wang, “Quality factor effect on the wireless range of microstrip patch antenna strain sensors,” *Sensors*, vol. 14, no. 1, pp. 595–605, 2014.
- [24] I. R. Shishir, S. Mun, H. C. Kim, J. W. Kim, and J. Kim, “Frequency-selective surface-based chipless passive RFID sensor for detecting damage location,” *Structural Control and Health Monitoring*, vol. 24, no. 12, article e2511, 2017.
- [25] S. Caizzone and E. DiGiampaolo, “Wireless passive RFID crack width sensor for structural health monitoring,” *IEEE Sensors Journal*, vol. 15, no. 12, pp. 6767–6774, 2015.
- [26] J. Zhang and G. Y. Tian, “UHF RFID tag antenna-based sensing for corrosion detection & characterization using principal component analysis,” *IEEE Transactions on Antennas and Propagation*, vol. 64, no. 10, pp. 4405–4414, 2016.
- [27] R. Martínez-Castro, S. Jang, J. Nicholas, and R. Bansal, “Experimental assessment of an RFID-based crack sensor for steel structures,” *Smart Material and Structures*, vol. 26, no. 8, article 085035, 2017.
- [28] A. M. J. Marindra and G. Y. Tian, “Chipless RFID sensor tag for metal crack detection and characterization,” *IEEE Transactions on Microwave Theory and Techniques*, vol. 66, no. 5, pp. 2452–2462, 2018.
- [29] A. M. J. Marindra and G. Y. Tian, “Multiresonance chipless RFID sensor tag for metal defect characterization using principal component analysis,” *IEEE Sensors Journal*, vol. 19, no. 18, pp. 8037–8046, 2019.
- [30] T. V. Padmavathy, D. S. Bhargava, P. Venkatesh, and N. Sivakumar, “Design and development of microstrip patch antenna with circular and rectangular slot for structural health monitoring,” *Personal and Ubiquitous Computing*, vol. 22, no. 5–6, pp. 883–893, 2018.
- [31] S. Xue, K. Xu, L. Xie, and G. Wan, “Crack sensor based on patch antenna fed by capacitive microstrip lines,” *Smart Materials and Structures*, vol. 28, no. 8, article 085012, 2019.
- [32] O. Rees-Lloyd, P. Charlton, S. Mosey, and R. Lewis, “Effects of relative motion on a Rayleigh wave electromagnetic acoustic transducer operating on aluminium,” *Insight*, vol. 61, no. 2, pp. 83–89, 2019.
- [33] Y. J. He and Z. Z. Pan, “Design of UHF RFID broadband anti-metal tag antenna applied on surface of metallic objects,” in *2013 IEEE Wireless Communications and Networking Conference (WCNC)*, pp. 4352–4357, Shanghai, China, April 2013.
- [34] T. Bjorninen, A. Z. Elsherbeni, and L. Ukkonen, “Low-profile conformal UHF RFID tag antenna for integration with water bottles,” *IEEE Antennas and Wireless Propagation Letters*, vol. 10, pp. 1147–1150, 2011.
- [35] T. D. Amalraj and R. Savarimuthu, “Design and analysis of microstrip patch antenna using periodic EBG structure for c-band applications,” *Wireless Personal Communications*, vol. 109, no. 3, pp. 2077–2094, 2019.

Research Article

Estimation of Particulate Levels Using Deep Dehazing Network and Temporal Prior

SeHee Jung ¹, SungMin Yang,² Eunseok Lee,¹ YongHak Lee,² Jisun Ko,¹ Sungjae Lee,¹ JunSang Cho,³ Jaehwa Lee,^{4,5} and SungHwan Kim ²

¹AI Analytics Team, DeepVisions, Seoul, Republic of Korea

²Department of Applied Statistics, Konkuk University, Seoul, Republic of Korea

³Industry University Cooperation Foundation Konkuk University, Seoul, Republic of Korea

⁴Earth System Science Interdisciplinary Center, University of Maryland, College Park, MD, USA

⁵NASA Goddard Space Flight Center, Greenbelt, MD, USA

Correspondence should be addressed to SungHwan Kim; shkim1213@konkuk.ac.kr

Received 7 May 2020; Revised 2 June 2020; Accepted 11 June 2020; Published 7 July 2020

Academic Editor: Bin Gao

Copyright © 2020 SeHee Jung et al. This is an open access article distributed under the Creative Commons Attribution License, which permits unrestricted use, distribution, and reproduction in any medium, provided the original work is properly cited.

Particulate matters (PM) have become one of the important pollutants that deteriorate public health. Since PM is ubiquitous in the atmosphere, it is closely related to life quality in many different ways. Thus, a system to accurately monitor PM in diverse environments is imperative. Previous studies using digital images have relied on individual atmospheric images, not benefiting from both spatial and temporal effects of image sequences. This weakness led to undermining predictive power. To address this drawback, we propose a predictive model using the deep dehazing cascaded CNN and temporal priors. The temporal prior accommodates instantaneous visual moves and estimates PM concentration from residuals between the original and dehazed images. The present method also provides, as by-product, high-quality dehazed image sequences superior to the nontemporal methods. The improvements are supported by various experiments under a range of simulation scenarios and assessments using standard metrics.

1. Introduction

Particulate matters (PM) are small particles suspended in the air, generally having an aerodynamic diameter smaller than or equal to $10\ \mu\text{m}$ (micrometers). PM originates from anthropogenic activities, (e.g., combustion of fossil fuel, dust) as well as natural sources (e.g., mineral dust, volcanic ash). PM measurements are commonly made for particles with an aerodynamic diameter smaller than or equal to $2.5\ \mu\text{m}$ ($\text{PM}_{2.5}$) and $10\ \mu\text{m}$ (PM_{10}). The size of PM is directly associated with health problems [1]. Inhaling the small particles is known to be hazardous as they can infiltrate in depth into the respiratory system [2]. In this regard, $\text{PM}_{2.5}$ has been widely used as a key indicator of the air quality index, and thus, we focus on $\text{PM}_{2.5}$ in this study (hereafter abbreviated as PM for brevity). Many experts point out that the recent increases of PM in many parts of the world are attributed to the rapid

growth in global energy consumption [3]. Over the years, efforts have been made to identify adverse effects of PM on public health and environment [4–6]. Surprisingly, the large-scale retrospective cohort study of lung cancer by the World Cancer Institute reported that PM is ascertained as primary carcinogens, as the risk of lung cancer increased by 22% for an increase of PM by $10\ \mu\text{g}/\text{m}^3$ [7]. The air pollution from PM has been one of the most controversial issues over East Asia. This has become no longer negligible, and media as well as researchers try to inform the public of its detrimental effects [8]. Particularly, it was reported that the annual mean PM concentration in South Korea is twice as high as in the Organisation for Economic Co-operation and Development (OECD; <https://www.oecd.org/>) countries [9]. Under this circumstance, it is imperative to build an accurate air monitoring system to facilitate alerting the public prevention. The Korean government drastically expanded the PM monitoring

network to help improve PM forecast service to a remarkable extent. However, there are still not enough PM monitoring stations to cover the whole country. Moreover, most of the stations are distributed in urban areas (e.g., Seoul, Busan), leaving many suburban and rural undermonitored.

Two different types of approaches can be used to estimate PM concentrations: sensor-based approaches and vision-based approaches.

1.1. Sensor-Based. Improvements in PM measurements using sensor-based approaches have been made to develop more precise sensor units [10]. There are two types of devices [11], i.e., microbalance PM monitoring stations (accurate but expensive [12]) and portable light-scattering-based PM monitors [13, 14]. For instance, the Korea Meteorological Administration (KMA) now operates 475 measuring stations and publicly reports PM concentration levels (i.e., limited to the station vicinity) every hour [15]. Most of the instruments operated by KMA are Tapered Element Oscillating Microbalance (TEOM), which is designed to directly weight PM on the filter [11]. Although highly accurate, TEOM is relatively expensive to install and maintain (approximately 200K USD per year) [16] and is bound to space limitations, thereby undermining practicality. The light-scattering method is relatively affordable. In [11, 17], collected PM via airflow structure are measured by densely deployed sensors. However, both methods relying on large-scale sensing nodes inevitably suffer from the expensive maintenance costs for high coverage and reliability. Recently, several newly developed devices for mobile facility (e.g., balloons and drones) are very interesting [10, 18, 19], but carrying sensors to acquire data is still highly energy-intensive and less practical to use.

1.2. Vision-Based. This approach is less explored compared to the sensor-based approach, and so there is a lot of room for improvement. To the best of our knowledge, all the vision-based studies exploit only individual images (e.g., [20–22]). In this case, it is fairly sensitive to motion blurring frequently caused by camera or subject movements. Specifically, Liu et al. [20] manually determined several regions of interest targeting distant objects to derive the transmission map. The explanatory power of the transmission map for PM estimation has proven its efficiency [20–23]. However, the need for selecting regions of interest is the pain point. Li et al. [21] leveraged heterogeneous data composed of GPS, camera lens, magnetic sensor, official station, and image data. Combining these multiple data, they generate high-dimensional features using kernel methods. Pan et al. [22] extracted haze effects using Adaptive Transmission Map [24] and pass derived features to the deep neural network designed on the basis of the well-known Boltzmann machine [25]. Since it is assumed that transmission values in a local patch (a.k.a. window) are the same constant, the dehazed images inevitably contain blocking artifacts [22, 26, 27]. The rest of this paper is organized as follows. In Sections 2 and 3, we introduce related works and the proposed method, respectively. Section 4 describes the numerical experiments.

We discuss the results and conclude in Section 5.

2. Related Work

According to the atmospheric scattering model (ASM), two factors are involved in the formation of a haze image: (1) direct attenuation and (2) airlight. When we take a photo, reflected radiance coming from objects is attenuated while reaching the camera. This is due to the effects of atmosphere absorption (a.k.a. direct attenuation), and the intensity of attenuation is proportional to camera distance (scene depth). In addition to this, there is another light, called airlight, resulting from scattering of neighboring light sources (e.g., sun) by haze [28]. Importantly, airlight is known to shift the color range of the object, and direct attenuation describes the scene radiance and its decay. Figure 1 illustrates how image degradation occurs under haze conditions. With a little of algebra, this process can be formulated as follows:

$$\mathbf{I}(\mathbf{x}) = \mathbf{J}(\mathbf{x})t(\mathbf{x}) + \mathbf{A}(1 - t(\mathbf{x})), \quad (1)$$

where $\mathbf{x} \in \mathbb{R}^2$ denotes the pixel, $\mathbf{I} \in \mathbb{R}^3$ is the observed haze image in RGB channels, $\mathbf{J} \in \mathbb{R}^3$ is the haze-free image, $t \in [0, 1]$ is the medium transmission describing the portion of the scene radiance that reaches the camera, and \mathbf{A} is the global atmospheric light. Note that \mathbf{A} is assumed to be homogeneous throughout the image and determined using empirical techniques. The first term $\mathbf{J}(\mathbf{x})t(\mathbf{x})$ on the right-hand side of equation (1) represents direct attenuation, and the second term $\mathbf{A}(1 - t(\mathbf{x}))$ corresponds to airlight. The farther the distance between a camera and objects is, the thicker the atmospheric layer exists between them.

$$t(\mathbf{x}) = e^{-\beta d(\mathbf{x})}, \quad (2)$$

where β is the scattering coefficient of atmosphere, and $d(\mathbf{x})$ is the distance from the object to the camera. Equation (2) indicates that the scene radiance is attenuated exponentially with the scene depth d . Here, it is intuitively understandable that some haze effect $\mathbf{H}(\mathbf{x})$ deteriorates the haze-free image $\mathbf{J}(\mathbf{x})$ (i.e., $t(\mathbf{x}) = 0$), causing the haze image $\mathbf{I}(\mathbf{x})$. Starting from this simple idea, we can consider the following relation:

$$\mathbf{I}(\mathbf{x}) = \mathbf{J}(\mathbf{x}) + \mathbf{H}(\mathbf{x}). \quad (3)$$

Related to image dehazing (a.k.a. haze removal), we restore \mathbf{J} , \mathbf{A} , and t from the observed haze image \mathbf{I} .

3. Proposed Method

To measure PM via image sequences (i.e., video clip) is the ultimate goal of our study, and the deep neural network serves as a feature extractor. To achieve our goal, we first learn the deep dehazing network that extracts informative features based on strong correlation with PM concentration levels. In this section, we introduce two strategies working together for the network: (1) deep compression for energy efficiency in light of the model architecture and (2) temporal priors to capture haze-related features in image sequences. The specific design of our dehazing network is presented in Figure 2.

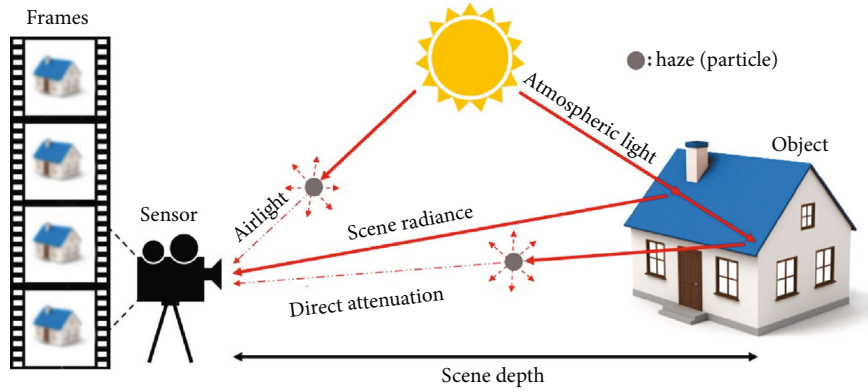


FIGURE 1: Hazy objects in multiple image sequences via the atmospheric scattering model.

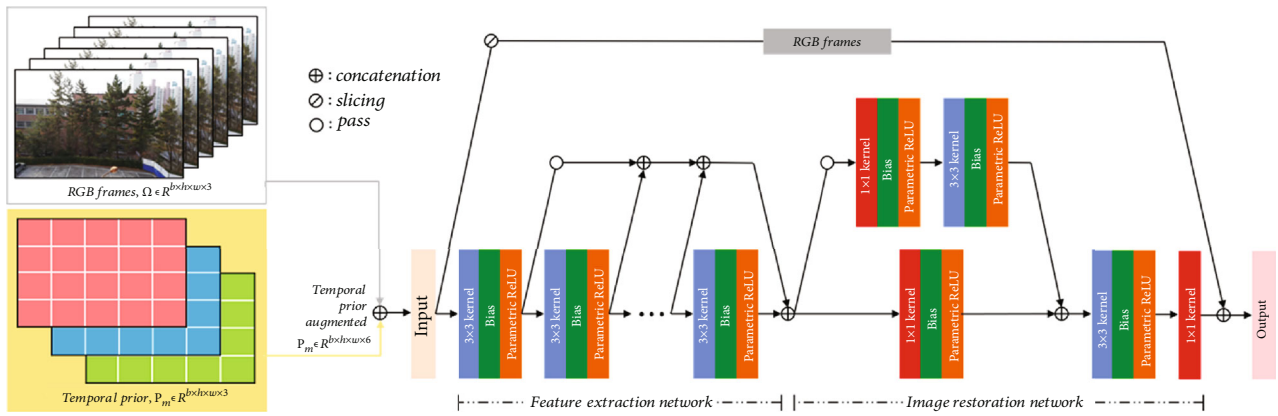


FIGURE 2: The illustration of dehazing network architecture. The dehazing network consists of two parts with specific roles: (1) feature extraction and (2) image restoration.

3.1. Network Architectures in Favor of Feature Extraction

3.1.1. Network Pruning. Network depth in CNN plays a decisive role in extracting various levels of features [29]. Inspired by this, we formulate the feature extraction network (FEN) at the front part of our dehazing network with deep cascaded convolutional layers of 436 kernels as in Figure 2. However, going deep convolutions involves too many parameters in the network and high computational cost. We thus seek to simplify the network without loss of accuracy. To address this hurdle, we compress the FEN using network pruning (NP). This has been widely used to reduce network complexity and prevent overfitting [30–32]. We also eliminate a waste of unnecessary parameters in our network without performance loss. Since the local feature is more important than the global feature in image restoration [33], we reduced the number of kernels in a row (see Table 1). This technique (a.k.a. pruned network) outperforms the original network having far more connections with plain and dense architecture. This in turn enabled the FEN to be less complex, but still deep enough to extract the necessary features for PM measurements. Based on the deep cascaded CNN architecture, the FEN grasps all the levels of features from local to global.

3.1.2. Parallelized 1×1 CNN Layer. In the second place, we adopt in the network the parallelized 1×1 CNN Layers

(P1CL, a.k.a. Network In Network [34]) to image restoration network (IRN) that appears in the second half of our dehazing network in Figure 2. The P1CL proves its applicability to enhance the representational power of neural networks [34]. GoogLeNet fully exploits this technique not only to make the network deep in the name of the inception module but also to reduce the dimensions inside these modules [35]. Inspired by GoogLeNet, we place the P1CL in front of the IRN to reduce the dimension of the feature maps accumulated through the FEN. This does not simply imply more of dimension reduction. In doing so, we compress the feature maps so as to narrow down the scope of involving features. Besides, the P1CL also includes the use of rectified linear activation [36]. In general, each P1CL consists of one or more 1×1 convolutions followed by a nonlinear activation function (e.g., ReLU), which adds more nonlinearity and thereby helps approximate the highly nonlinear function such as ASM. Taking all together, we form the IRN approximating the following equation derived from equation (3) with a little algebra:

$$\mathbf{H}(\mathbf{x}) = \mathbf{J}(\mathbf{x})(t(\mathbf{x}) - 1) + \mathbf{A}(1 - t(\mathbf{x})), \quad (4)$$

where $\mathbf{H}(\mathbf{x})$ means the haze effect and the two terms $\mathbf{J}(\mathbf{x})(t(\mathbf{x}) - 1)$ and $\mathbf{A}(1 - t(\mathbf{x}))$ correspond to the lost scene radiance (e.g., by scattering or absorbing) and the shift

TABLE 1: The architecture of the proposed dehazing network. In the table, b , h , and w represent batch size, height, and width, respectively. *concat* is short for concatenation.

Layer	Kernel	Input size	Output size
fen_1	$3 \times 3 \times 96$	$b \times h \times w \times 6$	$b \times h \times w \times 96$
fen_2	$3 \times 3 \times 83$	$b \times h \times w \times 96$	$b \times h \times w \times 83$
fen_3	$3 \times 3 \times 72$	$b \times h \times w \times 83$	$b \times h \times w \times 72$
fen_4	$3 \times 3 \times 61$	$b \times h \times w \times 72$	$b \times h \times w \times 61$
fen_5	$3 \times 3 \times 51$	$b \times h \times w \times 61$	$b \times h \times w \times 51$
fen_6	$3 \times 3 \times 41$	$b \times h \times w \times 51$	$b \times h \times w \times 41$
fen_7	$3 \times 3 \times 32$	$b \times h \times w \times 41$	$b \times h \times w \times 32$
<i>concat</i>	—	—	$b \times h \times w \times 436$
irn_1	$1 \times 1 \times 64$	$b \times h \times w \times 436$	$b \times h \times w \times 64$
irn_{21}	$1 \times 1 \times 32$	$b \times h \times w \times 436$	$b \times h \times w \times 32$
irn_{22}	$3 \times 3 \times 32$	$b \times h \times w \times 32$	$b \times h \times w \times 32$
<i>concat</i>	—	—	$b \times h \times w \times 96$
irn_3	$3 \times 3 \times 3$	$b \times h \times w \times 96$	$b \times h \times w \times 3$
irn_4	$1 \times 1 \times 3$	$b \times h \times w \times 3$	$b \times h \times w \times 3$

of the scene color, respectively. The main reason for parallel processing in IRN is to divide the computational tasks and thereby reduce the burden of the network. The upper and lower unit estimates the lost scene radiance and the shift of the scene, respectively. In the blessing of a parallel architecture, the IRN can expedite the work in a simultaneous processing fashion, and it also helps prevent overfitting problem with reduced network complexity. The residual between original and dehazed images can serve as an explanatory variable related to haze effects for predicting PM levels. Motivated by this, we set a model of the relationship between the variables of haze effects and PM levels. Using components stored in estimated haze effects $\hat{\mathbf{H}}$ (in Figure 3), we can estimate PM concentration levels.

3.2. Temporal Prior. Since the PM consists of infinitesimal particles floating in the air, they can be characterized by a transport phenomenon such as flow motions in video. Although we cannot directly identify flow motion of PM by tracking all particles, we can indirectly discover its effects through variability in the midst of multiple image sequences in video. As introduced by Kim et al. [37], differences between the original consecutive frames in both cases (safe $\leq 80 \mu\text{g}/\text{m}^3$ and harmful $> 80 \mu\text{g}/\text{m}^3$) are obviously distinctive. This previous work reinforces the plausibility of hypothesis that the image distinctions across images show PM concentration levels are considerably significant. This is motivated by the fact that the moving objects happen to create subtle changes. Stepping beyond the previous work, inspired by prior in Bayesian, we impose the fluid flow model proposed by Xie et al. [38] in order to additionally accommodate feature variations:

$$\mathbf{F}_t = \mathbf{T}(\mathbf{F}_{t-1}, \mathbf{P}_{t-1}), \quad (5)$$

where t is the time domain and \mathbf{F} , \mathbf{T} , and \mathbf{P} denote the fluid, the transport operator (a.k.a. advection or warp operator), and the temporal prior, respectively. Note that $\mathbf{p}_t \in \mathbb{R}^2$, the element of $\mathbf{P}_t \in \mathbb{R}^3$, is the vector, which has the velocity and flow direction field. For brevity, we replace the existing physical prior \mathbf{P}_{t-1} , where \mathbf{P}_{t-1} denotes the average over a period of time prior to t . More precisely, Figure 4 describes how the proposed temporal prior is made up based on sequential frames during the prior length, each of pixels calculating the average values of RGB across image frames. Taken together, we combine the original RGB (3 channels) and its corresponding temporal priors (3 channels) into augmented inputs for a total of six channels (see the first half of the network in Figure 2). When exploiting the priors almost consistent across image sequences, the network is expected to be superior in producing consistent haze effects, as compared to the model with no temporal prior.

4. Numerical Experiments

4.1. Datasets. In this section, we describe haze video datasets to apply. One of the challenges in creating real video datasets is that both consecutive haze frames and the corresponding haze-free frames are supposed to be perfectly matched up. To circumvent a little, artificial haze video datasets based on existing videos can be used to train dehazing networks [39–41]. Yet, synthetic haze effects hardly accommodate natural flow motions that disperse light, and thereby, this wrongly distorts pixel values. Instead, we collected datasets of various environments including both indoor and outdoor areas (refer to the sample haze images in Supplementary Material (available here)). Here, one note of caution is that since indoor environments are not directly exposed to the outside atmosphere, in the case of indoor, it is difficult to collect video clips with high PM levels. Therefore, we had to open all the windows when PM was high or sometimes directly generate PM by burning incense or spraying potassium chloride. The thumbnail images are shown in Table 2. The video clips were recorded with the *Raspberry Pi Camera Module V2* (Raspberry Pi Foundation; <http://www.raspberrypi.org/>) employing a low-cost CMOS sensor. In the stage of building datasets, we first mount the pi cameras on the tripods for image stabilization. While recording video clips, we concurrently measure PM levels using the *Aerocet 831 Handheld Particle Counter* (Met One Instruments; <http://www.metone.com/>), a high-precision device. With the help of the *Aerocet*, we collected the haze-free images under atmosphere where PM levels are less than or equal to 15 as the target images for training the network. For these data, we finally applied the optical flow [42] to the captured video clips for removing any spatial variances. All the datasets and the codes are available at the author’s website (<http://www.hifiai.pe.kr/>).

4.2. Results. To measure PM levels, the estimated haze effects per frame (matrix) are converted to statistic (scalar) such as mean, entropy, and variance [20, 43]. To assess

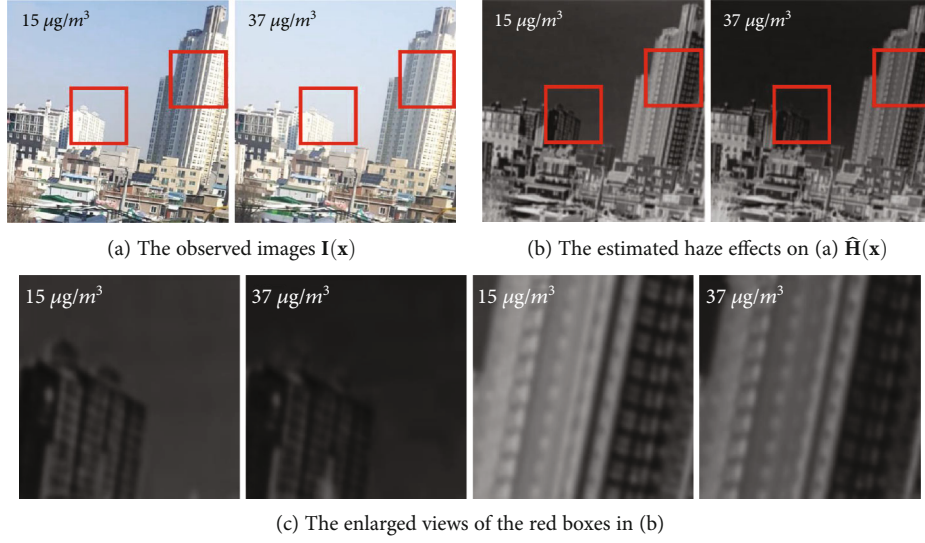


FIGURE 3: The differences between the estimated haze effects varied by PM concentration level ($15 \mu\text{g}/\text{m}^3$ and $37 \mu\text{g}/\text{m}^3$). The estimated haze effect images in RGB channels were converted to grayscale image for a clear comparison.

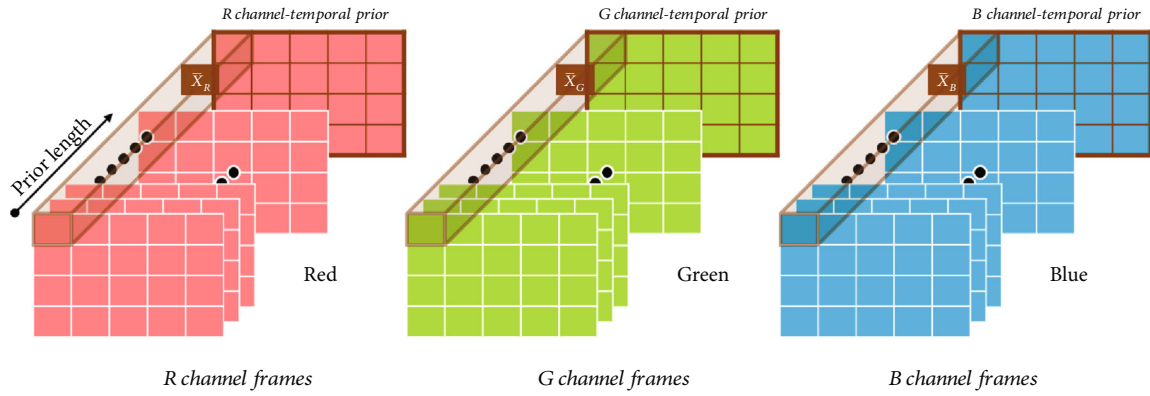


FIGURE 4: The illustration of temporal prior using RGB channels.

predictive power, we compare the true hazy effects with predicted hazy effects. To do so, we fit the three regression-type models: (1) random forest regression (RFR), (2) support vector regression (SVR) with the radial basis function (rbf) kernel, and (3) multilayer perceptron regression (MPR). The metric to evaluate prediction accuracy is as follows:

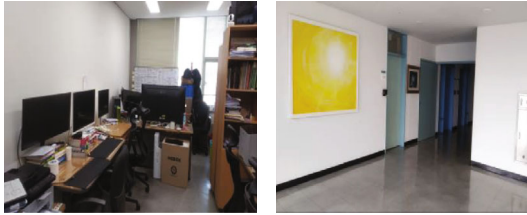
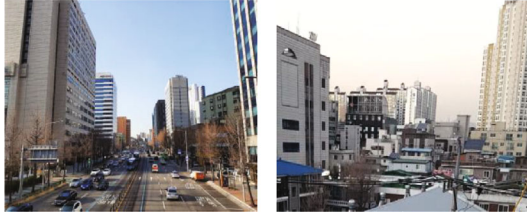

$$\text{acc} = \frac{1 - (|AQI_{\text{ground}} - AQI_{\text{predicted}}|)}{QI_{\text{ground}}}, \quad (6)$$

where AQI_{ground} and $AQI_{\text{predicted}}$ refer to statistic (e.g., mean, entropy, and variance) of $\mathbf{H}(\mathbf{x})$ from ground truth and the proposed model. Table 3 summarizes the accuracy results for the test sets, and all indoor and outdoor scenarios are equally assigned.

4.2.1. Indoor and Outdoor Environment. We collect over 2,000 video clips from the indoor office and corridors at the

Konkuk University over several months. Here, the proposed model presents the best performance of accuracy with 86.72% when adopting MLPR with prior and the entropy benchmark. Especially notable is that accuracy tends to increase when applying the temporal prior across all scenarios. In this sense, it is confirmed that temporal priors can provide the network with additional haze-related information. In addition, indoor environments are believed to be less sensitive to environmental factors, and thus, it is understandable that indoor experiments outperform outdoor as a whole. For outdoor experiments, we select two locations in South Korea populated with people in the midst of the residential areas and the building complex. For several months, we collect more than 3,000 video clips of each location. For reliability, we make sure that outdoor data consist of a widespread range of PM levels. In Table 3, SVR with entropy presents 72.16% and 82.45% for nonprior and prior, respectively. Interestingly, priors in outdoor data allow considerable accuracy

TABLE 2: Brief descriptions of selected regions and experiment chambers.

Category	Thumbnail	# of video clips
Indoor environments		2,000 for each site
Outdoor environments		3,000 for each site
Experimental chamber		1,000 for each experimental condition

gains compared to indoor scenarios. The results implicate that prior information can be effective especially in outdoor environments (e.g., windiness) in the midst of particulate flows.

4.2.2. Experimental Chamber. In simulations, it is essential to assess diverse environmental conditions. To this end, we especially design the experimental chamber to implement diverse conditions of interest. The experiments were carried out regarding four factors including wind, temperature, humidity, and illuminance. In the course of the experiments, the other confounding factors are well adjusted in the experiment chamber. We gather approximately 1,000 video clips across all experiment conditions. In Table 4, the results show that the MLPR with entropy consistently present high accuracy over 80% for almost all scenarios. Therefore, it is clearly confirmed that this prior-based model serves to adequately control environmental confounding factors that possibly intervene in haze effects.

5. Discussion

Undoubtedly, the latest AI has mainly focused on vision-based techniques (e.g., RGB and Lidar). Nonetheless, in the AI domain, infinitesimal materials still remain underestimated due to its invisible nature. In this regard, vision-based PM measurements are featured with many advantages of flexibility and accessibility in the view of real-time air quality monitoring and extension to spatial scales. Given our finding, even with a low-cost optical sensor, the proposed method can offer further benefits in business and cost savings in practical aspects. Moreover, this also serves as a predictive

TABLE 3: The accuracy results of the regression models for various environments. The best results pertaining to each condition are underlined.

	Nonprior			Prior		
	RFR	SVR	MLPR	RFR	SVR	MLPR
Indoor						
<i>Mean</i>	0.6903	0.5872	0.7546	0.7299	0.6139	0.7953
<i>Variance</i>	0.6645	0.8101	0.8152	0.6682	0.8239	0.8258
<i>Entropy</i>	0.6949	<u>0.8247</u>	0.8240	0.7054	0.8388	<u>0.8672</u>
Outdoor						
<i>Mean</i>	0.6228	0.4599	0.5882	0.6917	0.5197	0.6969
<i>Variance</i>	0.6157	0.6843	0.6891	0.7005	0.7760	0.7753
<i>Entropy</i>	0.6193	<u>0.7216</u>	0.7135	0.7127	<u>0.8245</u>	0.8132

model using the deep cascaded CNN and temporal prior in a methodological aspect. Compared to existing vision-based predictive models, the proposed model stretches into accommodating additional temporal prior features among image sequences, aiming at improving predictive power in the virtue of data augmentation. With various simulation designs (e.g., real data and experimental chamber data), we confirm that the proposed models are superior to the traditional models without temporal priors, showing outstanding predictive power. Further improvements can be made by exploiting the optimal length of frames in the context of optimizing predictive power. This effort can facilitate to export it to a gauging device and promote practical utility, since all of vision-based models strongly depend on well-controlled

TABLE 4: Experimental chamber study. The accuracy results of the regression models for various environmental conditions. The best results pertaining to each condition are underlined.

Nonprior	Normal state			Windiness			Prior			Normal state			Windiness		
	RFR	SVR	MLPR	RFR	SVR	MLPR	RFR	SVR	MLPR	RFR	SVR	MLPR	RFR	SVR	MLPR
Mean	0.7586	0.6412	0.7431	0.6403	0.5986	0.6653	0.7620	0.6441	0.7899	0.6951	0.4670	0.7235	0.6951	0.4670	0.7235
Variance	0.7116	<u>0.7805</u>	0.7470	0.6319	0.6951	0.7249	0.6728	0.7995	0.8093	0.6357	0.6428	0.7764	0.6357	0.6428	0.7764
Entropy	0.6511	0.7523	0.7528	0.7074	<u>0.7780</u>	0.6057	0.6934	0.8674	<u>0.8699</u>	0.7186	<u>0.8428</u>	0.8101	0.7186	<u>0.8428</u>	0.8101

Nonprior	Temperature (low) (20°C)			Temperature (high) (40°C)			Prior			Temperature (low) (20°C)			Temperature (high) (40°C)		
	RFR	SVR	MLPR	RFR	SVR	MLPR	RFR	SVR	MLPR	RFR	SVR	MLPR	RFR	SVR	MLPR
Mean	0.6906	0.5189	0.7254	0.6105	0.5143	0.6856	0.7154	0.5162	0.8123	0.7636	0.5810	0.8094	0.7636	0.5810	0.8094
Variance	0.7101	0.7567	0.7674	0.7083	0.7410	0.7528	0.6510	0.7854	<u>0.8518</u>	0.6883	0.7681	0.8082	0.6883	0.7681	0.8082
Entropy	0.7517	<u>0.7781</u>	0.7056	0.6505	<u>0.7696</u>	0.7387	0.7215	0.8304	0.8319	0.7271	0.8330	<u>0.8334</u>	0.7271	0.8330	<u>0.8334</u>

Nonprior	Humidity (low) (25%)			Humidity (high) (50%)			Prior			Humidity (low) (25%)			Humidity (high) (50%)		
	RFR	SVR	MLPR	RFR	SVR	MLPR	RFR	SVR	MLPR	RFR	SVR	MLPR	RFR	SVR	MLPR
Mean	0.6910	0.6397	0.6666	0.6593	0.6317	0.7234	0.7319	0.5523	0.7854	0.7462	0.5699	0.7734	0.7462	0.5699	0.7734
Variance	0.7218	0.7581	0.6977	0.6745	0.6612	0.6715	0.6821	0.8149	0.7724	0.6770	0.7675	0.7379	0.6770	0.7675	0.7379
Entropy	0.7203	<u>0.7827</u>	0.6660	0.6679	<u>0.7674</u>	0.6869	0.7466	0.8054	<u>0.8524</u>	0.7451	0.8174	<u>0.8468</u>	0.7451	0.8174	<u>0.8468</u>

Nonprior	Illuminance (low) (100 lx)			Illuminance (high) (300 lx)			Prior			Illuminance (low) (100 lx)			Illuminance (high) (300 lx)		
	RFR	SVR	MLPR	RFR	SVR	MLPR	RFR	SVR	MLPR	RFR	SVR	MLPR	RFR	SVR	MLPR
Mean	0.6659	0.5286	0.7038	0.6562	0.5634	0.7140	0.7131	0.5506	0.6905	0.6672	0.5185	0.7522	0.6672	0.5185	0.7522
Variance	0.6433	0.7024	0.6046	0.6450	0.7513	0.6685	0.6241	0.7861	0.7757	0.7384	0.7135	0.8104	0.7384	0.7135	0.8104
Entropy	0.6588	<u>0.7821</u>	0.6280	0.6615	<u>0.7764</u>	0.6800	0.6825	0.8018	<u>0.8031</u>	0.6926	0.8355	<u>0.8764</u>	0.6926	0.8355	<u>0.8764</u>

radiance, which considerably discourages vision-based measurement techniques at times. To address this issue, we plan on developing alternative prediction models that account for particulate-related features only. We leave these topics for future research.

Data Availability

All the datasets and the codes are available at the author's website (<http://www.hifai.pe.kr/>).

Conflicts of Interest

The authors declare that there is no conflict of interest regarding the publication of this paper.

Acknowledgments

This research was supported by Konkuk University Researcher Fund in 2019, Konkuk University Researcher Fund in 2020, and the National Research Foundation of Korea (NRF) funded by the Ministry of Education, Science and Technology (2020R1C1C1A01005229).

Supplementary Materials

Fig. S1: the sample haze images. (a) Konkuk University office. (b) The residential area. (c) The experimental chamber. (*Supplementary Materials*)

References

- [1] K. H. Kim, E. Kabir, and S. Kabir, "A review on the human health impact of airborne particulate matter," *Environment International*, vol. 74, pp. 136–143, 2015.
- [2] February 2020, http://www.nbrienvic.nic.in/Database/1_2463.aspx.
- [3] Y. Wang, "The analysis of the impacts of energy consumption on environment and public health in China," *Energy*, vol. 35, no. 11, pp. 4473–4479, 2010.
- [4] J. D. Sacks, L. W. Stanek, T. J. Luben et al., "Particulate matter-induced health effects: who is susceptible?," *Environmental Health Perspectives*, vol. 119, no. 4, pp. 446–454, 2011.
- [5] A. Mukherjee and M. Agrawal, "World air particulate matter: sources, distribution and health effects," *Environmental Chemistry Letters*, vol. 15, no. 2, pp. 283–309, 2017.
- [6] Q. Zhang, Y. Niu, Y. Xia et al., "The acute effects of fine particulate matter constituents on circulating inflammatory biomarkers in healthy adults," *Science of the Total Environment*, vol. 707, article 135989, 2020.
- [7] O. Raaschou-Nielsen, Z. J. Andersen, R. Beelen et al., "Air pollution and lung cancer incidence in 17 European cohorts: prospective analyses from the European Study of Cohorts for Air Pollution Effects (ESCAPE)," *The Lancet Oncology*, vol. 14, no. 9, pp. 813–822, 2013.
- [8] H. C. Kim, S. Kim, B.-U. Kim et al., "Recent increase of surface particulate matter concentrations in the Seoul Metropolitan Area, Korea," *Scientific Reports*, vol. 7, no. 1, pp. 1–7, 2017.

- [9] OECD, *OECD Economic Surveys: Korea 2018*, OECD Publishing, 2018.
- [10] Y. Yang, Z. Hu, K. Bian, and L. Song, "ImgSensingNet: UAV vision guided aerial-ground air quality sensing system," in *IEEE INFOCOM 2019 - IEEE Conference on Computer Communications*, pp. 1207–1215, Paris, France, France, 2019.
- [11] Y. Cheng, X. Li, Z. Li et al., "AirCloud: a cloud-based air-quality monitoring system for everyone," in *Proceedings of the 12th ACM Conference on Embedded Network Sensor Systems - SenSys '14*, pp. 251–265, Memphis, Tennessee, USA, 2014.
- [12] March 2020, <https://www.thermofisher.com/order/catalog/product/TEOM1405>.
- [13] March 2020, <https://metone.com/products/aerocet-831-handheld-particle-counter>.
- [14] March 2020, <http://www.dylospromod.com/dcproairqumo.html>.
- [15] March 2020, <https://www.airkorea.or.kr/web/stationInfo?pMENU=93>.
- [16] Y. Zheng, F. Liu, and H. P. Hsieh, "U-air: when urban air quality inference meets big data," in *Proceedings of the 19th ACM SIGKDD international conference on Knowledge discovery and data mining - KDD '13*, pp. 1436–1444, Chicago, Illinois, USA, 2013.
- [17] Y. Gao, W. Dong, K. Guo et al., "Mosaic: a low-cost mobile sensing system for urban air quality monitoring," in *IEEE INFOCOM 2016 - The 35th Annual IEEE International Conference on Computer Communications*, pp. 1–9, San Francisco, CA, USA, 2016.
- [18] J. Li, Q. Fu, J. Huo et al., "Tethered balloon-based black carbon profiles within the lower troposphere of Shanghai in the 2013 East China smog," *Atmospheric Environment*, vol. 123, pp. 327–338, 2015.
- [19] K. Weber, G. Heweling, C. Fischer, and M. Lange, "The use of an octocopter UAV for the determination of air pollutants—a case study of the traffic induced pollution plume around a river bridge in Duesseldorf, Germany," *International Journal of Education and Learning Systems*, vol. 2, 2017.
- [20] C. Liu, F. Tsow, Y. Zou, and N. Tao, "Particle pollution estimation based on image analysis," *PLoS One*, vol. 11, no. 2, article e0145955, 2016.
- [21] S. Li, T. Xi, Y. Tian, and W. Wang, "Inferring fine-grained PM_{2.5} with Bayesian based kernel method for crowdsourcing system," in *GLOBECOM 2017 - 2017 IEEE Global Communications Conference*, pp. 1–6, Singapore, Singapore, 2017.
- [22] Z. Pan, H. Yu, C. Miao, and C. Leung, "Crowdsensing air quality with camera-enabled mobile devices," in *Twenty-Ninth IAAI Conference*, San Francisco, California, USA, 2017.
- [23] H. Wang, X. Yuan, X. Wang, Y. Zhang, and Q. Dai, "Real-time air quality estimation based on color image processing," in *2014 IEEE Visual Communications and Image Processing Conference*, pp. 326–329, Valletta, Malta, 2014.
- [24] A. Levin, D. Lischinski, and Y. Weiss, "A closed-form solution to natural image matting," *IEEE transactions on pattern analysis and machine intelligence*, vol. 30, no. 2, pp. 228–242, 2007.
- [25] G. E. Hinton and R. R. Salakhutdinov, "Reducing the dimensionality of data with neural networks," *Science*, vol. 313, no. 5786, pp. 504–507, 2006.
- [26] K. He, J. Sun, and X. Tang, "Single image haze removal using dark channel prior," *IEEE Transactions on Pattern Analysis and Machine Intelligence*, vol. 33, no. 12, pp. 2341–2353, 2011.
- [27] C. Li, J. Guo, F. Porikli, H. Fu, and Y. Pang, "A cascaded convolutional neural network for single image dehazing," *IEEE Access*, vol. 6, pp. 24877–24887, 2018.
- [28] V. Natarajan, "Enhanced single image uniform and heterogeneous fog removal using guided filter," in *Artificial Intelligence and Evolutionary Computations in Engineering Systems*, S. Dash, K. Vijayakumar, B. Panigrahi, and S. Das, Eds., vol. 517 of *Advances in Intelligent Systems and Computing*, pp. 453–463, Springer, Singapore, 2017.
- [29] K. He, X. Zhang, S. Ren, and J. Sun, "Deep residual learning for image recognition," in *2016 IEEE Conference on Computer Vision and Pattern Recognition (CVPR)*, pp. 770–778, Las Vegas, NV, USA, 2016.
- [30] S. Han, H. Mao, and W. J. Dally, "Deep compression: compressing deep neural networks with pruning, trained quantization and Huffman coding," 2015, <https://arxiv.org/abs/1510.00149>.
- [31] S. Han, J. Pool, J. Tran, and W. Dally, "Learning both weights and connections for efficient neural network," in *Advances in Neural Information Processing Systems*, pp. 1135–1143, Curran Associates, Inc., 2015.
- [32] J. Yamanaka, S. Kuwashima, and T. Kurita, "Fast and accurate image super resolution by deep CNN with skip connection and network in network," in *Neural Information Processing*, D. Liu, S. Xie, Y. Li, D. Zhao, and E. S. El-Alfy, Eds., vol. 10635 of *ICONIP 2017. Lecture Notes in Computer Science*, pp. 217–225, Springer, Cham, 2017.
- [33] D. M. Strong, P. Blomgren, and T. F. Chan, "Spatially adaptive local-feature-driven total variation minimizing image restoration," in *Statistical and Stochastic Methods in Image Processing II*, vol. 3167, pp. 222–233, San Diego, CA, USA, 1997.
- [34] M. Lin, Q. Chen, and S. Yan, "Network in network," 2013, <https://arxiv.org/abs/1312.4400>.
- [35] C. Szegedy, W. Liu, Y. Jia et al., "Going deeper with convolutions," in *2015 IEEE Conference on Computer Vision and Pattern Recognition (CVPR)*, pp. 1–9, Boston, MA, USA, 2015.
- [36] A. Krizhevsky, I. Sutskever, and G. E. Hinton, "Imagenet classification with deep convolutional neural networks," *Advances in neural information processing systems*, pp. 1097–1105, Curran Associates Inc., 2012.
- [37] S. Kim, S. Jung, S. Yang et al., "Vision-based deep Q-learning network models to predict particulate matter concentration levels using temporal digital image data," *Journal of Sensors*, vol. 2019, 10 pages, 2019.
- [38] Y. Xie, E. Franz, M. Chu, and N. Thuerey, "tempoGAN: a temporally coherent, volumetric gan for super-resolution fluid flow," *ACM Transactions on Graphics*, vol. 37, no. 4, pp. 1–15, 2018.
- [39] B. Cai, X. Xu, and D. Tao, "Real-time video dehazing based on spatiotemporal mrf," in *Advances in Multimedia Information Processing - PCM 2016. PCM 2016*, E. Chen, Y. Gong, and Y. Tse, Eds., vol. 9917 of *Lecture Notes in Computer Science*, pp. 315–325, Springer, Cham, 2016.
- [40] W. Ren and X. Cao, "Deep video dehazing," in *Advances in Multimedia Information Processing - PCM 2017. PCM 2017*, B. Zeng, Q. Huang, A. Saddik, H. Li, S. Jiang, and X. Fan,

Eds., vol. 10735 of Lecture Notes in Computer Science, pp. 14–24, Springer, Cham, 2017.

- [41] B. Li, X. Peng, Z. Wang, J. Xu, and D. Feng, “End-to-end united video dehazing and detection,” in *Thirty-Second AAAI Conference on Artificial Intelligence*, New Orleans, Louisiana, USA, 2018.
- [42] D. Sun, S. Roth, and M. J. Black, “Secrets of optical flow estimation and their principles,” in *2010 IEEE Computer Society Conference on Computer Vision and Pattern Recognition*, pp. 2432–2439, San Francisco, CA, USA, 2010.
- [43] W. Yuchi, E. Gombojav, B. Boldbaatar et al., “Evaluation of random forest regression and multiple linear regression for predicting indoor fine particulate matter concentrations in a highly polluted city,” *Environmental Pollution*, vol. 245, pp. 746–753, 2019.

Research Article

Fast Traffic Sign Detection Approach Based on Lightweight Network and Multilayer Proposal Network

Hoanh Nguyen 

Faculty of Electrical Engineering Technology, Industrial University of Ho Chi Minh City, Ho Chi Minh City, Vietnam

Correspondence should be addressed to Hoanh Nguyen; nguyenhoanh@iuh.edu.vn

Received 3 March 2020; Revised 15 May 2020; Accepted 3 June 2020; Published 19 June 2020

Academic Editor: Bin Gao

Copyright © 2020 Hoanh Nguyen. This is an open access article distributed under the Creative Commons Attribution License, which permits unrestricted use, distribution, and reproduction in any medium, provided the original work is properly cited.

Vision-based traffic sign detection plays a crucial role in intelligent transportation systems. Recently, many approaches based on deep learning for traffic sign detection have been proposed and showed better performance compared with traditional approaches. However, due to difficult conditions in driving environment and the size of traffic signs in traffic scene images, the performance of deep learning-based methods on small traffic sign detection is still limited. In addition, the inference speed of current state-of-the-art approaches on traffic sign detection is still slow. This paper proposes a deep learning-based approach to improve the performance of small traffic sign detection in driving environments. First, a lightweight and efficient architecture is adopted as the base network to address the issue of the inference speed. To enhance the performance on small traffic sign detection, a deconvolution module is adopted to generate an enhanced feature map by aggregating a lower-level feature map with a higher-level feature map. Then, two improved region proposal networks are used to generate proposals from the highest-level feature map and the enhanced feature map. The proposed improved region proposal network is designed for fast and accuracy proposal generation. In the experiments, the German Traffic Sign Detection Benchmark dataset is used to evaluate the effectiveness of each enhanced module, and the Tsinghua-Tencent 100K dataset is used to compare the effectiveness of the proposed approach with other state-of-the-art approaches on traffic sign detection. Experimental results on Tsinghua-Tencent 100K dataset show that the proposed approach achieves competitive performance compared with current state-of-the-art approaches on traffic sign detection while being faster and simpler.

1. Introduction

Vision-based traffic sign recognition plays an essential role in intelligent transport systems such as an automated driving system and an advanced driver assistance system. A traffic sign recognition system normally includes two stages: traffic sign detection and traffic sign recognition. Traffic sign detection takes images captured from a camera to locate exactly traffic sign regions, while traffic sign recognition classifies each traffic sign into a corresponding class. Detected traffic signs from a detection stage are utilized as inputs for a recognition stage. Thus, the accuracy of traffic sign detection has a dramatic effect on the accuracy of the whole system. Many approaches have been proposed to detect traffic sign [1]. Traditional methods [2–7] are usually based on hand-crafted features such as color, texture, edge, and other low-level features to detect traffic sign in an image. In driving environ-

ment, due to the diversity of the traffic sign appearance, the occlusion of traffic sign by other objects, and the effect of lighting conditions, traditional methods for traffic sign detection showed poor performance.

With the fast development of deep learning recently, many deep learning-based approaches for traffic sign detection [8–15] have been proposed and showed outstanding performance compared with traditional approaches. Deep learning-based methods for traffic sign detection first create traffic sign candidates, and classifiers are then used to identify traffic sign and background class. Although deep learning-based methods for traffic sign detection performed well in difficult driving environments, the performance of these methods is still low in challenging conditions as discussed below:

- (i) The size of traffic signs is quite small in traffic scene images, and small traffic sign detection is much more

challenging than large traffic sign detection. Most recent methods for traffic sign detection are focused on a large traffic sign. Thus, the performance of these methods is limited on small traffic sign detection

- (ii) The inference speed of the traffic sign detection method is a large concern in driving environments where vehicles are unlikely to be equipped with high-end hardware components. Most recent methods for traffic sign detection are implemented on high-end systems. Thus, it is necessary to build a faster framework for traffic sign detection in driving environments

To tackle these issues, this paper designs a deep learning-based framework for fast and efficient traffic sign detection. The proposed framework uses ESPNetv2 network [16] as the based convolution layers for increasing the processing speed. To enhance the performance of the proposed framework on small traffic sign detection, a deconvolution module is used to create an enhanced feature map from convolution feature maps generated by the base network. In the proposal generation process, two improved region proposal networks (RPNs) are adopted to generate both large and small traffic sign proposals from input convolution layers. The improved region proposal network is designed based on the original region proposal network [17] for fast and efficient proposal generation. The proposed approach is evaluated on the German Traffic Sign Detection Benchmark dataset and Tsinghua-Tencent 100K dataset. The results show that the proposed approach achieves competitive performance compared with current state-of-the-art approaches while being faster and simpler. The main contributions of this paper can be summarized as follows:

- (i) For the purpose of fast and efficient traffic sign detection, this paper adopts a lightweight deep network as the base network. The proposed base network substantially reduces the computational costs of the whole framework
- (ii) To generate proposals, this paper designs a novel RPN based on the original RPN to increase the inference speed and detection accuracy of the proposed framework. In the improved RPN, 1×1 convolution layer is first used after the input feature maps to reduce the number of parameters. Then, dilated convolution is used to enlarge the receptive field, thus including more information from other areas to help recognize the boundaries of objects and maintaining the number of parameters. The proposed RPN can be adopted in other object detection tasks such as pedestrian detection and vehicle detection
- (iii) To improve the performance of the proposed network on small traffic sign detection, a deconvolution module is used to generate enhanced feature map, which contains more discriminative representation for small traffic signs. The deconvolution module

enhances the shallow feature map from a lower feature layer with a deeper feature map from a higher feature layer

- (iv) To further improve the detection performance of the proposed network, a region proposal generation module including two improved RPNs is designed to produce a set of good proposals from the enhanced feature map and the highest-level feature map
- (v) Experimental results on public datasets show that the proposed approach achieves comparable accuracy compared with other state-of-the-art approaches on traffic sign detection while being faster and simpler. The proposed framework can be applied in real-time intelligent transport systems

The remaining of this paper is organized as follows. Section 2 reviews the related work. Section 3 details the proposed framework. Section 4 provides the experimental results and comparison between the proposed method and other methods on public datasets. Finally, the conclusions are drawn in Section 5.

2. Related Work

2.1. Traffic Sign Detection. Vision-based traffic sign detection can be divided into two groups: traditional method and deep learning-based method. Traditional methods are usually based on hand-crafted features such as color and shape to detect traffic signs. Bahlmann et al. [2] proposed using a set of Haar wavelet features obtained from AdaBoost training to detect traffic signs and Bayesian generative modeling for classification. Salti et al. [3] proposed an approach based on interest region extraction rather than sliding window detection. In addition, the SVM classifier which takes histogram of oriented gradients in the regions of interest as the input feature is used for classification. In [4], the authors utilized circle detection algorithm and an RGB-based color thresholding technique to detect traffic sign. For traffic sign recognition, an ensemble of features including histogram of oriented gradients, local binary patterns, and Gabor features is employed within a support vector machine classification framework. Timofte et al. [5] proposed to combine 2D and 3D techniques to improve results of traffic sign detection and recognition. In [6], a localization refinement approach for traffic sign candidates was proposed. Color and shape priors are utilized in an iterative optimization approach to accurately segment the traffic signs as foreground objects. In [7], the authors proposed a system with three working stages: image preprocessing, detection, and recognition. The proposed system demonstrated that using RGB color segmentation and shape matching followed by a support vector machine classifier leads to promising results. Manual features, such as histogram of oriented gradients and enhancement information of typical color or geometric shape, tend to fail in many difficult driving environments. Thus, traditional methods for traffic sign detection showed poor performance.

Recently, with the fast development of deep convolutional neural networks (CNN), many methods for traffic sign detection based on deep CNN have been proposed and showed better performance compared with traditional methods. Wu et al. [10] proposed to use support vector machines to transform the original image into the gray scale image at first stage. A convolutional neural network with fixed and learnable layers was then used for detection and recognition traffic signs. In [11], the authors proposed a novel framework with two deep learning components, including fully convolutional network-guided traffic sign proposals and deep CNN for object classification. Zhu et al. [9] proposed a fully convolutional network which performs both detection and classification simultaneously. Liu et al. [8] proposed the multiscale region-based convolutional neural network which uses a multiscale deconvolution operation to upsample the features of the deeper convolution layers and concatenates them to those of the shallow layer to construct the fused feature map. In [12], a detector based on faster R-convolutional neural networks and the structure of MobileNet was designed and implemented for detecting traffic sign in driving environments. Moreover, color and shape information has been used to refine the localizations of small traffic signs. Yang et al. [13] designed a novel detection module based on traffic sign proposal extraction and classification built upon a color probability model and a color histogram of oriented gradient. Then, a convolutional neural network is used to further classify the detected signs into their subclasses within each superclass. Li et al. [14] proposed a model with three stages: channel-wise coarse feature extraction is first adopted to produce coarse feature maps with much information loss, channel-wise hierarchical feature refinement is then used to refine hierarchical features, and hierarchical feature map fusion is used at the final stage to fuse hierarchical feature maps to generate the final traffic sign saliency map. In [15], the authors introduced an attention network to Faster R-CNN for finding potential region of interest and roughly classifying them into three categories according to color feature of the traffic signs. Then, the fine region proposal network is designed to produce the final region proposals from a set of anchors per feature map location. Zhang et al. [18] proposed a cascaded R-CNN to obtain the multiscale features in pyramids and a multiscale attention method to obtain the weighted multiscale features by dot product and softmax to highlight the traffic sign features and improve the accuracy of the traffic sign detection. In [19], the authors proposed novel lightweight networks that can obtain higher recognition precision while preserving less trainable parameters in the models. In addition, a new module combines two streams of feature channels with dense connectivity was introduced to improve the accuracy of traffic sign recognition.

2.2. Small Object Detection. In a traffic scene image, traffic signs usually occupy only a small portion of the entire image. In addition, small object detection is much more challenging than large object detection. Thus, many deep learning frameworks have been proposed to enhance the information representation of small objects in convolution feature maps.

Zhang et al. [20] proposed a model that consists of a region proposal network that generates candidate object regions and an object detection network that incorporates multiscale features and global information. In [21], the authors proposed a unified deep CNN for fast multiscale object detection. In this framework, the detection is performed at various intermediate network layers to enable the detection of all object scales. Cao et al. [22] proposed an improved algorithm based on faster region-based CNN for small object detection. An improved loss function based on intersection over union, the multiscale convolution feature fusion, and the improved nonmaximum suppression algorithm is introduced to enhance the performance for small object detection. Li et al. [23] proposed a new perceptual generative adversarial network model that improves small object detection through narrowing representation difference of small objects from the large ones. Wei et al. [24] proposed three enhancements for CNN-based visual object detection for advanced driving assistance systems, including using deconvolution and fusion of CNN feature maps to create enhanced feature maps, adopting soft nonmaximal suppression to address the object occlusion challenge, and setting anchor boxes properly for better object matching and localization. In [25], Lin et al. exploited the inherent multiscale, pyramidal hierarchy of deep convolutional networks to construct feature pyramids with marginal extra cost.

3. Proposed Framework

Figure 1 illustrates the overall framework of the proposed approach. The base network based on ESPNetv2 network [16] first takes input image to generate convolution feature maps. To improve the ability of the proposed framework on detecting of small traffic signs, a deconvolution module is used to aggregate an output feature map at layer 2 with an output feature map at layer 3 to create an enhanced feature map. Then, two improved region proposal networks are adopted to generate proposals from the highest-level convolution feature map and the enhanced convolution feature map. The improved region proposal network includes a 1×1 convolution layer to reduce the number of parameters in the subsequent convolutional layers and a 3×3 dilated convolution to enlarge the receptive field, thus improving the detection accuracy and the inference speed of the proposal generation stage. In the detection network, a region of interest pooling layer is adopted to adjust the size of proposals to fixed size feature maps, and fully connected layers are used for classifying proposals and regressing the bounding box of proposals. In the following sections, the proposed approach is explained in detail.

3.1. The Base Network. Most of deep learning-based approaches for traffic sign detection are focused on detection accuracy. In driving environment, apart from the detection accuracy, the inference speed is also a large concern. Moreover, vehicles in driving environments are unlikely to be equipped with high-end graphic cards as powerful as used in research environments. Thus, it is necessary to build a

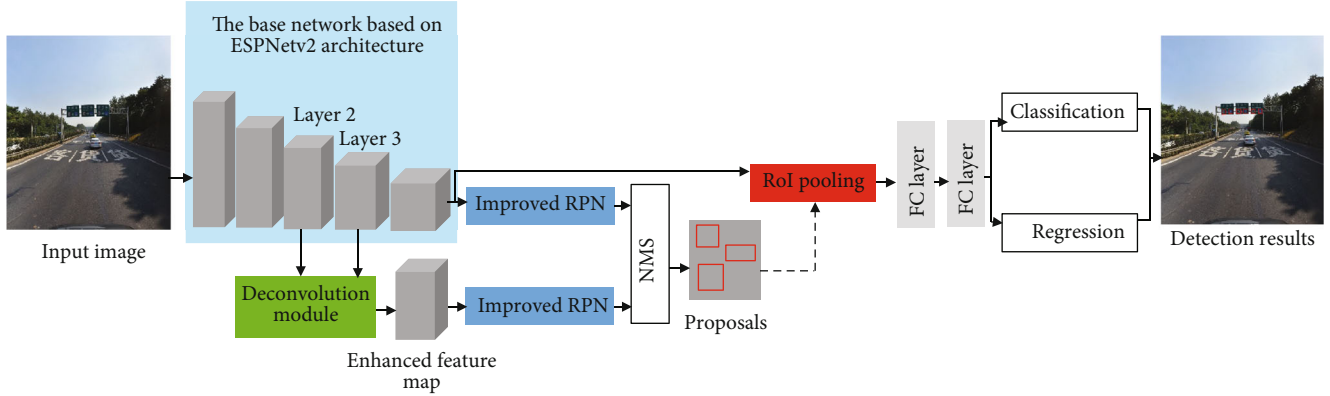


FIGURE 1: The overall framework of the proposed approach.

TABLE 1: Performance comparison of different efficient networks on the ImageNet validation set.

Network	# parameters	FLOPs	Top-1 accuracy
MobileNetv1 [27]	2.59 M	325 M	68.4
MobileNetv2 [29]	3.47 M	300 M	71.8
ShuffleNetv1 [30]	3.46 M	292 M	71.5
ESPNetv2	3.49 M	284 M	72.1

faster network for traffic sign detection in driving environments. In [26], Liu et al. showed that about 80% of the forward time is spent on the base convolution layers. Thus, using a faster base network can greatly improve the inference speed of the framework. ESPNetv2 network [16] is a fast and efficient network which uses depth-wise dilated separable convolutions instead of depth-wise separable convolutions [27] to learn representations from a large effective receptive field. Table 1 provides a performance comparison between ESPNetv2 and state-of-the-art efficient networks on the ImageNet 1000-way classification dataset [28]. As shown in Table 1, ESPNetv2 achieves the best performance with the smallest computational budgets (computational budget = 284 million FLOPs). In addition, ESPNetv2 has similarity in the number of parameters compared with ShuffleNetv1 and MobileNetv2 while being more accurate. Thus, ESPNetv2 architecture is adopted as the base network in this paper for fast and efficient traffic sign detection.

Supposing the resolution of input images is 224×224 , the architecture of the ESPNetv2 used in this paper is illustrated in Figure 2 with a kernel size, filter number, and output size. The ESPNetv2 network replaces standard convolutions by extremely efficient spatial pyramid of depth-wise dilated separable convolutions (EESP units) and strided extremely efficient spatial pyramid of depth-wise dilated separable convolutions (strided EESP units). At each layer, ESPNetv2 repeats the EESP units several times to increase the depth of the network. Figure 3 illustrates the structure of EESP unit (a) and strided EESP unit (b). The EESP unit first projects the high-dimensional input feature map into a low-dimensional

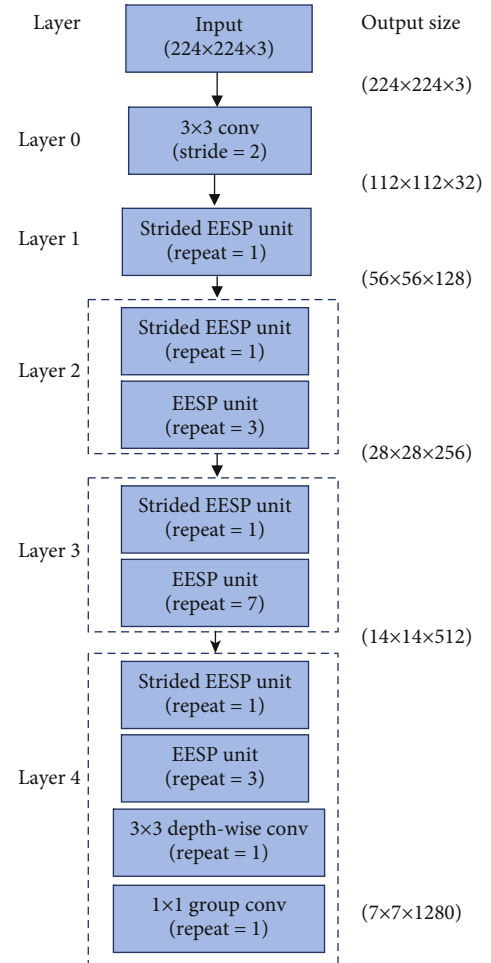
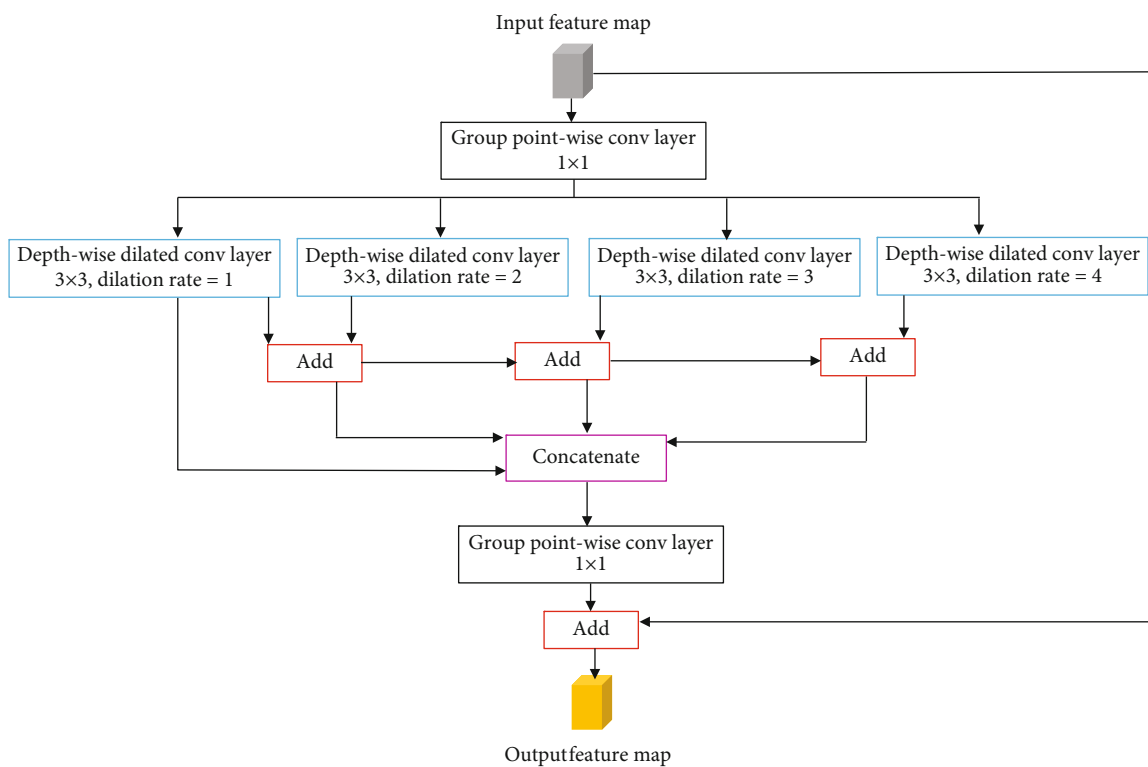
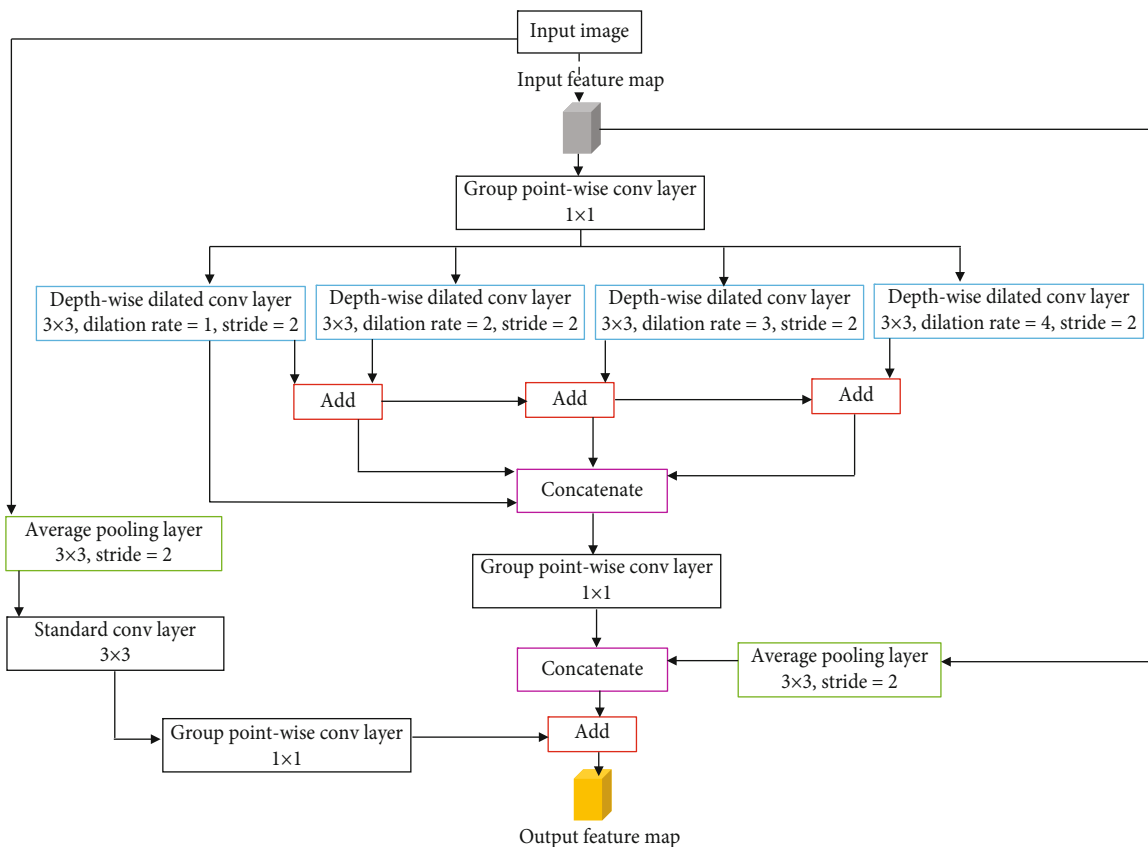


FIGURE 2: The structure of the ESPNetv2 network used in this paper.

space using group point-wise convolutions and then learns the representations in parallel using depth-wise dilated separable convolutions with different dilation rates. Different dilation rates in each branch allow the EESP unit to learn the representations from a large effective receptive field. With group point-wise and depth-wise dilated



(a)



(b)

FIGURE 3: The structure of EESP unit (a) and strided EESP unit (b). ESPNetv2 repeats the EESP units several times to increase the depth of the network.

separable convolutions, the total complexity of the EESP unit is reduced [16]. On the other hand, the strided EESP unit is used to learn representations efficiently at multiple scales. In the strided EESP unit, depth-wise dilated convolutions are replaced with their strided counterpart. In addition, an average pooling layer with stride 2 is added in the strided EESP unit as shown in Figure 3(b). To better encode spatial relationships and learn representations efficiently, an efficient long-range shortcut connection between the input image and the current downsampling unit is added in the strided EESP unit. This connection first downsamples the image to the same size as that of the feature map by repeating a 3×3 average pooling layer and then learns the representations using a stack of two convolutions. The first convolution is a standard 3×3 convolution that learns the spatial representations while the second convolution is a 1×1 point-wise convolution that learns linear combinations between the input and projects it to a high-dimensional space.

Features from the highest-level convolutional layer of the ESPNetv2 architecture could better describe the characteristics of large-scale traffic signs in an image, so the highest-level convolutional layer of the ESPNetv2 network is adopted to generate proposals to ensure the effectiveness of the method for large-scale traffic sign detection. For small-scale traffic signs, features from the larger scales (lower CNN layers) could better describe the characteristics of small-scale traffic signs. However, shallow feature maps from the low layers of feature pyramid inherently lack fine semantic information for object recognition. Thus, this paper adds a deconvolutional module, which fuses the feature map at layer 2 and layer 3 of the ESPNetv2 network, to generate enhanced feature map to better describe the characteristics of small-scale traffic signs. With this deconvolutional module, the semantics from higher layers can be conveyed into lower layers to increase the representation capacity. Details of the deconvolutional module will be explained in the next section.

3.2. Deconvolution Module. Deconvolution module has shown to be helpful for small object detection in DSSD [31]. To enhance a shallow feature map from a lower feature layer with a deeper feature map from a higher feature layer and improve detection performance on small traffic signs, this paper adds a deconvolution module to aggregate the output feature at layer 2 with output feature at layer 3. With a deconvolution module, the semantics from higher feature layer can be conveyed into a lower feature layer to increase the representation capacity. Figure 4 illustrates the architecture of the deconvolution module used in this paper. As shown in Figure 4, a 3×3 convolution layer is first connected with a lower-level feature map extracted after layer 2. For the deconvolution branch, a 2×2 deconvolution layer is used followed by a 3×3 convolution layer to upsample the corresponding higher-level feature map. A batch normalization layer is added after each convolution layer. The higher-level feature map is extracted after layer 3. The deconvolution layer is applied to enlarge the feature map size in order to match the size of the lower-level feature map. Notably, the

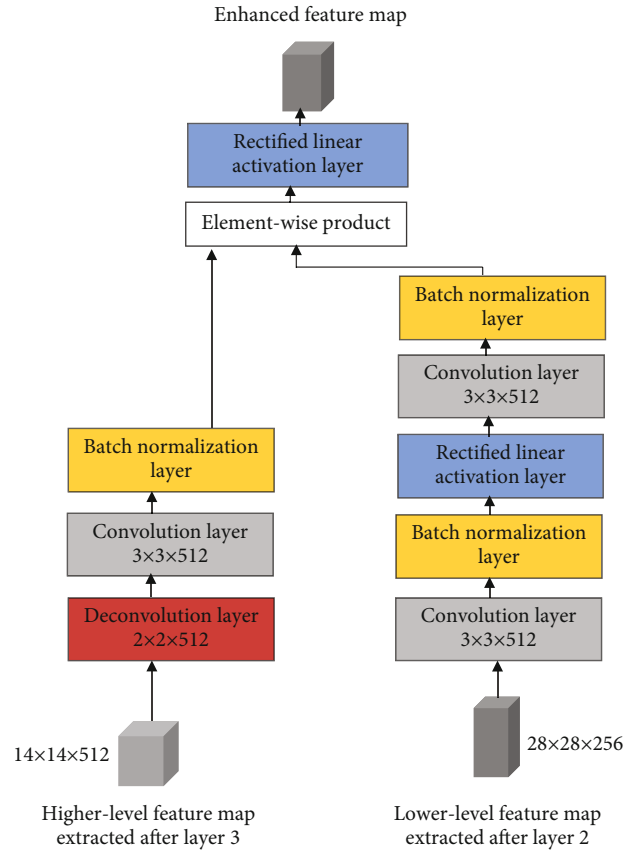


FIGURE 4: The structure of deconvolution module used in this paper.

deconvolution operation is different from the upsampling operation. Deconvolution operation provides a set of parameters by which to learn a nonlinear upsampling of the features in the deep layers while upsampling operation rescales an image to the desired size by using an interpolation method. Finally, the outputs of these two feature layers, which have the same spatial size and depth, are combined by an element-wise product and processed by a ReLU layer to produce an enhanced feature map.

3.3. Proposal Generation with Improved Region Proposal Network. The region proposal network (RPN) [17] is an efficient and accurate region proposal generation network which showed encouraging performance in general object detection. To increase the inference speed and detection accuracy of the proposed framework, this paper designs an improved RPN based on the RPN [17]. Figure 5 illustrates the structure of the original RPN (a) and the improved RPN (b) proposed in this paper. First, to compress the RPN and increase the inference speed, this paper reduces the number of channels of input feature maps to decrease the number of parameters in the RPN. Decreasing the input channels of input features can further reduce the number of parameters in the subsequent convolutional layers. ResNet [32] used a 1×1 convolution layer to reduce the number of input channels without losing accuracy while also gaining efficiency. Thus, this paper adopts a 1×1 convolution layer after input feature maps to reduce the number of parameters in the RPN. From the

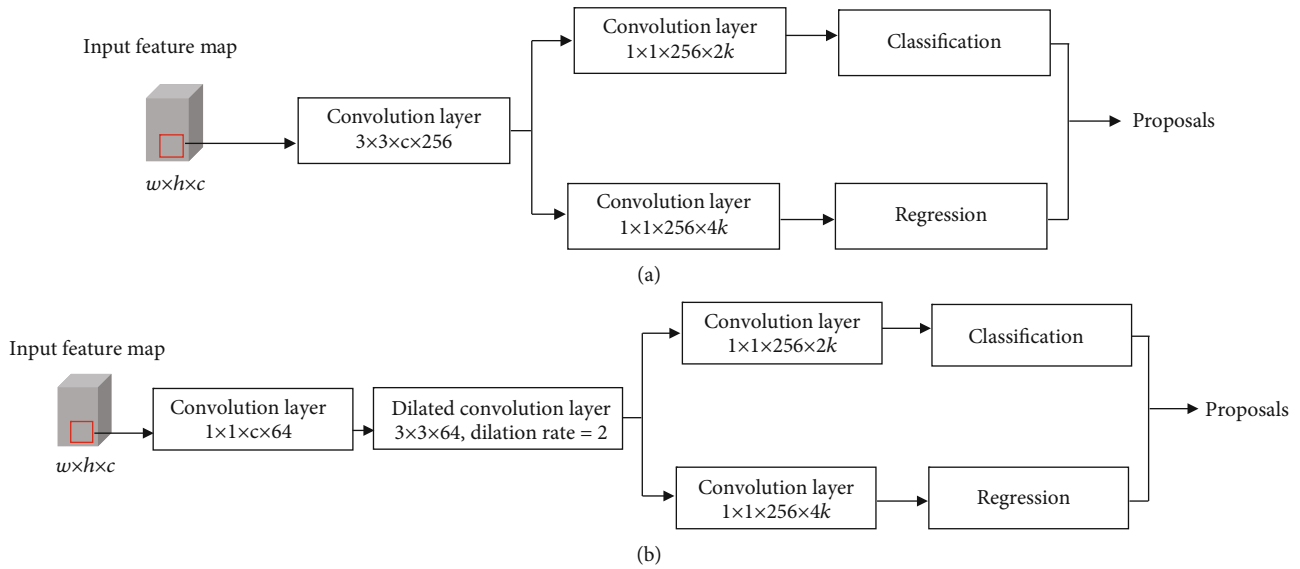


FIGURE 5: The structure of the original RPN (a) and the improved RPN proposed in this paper (b).

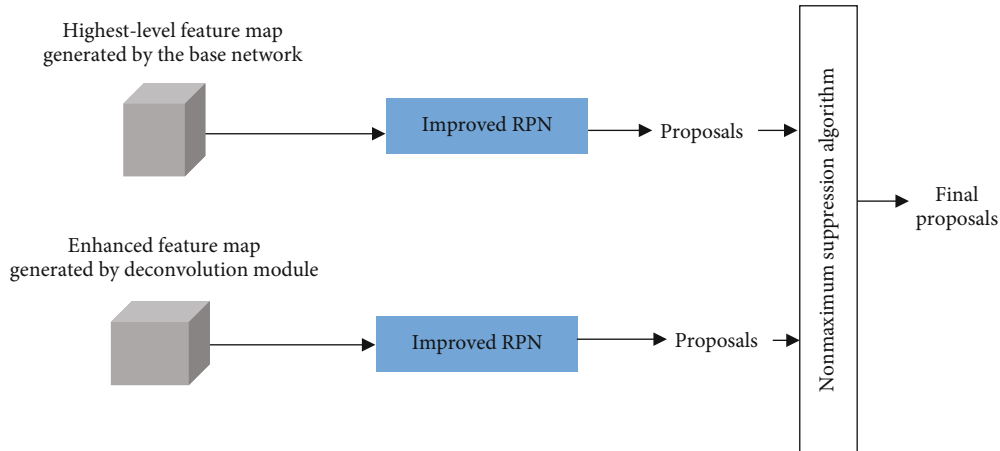


FIGURE 6: The architecture of the region proposal generation module.

experimental results, this paper reduces the number of input channels to 64 for obtaining good proposals and fast processing speed. Second, to improve the detection accuracy, dilated convolution [33] is adopted to replace standard convolution in the original RPN. Dilated convolution is a powerful module in the context of semantic segmentation. Dilated convolution is used to enlarge the receptive field, thus including more information from other areas to help recognize the boundaries of objects. Another advantage is that using dilated convolution does not increase the number of parameters or the amount of computation because the zero operations are skipped. The improved RPN proposed in this paper can be adopted in other object detection tasks, such as pedestrian detection and vehicle detection.

The enhanced feature map generated by the deconvolutional module could improve the resolution and semantic information for small-scale traffic signs, and the feature map from the highest convolutional layer of the ESPNetv2 network could better describe the characteristics of the

large-scale traffic signs in an image. The region proposal generation module is proposed to receive the enhanced feature map and the highest-level convolution feature map and produce a set of proposals to be further processed by the nonmaximum suppression (NMS) algorithm at the end of the region proposal generation module. The region proposal generation module includes two improved RPNs working on different convolution layers for generating proposals as shown in Figure 6. Each improved RPN first generates a set of anchor boxes from the input convolution feature map and then produces two different outputs for each of the anchor box. The first one is an objectness score, which means the probability that an anchor is an object. The second output is the bounding box regression for adjusting the anchors to better fit the object. Since anchors are usually highly overlapped with each other, nonmaximum suppression algorithm is adopted at the end of the region proposal generation module to solve the issue of duplicate proposals.

TABLE 2: Dataset summary.

Dataset	Number of images	Resolution (width \times height)	Ratio between training and testing images	Number of traffic signs	The size of traffic sign
GTSDB	900	1360 \times 800	2 : 1	1206	16 \times 16 to 128 \times 128
TT-100K	100000	2048 \times 2048	2 : 1	30000	2 \times 7 to 397 \times 394

3.4. Detection Network. The detection network includes a region of interest (RoI) pooling layer for adjusting the size of proposals to fixed size feature maps and fully connected (FC) layers for classifying proposals and regressing the bounding box of proposals. The RoI pooling layer uses max pooling to convert the features inside any valid region of interest into a small feature map with a fixed spatial extent of $H \times W$. RoI pooling works by dividing the $h \times w$ RoI proposal into a $H \times W$ grid of subwindows of approximate size $h/H \times w/W$ and then max-pooling the values in each subwindow into the corresponding output grid cell. RoI pooling avoids repeatedly computing the convolutional layers, so it can significantly speed up both train and test time. After extracting fixed size feature maps for each of proposals via RoI pooling, these feature maps are used for classification. The classification stage has two different goals: classify proposals into traffic sign and background class and adjust the bounding box for each of detected traffic sign according to the predicted class. Two FC layers with 2048 neurons are adopted in this paper to extract discriminative features for traffic sign. The features from each RoI are flattened into a vector and fed into two separate FC layers: a box classification layer and a box regression layer. The first FC layer is then fed into the softmax layer to compute the confidence probabilities of being traffic sign and background. The second FC layer with linear activation functions regresses the bounding box of detected traffic sign.

3.5. Training and Loss Function. Training process of the proposed framework includes two phases. First, the region proposal generation network is trained with training samples, and then, both the region proposal generation network and the detection network are trained. For convolution feature with resolution $M \times N$, there are total $M \times N \times k$ anchor boxes. These anchor boxes are highly overlapped with each other. Moreover, there are much more negative anchor boxes than positive anchor boxes, which will lead to bias during the training process if all anchor boxes are used for training. For an anchor box a_k at position (x_m, y_n) in an image, this paper first finds the best matching ground truth box for this anchor box based on the intersection of union (IoU) to create a training sample for this anchor box. The IoU between two anchor boxes a_k and a_i is defined as the following equation:

$$\text{IoU} = \frac{\text{area}(a_k \cap a_i)}{\text{area}(a_k \cup a_i)}. \quad (1)$$

Let a_{gtk} represents the best matching ground truth box for anchor box a_k , and $\text{IoU}_{a_k, a_{gtk}}$ represents the IoU overlap between anchor box a_k and ground truth box a_{gtk} . If $\text{IoU}_{a_k, a_{gtk}}$ is higher than 0.7, the anchor box a_k is selected as

positive anchor. If $\text{IoU}_{a_k, a_{gtk}}$ is lower than 0.3, the anchor is selected as negative anchor. Otherwise, this anchor will be discarded and is not used as a training sample. Then, 256 anchor boxes from one image are randomly sampled as a minibatch, where the ratio between positive and negative anchors is up to 1 : 1. The regression of the bounding box can be obtained from the anchor coordinates and the ground truth bounding box in a similar way presented in [17].

In this paper, the objective loss function is to minimize the weighted sum of classification loss L_{cls} and localization loss L_{reg} for the region proposal generation network and the detection network. The objective loss function is defined as follows:

$$L = \frac{1}{N} \sum_{i=1}^N L_{\text{cls}}(a_i, a_i^*) + \frac{1}{N_p} \sum_{i=1}^{N_p} L_{\text{reg}}(l_i, l_i^*), \quad (2)$$

where N is the size of training samples, N_p is the number of positive samples in training samples, a_i is the predicted probability of anchor i being a traffic sign, a_i^* is the corresponding ground truth label (1 for positive anchor and 0 for negative anchor), l_i is the predicted coordinate offsets for anchor i , and l_i^* is the associated offsets for anchor i relative to the ground truth. Since there is no ground truth bounding box matched with negative anchor boxes, bounding box regression is applied only for positive anchor boxes. In (2), the binary logistic loss is used for box classification, and smooth L1 loss [17] is adopted for box regression. With the above objective function, the network can be trained by backpropagation and stochastic gradient descent strategies.

At test time, test images are fed into feed-forward pass of the network. The proposal generation network generates proposal candidates with bounding boxes and classification confidences. Nonmaximum suppression (NMS) is adopted to select 256 proposals with higher confidences based on the predicted scores, and the detection network further refines the location and class scores for each proposal.

4. Experimental Results and Discussions

In order to compare the effectiveness of the proposed approach with other state-of-the-art approaches on traffic sign detection, this paper conducts experiments on two public datasets: German Traffic Sign Detection Benchmark and Tsinghua-Tencent 100K. The proposed approach is implemented on a Window system machine with Intel Core i7 8700 CPU, NVIDIA GeForce GTX 1080 GPU and 16Gb of RAM. TensorFlow is adopted for implementing deep CNN frameworks.

4.1. Dataset. In this paper, two public datasets are used to evaluate the effectiveness of the proposed approach,

TABLE 3: The numbers of traffic sign instances in each group size of TT-100K dataset.

Size	Small	Medium	Large
Numbers of instances	8953	10702	1512

including German Traffic Sign Detection Benchmark (GTSDB) [34] and Tsinghua-Tencent 100K (TT-100K) [9]. Table 2 summarizes related information of these datasets.

GTSDB is the most widely used dataset to evaluate traffic sign detection approaches. GTSDB contains 900 images and is divided into 600 training images and 300 testing images. The resolution of each image in this dataset is 1360×800 . Each image contains zero to six traffic signs which may appear in every perspective and under every lighting condition. All traffic signs in this dataset can be divided into four categories: prohibitory signs with red color and circular shape, danger signs with red color and triangular shape, mandatory signs with blue color and circular shape, and the rest of traffic signs with different shapes and colors which cannot be classified into these three categories. The sizes of the traffic signs in the images vary from 16×16 to 128×128 .

TT-100K contains 100,000 images with resolution 2048×2048 and covers large variations in illuminance and weather conditions. Of these, 10,000 images contain 30,000 traffic signs in total. The ratio between the training set and testing set is 2:1. Traffic signs in this dataset can be classified into three categories: prohibitory signs with mostly red circle and black information, mandatory signs with mostly blue circle and white information, and warning signs with mostly yellow triangle and a black boundary and information. Furthermore, based on the size of traffic signs in image, traffic signs in this dataset can be divided into three categories according to their size: small traffic signs (area < 322 pixels), medium traffic signs ($322 \text{ pixels} < \text{area} < 962$ pixels), and large traffic signs (area > 962 pixel). Table 3 shows the numbers of traffic sign instances in each group size. Compared with the GTSDB dataset, images in TT-100K dataset are higher resolution, and traffic sign instances are smaller and more diverse. To test the ability of the proposed framework on detection of different object sizes, this paper conducts experiments on all group sizes.

4.2. Evaluation Metrics. In order to compare the results of the proposed method with other methods on traffic sign detection, this paper adopts three widely used criteria for evaluating the proposed method, including precision (P), recall (R), and F -measure (F). These criteria are defined as follows:

$$\begin{aligned}
 P &= \frac{TP}{(TP + FP)}, \\
 R &= \frac{TP}{(TP + FN)}, \\
 F &= 2 \times \frac{(P \times R)}{(P + R)},
 \end{aligned} \tag{3}$$

where TP (True Positive) represents the correct detections of traffic signs, FP (False Positive) represents the wrong detections of traffic signs, and FN (False Negative) represents the

number of missed traffic signs. A traffic sign is considered as correct detection if the IoU between this traffic sign and ground truth traffic sign is at least 0.5.

4.3. Performance Results. In this section, several experiments are first conducted on the GTSDB dataset to evaluate the effectiveness of each proposed module. Then, this paper compares the performance of the proposed approach with other state-of-the-art approaches on the TT-100K dataset, including Faster R-CNN [17], SSD [26], Multiclass Network [9], and MR-CNN [8].

4.3.1. Experimental Results on GTSDB Dataset. To evaluate the effectiveness of each module of the proposed framework, this paper conducts several experiments on the GTSDB dataset and compares the detection results with original Faster R-CNN framework. In the first experiment, the base network in original Faster R-CNN (VGG-16 [35]) is replaced by the ESPNetv2 network. The RPN and the detection network are kept unchanged as in Faster R-CNN. In the second experiment, the improved RPN is used to replace the original RPN in Faster R-CNN. VGG-16 is kept as the base network in this experiment. In the third experiment, VGG-16 is replaced by ESPNetv2, and two improved RPNs are adopted to generate proposals from a convolution feature map after layer 2 and layer 4 of the ESPNetv2 network. In the final experiment, a deconvolution module is added as described in the previous section. At the same time, two improved RPNs are used to generate proposals from a convolution feature map generated by a deconvolution module and the highest-level convolution feature map. To find the best design of the deconvolution module, this paper uses both element-wise sum and element-wise product in the merging process of a deconvolution module. Table 4 shows the detection results and the inference speed of these experiments on GTSDB dataset. As shown in Table 4, the mAP of Faster R-CNN with ESPNetv2 network is 89.40%. By adding additional improved RPNs after layer 2 of the base network, the mAP increases by 5.14%. This result shows that the additional convolution layer with higher resolution can learn discriminative features of small traffic signs and lead to better performance of the framework. Moreover, by adding a deconvolution module to enhance a shallower convolution feature map with a deeper convolution feature map, the mAP increases by 7.5% and 7.62%. These results demonstrate that the convolution feature map constructed by fusing an upsampled deeper convolution layer with a deconvolution operation and a shallower convolution layer is more suitable for small traffic sign detection. For the inference speed, Faster R-CNN with an improved RPN module improves the speed by 0.13 second. In addition, the inference time of Faster R-CNN with ESPNetv2 network is improved by 0.71 second compared with original Faster R-CNN. These results show the effectiveness of the proposed RPN and ESPNetv2 architecture. Figure 7 shows the comparison of detection results of the proposed method (red boxes) and Faster R-CNN (blue boxes) on GTSDB dataset. As shown in Figure 7, the proposed method can locate exactly small traffic signs while Faster R-CNN cannot detect small traffic signs.

TABLE 4: Detection results of ablation experiments on GTSDb dataset.

Method	Detection mAP (%)	Inference time (s)
Faster R-CNN	91.17	0.81
Faster R-CNN+ESPNetv2 network	89.40	0.10
Faster R-CNN+improved RPN+VGG-16	92.20	0.68
Faster R-CNN+ESPNetv2 network+two improve RPNs	94.54	0.11
Faster R-CNN+ESPNetv2 network+two improved RPNs+deconvolution module with element-wise sum	96.90	0.16
Faster R-CNN+ESPNetv2 network+two improved RPNs+deconvolution module with element-wise product	97.02	0.18



FIGURE 7: Detection results of the proposed method (red boxes) and Faster R-CNN (blue boxes) on GTSDb dataset.

4.3.2. *Experimental Results on TT-100K Dataset.* To evaluate the effectiveness of the proposed method, this paper compares the detection results of the proposed method with the results of other state-of-the-art methods on TT-100K dataset, including Faster R-CNN [17], SSD [26], Multiclass Network [9], and MR-CNN [8]. Table 5 shows the comparison of

detection results on all three categories of the TT-100K dataset. As shown in Table 5, the performance of the proposed method outperforms both Faster R-CNN and SSD. More specific, in terms of F -measure, the performance of the proposed method outperforms Faster R-CNN by 51.8%, 19.3%, and 6.4% in a small, medium, and large group, respectively.

TABLE 5: Detection results of the proposed method and other methods on the Tsinghua-Tencent 100K dataset.

Methods	Small			Medium			Large			Inference time (s)
	P (%)	R (%)	F (%)	P (%)	R (%)	F (%)	P (%)	R (%)	F (%)	
Faster R-CNN [17]	24.1	49.8	32.5	65.6	83.7	73.6	80.8	91.2	85.7	2.15
SSD [26]	25.3	43.4	32.0	67.8	77.5	72.3	81.5	86.9	84.1	0.12
Multiclass Network [9]	81.7	87.4	84.5	90.8	93.6	92.2	90.6	87.7	89.1	5.62
MR-CNN [8]	82.9	89.3	86.0	92.6	94.4	93.5	92.0	88.2	90.1	—
Proposed method	80.1	89.0	84.3	91.3	94.6	92.9	92.5	91.8	92.1	0.28



FIGURE 8: Detection results of the proposed method on Tsinghua-Tencent 100K dataset. The regions of detection results are cropped and enlarged at the bottom of each image for better view.

Comparing with SSD, the performance of the proposed method is improved by 51.3%, 20.6%, and 8.0% in a small, medium, and large group, respectively. Since Faster R-CNN

and SSD framework are constrained by the size of its output convolution feature maps, these frameworks are unable to clearly detect small traffic signs. Comparing with Multiclass

Network, the proposed approach achieves a competitive result with a small group and outperforms with a medium and large group. For the inference time, the proposed method takes 0.28 second for processing an image, while Faster R-CNN framework takes up to 2.15 seconds. The ESP-Netv2 network and improved RPN used in this paper dramatically improve the inference time of the proposed approach. SSD is the fastest framework which takes only 0.12 second, but SSD shows worse performance than the proposed approach. From Table 5, MR-CNN achieves the best performance in a small and medium group. Because the inference speed is not mentioned in the original paper of MR-CNN and the code of the paper is not public, the inference time cannot compare directly. However, MR-CNN framework uses multiple deconvolution and concatenation operations at different layers of the base network, so this framework is high computational cost. The proposed approach achieves the best performance in a large group. Moreover, the proposed approach meets the real-time detection standard and can be directly applied to hardware used in driving environments. Figure 8 shows some detection results of the proposed method on Tsinghua-Tencent 100K dataset. As shown in Figure 8, the proposed method can detect small traffic sign instances which occupy less than 2% of image.

5. Conclusions

This paper proposes a deep learning-based framework for fast and efficient traffic sign detection. To improve the inference speed of the proposed framework, ESPNetv2 network is adopted as the based network. A deconvolution module is used to create an enhanced feature map which contains more representation capacity. Furthermore, an improved region proposal network, which includes a 1×1 convolution layer to reduce the number of parameters in the subsequent convolutional layers and a 3×3 dilated convolution to enlarge the receptive field, is designed to increase the performance of a proposal generation stage. In the experiments, two widely used datasets are adopted to evaluate the effectiveness of each enhanced module and the whole framework, including GTSDB dataset and TT-100K dataset. Experimental results on these datasets show that the proposed framework improves the performance of traffic sign detection under challenging driving conditions and meets the real-time requirement of an advanced driver assistant system.

Data Availability

The codes used in this paper are available from the author upon request.

Conflicts of Interest

The author declares that there are no conflicts of interest regarding the publication of this paper.

References

- [1] C. Liu, S. Li, F. Chang, and Y. Wang, "Machine vision based traffic sign detection methods: review, analyses and perspectives," *IEEE Access*, vol. 7, pp. 86578–86596, 2019.
- [2] C. Bahlmann, Y. Zhu, V. Ramesh, M. Pellkofer, and T. Koehler, "A system for traffic sign detection, tracking, and recognition using color, shape, and motion information," in *IEEE Proceedings. Intelligent Vehicles Symposium, 2005*, pp. 255–260, Las Vegas, NV, USA, 2005.
- [3] S. Salti, A. Petrelli, F. Tombari, N. Fioraio, and L. Di Stefano, "Traffic sign detection via interest region extraction," *Pattern Recognition*, vol. 48, no. 4, pp. 1039–1049, 2015.
- [4] S. K. Berkaya, H. Gunduz, O. Ozsen, C. Akinlar, and S. Gunal, "On circular traffic sign detection and recognition," *Expert Systems with Applications*, vol. 48, pp. 67–75, 2016.
- [5] R. Timofte, K. Zimmermann, and L. V. Gool, "Multi-view traffic sign detection, recognition, and 3D localisation," in *2009 Workshop on Applications of Computer Vision (WACV)*, pp. 1–8, Snowbird, UT, USA, December 2009.
- [6] Z. Zhu, J. Lu, R. R. Martin, and S. Hu, "An optimization approach for localization refinement of candidate traffic signs," *IEEE Transactions on Intelligent Transportation Systems*, vol. 18, no. 11, pp. 3006–3016, 2017.
- [7] S. B. Wali, M. A. Hannan, A. Hussain, and S. A. Samad, "An automatic traffic sign detection and recognition system based on colour segmentation, shape matching, and SVM," *Mathematical Problems in Engineering*, vol. 2015, Article ID 250461, 11 pages, 2015.
- [8] Z. Liu, J. Du, F. Tian, and J. Wen, "MR-CNN: a multi-scale region-based convolutional neural network for small traffic sign recognition," *IEEE Access*, vol. 7, pp. 57120–57128, 2019.
- [9] Z. Zhu, D. Liang, S. Zhang, X. Huang, B. Li, and S. Hu, "Traffic-sign detection and classification in the wild," in *2016 IEEE Conference on Computer Vision and Pattern Recognition (CVPR)*, pp. 2110–2118, Las Vegas, NV, June 2016.
- [10] Y. Wu, Y. Liu, J. Li, H. Liu, and X. Hu, "Traffic sign detection based on convolutional neural networks," in *The 2013 International Joint Conference on Neural Networks (IJCNN)*, pp. 1–7, Dallas, TX, 2013.
- [11] Y. Zhu, C. Zhang, D. Zhou, X. Wang, X. Bai, and W. Liu, "Traffic sign detection and recognition using fully convolutional network guided proposals," *Neurocomputing*, vol. 214, pp. 758–766, 2016.
- [12] J. Li and Z. Wang, "Real-time traffic sign recognition based on efficient CNNs in the wild," *IEEE Transactions on Intelligent Transportation Systems*, vol. 20, no. 3, pp. 975–984, 2019.
- [13] Y. Yang, H. Luo, H. Xu, and F. Wu, "Towards real-time traffic sign detection and classification," *IEEE Transactions on Intelligent Transportation Systems*, vol. 17, no. 7, pp. 2022–2031, 2016.
- [14] C. Li, Z. Chen, Q. M. J. Wu, and C. Liu, "Deep saliency with channel-wise hierarchical feature responses for traffic sign detection," *IEEE Transactions on Intelligent Transportation Systems*, vol. 20, no. 7, pp. 2497–2509, 2019.
- [15] T. Yang, X. Long, A. K. Sangaiah, Z. Zheng, and C. Tong, "Deep detection network for real-life traffic sign in vehicular networks," *Computer Networks*, vol. 136, pp. 95–104, 2018.
- [16] S. Mehta, M. Rastegari, L. Shapiro, and H. Hajishirzi, "Esp-netv2: a light-weight, power efficient, and general purpose convolutional neural network," in *2019 IEEE/CVF Conference on*

- Computer Vision and Pattern Recognition (CVPR)*, pp. 9190–9200, Long Beach, CA, USA, June 2019.
- [17] S. Ren, K. He, R. Girshick, and J. Sun, “Faster R-CNN: towards real-time object detection with region proposal networks,” *IEEE Transactions on Pattern Analysis and Machine Intelligence*, vol. 39, no. 6, pp. 1137–1149, 2017.
- [18] J. Zhang, Z. Xie, J. Sun, X. Zou, and J. Wang, “A cascaded R-CNN with multiscale attention and imbalanced samples for traffic sign detection,” *IEEE Access*, vol. 8, pp. 29742–29754, 2020.
- [19] J. Zhang, W. Wang, C. Lu, J. Wang, and A. K. Sangaiah, “Light-weight deep network for traffic sign classification,” *Annals of Telecommunications*, 2019.
- [20] H. Zhang, K. Wang, Y. Tian, C. Gou, and F.-Y. Wang, “MFR-CNN: incorporating multi-scale features and global information for traffic object detection,” *IEEE Transactions on Vehicular Technology*, vol. 67, no. 9, pp. 8019–8030, 2018.
- [21] Z. Cai, Q. Fan, R. S. Feris, and N. Vasconcelos, “A unified multi-scale deep convolutional neural network for fast object detection,” in *European Conference on Computer Vision*, pp. 354–370, Springer, 2016.
- [22] C. Cao, B. Wang, W. Zhang et al., “An improved faster R-CNN for small object detection,” *IEEE Access*, vol. 7, pp. 106838–106846, 2019.
- [23] J. Li, X. Liang, Y. Wei, T. Xu, J. Feng, and S. Yan, “Perceptual generative adversarial networks for small object detection,” in *2017 IEEE Conference on Computer Vision and Pattern Recognition (CVPR)*, pp. 1951–1959, Honolulu, HI, 2017.
- [24] J. Wei, J. He, Y. Zhou, K. Chen, Z. Tang, and Z. Xiong, “Enhanced object detection with deep convolutional neural networks for advanced driving assistance,” *IEEE Transactions on Intelligent Transportation Systems*, vol. 21, no. 4, pp. 1572–1583, 2020.
- [25] T. Lin, P. Dollár, R. Girshick, K. He, B. Hariharan, and S. Belongie, “Feature pyramid networks for object detection,” in *2017 IEEE Conference on Computer Vision and Pattern Recognition (CVPR)*, pp. 936–944, Honolulu, HI, 2017.
- [26] W. Liu, D. Anguelov, D. Erhan et al., “Ssd: single shot multibox detector,” in *Computer Vision – ECCV 2016*, pp. 21–37, Springer, 2016.
- [27] A. G. Howard, M. Zhu, B. Chen et al., *MobileNets: efficient convolutional neural networks for mobile vision applications*, CoRR, 2017.
- [28] O. Russakovsky, J. Deng, H. Su et al., “Imagenet large scale visual recognition challenge,” *International Journal of Computer Vision*, vol. 115, no. 3, pp. 211–252, 2015.
- [29] M. Sandler, A. Howard, M. Zhu, A. Zhmoginov, and L.-C. Chen, “Mobilenetv2: inverted residuals and linear bottlenecks,” in *2018 IEEE/CVF Conference on Computer Vision and Pattern Recognition*, pp. 4510–4520, Salt Lake City, UT, USA, June 2018.
- [30] X. Zhang, X. Zhou, M. Lin, and J. Sun, “Shufflenet: an extremely efficient convolutional neural network for mobile devices,” in *2018 IEEE/CVF Conference on Computer Vision and Pattern Recognition*, pp. 6848–6856, Salt Lake City, UT, USA, June 2018.
- [31] C. Y. Fu, W. Liu, A. Ranga, A. Tyagi, and A. C. Berg, “DSSD : deconvolutional single shot detector,” 2017, <https://arxiv.org/abs/1701.06659>.
- [32] K. He, X. Zhang, S. Ren, and J. Sun, “Deep residual learning for image recognition,” in *2016 IEEE Conference on Computer Vision and Pattern Recognition (CVPR)*, pp. 770–778, Las Vegas, NV, USA, June 2016.
- [33] F. Yu and V. Koltun, “Multi-scale context aggregation by dilated convolutions,” 2015, <https://arxiv.org/abs/1511.07122>.
- [34] S. Houben, J. Stallkamp, J. Salmen, M. Schlipsing, and C. Igel, “Detection of traffic signs in real-world images: the German traffic sign detection benchmark,” in *The 2013 International Joint Conference on Neural Networks (IJCNN)*, pp. 1–8, Dallas, TX, USA, August 2013.
- [35] K. Simonyan and A. Zisserman, “Very Deep deep Convolutional convolutional Networks networks for Large-scale Image image Recognition,” 2014, <https://arxiv.org/abs/1409.1556>.